A Circular Aperture Array for Ultrasonic Tomography and Quantitative NDE

Nielsen, Steen Arnfred

Publication date:
1998

Document Version
Publisher's PDF, also known as Version of record

RISØ DK9901015

Risø-R-1057(EN)

A Circular Aperture Array for Ultrasonic Tomography and Quantitative NDE

Steen Arnfred Nielsen

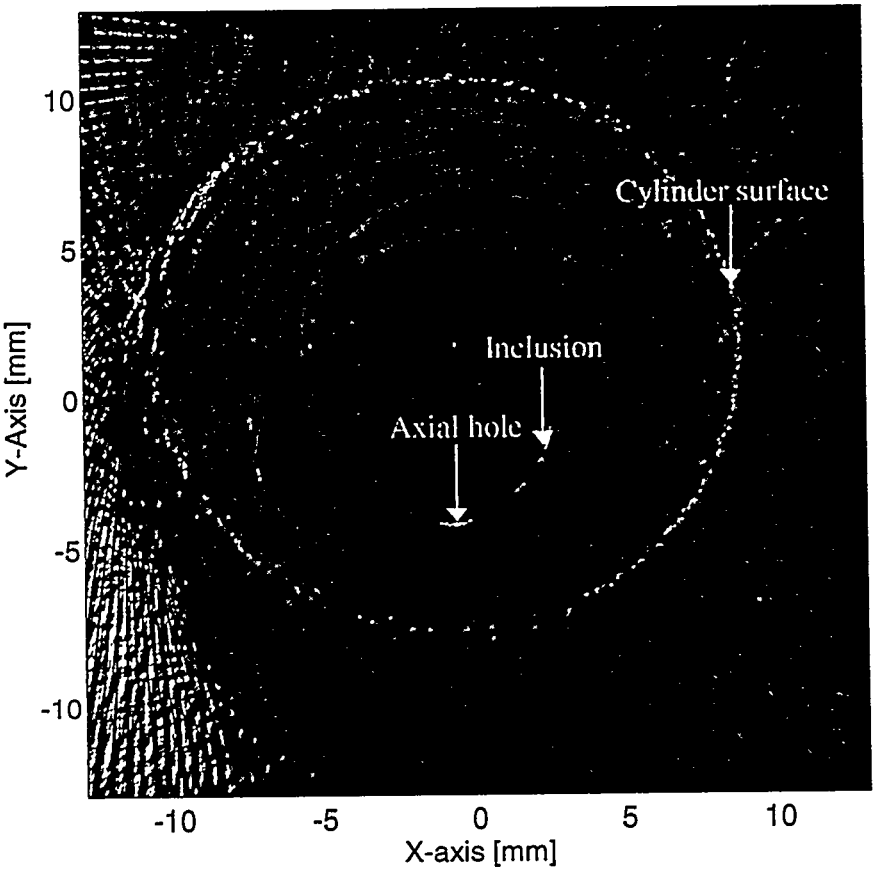

Risø National Laboratory, Roskilde, Denmark
August 1998

DISCLAIMER

Portions of this document may be illegible in electronic image products. Images are produced from the best available original document.

Risø-R-1057(EN)

A Circular Aperture Array for Ultrasonic Tomography and Quantitative NDE

Steen Arnfred Nielsen

Risø National Laboratory, Roskilde, Denmark
August 1998

Abstract. The main topics of this thesis are ultrasonic tomography and ultrasonic determination of elastic stiffness constants. Both issues are based on a synthetic array with transducer elements distributed uniformly along a circular aperture, i.e., a circular aperture array. The issues are treated both theoretically and experimentally by broadband pulse techniques.

Ultrasonic tomography from a circular aperture is a relatively new imaging technique in Nondestructive Evaluation (NDE) to acquire cross sectional images in bulk materials. In this thesis, experimental methods are demonstrated to reveal discontinuities in cylindrical Plexiglas specimens and *AlSi*-alloys.
Theoretical models for ultrasonic computed (projection) tomography, UCT, to acquire cross sectional images in bulk materials, are reviewed in relation to quantitative material parameters. A filtered backprojection algorithm is used to reconstruct images in four different experiments and results of attenuation, velocity and reflection tomograms in Plexiglas or *AlSi*-alloy cylinders are presented.
Two kinds of ultrasonic tomography are introduced: bistatic and monostatic imaging. Both techniques are verified experimentally by Plexiglas cylinders. Different reconstruction artifacts are discussed and theoretical resolution constraints are discussed for various configurations of the circular aperture array. The monostatic technique is used in volumetric imaging. In the experimental verification artificial and real discontinuities in a cylindrical *AlSi*-alloy are compared with similar discontinuities in a Plexiglas specimen. Finally, some limitations to UCT are discussed.

An ultrasonic method is presented to determine the elastic stiffness constants of fiber reinforced composites. The circular aperture array is used to determine five independent elastic stiffness constants of a unidirectional glass/PET (Poly Ethylene Teraphthalate) laminate.
Wave propagation in anisotropic materials with emphasis on fiber reinforced composites is discussed. Energy flux propagation and attenuation of ultrasonic waves are considered and velocity surfaces are calculated for different planes of interest. Relations between the elastic stiffness constants of a fiber reinforced composite and the elastic engineering constants of its constituents (fiber and matrix) are presented. Relations between elastic stiffness constants and engineering constants (i.e., Young's moduli, shear moduli and Poisson's ratios) are discussed for an orthotropic composite. Six micromechanical theories are reviewed, and expressions predicting the elastic engineering constants are evaluated. The micromechanical predicted elastic stiffness constants for the unidirectional glass/PET laminate are compared with ultrasonic and mechanical test results. Finally, the capabilities and limitations of the applied ultrasonic method are discussed.

Keywords: Synthetic circular aperture array, ultrasonic tomography, elastic stiffness constants, anisotropic fiber reinforced composites, broadband pulse techniques, immersion ultrasonic methods.

The cover picture shows an ultrasonic reflection tomogram acquired from a circular aperture array. The tomogram (i.e. cross section) shows an inclusion and a similar artificial hole in a cylindrical *AlSi*-alloy. The hole was drilled parallel with the axis of the cylinder and used to compare with natural discontinuities in the material. The cross-sectional dimension of the cylinder surface is seen to be about 18 mm.

ISBN 87-550-2400-9
ISSN 0106-2840

Information Service Department, Risø, 1998

Dansk resumé. Dansk titel: "Et cirkulært apertur array til ultralydtomografi og kvantitativ NDE".
I denne afhandling diskuteres to emner: ultralydtomografi (UCT) og bestemmelse af elastiske stivhedskonstanter. Begge emner er baseret på et syntetisk array, hvor ultralydtransducere er placeret langs en cirkulær apertur, dvs. et cirkulært apertur array. Emnerne er beskrevet både teoretisk og eksperimentelt med henblik på at benytte pulsteknikker.

Ultralydtomografi, baseret på et cirkulært apertur array, er en relativ ny metode til ikke-destruktiv bestemmelser af diskontinuiteter i cylindriske komponenter. I denne afhandling er det vist hvorledes ultralydtomografien kan benyttes til at give snit-billeder (tomogrammer) gennem Plexiglas og *AlSi*-legeringer, således at f.eks. indeslutninger kan karakteriseres.
Projektionstomografi er præsenteret med teoretiske modeller med henblik på at rekonstruere kvantitative UCT-materialeparametre. Den samme algoritme (*filtered backprojection*) er benyttet til at rekonstruere ultralydtomogrammer i fire forskellige eksperimenter, hvor dæmpnings-, hastigheds- og refleksions-tomogrammer er præsenteret.
To forskellige teknikker, *bistatic* og *monostatic*, er benyttet i det cirkulære apertur array til at generere ultralydtomogrammer af cylindriske emner. Forskellige rekonstruktionsfejl samt opløsningsevner er diskuteret for forskellige konfigurationer af det cirkulære apertur array. Den *monostatiske* teknik er benyttet til 3D-tomografi. I det sidste eksperiment sammenlignes kunstige og "rigtige" fejl i en cylindrisk *AlSi*-legering med tilsvarende fejl i et Plexiglas emne. Begrænsninger i ultralydtomografi diskuteres.

Elastiske konstanter i anisotrope materialer kan også bestemmes ikke-destruktivt ved hjælp af det cirkulære apertur. Det er diskuteret hvorledes elastiske konstanter i et fiber forstærket kompositmateriale kan bestemmes, som et supplement til kvantitativ NDE. Det cirkulære apertur er benyttet til at bestemme fem elastiske stivhedskonstanter i et glas/PET (Poly Ethylene Teraphthalat) laminat.
Bølgeudbredelse i anisotrope materialer med særlig henblik på fiberforstærkede kompositter er diskuteret. Energiflux og dæmpning af ultralydbølger er behandlet og hastighedprofiler er beregnet for forskellige kompositplaner. Relationer for elastiske stivhedskonstanter og ingeniør-konstanter er diskuteret for en orthotrop komposit. Seks mikromekaniske teorier for glas/PET laminatet er sammenlignet med ultralydresultaterne og mekaniske testresultater. Muligheder og begrænsninger er diskuteret for denne metode.

Nøgleord: syntetisk cirkulært apertur array, ultralydtomografi, elastiske stivhedskonstanter, anisotrope fiberforstærkede kompositter, pulsteknikker, immersion ultralydmetoder.

Contents

Appendices 139

List of Figures, Tables and Nomenclature 155

Photo Gallery 161

Preface

This dissertation has been submitted to the Technical University of Denmark (DTU) in partial fulfillment of the requirements for the degree of Doctor of Philosophy (Ph.D.).

The present Ph.D. study has mainly been carried out at the Materials Research Department (AFM), Risø National Laboratory (RISØ), Denmark in the period from February 1995 to August 1998. Within this period I was on parental leave and my Ph.D. study was equivalently prolonged. The study has been financed partly by The Danish Research Academy and partly by RISØ. The project has been supervised by:

Professor Leif Bjørnø, Department of Industrial Acoustics, DTU
Senior Scientist Svend Ib Andersen, AFM
Senior Scientist Jørgen T. Rheinländer, AFM
Project Manager Hans Erik Gundtoft, AFM.

Steen Arnfred Nielsen

Risø, August 1998

Acknowledgement

First of all I would like to thank my supervisors: Svend Ib Andersen, Jørgen T. Rheinländer and Hans Erik Gundtoft (AFM) for their continued support during the preparation of this thesis. Their research fields: Composite materials, Image processing and Non-destructive testing, have greatly inspired this thesis. I am also deeply indebted to Leif Bjørnø (DTU) for encouraging me to start this project and for helping me, whenever it was necessary. His knowledge of acoustical issues has been a great inspiration to me.

Furthermore, I would like to thank Prof. Hua Lee and Prof. Keith Kedward, for an inspiring visit to University of California at Santa Barbara (USCB). Hua Lee and Keith Kedward represent the leading scientists in the field of image processing and composite materials, respectively, and I had the opportunity to discuss fundamental issues which appear in this thesis. Keith Kedward was also so kind to introduce me to the laboratory facilities at McDonnell Douglas Aerospace, Long Beach, USA. I would like to thank Dr. Hagemaier, Dr. Masood Zaidi and Mr. Kent Rengel for there collaboration.
In addition several people have contributed with inspiring discussions: Dr. Lewis and Dr. Kent, USCB; Prof. Robert C. Waag, University of Rochester; Prof. Michel P. André, University of California, San Diego; Dr. Richard Chiao, General Electric; and Mr. Hass from IBT, Germany. I am especially grateful to Kaj Borum and Keld Lillegaard (AFM) for their practical assistance.

Finally, I would like to express my sincere gratitude to my wife Birgitte and my children Rune and Freja for their patience, understanding and encouragement during the Ph.D.-period.

1 Introduction

1.1 Background

The history of ultrasound, and mechanical wave propagation, is interesting and quite challenging. Ultrasound began as a discipline of physics, but found a practical application in underwater acoustics, as the sonar was introduced in the First World War. It became quickly a multipurpose tool for a variety of medical and non-destructive evaluation (NDE) problems.

Today, NDE problems may be divided into two groups. The first group of problems is associated with qualitative material parameters. For example, a relative image parameter that characterize *defects* (i.e., flaws, inclusions, cracks and voids) in a material.

The second group of problems is associated with quantitative material parameters. For example, an absolute determination of density, attenuation, velocity or elastic constants.

1.2 Scope and limitations of thesis

The main purpose of the present thesis is to give a theoretical and experimental description of a circular aperture system and its applications to ultrasonic tomography and to quantitative NDE.

The work is carried out under the following restrictions:

Ultrasonic tomography is discussed for isotropic and homogeneous Plexiglas specimens and *AlSi*-alloys. The ultrasonic velocity, attenuation and reflection projections (i.e., line integrals) are reconstructed using a filtered backprojection algorithm.

The point spread function for the backprojection process is presented, assuming point sources in a circular aperture array.

The elastic stiffness constants are discussed for an orthotropic or transverse isotropic fiber reinforced composite. Especially, elastic stiffness constants in a unidirectional glass/PET laminate are discussed.

The spelling and grammar in the thesis is intended to be *American* English.

1.3 Outline of thesis

The thesis is divided into four chapters, that may be read independently. The general structure of the thesis is illustrated in Fig. 1.1. The chapters 2 and 3 are devoted to ultrasonic tomography. The chapters 4 and 5 are devoted to ultrasonic determination of elastic stiffness constants.

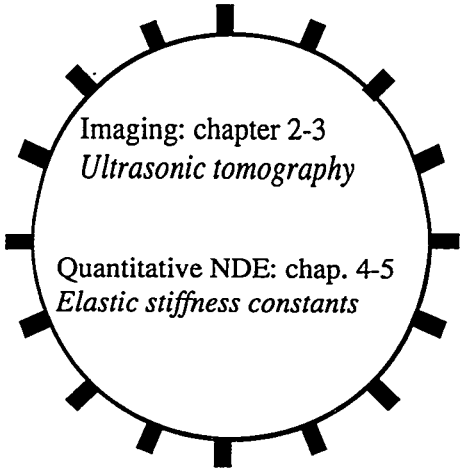

Figure 1.1. Principle structure in thesis.

The thesis is composed as follows:

In chapter 2, an ultrasonic imaging technique is discussed for generating two-dimensional cross-sections in cylindrical shaped materials. The technique is based on ultrasonic projections and is referred to as ultrasonic computed tomography (UCT). First, UCT is compared with conventional ultrasonic techniques and X-ray tomography. Some general requirements to the implementation of the UCT-technique are then discussed. Second, ultrasonic projection theory is reviewed in relation to quantitative material parameters and image reconstruction from projections are presented.
In the experimental technique (I), attenuation and velocity tomograms are presented of an elliptical hole positioned in a Plexiglas cylinder. A filtered backprojection algorithm is implemented with the choice of four different filters. Two different measurement strategies of time of flight projections are considered. High directive, broadband, transducers are applied for data acquisition and straight line propagation is assumed. See NIELSEN *et al.* (1995*a*). Experimental obtained attenuation and velocity tomograms are presented and compared with a theoretical model for the specific cases. See NIELSEN *et al.* (1995*b*).

In chapter 3, ultrasonic imaging techniques are discussed using a synthetic array with transducer elements distributed uniformly along a circular aperture. The circular aperture array is realized by object rotation and ultrasonic signals are acquired via two single mobile transducers, acting respectively as transmitter and/or receiver. Sound field parameters of two broadband, focused transducers are presented.
First, two kinds of ultrasonic tomography are introduced: bistatic and monostatic imaging. In the bistatic technique (II), diverging ultrasonic beams are used to insonify the cylindrical specimen, and the resultant transmitted signals are recorded by only considering received signals measured over a sector. In the monostatic technique (III) backscattered data are reconstructed using a backprojection technique. Both techniques are applied for imaging the same Plexiglas cylinders as used in chapter 2. See NIELSEN *et al.* (1997*a*).
Second, different reconstruction artifacts associated with UCT-tomograms are discussed, and theoretical resolution criteria are discussed for various configurations of the circular aperture array. An expression is derived for the lateral resolution and the point spread function is presented for an optimum pulse in the monostatic case.

In the experimental technique (IV), artificial and real discontinuities in a cylindrical *AlSi*-alloy are compared with similar discontinuities in a Plexiglas specimen. Several discontinuity types in Plexiglas and *AlSi*-alloy cylindrical specimens are studied by three different ultrasonic imaging techniques. See NIELSEN *et al.* (1998*a*). First, the synthetic circular aperture array is used to obtain circular C-scan images. These images displays the location of different discontinuity types. Second, reflection tomograms are generated from circular B-scan profiles (i.e., monostatic imaging). A relatively fast reconstruction algorithm is applied, based on the straight beam approximation. This approximation is assumed due to broadband, high frequency pulse propagation. Finally, by volumetric imaging: Three-dimensional information is obtained by stacking reflection tomograms from multiple planes. Finally, limitations to the UCT technique are discussed.

Chapter 4 discusses relations between the elastic stiffness constants of a fiber reinforced composite and the elastic engineering constants of its constituents (fiber and matrix). The aim is to identify the elastic stiffness constants for a unidirectional glass/PET (Poly Ethylene Teraphthatate) laminate.
First, a short introduction to fiber reinforced composites is given and terms like continuous fibers and unidirectional laminates are discussed. A classification scheme is then presented, in which the composites are divided according to layers, fiber length and fiber orientation. Second, parameters that may influence the elastic properties of the fiber reinforced composite are discussed. Fiber orientation, fiber concentration, composite homogeneity and elastic properties of the constituents are discussed. The glass/PET laminate is then introduced by microscope (ESEM) pictures.
Third, the number of elastic stiffness constants for four significant types of fiber reinforced composites are reviewed: general anisotropic, orthotropic, transverse isotropic and isotropic. Relations between elastic stiffness constants and engineering constants (i.e., Young's moduli, shear moduli and Poisson's ratios) are discussed for an orthotropic composite. Elastic engineering constants are combined to the fiber volume fraction. Six sets of equations predicting the engineering elastic constants are given. The theoretical elastic stiffness constants for the unidirectional glass/PET laminate are compared with experimentally obtained constants.

Chapter 5 presents an ultrasonic immersion method to determine the elastic stiffness constants of fiber reinforced composites. See NIELSEN *et al.* (1998*b*). The aim with this chapter is to identify the stiffness constants for the unidirectional glass/PET laminate and compare them with the micromechanical predictions and the mechanical test results discussed in chapter 4. The main component in the method is the circular aperture array introduced in chapter 3.
First, an introduction to qualitative and quantitative ultrasonic evaluation of anisotropic materials is given. Second, the theory of wave propagation in anisotropic materials is reviewed with emphasis on fiber reinforced composites. Energy flux propagation and attenuation of ultrasonic waves are considered and velocity surfaces are calculated for different planes of interest. It is shown how the Christoffel equation can be applied to determine nine elastic constants of orthotropic composites. Three ultrasonic waves are possibly: two quasi-waves and one pure wave. However, for special directions all these waves are pure. Energy flux propagation and attenuation of ultrasonic waves were considered and velocity surfaces were calculated, in two planes, for the three wave types. The deviation of energy flux propagation from the wave propagation is considered. Third, experimental methods that previously have been used to determine elastic stiffness constants are discussed. Contact and immersion methods in

combination with reflection and transmission methods are discussed, to determine the elastic stiffness constants. The circular aperture array is then used to determine the five independent elastic stiffness constants of the unidirectional glass/PET laminate. See NIELSEN *et al.* (1998*c*).
The obtained results are compared with a model for transverse isotropic materials. The capabilities and limitations of the applied ultrasonic method are also discussed. See NIELSEN *et al.* (1997*b*).

1.4 References in personal bibliography

NIELSEN, S.A. and BJØRNØ, L. (1995*a*). A broadband, high-frequency ultrasonic bistatic transducer. 18th Scandinavian Symposium in Physical Acoustics, Norway, 15-17.

NIELSEN, S.A.; BORUM, K.K. and GUNDTOFT, H.E. (1995*b*). Verifying an ultrasonic reconstruction algorithm for non-destructive tomography. Proc. 1st World Conference on Ultrasonics, Germany, 447-450.

NIELSEN, S.A. and BJØRNØ, L. (1997*a*). Bistatic circular array imaging with gated ultrasonic signals. Acoustical Imaging, Vol. 23, Edited by Lees and Farrari, Plenum Press, 441-446.

NIELSEN, S.A. and ANDERSEN, S.I. (1997*b*). Ultrasonic determination of elastic constants of fiber reinforced composites using a circular aperture array of transducers. Proc. of Polymeric Composites - Expanding the Limits, Denmark, 455-464.

NIELSEN, S.A.; RHEINLÄNDER, J.T.; BORUM, K.K. and GUNDTOFT, H.E. (1998*a*). Three-dimensional ultrasonic reflection tomography of cylindrical shaped specimens. European Conf. on NDT and Exhibition, Denmark, 2458-2465.

NIELSEN, S.A.; ANDERSEN, S.I. and BRØNSTED, P. (1998*b*). Immersion ultrasonic method to measure elastic constants in fiber reinforced composite material. 4th European Conference on Composites, ECCM CTS-4 Testing and Standarisation, Portugal, 71-79.

NIELSEN, S.A.; ANDERSEN, S.I. and TOFTEGAARD, H. (1998*c*). An ultrasonic circular aperture technique to predict elastic constants of fiber reinforced composites. Acoustical Imaging, Vol. 24, Edited by H. Lee, Plenum Press (In Press).

BJØRNØ, L. and NIELSEN, S.A. (1994). A novel broadband, high-frequency ultrasonic transducer. 11th Int. FASE Symp., Valencia, 81-84.

RHEINLÄNDER, J.T.; NIELSEN, S.A.; BORUM, K.K. and GUNDTOFT, H.E. (1997). NDE of polymeric composites: a comparison of techniques. Proc. of Polymeric Composites - Expanding the Limits, Denmark, 101-125.

GUNDTOFT, H.E.; BORUM, K.K. and NIELSEN, S.A. (1998). On-line eccentricity measurements during fabrication of aluminium tubes. European Conf. on NDT and Exhibition, Denmark, 3152-3159.

BORUM, K.K.; GUNDTOFT, H.E.; RHEINLÄNDER, J.T.; NIELSEN S.A.; BAGGER, C. and LINDEROTH, S. (1998). Non-destructive evaluation of ceramics used for solid oxide fuel cells. European Conf. on NDT and Exhibition, Denmark, 959-966.

2 Ultrasonic Computed Tomography

In this chapter, an ultrasonic imaging technique is discussed for generating two-dimensional cross-sections in cylindrical shaped materials. The technique is based on ultrasonic projections and will be referred to as ultrasonic computed tomography (UCT).
Section 2.1 compares UCT with conventional ultrasonic techniques and X-ray tomography. Some general requirements to an implementation of the UCT-technique are discussed. In section 2.2, ultrasonic projection theory is reviewed in relation to quantitative material parameters. Section 2.3 describes image reconstruction from projections. The Fourier Slice Theorem and a filtered back-projection algorithm are discussed. The latter is verified by experiment (I). Results of attenuation and velocity tomograms are presented in section 2.4. Section 2.5 summarizes this chapter.

2.1 Introduction to ultrasonic computed tomography (UCT)

Ultrasonic computed tomography (UCT) is a relatively new imaging technique in nondestructive evaluation (NDE) of solid materials, but has been used in medical diagnostics for several years. It offers an improved characterization of discontinuities (inhomogeneties or defects) compared to the conventional A-, B- and C-scan technique. See, e.g., KRAUTKRÄMER *et al.* (1990) and BIRKS *et al.* (1991). In the UCT-technique, solid materials under investigation are insonified by ultrasound and the transmitted (or reflected) signals are, in principle, used to reconstruct a two-dimensional cross-sectional tomogram in the material. A tomogram is simply a picture of a slice. Tomo comes from the Greek word *tomos*, meaning slice, and gram refers to a graphical representation. Ideally, this tomogram relates the material structure within an infinitesimal thin two-dimensional cross-sectional plane without any interference from other planes. Furthermore, the tomogram may be displayed in the material at any desired location and with any desired orientation.

Ultrasonic computed tomography is different from the conventional ultrasonic techniques. While, for example, C-scan images are obtained from one direction (projection) through a material, UCT-images are normally generated from several directions in order to construct the tomogram. Thus, the UCT-technique eliminates the superposition (overlapping) of features that may occur when a three-dimensional structure is displayed in a two-dimensional image format. This superposition makes discontinuity detection more difficult because discontinuities outside the plane of interest are included. As a result, the discontinuity cannot be distinguished from other discontinuities. This means, that a C-scan image only shows a shadow of all discontinuities in a specified direction, while an UCT tomogram may display a much more detailed image of a single slice in the material. Therefore, compared with the C-scan image, the UCT-tomogram may improve the physical characterization of internal discontinuities in the material.
However, an UCT-tomogram is the result of an advanced digital processing procedure on UCT-projections, whereas a C-scan image requires virtually no data processing at all. Using computers to reconstruct the tomogram, also provides access to image enhancement algorithms (ERMERT *et al.* 1995).

The tomogram may be extended to three dimensions. One can insonify the whole volume of the material and reconstruct the three-dimensional image directly. See, e.g., SIRE *et al.* 1991. The more conventional technique is, however, the indirect one of insonifying one slice in the material at a time and reconstructing separate two-dimensional tomograms of them. By stacking several of these two-dimensional tomograms a three-dimensional image can be formed. This will be discussed in chapter 3. Despite some advantages, the direct three-dimensional reconstruction approach was not attempted because of the experimental and computing difficulties involved. Furthermore, the cost of two-dimensional arrays and, e.g., multiplexing hardware is not at the present time justifiable for most NDE applications.

2.1.1 UCT compared with X-ray CT

In this chapter, the UCT-technique is discussed based on ultrasonic broadband techniques and the principles of the well-established X-ray computed tomography (X-ray CT). Although this section is about UCT some comments on X-ray CT may clarify and aid the understanding of ultrasonic tomography. The principles in X-ray CT are the following: the intensity of a collimated X-ray beam passing through the material is measured by an array of detectors located on the other side of the material. The material is then rotated slightly, and a new set of measurements is made; this process is repeated until the material has been rotated 180°. The measured projections are processed by a computer, according to a reconstruction algorithm, to produce a tomogram of the X-ray attenuation coefficients in the irradiated cross section.
This reconstruction algorithm is based on the discovery by the Austrian mathematician RADON (1917). He proved that a three-dimensional object can be reconstructed uniquely from an infinite set of its projections. In practice, however, an infinite set of projections cannot be obtained and a finite (discrete) set must be used.
The area that has benefited most from this information retrieval technique is medical X-ray diagnosis. See, e.g., BLYTH *et al.* (1979), NAHAMOO *et al.* (1981). Although some examples of X-ray CT applied to metals and polymeric materials are found in e.g. PHILLIPS *et al.* (1997), ARMISTEAD *et al.* (1989) and PERSSON *et al.* (1983). Consequently, the inventors of X-ray CT, Hounsfield and Cormack, were awarded the 1972 Nobel Prize for Physiology and Medicine for their achievements (WADE 1980). Recently, attempts to make three-dimensional X-ray CT for medical applications have been performed using a cone beam reconstruction. See, e.g., MARTZ *et al.* (1993).

The UCT-technique has some technical advantages over X-ray CT. Whereas, X-ray CT characterizes materials by attenuation measurements only, UCT may involve either ultrasonic velocity, attenuation or reflection measurements. Furthermore, in contrast to X-ray CT, UCT is more effective due to its high penetration depth. Unfortunately, there are some major differences between the propagation of ultrasound and X-radiation, even for isotropic materials, which makes it difficult to apply UCT-imaging to NDE. The interaction of ultrasound with materials of NDE interest involves considerable refraction (see, e.g., ROSE *et al.* 1990 and BETTS *et al.* 1995) as well as: attenuation (TSAO 1983), reflection, scattering, and diffraction. See MUELLER *et al.* (1979, 1980) and CAPINERI *et al.* (1988, 1992).
Refraction, in particular, is much more significant with ultrasound than with X-rays. When an ultrasonic wave propagates through a material it undergoes refraction at almost every interface between material layers of different refractive index (i.e., relative sound velocity). This may lead to bending of the ultrasonic

beam. Thus, in contrast to X-rays and X-ray CT, UCT-imaging is made difficult by the fact that rays of ultrasonic energy do not necessarily travel along straight lines.
Diffraction and scattering are also far more important for ultrasound than for X-rays because of the wavelength differences between X-rays and ultrasound.
Finally, the ultrasonic beam can also be totally reflected at strong boundaries (e.g. water/solid interface), which may degrade the final tomogram. At weak boundaries (e.g. water/tissue interface), the ultrasonic beam may also be transmitted or reflected. Transmission and reflection are, therefore, two types of ultrasonic tomography representing different material parameters. Transmission tomography is similar to the well known *through-transmission* technique. Reflection tomography is in principle similar to the *pulse echo* technique and will be discussed further in chapter 3. Transmission tomography can be subdivided into two types depending on the material properties. If the speed-of-sound through the material is constant, then the attenuation at each pixel is the parameter to be determined (which is similar to X-ray CT). If the attenuation of the ultrasonic wave remains small throughout the material, then the speed-of-sound at each pixel is the parameter to be determined.
The above mentioned disadvantages are even more serious in materials containing gas filled voids or in anisotropic structures (see chapter 4 and 5).

2.1.2 UCT requirements

The implementation of the UCT-technique requires scanning hardware and the corresponding reconstruction software, as seen diagrammatically in Fig. 2.1. The scanning hardware consists of two main parts. The first part is the data *acquisition* system, which registers amplitude and time of arrival of the ultrasonic signals as well as the position of the measurement. Depending on the scanning requirements and the geometry of the specimen to be examined, either a single or an array of transducers can be used. The single transducer may perform either linear or circular scanning, or it may follow the profile of the specimen. The data are digitized and sent to a computer for further analysis together with scanning data; e.g., the number of transducers used, the scanning and the sampling rate of the digitizer. The second part is the storage system, which acquires the scanned data (i.e. the ultrasonic projections) and stores in a required format.
In the computer, the scanned data are processed (reconstructed) and arranged according to a required format using a *reconstruction* algorithm. It is through this algorithm that the computer converts the obtained data into a recognizable tomogram. Finally, the UCT-tomogram can be displayed in a two- or three-dimensional plot or shown on a TV screen.

In conclusion, there are two main tasks in UCT. One is to acquire information about the slice from ultrasonic projections. The other is to use the information to compute an image of the slice using a suitable reconstruction algorithm. The two tasks are dedicated to the next two sections.

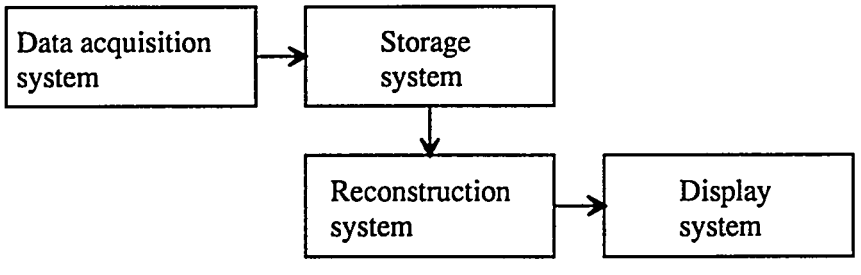

Figure 2.1. Requirements for ultrasonic computed tomography.

2.2 Ultrasonic projections

Ultrasonic imaging has been applied mainly for medical applications. See, e.g., HAVLICE *et al.* (1979), WADE (1980), DEANS *et al.* (1983), SEHGAL *et al.* (1988) and KARPELSON *et al.* (1990). But it has also been applied for seismic applications. See LYTLE *et al.* (1980), BISHOP *et al.* (1985), BREGMAN *et al.* (1989) and HATTON *et al.* (1990). These investigators were among the first to examine ultrasonic imaging theoretically and a few of them experimentally.
Only a few publications discuss the applications of ultrasonic imaging to NDE of polymeric materials, such as: isotropic polymers (see, e.g., TSAO 1983, CROSTACK *et al.* 1988 and ROSE *et al.* 1990, KLINE *et al.* 1989 and 1990) and anisotropic polymers, e.g., fiber reinforced composites (see, e.g., KLINE *et al.* 1992 and 1993, CHOW *et al.* 1993, WANG *et al.* 1992 and 1994). See also KINO (1979), HUTCHINS *et al.* (1989) and JANSEN *et al.* (1993) for a comprehensive review of the UCT-technique to metals.

Considering the arrangement of the ultrasonic transducers, UCT can, as mentioned, be classified into two categories: transmission and reflection tomography. Transmission tomography is, in principle, effective in the determination of a small variation in density of the material, such as residual stresses in a structural specimen (HILDEBRAND *et al.* 1981). In this chapter, it will be used to determine attenuation and speed-of-sound variations in a Plexiglas cylinder. Reflection tomography is most effectively used in characterization of the locations and sizes of discontinuities, but it may also, e.g., be used to characterize the configurations of voids in an otherwise homogeneous material (TSAO 1983). Reflection tomography will be discussed in chapter 3.

2.2.1 Radon transformation of ultrasonic attenuation

GREENLEAF *et al.* (1975) were the first to demonstrate that ultrasonic parameters can be combined into an image representing the distribution of quantitative material parameters. His group measured transmission-loss in liver and mapped the distribution of the attenuation coefficient. Later, BATES *et al.* (1979) and JAGO *et al.* (1991) have improved experimental transmission UCT for medical applications.
Two transducers are required in transmission tomography, as seen in Fig. 2.2; one to transmit ultrasonic pulses and another, on the opposite side of the specimen, to receive them. The transducers and the specimen are here immersed in water. There are essentially two kinds of measurements that can be made with these pulses. One possibility is to compare the transmitted and received pulse amplitudes. The other possibility is to measure ultrasonic time-of-flight. A mapping of one kind of these measurements will yield quite a different picture than that of the other kind.

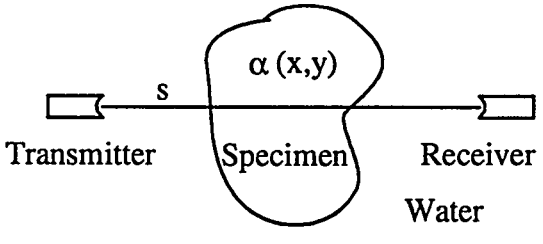

Figure 2.2. Transmission UCT in water.

Under the most ideal conditions (e.g., ignoring absorption in water), the pressure amplitude of the pulse at the transmitting transducer, p_t, may be related to the pressure amplitude of the pulse, p_r, at the receiving transducer

$$p_r = p_t \exp\left(-\int_{-\infty}^{\infty} \alpha(x,y)ds\right) \tag{2.1}$$

where $\alpha(x,y)$ is the attenuation coefficient along the line s in the Figure. The line (or ray) is defined by polar coordinates (ρ, θ) in Fig. 2.3.

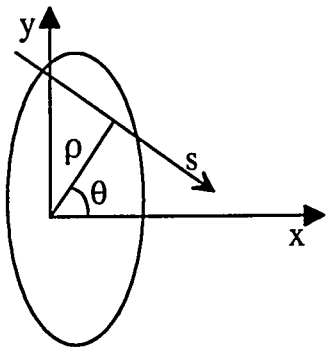

Figure 2.3. Polar coordinate system defining the line s.

The integral of $\alpha(x,y)$ along the line s is called a line integral and a set of line integrals forms a projection. From Eq. (2.1), the line integral $\langle p(\rho,\theta)\rangle$ is defined as

$$\langle p(\rho,\theta)\rangle = \ln\left(\frac{p_t}{p_r}\right) = \int_{-\infty}^{\infty} \alpha(x,y)ds \tag{2.2}$$

Using the polar coordinate system $(x,y) = (\rho\cos\theta - s\sin\theta, \rho\sin\theta + s\cos\theta)$, Eq. (2.2) becomes the original Radon transform

$$\langle p(\rho,\theta)\rangle = \int_{-\infty}^{\infty} \alpha(\rho\cos\theta - s\sin\theta, \rho\sin\theta + s\cos\theta)ds. \tag{2.3}$$

Now substituting $\rho = x\cos\theta + y\sin\theta$, Eq. (2.2) may be written as

$$\langle p(\rho,\theta)\rangle = \frac{1}{|\sin\theta|}\int_{-\infty}^{\infty} \alpha(x, \frac{\rho}{\sin\theta} - x\cot\theta)dx \tag{2.4}$$

and applying the Dirac delta function (i.e., the impulse function: $\delta(x) = 0$ if $x \neq 0$, $\delta(0) = \infty$ and $f(a) = \int_{-\infty}^{\infty} f(y)\delta(y-a)dy$, the projection can be simplified to

$$\langle p(\rho,\theta)\rangle = \frac{1}{|\sin\theta|}\int_{-\infty}^{\infty}\int_{-\infty}^{\infty} \alpha(x,y)\delta(y - \frac{\rho}{\sin\theta} + x\cot\theta)dxdy \tag{2.5}$$

giving the expression

$$\langle p(\rho,\theta)\rangle = \int_{-\infty}^{\infty}\int_{-\infty}^{\infty}\alpha(x,y)\delta(\rho - x\cos\theta - y\sin\theta)dxdy \qquad (2.6)$$

where $\langle p(\rho,\theta)\rangle$ can be recognized as the Radon transformed of $\alpha(x,y)$, denoted as $\langle p(\rho,\theta)\rangle = \Re\{\alpha(x,y)\}$. Thus, the Radon transform expresses a line integral along a straight line $\rho = x\cos\theta + y\sin\theta$ intersecting a finite region of a plane. A comprehensive review of the Radon transform is found in, e.g., HELGASON (1980), DEANS (1983), JAIN (1989) and TOFT (1991, 1994 and 1995).

A collection of parallel line integrals, as a function of ρ (for a given value of θ), defines a parallel projection of $\alpha(x,y)$ for the angle θ. The parallel projection can be measured, for example, by moving the transducers along parallel lines on opposite sides of the specimen, as shown in Fig. 2.4. The prototype discussed in this chapter for such imaging consists of a pair of transducers mounted on an assembly that moves linearly in steps of few millimeters; rotate about the center axis and can move up and down to scan different planes. See the experimental method (I).

An alternative way to generate projections is to integrate a function along a set of lines from a point source. Another setup developed in chapter 3 for such imaging assumes divergent rays, which propagate from a transmitter to a series of receivers arranged on an arc with a constant angular spacing (equiangular). Such projections are called fan-beam (divergent beam) projections (PETERS *et al.* 1977 and HORN 1979). See the experimental method (II).

The total angular range of scanning is about 180° with parallel projections and 360° with fan-beam projections (refer to section 2.3). However, rays from different fan-beam projections can be rearranged into set of parallel beam projections and then only 180° rotation is required. Therefore, an understanding of parallel projections and their reconstruction is very important in UCT.

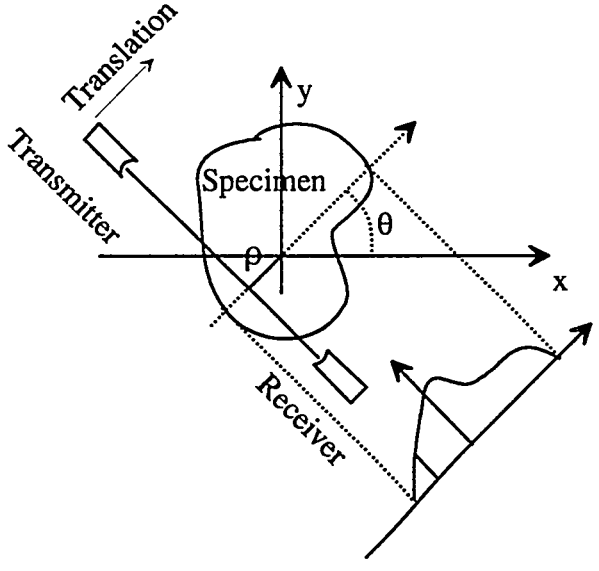

Figure 2.4. A single parallel projection created from a linear translation of ultrasonic transducers.

2.2.2 Radon transformation of ultrasonic velocity

The second possibility in transmission UCT is to measure the time for the pulse to travel between the transmitter and the receiver. These time-of-flight (TOF) measurements may be used to reconstruct an image of the velocity distribution within the specimen or, similar, an image of the index-of-refraction (GLOVER *et al.* 1977 and KAK 1988). As the sound velocity in an isotropic, homogeneous material is a function of the elastic moduli and density, and its quantity can be measured quite accurately, measurements of local speed-of-sound variations can be used to quantitatively characterize material microstructure. This is explained further in chapter 4 and 5.

Time-of-flight can be incorporated in transmission UCT by considering the simple linear model in Fig. 2.5.

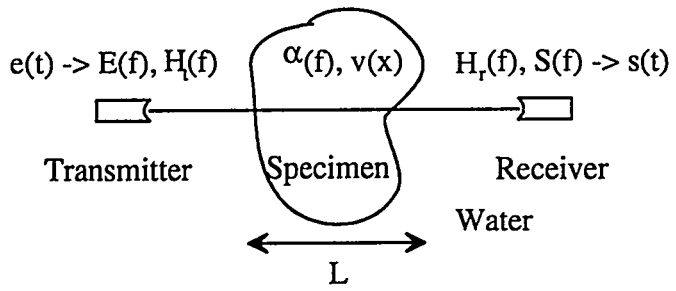

Figure 2.5. Model to incorporate time-of-flight projections in transmission UCT.

In this model, an impulse response, *e(t)*, is applied to the transmitting transducer with *E(f)* as it's Fourier transformed (frequency response). Let *s(t)* and *S(f)* be the impulse response and its Fourier transform, respectively, of the receiving transducer after propagation along a linear path, *L*, in an isotropic, homogeneous material.

The relation between *S(f)* and *E(f)* is

$$S(f) = E(f)H_t(f)H_r(f)\exp\left(-\int_L \left(\alpha(f) + i2\pi f\, v(x)^{-1}\right)dx\right) \qquad (2.7)$$

where $H_t(f)$ and $H_r(f)$ are the transfer functions of the transmitter and the receiver, respectively. $\alpha(f)$ is the attenuation coefficient and $v(x)$ the speed-of-sound, respectively, of the specimen. The Fourier transform of the received signal, without specimen, is

$$S_o(f) = E(f)H_t(f)H_r(f)\exp\left(-\int_L \left(i2\pi f\, v_o^{-1}\right)dx\right) \qquad (2.8)$$

where v_o is the velocity in water (ignoring absorption in water).
Inserting Eq. (2.8) in (2.7) gives

$$S(f) = S_o(f)\exp\left(-\int_L \alpha(f)dx\right)\exp\left(-i2\pi\int_L \left(v(x)^{-1} - v_o^{-1}\right)dx\right) \qquad (2.9)$$

which in signal (temporal) space can be written as

$$s(t) = s_o(t - \Delta t) \qquad \Delta t = v_o^{-1} \int_L (n(x) - 1) dx \tag{2.10}$$

Δt is the delay time between the two impulse responses (i.e., received pulses), with and without the specimen present and $n(x) = v_o / v(x)$ is the refractive index. Eq. (2.10) now meets the criteria for the Radon transform in that: (*i*) it defines a measurable quantity, Δt, that is given by a line integral of the reconstructable material parameter, $n(x)$-*1*, multiplied by a unit length, and (*ii*) the reconstruction parameter is zero everywhere outside the reconstruction region.

Expression (2.9) also shows that it is possible to connect the attenuation coefficient or refractive index (or, equivalently, the velocity) to the Radon transform and the two acoustic parameters can, therefore, be substituted by the parameter $\mu(x,y)$ (i.e., $\mu(x,y) = \alpha(x,y)$ or $\mu(x,y) = n(x,y)$). Thus, the idea in UCT is to measure $\mu(x,y)$ in a scanning plane and generate projections from sufficient directions. The image of these projections $\langle p(\rho,\theta) \rangle$ is called a *sinogram* (KAK 1979). The attenuation coefficient or refractive index in every point (pixel) can then be reconstructed from UCT projections using an inversion algorithm, which will be described in the next section.

2.3 Image reconstruction from projections

In all of its many forms, tomographical imaging is based on the concept that for radiation propagation through a material, whether electromagnetic or ultrasonic (i.e., X-ray CT or UCT), the quantities that can be measured experimentally (e.g., signal amplitude or time-of-flight) will be line integrals along the travel path. Thus, most reconstruction algorithms are based on the assumption, that projections are line integrals of the quantity of interest. The extent to which this assumption is violated determines the magnitude of artifacts visible in the tomogram. For the reconstruction of a two-dimensional tomogram from one-dimensional projections several algorithms may be used, and all may be regarded as techniques for approximating the inversion of the Radon transform. However, they are by no means all equivalent due to various approximations and numerical methods for computer implementation.

Three basic reconstruction classes may be identified for UCT, as seen in Fig 2.6:
(i) One reconstruction class is based on iterative methods and known as Algebraic Reconstruction Techniques (ART). In the basic ART one begins with a guess of a two-dimensional array of numbers representing the reconstructed cross section and then repeatedly modifies the guess in systematic fashion until the reconstruction quantity stop changing. Each time only one measurement is considered. The process continues until a chosen convergence criterion is satisfied or the number of iterations reaches a preset number. An early version of the ART using ray-tracing techniques was developed by JOHNSON *et al.* (1975) and used to reconstruct ultrasonic related parameters in highly refracting materials. A more comprehensive review of the ART is given by, e.g., HUANG *et al.* (1978), KLINE *et al.* (1989 and 1990), WANG *et al.* (1992 and 1994) and SUBBARAO *et al.* (1997).
(ii) Another reconstruction class is Fourier domain algorithms, which offers the advantage of faster image reconstruction compared to the iterative type algorithms. However, numerical artifacts due to interpolation can decrease the performance as noticed by CROSTACK *et al.* (1988). Fourier domain algorithms are based on the Fourier Slice Theorem, which provides a connection between the two-dimensional Fourier transform of a function, and the one-dimensional Fourier transform of the Radon transform of the function. The Fourier Slice Theorem is derived in section 2.3.1.
(iii) The third class is the filtered back-projection algorithms (RAMACHANDRAN *et al.* 1971, KAK 1979 and DEVANEY 1987), which is a combination of filtering and integration. The algorithm is computationally more efficient than the iterative type algorithms.

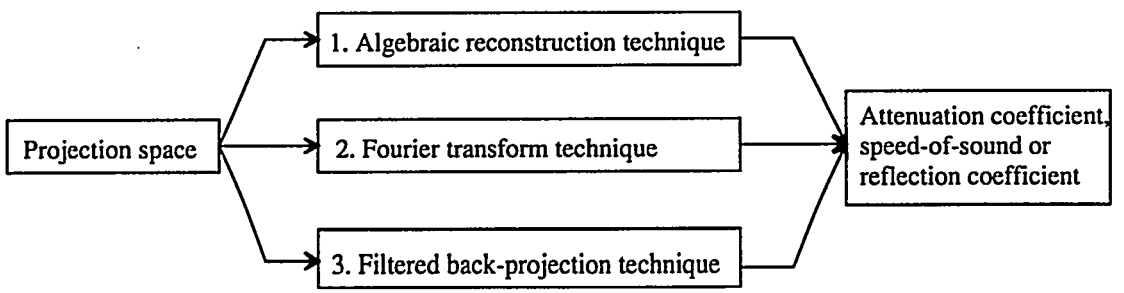

Figure 2.6. Three reconstruction algorithms for UCT, that determines a function from its projections.

The filtered back-projection algorithm has been chosen in this study because it is relatively simple to implement, gives reasonable short processing time, and allows some flexibility in the reconstruction via the choice of the projection filter. It is assumed that the projections are uniformly sampled, which is the case most often encountered in practice. The filtered back-projection algorithm is derived in section 2.3.2.

2.3.1 The Fourier Slice Theorem

The Fourier Slice Theorem (or Central Slice Theorem) makes it possible to reconstruct the Radon transform of a function by use of one-dimensional Fourier transforms and two-dimensional Fourier transforms. It can be proven in the following way: The two-dimensional Fourier transform of $\mu(x,y)$ is defined as (KAK 1979)

$$G(\sigma,\gamma)=\int_{-\infty}^{+\infty}\int_{-\infty}^{+\infty}\mu(x,y)\exp(-2i\pi(\sigma x+\gamma y))dxdy \tag{2.11}$$

where (σ,γ) is equal to $(\upsilon\cos\theta,\upsilon\sin\theta)$ in polar frequency parameters. Inserting these parameters in equation (2.11) gives

$$G(\upsilon\cos\theta,\upsilon\sin\theta)=\int_{-\infty}^{+\infty}\int_{-\infty}^{\infty}\mu(x,y)\exp(-2i\pi\upsilon(x\cos\theta+y\sin\theta))dxdy \tag{2.12}$$

Using the Dirac delta function (see Eqs. (2.4-2.5)), equation (2.12) becomes

$$G(\upsilon\cos\theta,\upsilon\sin\theta)=\int_{-\infty}^{+\infty}\left[\int_{-\infty}^{+\infty}\int_{-\infty}^{+\infty}\mu(x,y)\delta(\rho-x\cos\theta-y\sin\theta)dxdy\right]\exp(-2i\pi\upsilon\rho)d\rho \tag{2.13}$$

and by substituting Eq. (2.6) into Eq. (2.13) one gets

$$G(\upsilon\cos\theta,\upsilon\sin\theta)=\int_{-\infty}^{+\infty}\langle p(\rho,\theta)\rangle\exp(-2i\pi\upsilon\rho)d\rho \tag{2.14}$$

Eq. (2.14) proofs the Fourier Slice Theorem. This theorem states that the two-dimensional Fourier transform $G(\upsilon\cos\theta,\upsilon\sin\theta)$ of the function $\mu(x,y)$ is equal to the one-dimensional Fourier transform of the Radon transform $\langle p(\rho,\theta)\rangle$ of the function $\mu(x,y)$, evaluated on a line through the origin in the direction θ. The line is seen in Fig. 2.7.

From this theorem, the Fourier transform of the projections can be established and, in principle, the two-dimensional inverse Fourier transform will provide a reconstruction of the function $\mu(x,y)$. In practice, this procedure may involve interpolation in the frequency domain before the inverse transformation can be obtained.

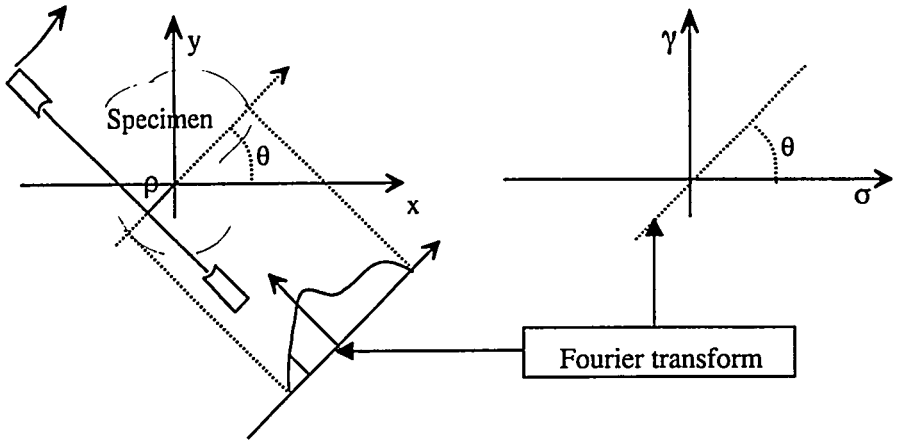

Figure 2.7. The Fourier Slice Theorem relates the one-dimensional Fourier transform of a parallel projection to the two-dimensional Fourier transform of the specimen parameter along a radial line subtended at an angle θ.

2.3.2 The filtered back-projection algorithm

A frequently used reconstruction algorithm is the filtered back-projection algorithm (KAK 1979). In this section, a variation of this algorithm is derived. The two-dimensional inverse Fourier transform of $G(\sigma,\gamma)$ is

$$\mu(x,y)=\int_{-\infty}^{+\infty}\int_{-\infty}^{+\infty} G(\sigma,\gamma)\exp(2i\pi(\sigma x+\gamma y))d\sigma d\gamma \qquad (2.15)$$

using $(\sigma,\gamma)=(\upsilon\cos\theta,\upsilon\sin\theta)$ and $\rho = x\cos\theta + y\sin\theta$ this equation becomes

$$\mu(x,y)=\int_0^{2\pi}\int_0^{+\infty} \upsilon G(\upsilon\cos\theta,\upsilon\sin\theta)\exp(2i\pi\upsilon\rho)d\upsilon d\theta \qquad (2.16)$$

and taking the numerical value of the frequency υ, this gives

$$\mu(x,y)=\int_0^{\pi}\int_{-\infty}^{+\infty} |\upsilon| G(\upsilon\cos\theta,\upsilon\sin\theta)\exp(2i\pi\upsilon\rho)d\upsilon d\theta \qquad (2.17)$$

here the polar frequency parameters are used. Using the Fourier Slice Theorem (Eq. 2.14), one gets

$$\mu(x,y)=\int_0^{\pi}\int_{-\infty}^{+\infty} |\upsilon|\left[\int_{-\infty}^{+\infty}\langle p(\rho,\theta)\rangle\exp(-2i\pi\upsilon\rho)d\rho\right]\exp(2i\pi\upsilon\rho)d\upsilon d\theta \qquad (2.18)$$

Thus, the coefficient $\mu(x,y)$ can be reconstructed form $\langle p(\rho,\theta)\rangle$ in two parts:
(*i*) the first part is a filtering part (indicated by $\forall$)

$$\mu^{\forall}(\rho,\theta)=\int_{-\infty}^{+\infty}|\upsilon|\left[\int_{-\infty}^{+\infty}\langle p(\rho,\theta)\rangle\exp(-2i\pi\upsilon\rho)d\rho\right]\exp(2i\pi\upsilon\rho)d\upsilon \quad (2.19)$$

The first integral in Eq. (2.19) is the inverse Fourier transformation of the square bracket [•] multiplied by the numerical value of the frequency υ (a high pass filter). The second integral in Eq. (2.19) (i.e., the square bracket [•]) is the Fourier transformation of the projection. This can also be seen as a convolution of the filter and the projection (convolution is an integral in the time domain while it is expressed as a multiplication in the frequency domain).
(*ii*) The second part is a back projection of the filtered projection, where the coefficient $\mu(x,y)$ is found as

$$\mu(x,y)=\int_0^{\pi}\mu^{\forall}(\rho,\theta)d\theta \quad (2.20)$$

and represents a summation of all line-integrals that passes through a point (x,y). Equation (2.19) and (2.20) are the two steps of the filtered back-projection algorithm, which may be used to reconstruct $\mu(x,y)$ from $<p(\rho,\theta)>$.
The multiplication with zero frequency $\nu = 0$ in Eq. (2.19) will imply that a so called DC-value cannot be obtained. This will generate artifacts in the tomogram, as discussed in chapter 3.
The relationship between the Fourier transform and the filtered back-projection technique described in the previous two subsections is shown diagrammatically in Fig. 2.8.

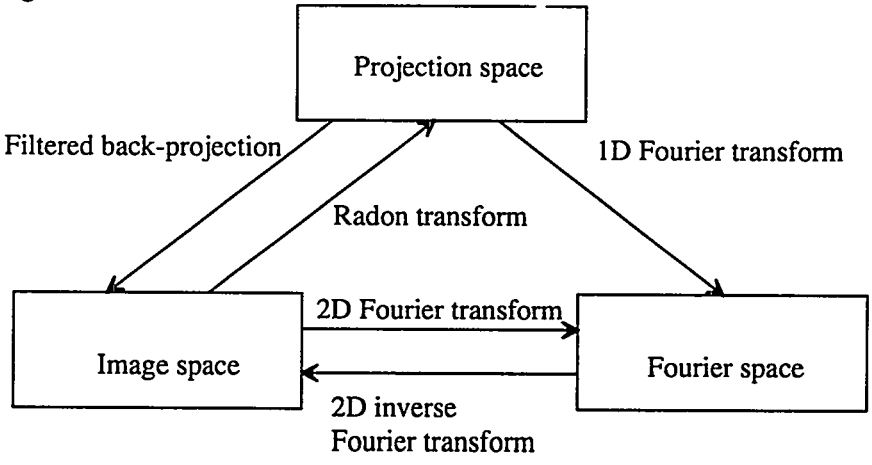

Figure 2.8. Fourier transformation connections between the image, projection and Fourier space.

The image space is the material parameters one wishes to determine (attenuation coefficient or sound velocity) and the projection space is the observed data (amplitude or time-of-flight) for a range of directions. One comes from the image space to the projection space via the Radon transform. The Fourier space is simply the two-dimensional Fourier transform of the image space, whereas the projection space is linked to the Fourier space via a series of one-dimensional Fourier transforms. Finally, one proceeds from the projection space directly to the image space via the inverse Radon transform using the filtered back-projection algorithm.

2.4 Experimental method (I)

This section contains experimental results showing UCT-tomograms of attenuation and velocity distributions in Plexiglas cylinders.
In practice, when applying discrete versions of the projection formulas, there are always questions concerning collection and pre-processing of data, numerical implementation of formulas, and post-processing of images. In addition, statistical and experimental limitations vary widely with application. For an ultrasonic transducer, for example, a few of these considerations include finite width of the aperture, various noise sources, relation of noise to different algorithms, resolution in the reconstructed image, artifacts in the reconstructed image, quantitative interpretation of the image and the relation between signal-to-noise ratio and gain.
Furthermore, as pointed out by KAK (1979) and DEFRANOULD (1981), the attenuation coefficient is frequency-dependent, which will distort the received signal and provide error in the TOF-measurement. Hence, the assumption of a straight propagation in polymeric materials, especially with strong reflectors, will only approximately be satisfied. With these restrictions in mind, the two kinds of projections may be applied.

Several methods of measuring TOF-projections were considered. But two methods were in particular investigated in detail. The first method considered here was the *correlation method.* See, e.g., SCHOMBERG *et al.* (1990) and LEISK *et al.* (1996). In this case, a cross-correlation is performed between the signals obtained with the specimen present and absent. The maximum value of this cross-correlation function automatically yields the difference between the two times. The method has the advantage that, because it determines the largest amplitude pulse when pulses from multiple paths have been received, the size of high-and low speed regions is correctly represented. The main problem is that the method becomes unreliable when the amplitudes of the two signals being correlated are very different, for example after attenuation by the specimen, or when the pulse shape becomes significantly distorted, as could occur due to non-linear propagation in the specimen.
The second method considered was the *gating method* (or threshold method). As the name implies, a fixed gate level is set just above the signal noise level, and a pulse is assumed to arrive when the signal first crosses this gate level. To calculate the time-of-flight in the specimen this measurement must be made both for pulses that have traveled through the water only, and in this way have been attenuated minimal, and for pulses that have become attenuated after traveling through the specimen. The main problem with this method was the gate level itself. A level set to high risk missing the first part of the pulse, particular for attenuated signals, resulting in an over-estimate of the time-of-flight. A level set to low risk triggering on noise and possibly drastically underestimate the time-of-flight. Another problem was that this method tends to overestimate the size of regions with a higher speed of sound than their surroundings, and to underestimate the size of low speed regions. This is because the method always detects the first pulse to arrive, so that a high-speed region will be detected even if it intersects only a small portion of the ultrasonic beam.
Similarly, a low-speed region may not be detected at all if it is narrower than the beam width, since pulses traversing through such regions may appear after the arrival of energy traversing through surrounding areas.
After extensive experimentation with Plexiglas specimens, it has been found that, the correlation method can be very accurate in some situations. However, it becomes unreliable (i.e. not reproducible), when attenuation within the specimen is significant. The gating method never achieves the potential accuracy of

the correlation method, but is more reliable in most realistic cases where the received signals suffer from attenuation. This is the case for most polymer materials. Furthermore, the gating method was also applied for the amplitude measurements.
Consequently, all the TOF-projections and amplitude-projections presented in this thesis were obtained using the gating method.

2.4.1 Experimental specimens, setup and procedure

To verify the filtered back-projection algorithm, two cylindrical Plexiglas specimens with different ellipse shaped holes were prepared, as seen in Fig. 2.9. The specimens were 100 mm in diameter and 50 mm thick. The first specimen had a single centered (0,0) ellipse with dimension (8 mm x 20 mm). The second specimen had two ellipses with dimension (8 mm x 20 mm) and (16 mm x 40 mm), respectively. The smallest ellipse was rotated 90° and placed in (0, -14 mm), while the biggest ellipse was placed in (0, 14 mm). For details see Appendix 2.1.

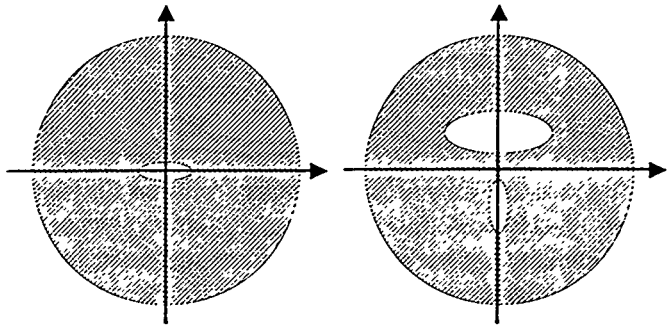

Figure 2.9. Plexiglas specimens with different ellipse shaped holes.

The scanning system consisted of a step motor controlled rotation table with the specimen and two diametrically positioned transducers on each side of the test specimen. A second step motor, was used to move the transducers in a linear direction for each rotation, as explained in Fig. 2.4.

In order to obtain approximate line conditions for the sound field, two focused transducers were used as transmitter and receiver, respectively. The transducers were pairs of 25 MHz Aerotech Alpha transducers (type V3073) with an aperture diameter of 6 mm and approximately 2 cm focus in water. The scanning system was placed in water and the following scanning procedure was applied: First, one of the samples was positioned on a rotation table and the distance between the transducers was optimized in order to receive a maximum signal. A time gate was then set to measure the peak amplitude and time delay of the transmitted signal. The corresponding time delay was taken to be the difference between the excitation pulse and the first arrival in the digitized waveform (a time-of-flight of 69 μs in water at 20°C corresponds approximately to a distance between the transducers of 102 mm (speed of sound was 1480 m/s)). Second, for each linear scan 64 samples of attenuation and time delays through the specimens were measured. Finally, after completion of one line scan, the sample was rotated 1° and the scan process was repeated until 180 projections were obtained. The time for one scanning was about 5 min.
The image reconstruction part, discussed in section 2.3.2, was implemented in a C-code, using the Fast Fourier Transform (*FFT*). A radix-2 *FFT*-algorithm was

used, which means that the number of rays in each projection had to be a power of 2.
Eq. (2.19) can be written as the following pseudo code. For each projection $\theta_t = \theta_{low} + t\Delta\theta$ calculate the line:

$$\rho_r = \rho_{low} + r\Delta\rho$$

$$\mu^{\forall}(\rho_r,\theta_t) = IFFT\left\{\begin{array}{l} FFT\{p(\rho_r) + ZP\} \\ \times FFT\{h(\rho_r) + ZP\} \\ \times FFT\{smoothing\} \end{array}\right\} \qquad (2.21)$$

where $t = 1..180$ and $r = 1..64$.
In Eq. (2.21), a zero-padded (*ZP*) projection $\langle p(\rho,\theta)\rangle$ was first Fourier transformed (zero padding involves padding the projection data with a sufficient number of zeros and will be discussed further in chapter 3).
Secondly, the projection was multiplied by a high-pass filter and a smoothing filter (see below). Then, the result was inverse Fourier transformed (*IFFT*) to yield a filtered projection.
Finally, the filtered projection was back-projected in the image domain according to Eq. (2.20). *Nearest neighbor* interpolation (*Round*) was applied (see KAK *et al.* 1988).
For each $x_m = x_{low} + m\Delta x$ calculate:

$$y_n = y_{low} + n\Delta y$$

$$\mu(m,n) \approx \Delta\theta \sum_{t=0}^{T} \mu^{\forall}(Round\left[\frac{x_m \cos\theta_t + y_n \sin\theta_t - \theta_{low}}{\Delta\theta}\right], t) \qquad (2.22)$$

where $m = 1..100$ and $n = 1..75$.

The experimental parameters are shown in Table 2.1.

Table 2.1. Experimental parameters for experiment (I)

Frequency	25 MHz
Wavelength Plexiglas (Water)	0.11 mm (0.06 mm)
Speed of sound Plexiglas (Water)	2720 m/s (1480 m/s)
Aperture length	53.8 mm
Distance between T and R*	102 mm
Aperture resolution (*r* samples)	0.84 mm (64)
Rotational resolution (*t* projections)	1° (180)
Image resolution (*m* x *n* pixels)	1.28 mm x 1.28 mm (100 x 75)
Dynamic range in image	5 bit (0-31 dB)
Reconstruction time (scan time)**	40 sec. (5 min.)

* Transmitter (T) and receiver (R). ** PC-486 (33 MHz).

Fig. 2.10 shows the frequency response of four high pass filters. The four filters are: the Ram-Lak filter (RL), the Shepp-Logan filter (SL), the Low-Pass Cosine filter (LPC) and the Generalized Hamming filter (GH). See JAIN *et al.* (1989) and HERMAN (1979) for details and definitions. The RL-filter has a sharp cutoff frequency and may be suitable in the presence of low noise. It gives the best resolution, but amplifies noise (HERMAN 1979). In the case of noise, a band-limiting window function (i.e., a smoothing function) can be multiplied to the RL-filter. The SL-filter is a ramp-function multiplied by a sinc-window. It is preferred over the RL-filter in the case of noise, but it gives a loss in resolution. The RL-filter will be discussed further in chapter 3.
For significant noise levels the two other filters may be used. The LPC-filter with a cosine-window and the GH-filter, with a value (0-100 %) to minimize the noise level.

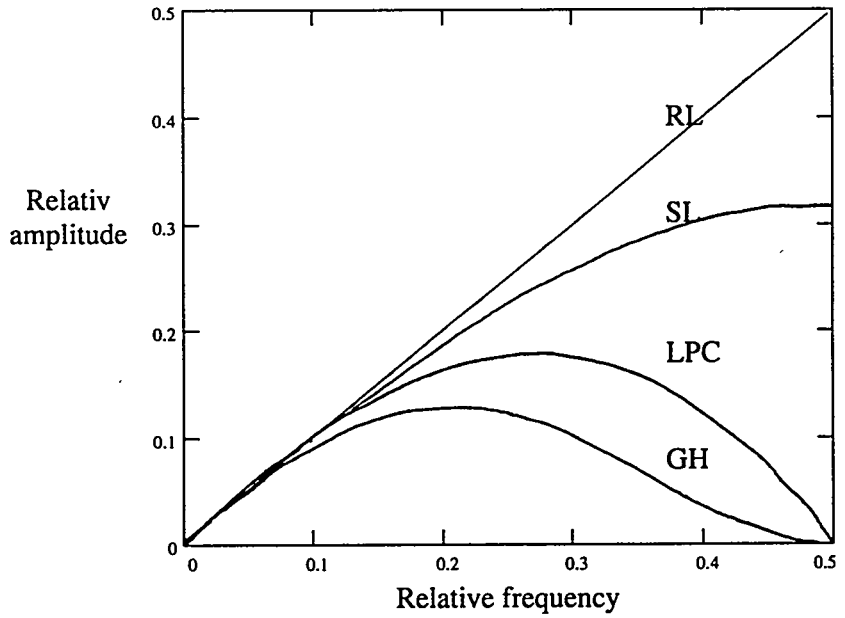

Figure 2.10. The frequency response of a Ram-Lak filter (RL), a Shepp-Logan filter (SL), a Low-Pass Cosine filter (LPC) and a Generalized Hamming filter (GH).

2.4.2 Results - Attenuation tomograms

Experimental results from the two cylindrical Plexiglas specimens were reconstructed using the filtered back-projection algorithm. See also NIELSEN *et al.* (1995). All reconstructions were obtained from 180 parallel projections, each with 64 samples and shown on 100 x 75 grids. Less than 40 seconds was used (on a PC- 486, 33 MHz) to reconstruct an UCT-tomogram.

Fig. 2.11 shows an attenuation UCT-tomogram in the Plexiglas cylinder with one ellipse (8 mm x 20 mm). The RL-filter was used in the reconstruction procedure. The ellipse shape of the artificial defect is seen clearly in the Plexiglas cylinder, although, the ultrasonic signals were effected by noise. The high amplitude value in the figure corresponds to water, while a low value corresponds to Plexiglas.

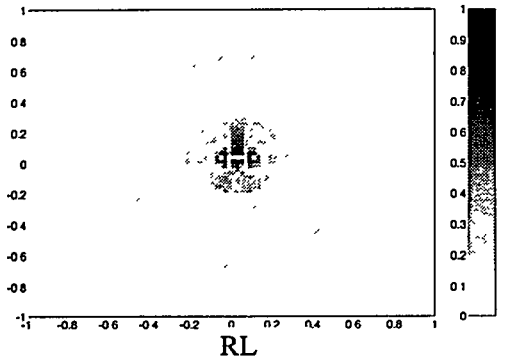

Figure 2.11. Experimental tomogram of amplitude coefficient in a Plexiglas cylinder with one ellipse (8 mm x 20 mm) (RL-filter used).

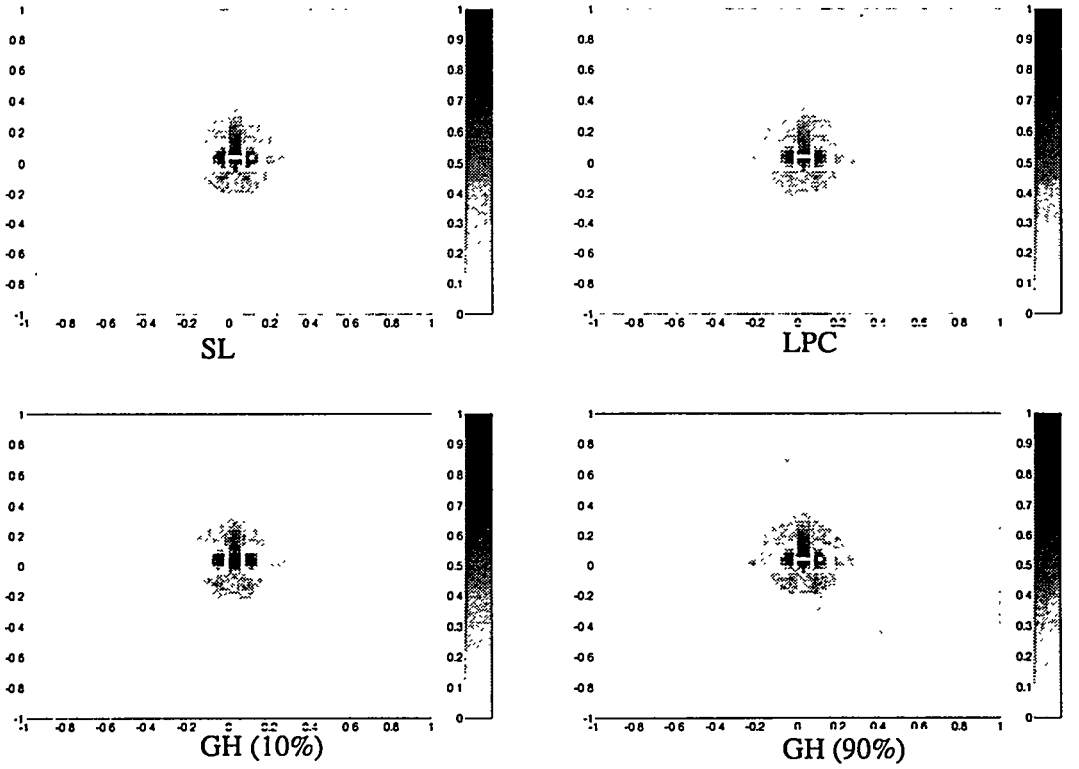

Figure 2.12. as Fig. 2.11, but with SL, LPC, GH(10%) and GH(90%)-filter, respectively.

Fig. 2.12 show UCT-tomograms of the same specimen, but the SL-, LPC-, GH(10%) and GH(90%)-filter were used, respectively, in the reconstruction procedure. A smoother tomogram is seen compared to Fig. 2.11, although, a decreased resolution was found. Thus, the digital filters may improve the image in the case of noise.
I both cases artifacts are seen as white pixels and a ring surrounding the ellipse. This was not expected. The reason for this particular look could be that the ultrasonic beam was bent due to the cylindrical shape of the specimen. Consequently, some or all of the transmitted energy was refracted away from the receiving aperture, depending on the angle of incidence. A second explanation could be that the received amplitude was modulated by attenuation from Plexiglas and water. The measured amplitude was, thus, a function not only of the specimen geometry but also of the bulk properties.

2.4.3 Discussion - Attenuation tomograms

In order to evaluate the experimental results, the experiment was simulated.
The amplitude tomograms were based on the filtered back-projection algorithm in which straight line propagation was assumed. To simulate a tomogram corresponding to a "perfect" tomogram a C-code was written, inspired by the Shepp-Logan Phantom Brain (SHEPP 1974). The code incorporates a model for ellipses in a cylindrical specimen, where the ellipses can be Radon transformed analytically. Both amplitude and TOF-projections could be simulated for various configurations of the ellipses in the cylinder. Moreover, by computer simulation different experimental setup characteristics could easily be reproduced, e.g., synthetic aperture length, number of transducer positions, parameters of acoustic coupling medium (water). The C-code was used to process simulated data, that were compared with the experimental data in Figs. 2.11-2.12. Both data sets were reconstructed with the same reconstruction algorithm Eq. (2.18).
Parallel $\mu(x,y)$ - projections were simulated in the cylinder containing the two forms of ellipses. The density function, μ_2, for the two ellipses was considered to be constant and different from the density function, μ_1, of the material as seen in Fig. 2.13. Moreover, the density function, μ_3, of the immersion fluid was set to be equal to μ_1. The Radon transformed of $\mu(x,y)$ is for example seen as a dotted line, at an angle θ from the x-axis and at a distance ρ from the origin. It was found from:

$$\langle p(\rho,\theta)\rangle = \mu_1(x,y)\, s_1(\rho,\theta) - \sum_{i=2}^{3}\left[\mu_{i-1}(x,y) - \mu_i(x,y)\right] s_i(\rho,\theta) \qquad (2.23)$$

where the ultrasonic path $s_i(\rho,\theta)$ was given as either

$$s_i(\rho,\theta) = \frac{2a_i b_i \sqrt{(a_i^2\cos^2\theta + b_i^2\sin^2\theta) - \rho^2}}{a_i^2\cos^2\theta + b_i^2\sin^2\theta} \qquad i = 1..3 \qquad (2.24)$$

or

$$s_i(\rho,\theta) = 0 \qquad \text{if } \rho^2 > a_i^2\cos^2\theta + b_i^2\sin^2\theta \qquad (2.25)$$

and a_i was the major semi-axis and b_i the minor semi-axis of the ellipse i.

The theoretical amplitude UCT-tomogram for the single ellipse is seen in Fig. 2.14. As the tomogram was simulated, it is free of measurement noise and does not exhibit any artifacts attributable to material discontinuities as could occur in practice. Therefore, the simulated tomogram is the best possible image that can be obtained with the filtered back-projection algorithm. Fig. 2.15 compares the horizontal cross section through (0,0) in Figs. 2.12 and 2.14. It is seen that the two experimentally obtained UCT-tomograms have strong oscillations around the ellipse (Gibb's phenomena).

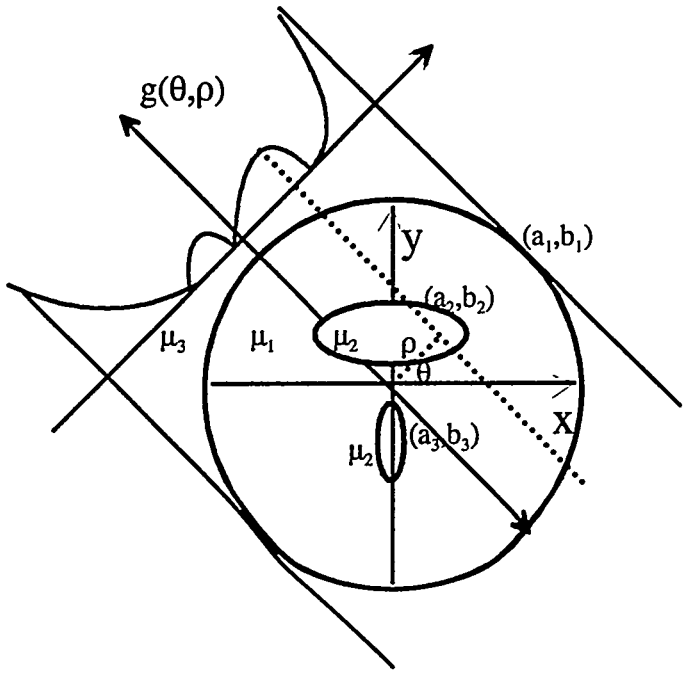

Figure 2.13. Parallel projection in cylindrical specimen with two ellipses.

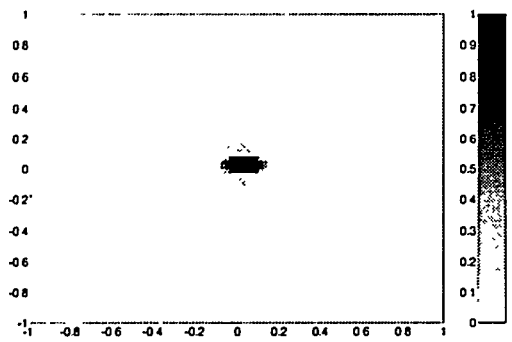

Figure 2.14. Theoretical UCT-tomogram of amplitude coefficient in a Plexiglas cylinder with one ellipse (8 mm x 20 mm).

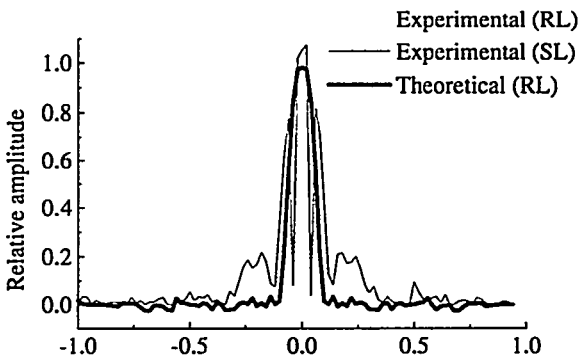

Figure 2.15. Horizontal cross section through (0,0) in Figs. 2.11, 2.12 and 2.14.

2.4.4 Results - Velocity tomograms

Fig. 2.16 shows the relation 1 - v_o/v_{plx} in the Plexiglas cylinder with two ellipses. The RL-filter was used again. The two ellipses are difficult to recognize compared with the theoretical refractive tomogram.

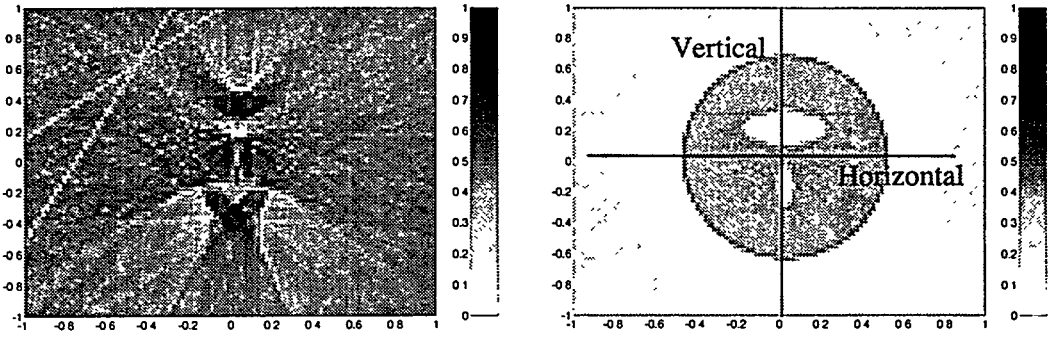

Figure 2.16. Experimental and theoretical tomograms of refractive index in a Plexiglas cylinder with two ellipses.

Fig. 2.17 shows the horizontal and vertical cross section through (0,0) in Fig. 2.16. It is seen that the refractive index for Plexiglas is reconstructed in some areas. The theoretical refractive index is 0.46 (= 1 - v_o/v_{plx} = 1 - 1480/2720).

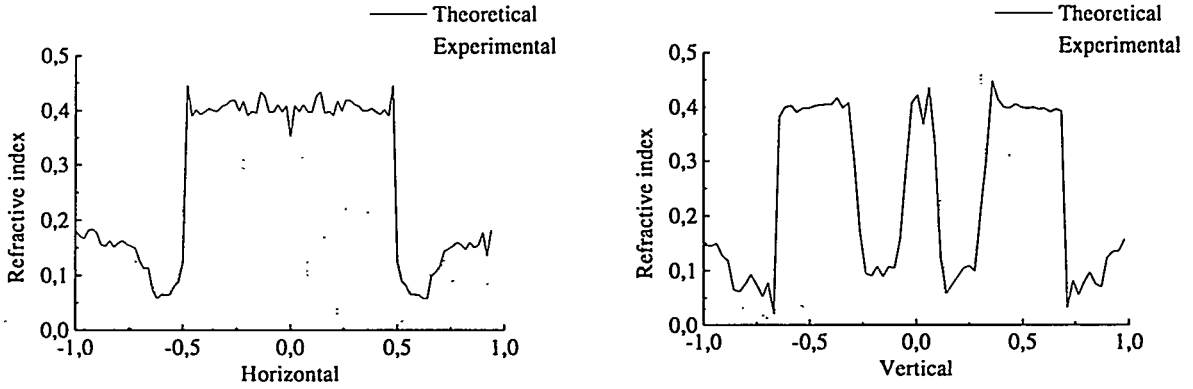

Figure 2.17. Horizontal and vertical cross section, respectively, through (0,0) in Fig. 2.16.

No significant results were obtained by filtering experimentally obtained velocity tomograms.

2.4.5 Discussion - Velocity tomograms

In order to clarify the assumption that the ultrasonic paths through the Plexiglas cylinder were straight lines, the simple model in Fig. 2.18 was used.

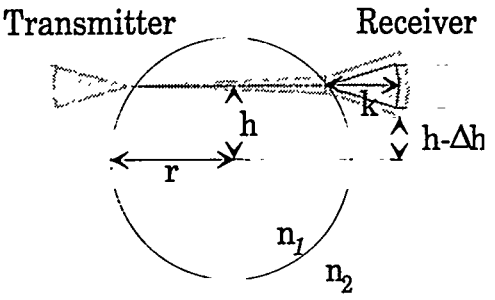

Figure 2.18. Model used to analyze ultrasonic refraction.

Depending on the distance from the center, h, and the receiver's distance from the cylinder, k, the central part of the ultrasonic beam is refracted the amount Δh.
Using Snell's law, the error $\Delta h/r$ can be expressed as

$$\frac{\Delta h}{r} = \left(1 + \frac{k}{r} - \sqrt{1 - \left(\frac{h}{r}\right)^2}\right) \cdot \tan\left(A\sin\left(\frac{h}{r}\right) - A\sin\left(\frac{hn_1}{rn_2}\right)\right) \qquad (2.26)$$

where the n_1 and n_2 are the absolute refractive indices of Plexiglas and water, respectively GREENLEAF *et al.* 1975. The error is calculated and seen in Fig. 2.19, as a function of receiver distance from the cylinder, k, and from the cylinder center, h.

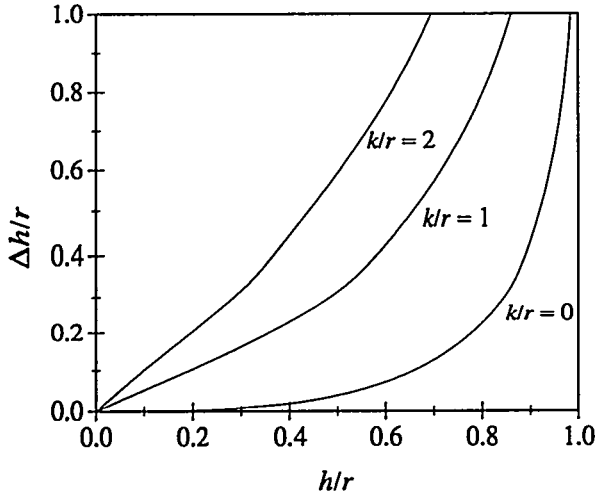

Figure 2.19. Error caused by deviation from straight line approximation. Receivers from center of ellipse, h, and from cylinder, k.

The Figure indicate as expected, that the transmitter and receiver should be as close as possible to the cylinder in order to minimize the refraction effect, i.e., k and h should be small.

2.5 Summary and conclusions

In this chapter, the fundamental theory for ultrasonic computed tomography (UCT) using parallel projections was established (section 2.1, 2.2 and 2.3). To the authors knowledge, the established theory for UCT has up to this point been very limited in the literature. The presented theory for parallel projections was applied in a *simple* UCT experiment and different parameters influencing the tomogram were investigated (section 2.4).

Section 2.1: Ultrasonic computed tomography (UCT) was compared with conventional ultrasonic techniques and X-ray CT. Furthermore, general requirements to the implementation of the UCT-technique were discussed and illustrated in Fig. 2.1.
UCT was divided into two major tasks: Data acquisition of ultrasonic projections and image reconstruction from these projections, into an UCT-tomogram.

Section 2.2: Two different UCT-projection types (amplitude or time-of-flight) were discussed for transmission tomography where straight line propagation was assumed (Figs. 2.2-2.5). Both projections were related to the Radon transform. A third projection type will be discussed in chapter 3.

Section 2.3: Image reconstruction from projections was discussed for three basic reconstruction classes (Fig. 2.6). The Fourier Slice Theorem was introduced (Fig. 2.7) and used to derive an expression for the filtered backprojection algorithm. Connections between the image, projection and Fourier space were illustrated (Fig. 2.8).

Section 2.4: In the first experiment (I) attenuation and velocity tomograms of a water filled ellipse positioned in a Plexiglas cylinder (Fig. 2.9) was obtained. The filtered backprojection algorithm was implemented with the choice of four different filters (Fig. 2.10). Two different measurement strategies of time of flight projections were considered. Highly directive transducers were applied for data acquisition (Table 2.1). Experimentally obtained attenuation tomograms were presented (Figs. 2.11-2.12) and compared with a theoretical model for the case (Figs. 2.13-2.15). Experimentally obtained velocity tomograms were presented (Fig. 2.16) and compared with theoretical models for the case (Figs. 2.17-2.19).

In conclusion, the attenuation tomograms of the small ellipse exhibited good quantitative agreement with the known composition of the testing material. Digital filters could be used to smooth the UCT-image in the presence of noisy parallel projections. However, little quantitative agreement was obtained for time-of-flight tomograms of two ellipses.
The reason could be large changes in the refractive index of the material, i.e., the difference in characteristic impedance between water and the Plexiglas cylinder. This could cause ultrasonic wave propagation to deviate from the straight-ray model. Consequently, some or all of the transmitted energy would be refracted out of the receiving aperture depending on the angle of incidence. Hence, a major limitation in experiment (I) was refraction of the ultrasonic beam and consequently deviations from the straight-ray model.

2.6 References to chapter 2

ARMISTEAD, R.A. and YANCEY, R.N. (1989). Computed tomography for non-destructive testing of advanced engineering materials. Materials Evaluation, Vol. 47, 487-491.

BATES, R.H.T. and MCKINNON, G.C. (1979). Towards improving images in ultrasonic transmission tomography. Australasian Physical Sciences in Medicine, Vol. 2-3, No. 80, 134-140.

BETTS, M.; HEALEY, A. and LEEMAN, S. (1995). A new field measurement technique for ultrasonic computed tomography. In Acoustical Imaging, Vol. 21, Ed. J.P. Jones, Plenum Press, 313-320.

BIRKS, A.S and GREEN, R.E. (1991). Ultrasonic testing. Nondestructive testing handbook, Vol. 7, American Society for Non Destructive Testing.

BISHOP, T.N.; BUBE, K.P.; CUTLER, R.T.; LANGAN, R.T.; LOVE, P.L.; RESNICK, J.R.; SHUEY, R.T.; SPINDLER, D.A. and WYLD, H.W. (1985). Tomographic determination of velocity and depth in laterally varying media. Geophysics, Vol. 50, No. 6, 903-923.

BLYTH, B.; CAVAYE, G.; CLEARY, M.; FLEMING, R.; KOCH, R.; MEARA, L.; MCCAFFREY, J. and WHITING, J. (1979). An ultrasonic computer-assisted tomographic scanner. Australasian Physical Sciences in Medicine, Vol. 2-3, No. 80, 141-153.

BREGMAN, N.D.; BAILEY, R.C. and CHAPMAN, C.H. (1989). Crosshole seismic tomography. Geophysics, Vol. 54, No. 2, 200-215.

CAPINERI, L.; CASTELLINI, G.; MASOTTI, L. and ROCCHI, S. (1988). Broadband tomography system. International School of Physical Acoustics, 3rd Course on Ultrasonic Signal Processing, Erice, Italy. Publisher: World Scientific, Singapore, 245-253.

CAPINERI, L.; TATTERSALL, H.G.; TEMPLE, J.A.G. and SILK, M.G. (1992). Time-of-flight diffraction tomography for NDT applications, Ultrasonics, Vol. 30, No. 5, 275-288.

CHOW, T.M.; HUTCHINS, D.A. and MOTTRAM, J.T. (1993). Simultaneous acoustic emission and ultrasonic tomographic imaging in anisotropic polymer composite material, Journal of the Acoustical Society of America, Vol. 94, No. 2, 944-953.

CROSTACK, H.A; MORLO, H. and NIEHUS, R. (1988). Fehlerbeschribung mit einem midifizerten tomographieverfahren in der zerstörungsfrien werkstoffprüfung mit ultraschall (Description of failings with a modified tomographic process in non-destructive materials testing with ultrasonics). Materialprüfung, Vol. 30, 27-32.

DEANS, S.R. (1983). The Radon transform and some of its applications, John Wiley and Sons, New York.

DEFRANOULD, P. (1981). Acoustical Fan-beam measurements by transducer arrays for tomography reconstruction. IEEE Transactions on Sonics and Ultrasonics, Vol. SU-28, No. 6., 418-425.

DEVANEY, A.J. (1987). A fast filtered backprojection algorithm for ultrasound tomography. IEEE Transactions on Ultrasonics, Ferroelectrics and Frequency control, Vol. UFFC-34, No. 3, 330-340.

ERMERT, H.; PALLAKOWSKI, M. and BERNUS, L. (1995). Acoustical imaging using an optimal combination of signal prefiltering and pulse compression. In Acoustical Imaging, Vol. 21, Ed. J.P. Jones, Plenum Press, 337-347.

GLOVER, G.H. and SHARP, J.C. (1977). Reconstruction of ultrasonic propagation speed distributions in soft tissue: Time-of-flight tomography. IEEE Transactions on Sonics and Ultrasonics, Vol. SU-24, No. 4, 229-234.

GREENLEAF, J.F.; JOHNSON, S.A.; SAMAYOA, W.F. and DUCK, F.A. (1975). Algebraic reconstruction of spatial distributions of acoustic velocities in tissue from their time-of-flight profiles. In Acoustical Holography, Vol. 6, Ed. N. Booth, Plenum Press, 71-90.

HATTON, L.; WORTHINGTON, M.H. and MARKIN, J. (1990). Seismic data processing. Theory and practice. Blackwell Scientific Publications.

HAVLICE, J.F. and TAENZER J.C. (1979). Medical Ultrasonic Imaging: An Overview of Principles and Instrumentation. Proc. of the IEEE, Vol. 67, No. 4, 620-640.

HELGASON, S. (1980). The Radon transform. Progress in mathematics, Vol. 5, Birkhouser, USA.

HERMAN, G.T. (1979). Image reconstruction from projections. Implementation and applications. Springer-Verlag, New-York.

HILDEBRAND, B.P. and HARRINGTON, J.P. (1981). Mapping of materials stress with ultrasonic tomography, Materials Evaluation, Vol. 39, No. 4, 383-390.

HORN, B.K.P. (1979). Fan-beam reconstruction methods. Proc. of the IEEE, Vol. 67, No. 12, 1616-1623.

HUANG, H.K. and LEDLEY, R.S. (1978). Scanning methods and reconstruction algorithms for computerized tomography. In Medical Imaging Techniques, Plenum Press, 313- 327.

HUTCHINS, D.A.; HU, J.K.; YOUNG R.P; STONER, R.; JANSEN, D. and ZHANG, Q.L. (1989). Ultrasonic tomography of metals using noncontact transduction. Journal of the Acoustical Society of America, Vol. 85, No. 2, 747-752.

JAIN, A.K. (1989). Fundamentals of digital image processing, Prentice Hall, USA.

JAGO, J.R. and WHITTINGHAM, T.A. (1991). Experimental studies in transmission ultrasound computed tomography. Phys. Med. Biol., Vol. 36, No.11, 1515-1527.

JANSEN, D.P.; HUTCHINS, D.A. and YOUNG, R.P. (1993). Ultrasonic tomography using scanned contact transducers. Journal of the Acoustical Society of America, Vol. 93, No. 6, 3242-3249.

JOHNSON, S.A.; GREENLEAF, J.F.; SAMAYOA, W.A.; DUCK, F.A. and SJOSTRAND, J. (1975). Reconstruction of three-dimensional velocity fields and other parameters by acoustic ray tracing. In Ultrasonic Symposium Proceedings, IEEE Cat. 75ch0994-4su, IEEE, New York, 46-51.

KAK, A. (1979). Computerized tomography with X-ray, emission, and ultrasound sources. Proc. of the IEEE, Vol. 67, No. 9, 1245-1272.

KAK, A.C. and SLANEY, M. (1988). Principles of computerized tomographic imaging, IEEE Press, USA.

KARPELSON, A.E.; ARISTOV, V.V. and GUSEV, E.A. (1990). Possibilities of ultrasonic reconstruction tomography. Sovjet Journal of Nondestructive Testing, Vol. 26, No. 6, 367-80.

KINO, G.S. (1979). Acoustic imaging for nondestructive evaluation. Proc. of the IEEE Vol. 67, No. 4, 510-525.

KLINE, R.A. and WANG, Y.Q. (1989). Tomographic imaging of material property variations in polymers. IEEE Ultrasonic Symposium, Vol. 2, Ed. B.R. McAvoy, 827-830.

KLINE, R.A. and WANG, Y.Q. (1990). Application of tomographic imaging principles to the ultrasonic characterization of polymers. Materials Evaluation, Vol. 48, No. 11, 1385-1391.

KLINE, R.A. and WANG, Y.Q. (1992). A technique for ultrasonic tomography in anisotropic media. Journal of the Acoustical Society of America, Vol. 91, No. 2, 878-884.

KLINE, R.A. (1993). Ultrasonic computed tomography for anisotropic materials characterization. IEEE Ultrasonic Symposium, Vol. 1, Ed. B.R. McAvoy, 677-686.

KRAUTKRÄMER, J. AND KRAUTKRÄMER, H. (1990). Ultrasonic testing of materials, 4th edition, Springer-Verlag, Germany.

LEISK, G.G and SAIGAL, A. (1996). Digital computer algorithms to calculate ultrasonic wave speed. Materials Evaluation, Vol. 3, 840-843.

LYTLE, R.J and DINES, K.A. (1980). Iterative ray tracing between boreholes for underground image reconstruction. IEEE Transactions on Geoscience and Remote Sensing, Vol. GE-28, No. 3., 234-240.

MARTZ, H.E; SCHNEBERK, D.J. and ROBERSON, G.P. (1993). Three dimensional nonintrusive imaging of obscured objects by X-ray and gamma-ray computed tomography. Proc. of the International Society for Optical Engineering, Ed. Del Grande, Vol. 1942, 236-249.

MUELLER, R.K; KAVEH, M. and WADE, G. (1979). Reconstructive tomography and applications to ultrasonics. Proc. of the IEEE, Vol. 67, No. 4, 567-587.

MUELLER, R.K; KAVEH, M. and IVERSON, R.D. (1980). A new approach to acoustic tomography using diffraction techniques. In Acoustical Imaging, Vol. 8. Ed. A. Metherell, Plenum Press, New York, 615-628.

NAHAMOO, D.; CRAWFORD, C.R. and KAK, A.C. (1981). Design constraints and reconstruction algorithms for traverse-continuos-rotate CT scanners. IEEE Transactions on Biomedical Engineering, Vol. BME-28, No. 2., 79-98.

NIELSEN, S.A.; BORUM, K.K. and GUNDTOFT, H.E. (1995*b*). Verifying an ultrasonic reconstruction algorithm for non-destructive tomography. Proc. of 1st World Conference on Ultrasonics, 447-450.

PERSSON, S. and ÖSTMAN, E. (1983). The use of computed tomography in non-destructive testing of polymeric materials, aluminium and concrete: Part 1 - Basic principles. Polymer Testing, Vol. 6, 407 - 414.

PETERS, T.M. and LEWITT, R.M. (1977). Computed tomography with fan beam geometry. Journal of Computer Assisted Tomography, Vol. 1, 429-436.

PHILLIPS, D.H. and LANNUTTI, J.J. (1997). Measuring physical density with X-ray computed tomography. NDT&E International, Vol. 30, No. 6, 339-350.

RADON, J. (1917). Über die bestimmung von funktionen durch ihre integralwerte längs gewisser mannigfaltigkeiten (On the determination of functions from their integrals along certain manifolds. An English translation can be found in S.R. Deans: The Radon transform and some of its applications, Appendix A.). Berichte Saechsische Akademie der Wissenschaften, Vol. 69, 262-277.

RAMACHANDRAN, G.N. and LAKSHMINARAYANAN, A.V. (1971). Three-dimensional reconstruction from radiographs and electron micrographs: Application of convolution instead of Fourier transforms. Proc. Natl. Acad. Sci. Us., Vol. 68, 2236-2240.

ROSE, J.L. and DITRI, J.J. (1990). Ultrasonic computed tomography considerations in the NDE of solid materials. Ultrasonics Symposium Proceedings (Cat. No. IEEE 90ch2938-9), (ed.) B.R. McAvoy, Vol. 2, New York, 991-995.

SCHOMBERG; H; BEIL, W. MCKINNON, G.C. PROKSA, R. and TSCHENDEL, O. (1990). Towards high-resolution computerized tomography. IEEE Ultrasonic symp., Vol. 2, Ed. B.R. McAvoy, 737-740.

SEHGAL, C.M, LEWALLEN, D.G.; NICHOLSEN, J.A.; ROBB, R.A and GREENLEAF, J.F. (1988). Ultrasound transmission and reflection computerized tomography for imaging bones and adjoining soft tissues. IEEE Ultrasonic Symposium, Vol. 1, (ed.) B.R. McAvoy, 849-852.

SHEPP, L.A. and LOGAN, B.F. (1974). Reconstructing interior head tissue from X-ray transmissions, IEEE Trans. Nucl. Sci., Vol. NS-21, No. 3, 228-236.

SIRE, P.; GRANGEAT, P.; LEMASSON, P.; MÉLENNEC, P. and PIZO, P. (1991). NDT applications of the 3D Radon transform algorithm for cone beam reconstruction, Mat. Res. Soc. Symp. Proc., Vol. 217, Ed. J.L. Ackerman and W.A. Ellingson, 129-134.

SUBBARAO, P.M.V; MUNSHI and MURALIDHAR, K. (1997). Performancee of iterative tomographic algorithms applied to non-destructive evaluation with limited data. NDT&E International, Vol. 30, No. 6, 359-370.

TOFT, P. (1991). Radontransformationen. Lecture notes from Electronics Institute, Technical University of Denmark, Denmark (In Danish).

TOFT, P. (1994). Reconstruction's of CT and PET images, Lecture notes from Electronics Institute, Technical University of Denmark, Denmark.

TOFT, P. (1995). Using the inverse Radon transform in PET. (Unpublished).

TSAO, M.C. (1983). Industrial ultrasonic tomography principle, practice and limitation. Materials Evaluation. Vol. 41, 1248-1254.

WADE, G. (1980). Ultrasonic imaging by reconstructive tomography. In Acoustical Imaging, Vol. 9, Ed. K.Y. Wang, Plenum Press, 379-431.

WANG, Y.Q.; KLINE, R.A.; MIGNOGNA, R. and DEL SANTO, P.P. (1992). Techniques for acoustic tomography in anisotropic media, Ultrasonics Symposium (Cat. No.92CH3118-7), Vol. 1, 635-638.

WANG, Y.Q. and KLINE, R.A. (1994). Ray tracing in isotropic and anisotropic materials: Application to tomographic image reconstruction, The Journal of the Acoustical Society of America., Vol. 95, No. 5, 2525-2532.

3 Circular Aperture Array Tomography

In this chapter, ultrasonic imaging techniques are discussed using a synthetic array with transducer elements distributed uniformly along a circular aperture. The techniques are based on ultrasonic projections and are, as mentioned in chapter 2, referred to as ultrasonic computed tomography (UCT).
Section 3.1 introduces two kinds of ultrasonic tomography: bistatic and monostatic imaging. Experimental requirements are discussed for the two reconstruction techniques. Both techniques are applied for imaging the same Plexiglas cylinders as used in chapter 2.
Section 3.2 discusses bistatic reconstruction for the synthetic circular aperture array. An experimental technique (II) is reviewed in relation to a quantitative material parameter and different reconstruction artifacts are discussed.
Section 3.3 discusses monostatic reconstruction and a related experimental technique (III). Theoretical resolution criteria are discussed for various configurations of the circular aperture array.
Section 3.4 verifies the monostatic technique by volumetric imaging. In this experimental technique (IV) artificial and real discontinuities in a cylindrical *AlSi*-alloy are compared with similar discontinuities in a Plexiglas specimen.
Section 3.5 discusses limitations to UCT and summarizes this chapter.

3.1 Ultrasonic computed tomography using a circular aperture array

Ultrasonic computed tomography (UCT) using parallel projections and the filtered backprojection algorithm was discussed in chapter 2. It was concluded that one of the most important artifacts in these tomograms of cylindrical specimens was refraction of the sound path when the beam was incident at angles different from normal. Consequently, the main purpose of this chapter is to explore experimental techniques that seek to acquire refraction limited ultrasonic signals in a synthetic circular aperture array.
The imaging system considered here has N transducer elements of the array placed uniformly along a circular aperture with radius R, as shown in Fig. 3.1. The circular aperture array may obtain ultrasonic signals in a bistatic or monostatic mode, respectively. In the bistatic mode a forward transmitted ultrasonic sound field is received over a circular arc of receivers, whereas in monostatic mode a transducer acts both as transmitter and receiver. In the latter mode, a short ultrasonic pulse is transmitted into the specimen and the amplitude of the backscattered sound pulse is measured by the same transducer. The flexibility of the synthetic circular aperture array will be more evident in subsection 3.1.1.
The bistatic (i.e., *through-transmission*) mode has usually been used to reconstruct an image of the object's attenuation coefficient or the index-of-refraction (GLOVER *et al.* 1977), as mentioned in chapter 2, while the monostatic (i.e. *pulse-echo*) mode typically has been used to reconstruct a cross-section of the object's reflection coefficient (ROEHRLEIN *et al.* 1985). However, the goals of these studies were purely theoretical or intended for medical applications, e.g., mammography (imaging of the female breast). The present studies are more experimental and particular suitable for imaging specimens with roughly circular symmetry, such as cylinders or pipes related to materials research and NDE.

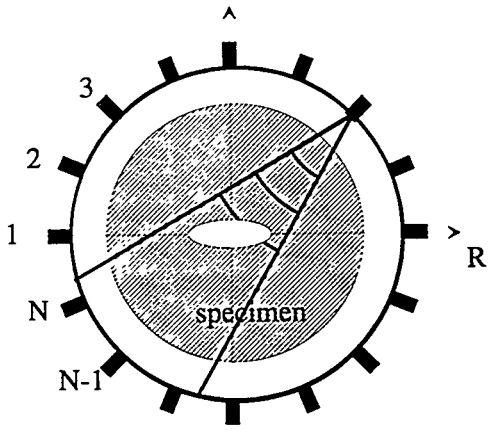

Figure 3.1. Schematic representation of a circular aperture array with uniformly distributed transducer elements along a radius R. A transducer transmits and receives, respectively, a short pulse (monostatic mode) while a sector of transducers receives the transmitted pulse (bistatic mode). The process is repeated for N transducer elements.

3.1.1 General experimental requirements

Mechanical circular movements of two ultrasonic transducers were applied to synthesize the circular aperture array. The approach is referred to as a synthetic circular aperture array or simply a circular aperture array (KRAUS 1983 and LANGENBERG *et al.* 1986). The synthetic aperture was chosen in preference to a fixed circular aperture system due to its flexibility. Not only did the use of only two transducers allow to change transducer configurations (e.g., center frequency, focal length and transducer aperture), but also to image large specimens. The setup and the signal processing was also much simpler than those needed for ultrasonic tomography based upon fixed transducer array systems. However, a requirement of faster scan time may benefit from a fixed aperture with electronically scanning rather than this mechanical scanning (MACOVSKI 1979).

The scanning facilities used in this experiment were the following: The synthetic circular aperture array, shown in Fig. 3.2, was positioned in a water filled tank with dimensions 70 cm (w) x 107 cm (l) x 47 cm (d). The size of the specimens was therefore restricted by these scanning tank dimensions. The design specification for the present UCT-system was to image a 10 cm x 10 cm object field with a resolution of 2 mm. No constraint was placed on the scanning time, although, the image reconstruction time should be minimized.

Ultrasonic signals obtained from the simple acrylic (PMMA, Plexiglas®, Perspex®) specimens (see Appendix 2.1) with a water filled elliptical hole was used in the subsequent sections to evaluate the two scanning modes of the circular aperture array. The speed of sound in Plexiglas was measured to (2727 ± 20) m/s and the speed of sound in water was measured to (1480 ± 20) m/s at a temperature about 20°C.

The cylindrical Plexiglas specimen could be rotated, about the center of rotation, by a step motor (turn table) controlled by a computer. The receiving transducer could also be rotated around the specimen by a second step motor (and a gearing) controlled by the same computer. This allowed high flexibility in the experimental procedure. Data acquisition was performed by an ultrasonic inspection system HFUS 2000 with a peak detection gate. Transmitted and reflected ultrasonic signals were digitized with a high-speed digitizer at 6.25 MHz

and data was stored in a special dimension (DIM) file format containing all scanning information such as number of receivers, number of projections etc. Approximately 0.5 Mbytes data were required per file.

Two broadband transducers, one acting as a transmitter and the other as a receiver, were mounted normal to the cylinder axis on each side of the specimen with a well-defined distance to the specimen. The transmitter and the receiver were high-frequency piezoelectric ceramic immersion transducers, as specified below.
In the UCT-theory, it was assumed that the applied ultrasonic beam had an ideal fan shape, i.e., wide in the horizontal plane of the circular aperture; and the central line (acoustical axis) of the beam pattern was directed to the center of the circular aperture. It was also assumed that the beam was collimated in the vertical plane (i.e., perpendicular to the circular aperture) in order to insonify an infinitesimal thin slice of the specimen.
A wide angle beam can be obtained with a small point transducer, but in practical limited energy would then be radiated into the specimen. A solution could be using of a large aperture transducer with a mask (ZEQIRI *et al.* 1998). The second assumption requires a transducer with a rectangular or focused aperture. In this chapter the bistatic and monostatic mode of the circular aperture array were verified using either circular or cylindrical focused transducers.

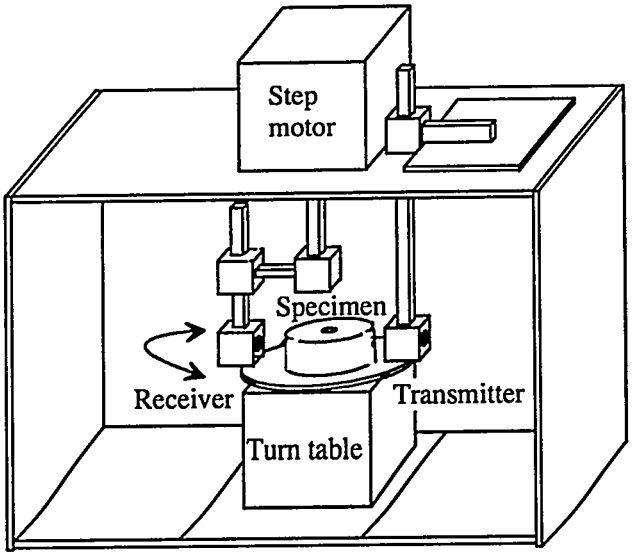

Figure 3.2. Experimental configuration of the tomographical system. One step motor rotates and controls the receiver while another step motor rotates the specimen. The transmitter is fixed.

Table 3.1 presents the most important sound field data from the transducer with circular focus. It has a "low" center frequency, about 100% bandwidth and a "large" aperture diameter. The beam profile of the transducer (in water) was examined in a separated setup (see Appendix 3.1). The length of the (-6 dB) focal zone of the beam was found to be about 36 mm. The (-6 dB) beam diameter were found to be circular and about 2.7 mm at the focus (29.6 mm from the transducer). Hence, the term "circular focus" is addressed to this transducer. Using the focus distance and the lateral resolution, it gave a (-6 dB) half angle beam spread of about 2.6°.

Table 3.2 presents the relevant sound field data from the transducer with cylindrical focus. It has, compared to the former, a "higher" center frequency, but a "smaller" aperture diameter. The length of the focal zone was 36 mm and a cylindrical lateral resolution, i.e., a minor (-6 dB) sound plane of 0.5 mm and a major sound plane of 3.4 mm. Thus, the term "cylindrical focused" is addressed to this transducer (see Appendix 3.1). Again using the focus distance and the major sound plane of the lateral resolution, it gave a (-6 dB) half angle beam spread of about 3.3°.

Table 3.1. Ultrasonic immersion transducer with circular focus.

Panametrics, Inc. (No.)	M306 (159967)
Center frequency	2.25 MHz
Bandwidth (-6 dB) Approx.	2 MHz
Aperture diameter	12.5 mm
Length of focal zone in water (-6 dB)	36 mm (17 - 53 mm)
Near field distance in water	60 mm
Circular lateral resolution* δ_{-6dB}	2.7 mm
Half angle beam spread α_{-6dB}	2.6°

*-6 dB beam diameter in water 29.6 mm from the transducer.

Table 3.2. Ultrasonic immersion transducer with cylindrical focus.

Panametrics, Inc. (No.)	V314 (50092)
Center frequency	10.0 MHz
Bandwidth (-6 dB) Approx.	5 MHz
Aperture diameter	8 mm
Length of focal zone in water (-6 dB)	36 mm (29 - 65 mm)
Near field distance in water	110 mm
Cylindrical lateral resolution* δ_{-6dB}	0.5 / 3.4 mm
Half angle beam spread α_{-6dB}	3.3°

*-6 dB beam diameter in water 29.6 mm from the transducer.

3.2 Bistatic image reconstruction - Experimental technique (II)

In this section, the bistatic image technique is discussed. It involves two transducers placed along the circular aperture. One of the transducers transmits a "wide" ultrasonic beam and the second transducer receives the forward transmitted sound field over a sector (arc) of receivers. Insonifying a specimen with a diverging ultrasonic beam is addressed to as a fan-beam insonification (see, e.g., SOUMEKH 1994).

3.2.1 Experimental procedure (II)

The scanning procedure in the bistatic mode was the following. First, the cylindrical focused transducer, presented in Table 3.2, was used to transmit a fan-beam. Second, ultrasonic signals were received along a 73.5° sector, applying 128 receiver positions. This corresponded to a sector resolution of $\Delta\theta$ = 0.57 °/rec. Third, the signals were amplified and displayed on a digital oscilloscope, where a time gate was set to measure the peak amplitude for each received signal. Finally, the specimen was rotated $\Delta\phi$ = 0.38 °/proj. and the sector was scanned again until the required number of amplitude projections were measured. In this experiment 939 fan-beam projections were measured, corresponding to 360° rotation of the specimen. The total scanning time was about 8 minutes for acquiring the 128 receiver positions and the 939 fan-beam projections. However, before introducing the Plexiglas specimen, a reference measurement in a Plexiglas specimen without ellipse was performed. Data acquisition with the specimen present could then proceed. The experimental parameters are presented in Table 3.3.

Table 3.3. Experimental parameters (II) for bistatic imaging.

Center frequency	10.0 MHz
Wavelength. Plexiglas (Water)	0.27 mm (0.148 mm)
Sound velocity. Plexiglas (Water)	2727 m/s (1480 m/s)
Aperture radius R (sector angle)	73 mm (73.5°)
Aperture resolution $\Delta\phi$ (N samples)	0.38 °/proj. (360°/939)
Sector resolution $\Delta\theta$ (N samples)	0.57 °/rec. (73.5° /128)
Image resolution (1024x1024 pixels)	117 μm x 49 μm (120 x 50 mm^2)
Dynamic range of image	5 bit (0-31 dB)
Reconstruction time* (scan time**)	15 min. (8 min.)

* Pentium (166 MHz). ** for the specified tomogram.

DRIKE *et al.* (1976) and WANG (1977) introduced the idea of reordering a set of fan-beam projections into an equivalent set of parallel projections. The advantage of reordering fan-beam projections is that the fast and efficient filtered backprojection algorithm can be utilized directly (see also PETERS *et al.* 1977 and DEFRANOULD 1981). By selecting single beams from each of several fan-beams, the required sets of parallel beams may be obtained. The technique of reordering a fan-beam into parallel beams, is illustrated in Fig. 3.3. A subset of fan-beams is shown, where a single beam has been marked to yield a set of parallel beams. Alternatively, a direct inversion technique of fan-beam projections (HORN 1979) can be used, although, it appears to be computationally excessive. In this experiment, the fan-beam tomogram was reconstructed using the filtered backprojection algorithm, mentioned in chapter 2. The algorithm was used because it is relatively simple to implement, gives reasonably short processing

time, and allows some flexibility in the reconstruction via the choice of the projection filter. Here the process of backprojection simply involved taking an "amplitude" fan-beam projection and extending each value across image space back in the same direction along which the projection was obtained, i.e., each sample in the forward scattered data was reconstructed according to its angular position. By repeating this operation for every projection an image of the attenuation distribution was found. QIN *et al.* (1989) refers to this image as a hologram instead of a fan-beam tomogram.

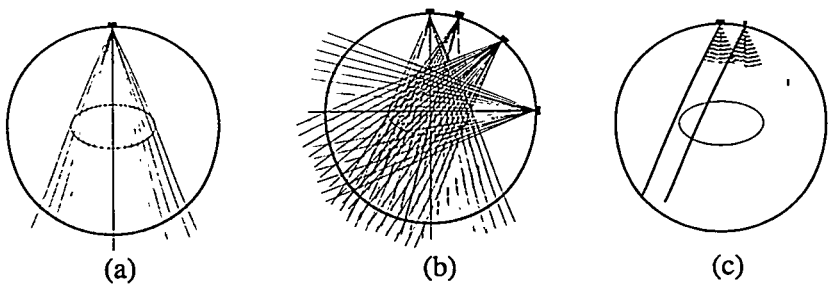

Figure 3.3. Bistatic imaging of an ellipse shaped target based on geometrical approximated diverging fan-beams on a circular aperture (a) one fan-beam, (b) four fan-beams and (c) a set of parallel beams chosen from two fan-beams.

3.2.2 Results - fan-beam tomograms

The fan-beam projections were confined within a sector of two polar angles, defined by the minimum signals that could be measured by the receiver. These minimum amplitude signals provided a practical limitation to this technique, together with a limited sensitivity of the transducers. Fig. 3.4 shows a typical fan-beam projection profile (cross section) of the transmitted amplitude data as a function of the receiver position. The experimental data, shown as black dots, are fitted by a polynomial fit.

In order to avoid difficulties in calculating realistic sound fields off-axis, amplitude data from the reference Plexiglas specimen (without the ellipse) were subtracted from the amplitude data in Fig. 3.4. Fig. 3.5 shows the resulting "normalized" UCT-tomogram of attenuation in the Plexiglas specimen, where the dark central region represents the water filled ellipse (8 mm x 20 mm) with low attenuation and the bright region represents the Plexiglas specimen with high attenuation.

The bright spots inside the ellipse, degrading the quantitative interpretation of the image, may be due to diffraction and will be discussed further in section 3.5.

The circular appearance of the ellipse, degrading the qualitative interpretation of the image, was due to experimental difficulty in aligning the specimen on the rotational axis. The positioning of the specimen should be compensated for in future measurements.

Comparing with the experimental procedure (I), the same quantitative amplitude tomogram may be obtained in this experiment. However, the fan-beam tomogram is more difficult to obtain, because it needs a reference specimen to compensate for beam spreading (and diffraction) and the specimen alignment limit the applications. Finally, a more sensitive transducer with a wider beam should be used.

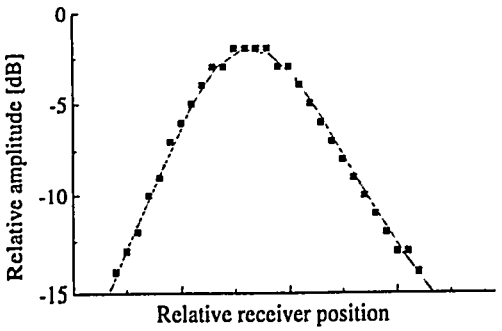

Figure 3.4. Fan-beam projection profile as a function of receiver position. Relative units.

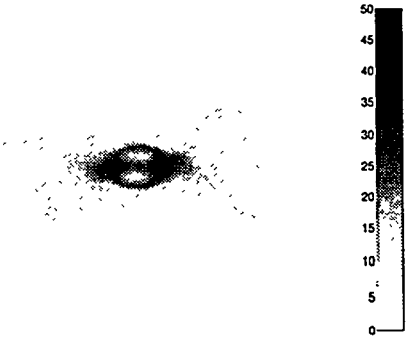

Figure 3.5. Fan-beam tomogram of a water-filled ellipse in a Plexiglas cylinder. Relative units.

3.2.3 Discussion - reconstruction artifacts

Besides from noise and experimental artifacts (errors), at least three reconstruction artifacts lead to a degradation of the tomogram:

- algorithm specific artifacts,
- insufficient number of projections and receivers,
- insufficient scan radius.

The discrete version of the filtered backprojection algorithm involved approximations to the continuous version of the algorithm. These approximations are addressed as algorithm specific artifacts. The filtered backprojection algorithm was, as mentioned, based on the Fast Fourier Transform (FFT base 2) and consequently, the number of receivers had to be a number of 2^n (e.g., 128 or 256) and the projections had to be of finite bandwidth. Projections of finite bandwidth are unlikely in practice, because the ellipse has a final spatial dimension. The algorithm specific artifact of this kind may introduce a DC-shift in the tomogram. But this artifact can be eliminated by zero-padding the projections before using the FFT (KAK 1979).
Two different theoretical reconstructions, based on the model developed in chapter 2, of an ellipse inside a cylindrical specimen are compared and cross sections through the major axis are shown in Fig. 3.6.

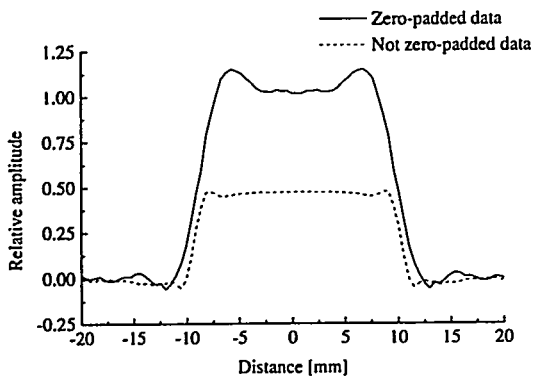

Figure 3.6. Algorithm specific artifact partly eliminated by zero-padding.

The dashed line represents a reconstruction with 128 receiver positions in a projection, while the solid line represents a similar reconstruction using a zero-padded projection. In this projection the 128 samples were padded with 128 zeros to make 256, which is required by the FFT. The cross section demonstrate clearly the DC-shift in the amplitude.

Insufficient number of projections (views) and receivers was another important artifact. Fig. 3.7 compares 12 different simulated reconstructions of an ellipse with dimensions 16 mm x 40 mm. The reconstruction artifacts are visualized by normalizing the image between 0 and 20. Hence, the level inside the ellipse corresponds to 20 and the level of the cylindrical Plexiglas specimen to 0. All images are displaced on 100 x 100 grids. The number of projections, seen from left to right, were arbitrary chosen to be 5, 180 or 1025. The small number of projections illustrates to few views, while the highest number illustrates an unnecessary high number of views. The number of receivers, seen from top to bottom, were chosen to be 4, 128, 256 or 1024. The top images correspond to an under-sampled projection and the bottom images correspond to an over-sampled projection.

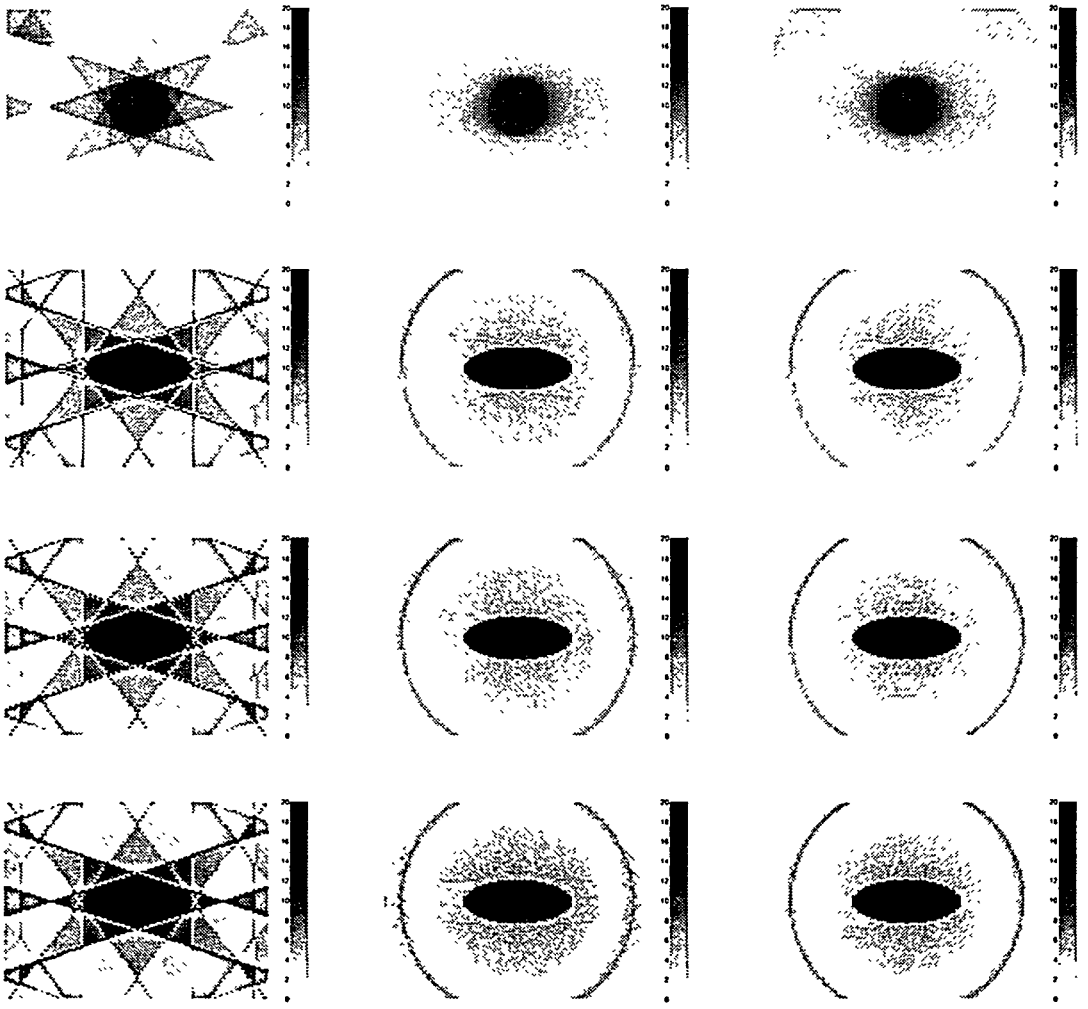

Figure 3.7. Number of projections (from left to right: 5, 180 and 540) and receivers (from top to bottom: 4, 128, 256 and 1024).

The tomograms imply that the number of projections, M, should be higher than the number of receivers, N. This is in accordance with the analytical ratio for parallel projections: $M / N = \pi/2$, as shown by BLYTH (1979). The ratio was $M / N = 939/128 \approx 7.3$ for this experiment (II), while the ratio was $M / N = 180/64 \approx 2.8$ for experiment (I) in chapter 2. The tomograms demonstrate also that a too small number of projections (left column) may lead to star pattern artifacts (Moiré patterns).
Finally, insufficient scan radius, SR, was considered in a circular aperture with radius $R = 73$ mm. The scan radius was defined as $SR = R \sin \alpha$, where α was the sector defined by the fan-beam. Fig. 3.8 shows four UCT-tomograms for an increasing scan radius (SR = 10, 30, 50 and 70 mm).

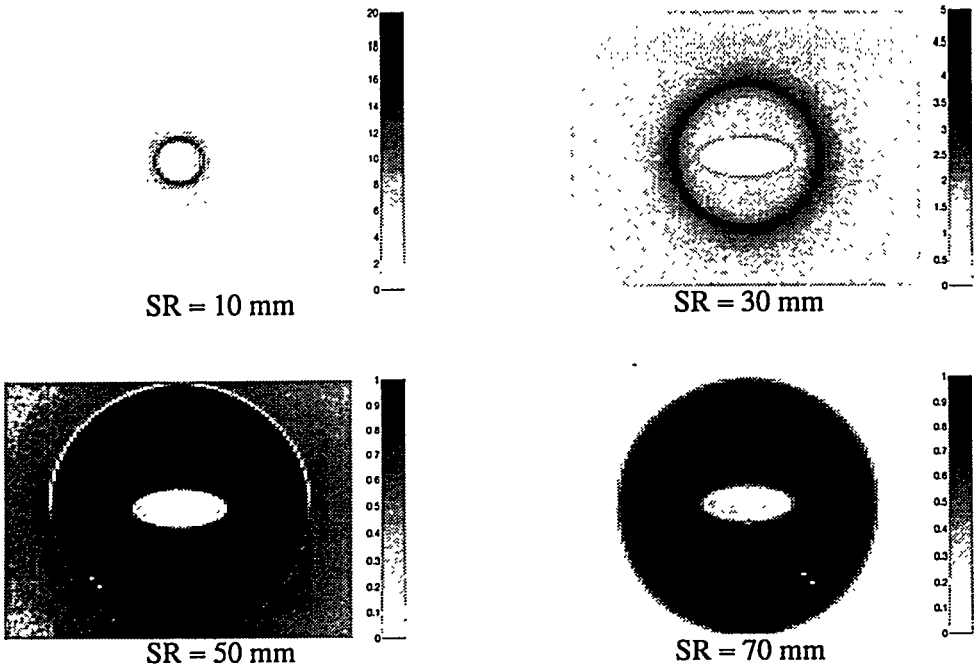

Figure 3.8. UCT-tomogram as a function of scan radius (SR = 10, 30, 50 and 70 mm).

Fig. 3.9. shows the corresponding horizontal cross sections through (0,0) in Fig. 3.8.

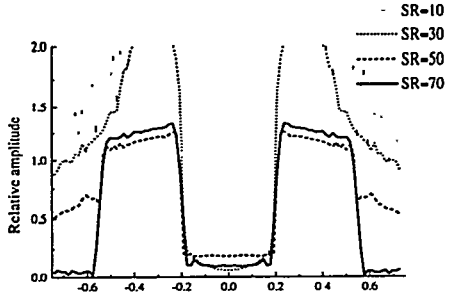

Figure 3.9. Horizontal cross sections through (0,0) of the four tomograms in Fig. 3.8.

These cross sections, and the tomograms in Fig. 3.8, indicate that the ultrasonic fan-beam should be wide enough to cover the entire imaging area. Hence, in this case $SR > 50$ mm. This was not the case with the applied transducer (SR $\approx$ 4 mm) and may explain the circular appearance in Fig. 3.5.

3.3 Monostatic image reconstruction - Experimental technique (III)

In this section, the monostatic image technique is discussed for the circular aperture array. The section includes an experimental procedure for obtaining a two-dimensional tomogram from backscattered ultrasound. A backprojection technique for reconstructing reflectivity over a circular domain is developed and compared with the straight line case in chapter 2. An analytical expression for the backprojection point spread function (PSF), i.e., the reconstruction of a point reflector, is then derived. Finally, a theoretical optimum resolution function is obtained and in order to use existing theory, the incident wave is assumed to be a diverging broadband insonification.

The task of deriving the structure of a specimen from scattering radiation has been known traditionally as the inverse scattering problem. Using ultrasound, essentially the same problem has been referred to by a variety of names, including diffraction tomography (ANDRÉ *et al.* 1996 and 1997) and reflection tomography (NORTON *et al.* 1979 and 1981). In the former treatment (i.e., diffraction tomography), the circular aperture consisted of an array of 1024 transducer elements, where each transducer was used in turn as a transmitter while all remaining transducers received simultaneously. The reconstruction process was performed in the frequency domain, taking the beam pattern of the transducers into account. In the latter treatment (i.e. reflection tomography), the circular aperture was assumed to consist of an array of continuous-wave point transducers. The reconstruction process was performed in the time domain.
The treatment used here differs in three aspects. First, the transducers transmit broadband signals (pulses) rather than monochromatic waves. Secondly, the transducers are directive (focused) rather than omni-directional point sources. Finally, each element serves as its own receiver, i.e., the elements are not taken in pairs, but used individually in a *pulse-echo* mode. An apparent advantage of using each element in pulse-echo mode is that only backscattered sound is observed. Another advantage is that it only requires one transducer element at a time. A major disadvantage is, that it is not possible to correlate, quantitatively, the backscattered signals with the local properties of advanced polymeric materials. A discussion of advanced materials and quantitative NDE is devoted to the remaining chapters.
While the bistatic approach had the opportunity to apply both narrowband and broadband signals, only the latter type is acceptable in monostatic imaging. Furthermore, monostatic imaging makes a number of other assumptions. Most important, it is necessary for the Born approximation to be valid (CHIAO *et al.* 1994). This means that the scattered field should be small compared to the incident field and attenuation due to scattering may be treated as negligible. Hence, the scattering object must be weak scattering and multiple reflections may be regarded as insignificant. Second, the scatters in the specimen must be isotropic scatters so that the field scattered by any scatters is identical no matter from what direction the incident field arrives. Finally, velocity and absorption changes must be small in order not to introduce errors in the round-trip delay time. In a real medium, all of these assumptions will be violated to some degree and some image artifacts will result, depending on the degree of violation.

Monostatic imaging, using point transducers distributed around a circle, leads to line integrals of the object reflectivity function over circular arcs (NORTON 1979*a*). If a point transducer emits a circular wave within the plane of the circular array, then the received electric signal is proportional to the integral of the

reflectivity from all point scatters lying along a circle (or ellipse, if a different point transducer is used as receiver). By applying backprojection techniques over circular arcs a reflectivity image of the specimen can be reconstructed in the following way: Let $f(r,\theta)$ be the two-dimensional reflectivity function of an object, in the plane of a circular aperture array. Backprojection of a backscattered signal, g, over circular arcs is then found as

$$f(r,\theta) = \int_0^{2\pi} g(2\rho(\phi;r,\theta))d\phi \tag{3.1}$$

where, the origin of a polar coordinate system is the center of the array, as shown in Fig. 3.10, and the distance from the transducer element (R,ϕ) to the reconstruction point at (r,θ) is given by the *Cosine* relation

$$\rho(\phi;r,\theta) = \sqrt{R^2 + r^2 - 2Rr\cos(\theta - \phi)} \tag{3.2}$$

The backprojection technique may be extended to three dimensions, i.e., reconstruction over a spherical rather than circular domain (NORTON *et al.* 1981).

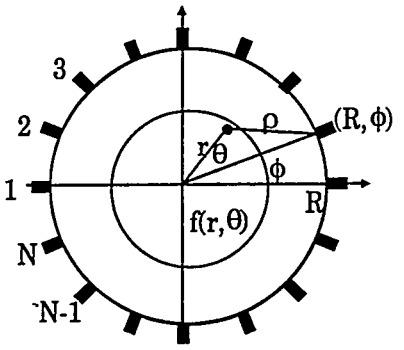

Figure 3.10. Geometry of circular aperture array.

The "integration over circular arcs" interpretation of backscattering from point scatters suggests that a possible effective approach to reconstruct the scattering distribution would consist of backprojecting and coherently adding the backscattered signals over circular arcs in the image domain. This backprojection is analogous to backprojection techniques used in chapter 2. One difference is that in the latter case, the backprojection is performed along straight lines, whereas in this case, the backprojection is carried out over circular arcs. The process of backprojection over straight lines, without prior filtering, was expressed as

$$\mu(x,y) = \int_0^{2\pi} \mu^{\forall}(\rho,\phi)d\phi \tag{2.20'}$$

where $\mu(\rho,\phi)$ was a one-dimensional projection at all angles through $\mu(x,y) = \mu(r\cos\theta, r\sin\theta)$ and

$$\rho(\phi;r,\theta) = x\cos\theta + y\sin\theta = r(\cos\theta\cos\phi + \sin\theta\sin\phi) = r\cos(\theta - \phi) \tag{3.3}$$

In comparison, the circular arc in Eq. (3.2) may be expanded and approximated using $(r/R)^2 << 1$ to

$$\rho(\phi;r,\theta) = R\sqrt{1+(r/R)^2 - 2rR^{-1}\cos(\theta-\phi)} \approx R - r\cos(\theta-\phi) \quad (3.4)$$

Thus, Eqs. (3.3) and (3.4) are identical, beside from a shift in origin of R. Moreover, when the aperture radius becomes very large compared to the size of the specimen, the circular arcs that intersect the specimen are approximately straight lines over the region of interest. As a result, in the limit $R \rightarrow \infty$, the reconstruction is reduced to that of the Radon transformed and demonstrate the close relation to the straight line case in chapter 2.

3.3.1 Experimental procedure (III)

Only one transducer was applied at a time in the monostatic imaging procedure. Hence, the transducer was used both as transmitter and receiver, which is similar to the well-known *pulse-echo* technique (KRAUTKRÄMER *et al.* 1990). Scanning systems that are required to measure backscattered signals, at high signal-to-noise ratios, must have a receiving transducer with high sensitivity (because in this case most ultrasonic energy is scattered in the forward direction). The circular focused transducer, presented in Table 3.1, had higher sensitivity compared with the cylindrical focused. It was therefore applied in this experiment. In the monostatic procedure, a broadband pulse was transmitted into the specimen and the backscattered pulse was received by the same transducer to form an A-scan. The transducer was then rotated along the circular aperture in Fig. 3.10 and successive scans from N directions were obtained. Finally, the N×A-scans were combined into a single projection representing the distribution of reflectivity within the specimen. The latter is similar to a "circular B-scan", which will be discussed further in section 3.4.

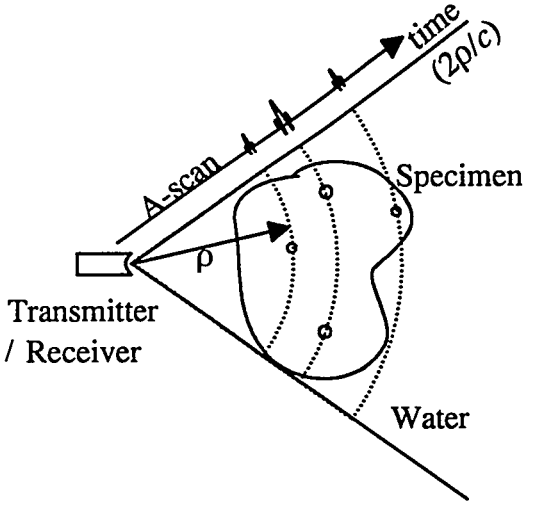

Figure 3.11. Arcs, centered at the transducer position, forms an A-scan in monostatic UCT.

To reconstruct the tomogram, the A-scans were backprojected over an arc of radius ρ in the image space, assuming that the A-scans represented line integrals (sums) of echo's arising from scattering points lying along an arc. This arc corresponded to a round-trip delay of $2\rho/c$, where c is the speed of sound, as indicated schematically in Fig. 3.11. Finally, the summation of the backprojected A-

scans for every transducer element position formed the image of the specimen reflectivity function. Hence, each A-scan contributed one value to each image point.
In the present case, a peak detection gate was set to cover only the reflected signals from the ellipse. The gate threshold was set above the average level of material noise. A total of 1469 transducer positions (projections) were used over 360° ($\Delta\phi$ = 0.24° /proj.), each projection containing 256 samples. The positioning accuracy of the specimen, which was critical in experiment (I), was estimated to be less than 0.2 mm. The experimental parameters are presented in Table 3.4.

Table 3.4. Experimental parameters (III) for monostatic imaging.

Frequency	2.25 MHz
Wavelength. Plexiglas (Water)	1.2 mm (0.7 mm)
Sound velocity. Plexiglas (Water)	2720 m/s (1480 m/s)
Aperture radius (sector angle)	73 mm (360°)
Time resolution $\Delta\tau$ (samples)	80 ns (256)
Aperture resolution $\Delta\phi$ (*N* samples)	0.24 °/proj. (360°/1469)
Image resolution (1024x1024 pixels)	54 μm x 24 μm (55 x 25 mm^2)
Dynamic range of image	5 bit (0-31 dB)
Reconstruction time* (scan time**)	15 min. (8 min.)

* Pentium (166 MHz). ** for the specified tomogram.

Fig. 3.12 shows the geometry of monostatic imaging using an ultrasonic fan-beam transducer, where a two-dimensional slice in the specimen has to be imaged. The sound beam has an ideal fan-beam shape, as assumed in the UCT-theory, and it is collimated in the direction perpendicular to the slice.

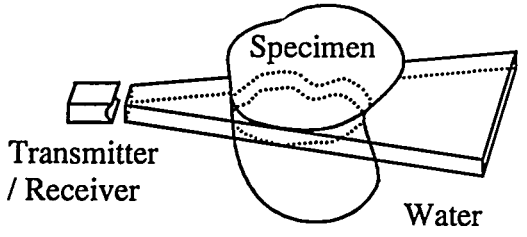

Figure 3.12. An ultrasonic fan-beam transducer used in monostatic imaging.

In this case the transducer had neither fan-beam shape nor was it perfectly collimated. In stead, the beam was focused and had a finite thi ning that the received signals arose from a finite sized slice of the re Water ld. Consequently, it was not perfectly two-dimensional (it took into account scattering from outside the slice), but the straight line approximation was applicable.

In analogy with backprojection along straight lines, the backprojection procedure of the A-scans lead to a blurring of the tomogram. The shape of the blurring function is dependent of the pulse shape, as discussed in subsection 3.3.4, plus a smaller term resulting from the curvature of the circles.
To avoid this blurring, the A-scans can be convolved with a filter before backprojection, in principle, to eliminate the sidelobe artifacts introduced in the backprojection process. This optimum filter is as shown below, surprisingly, similar to the filter used in experiment (I). Hence, it seems appropriate to form an image of the specimen by first filtering each line integral data with a filter

function and then backprojecting the data over the same lines on which they were measured.

Alternatively, an optimally-shaped pulse could be received with a temporal frequency content similar to the transfer function of the backprojection filter. The latter would give an ideal reconstruction without filtering, as discussed in subsection 3.3.4.
Finally, the focal point of the transducer could be considered as a point source (MOSHFEGHI *et al.* 1985*a,b*). The center for the circular waves was then not the transducer position, but the point focus. This focus was an offset from the specimen by a distance $F_{ref} = SR\,c_0(c-c_0)^{-1}$, where SR was the scan radius, c and c_0 was the speed of sound of the specimen and water, respectively. Thus, the point focus was effectively a virtual source of the ultrasonic fan-beam. The A-scan had then to be corrected in time so that zero-time corresponds to this virtual transducer position and not the real transducer position.

3.3.2 Results - reflection tomograms

Fig. 3.13 shows the experimental reflection data obtained as a function of the receiver position and relative delay time. The minimum time delay, A, and the maximum time delay, B, between two reflections in Fig. 3.13 corresponds to the major and minor axis of the ellipse. The ratio A/B = 0.4 is in agreement with the ratio between the minor and major axis of the ellipse. A typical UCT tomogram of the ellipse based on the reflection coefficient is presented in Fig. 3.14. The tomogram shows the ellipse in the Plexiglas specimen on a matrix size of 1024x1024 pixels. The dark regions in the figure indicate a high reflectivity, representing the Plexiglas-water interface of the ellipse.

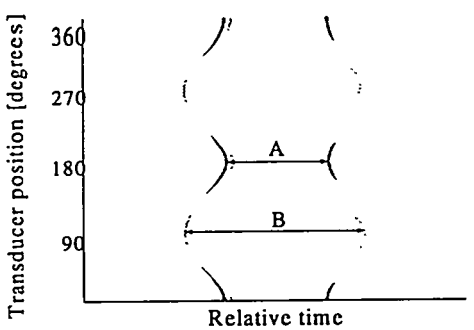

Figure 3.13. Backscattered data as a function of transducer position and relative propagation time.

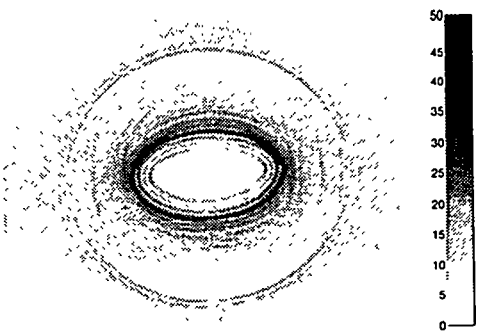

Figure 3.14. Reflection tomogram of an ellipse in a cylindrical Plexiglas specimen.

This is in accordance with the fact that large acoustical impedance mismatch between water and Plexiglas reflects the majority of incident sound energy.
Comparing with experiment (I) and (II), a different tomogram was obtained by this technique. The reflection tomogram exhibit a better qualitative impression of the size of the ellipse (see section 3.4).

3.3.3 Discussion - resolution in UCT

Resolution in ultrasonic imaging is characterized by the spectral properties of the transducer used in the imaging system. While the term *resolution* often relates to lateral (transverse) resolution, axial (range or radial) resolution must also be defined for monostatic UCT.

The most widely used *tomographic* technique is the conventional B-scan technique. It produces, depending on the beam focusing, poor lateral resolution compared to the axial resolution. If all such B-scans are added with respect to their angular orientation in the circular aperture, the result may be an UCT-tomogram with a resolution, that is an average of the lateral and the axial B-scan resolution (KINO *et al.* 1979, HAVLICE *et al.* 1979 and ROEHRLEIN *et al.* 1985).
The basic lateral resolution available in a conventional ultrasonic imaging system is controlled by the dimension of the (-6 dB) beam diameter δ_{-6dB} (KEATING *et al.* 1979, HERMENT *et al.* 1987); or theoretically by the Rayleigh two point resolution criterion δ_{Rayl} (GOODMAN 1996 and KINO 1987), i.e., the minimum geometrical separation of two points given by

$$\delta_{Rayl} = 1.22F\frac{\lambda}{D}, \qquad \delta_{-6dB} \approx F\frac{\lambda}{D} \tag{3.5}$$

where F is the focal length, λ is the ultrasonic wavelength and D is the transducer aperture.
The axial resolution is controlled by the duration of the incident pulse, τ, which in the time domain corresponds to

$$\tau \approx \frac{1}{\Delta f_{-6dB}} \tag{3.6}$$

where Δf_{-6dB} is the (-6 dB) bandwidth of the transducer (QIN *et al.* 1989 and ERMERT *et al.* 1995).
Thus, in conventional imaging systems good lateral resolution is achieved by using a large aperture transducer with a high center frequency and good axial resolution is achieved by using a broad bandwidth transducer. The center frequency for such a transducer is controlled by the thickness of the piezoelectric element, while the bandwidth is controlled by the backing properties (NIELSEN *et al.* 1995*a,b* and BJØRNØ *et al.* 1995). However, there are limitations in approaching higher frequencies and higher bandwidths due to the attenuation of the specimen, which has to be imaged, and the fluid which is surrounding the specimen. Hence, the resolution of a B-scan image depends mostly on the transducer aperture and a trade-off between transducer frequency and bandwidth has to be made.

One way to improve lateral resolution, according to Eq. (3.5), is to synthesize a receiver aperture which is larger than the actual aperture. Two different approaches can be used, as mentioned previously: 1) the receiver aperture may be synthesized by multiplexing transmitters, so that no motion is involved, i.e. a fixed array. 2) the receiver aperture may be synthesized by motion of either specimen, receiver or transmitter, or any two of these. The latter approach was used in this thesis.

In the following, the lateral resolution is derived for the bistatic experiment (II), while the lateral resolution for the monostatic experiment (III) is derived in subsection 3.3.4.

Consider first a transducer in the bistatic experiment (II), having a half angle beam spread, α, smaller than $Arc\sin(SR/R)$, where SR is the scan radius and R is the aperture radius in the circular aperture array. The effective transmitting aperture diameter, D_1, defined in Fig. 3.15a, is then

$$D_1 = 2\beta R \qquad \text{when } \alpha < Arc\sin\left(\frac{SR}{R}\right) \tag{3.7}$$

where β is an angle, which can be found from the *Sinus relation*, i.e.,

$$\frac{SR}{\sin\alpha} = \frac{R}{\sin(\pi - \alpha - \beta)} \tag{3.8}$$

Substituting (3.8) into (3.7) yields

$$D_1 = 2R \cdot Arc\sin\left(\frac{R\sin\alpha}{SR}\right) - \alpha R \tag{3.9}$$

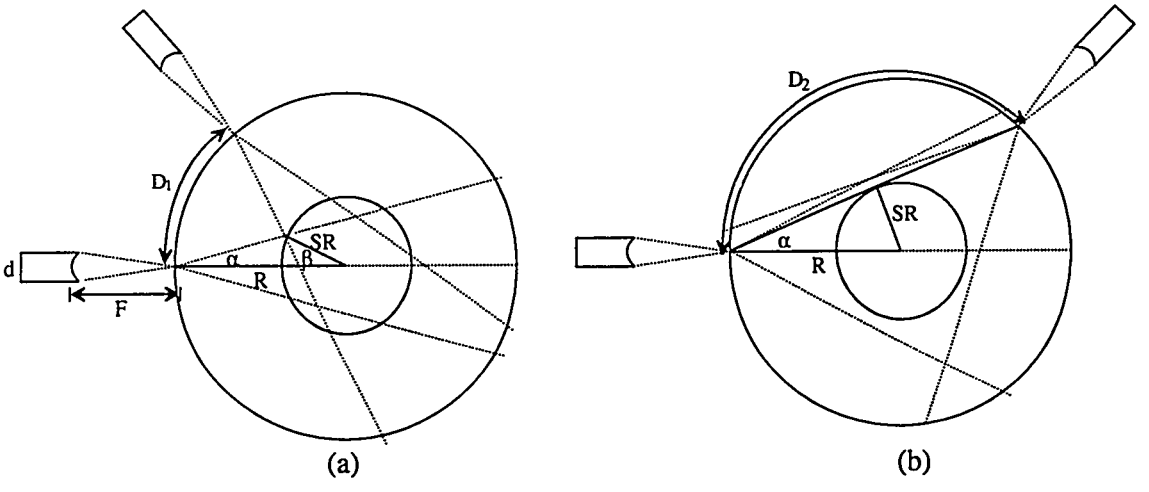

Figure 3.15. Effective transmitting apertures, D_1 and D_2, in bistatic imaging.

Consider next the bistatic experiment with a transducer having a half angle beam spread, α, equal to or greater than $Arc\sin(SR/R)$. The effective transmitting aperture diameter, D_2, defined in Fig. 3.15b, is then limited by the viewing angle of the specimen

$$D_2 = (\pi - 2\alpha)R \qquad \text{when } \alpha \geq Arc\sin\left(\frac{SR}{R}\right) \tag{3.10}$$

or

$$D_2 = 2R \cdot Arc\cos\left(\frac{SR}{R}\right) \tag{3.11}$$

Combining Eqs. (3.5), (3.9) and (3.11) gives an expression for the lateral resolution in the bistatic experiment

$$\delta_{-6dB} = \begin{cases} \dfrac{F\lambda}{2R \cdot Arc\sin\left(\dfrac{R\sin\alpha}{SR}\right) - \alpha R} & \alpha < Arc\sin\left(\dfrac{SR}{R}\right) \\ \dfrac{F\lambda}{2R \cdot Arc\cos\left(\dfrac{SR}{R}\right)} & \alpha \geq Arc\sin\left(\dfrac{SR}{R}\right) \end{cases} \tag{3.12}$$

As an example, consider SR = 50 mm. The cylindrical focused transducer in the bistatic imaging system had the parameters: F_o= 29.6 mm, α_{-6dB} = 3.3° (Table 3.2), λ_o= 0.1 mm and R=73 mm (Table 3.3). The lateral resolution can then be found from Eq. (3.12) to δ_{-6dB} = 0.5 mm which is, as expected, smaller than presented in Table 3.2.

3.3.4 Discussion - PSF of backprojection

Now, consider the monostatic experiment (III). The lateral resolution can be found by considering the temporal impulse response, $h(t)$, of the experiment. It is assumed that it is a linear system consisting of a point transducer and a point scatter, separated by the distance ρ (see e.g. Fig. 3.11). The shape of this impulse response is, in general, depending on the characteristics of the transducer and the propagation medium. However, in the present analysis the amplitude will be considered as proportional to the target reflectivity, while the shape will be treated as invariant with respect to target position. Mathematically, the time delay, t, will be measured in units of distance, $\hat{t} = tc$, rather than time, in order to eliminate speed of sound, c, of the specimen.
Hence, for a transmitted pulse, $p_t(\hat{t})$, the received pulse is given by

$$p_r(t - 2\rho) = p_t(\hat{t}) * h(\hat{t} - 2\rho) \tag{3.13}$$

where * denotes the convolution operator and $h(\hat{t} - 2\rho)$ the impulse response. Hence, knowledge of the impulse response allows one to determine the shape of the received pulse by controlling the shape of the transmitted waveform, or equivalently, by inserting a filter at the receiver, as noted by NORTON *et al.* (1979*a*).
In order to determine the impulse response, the backprojection process Eq. (3.1) is used to reconstruct the image of a single scatter at (r_0,θ_0). This reconstruction is called the point spread function (PSF) of a point reflector. The PSF may be regarded as the two-dimensional analog of the impulse response of the above linear system. It is characterized by a sharp mainlobe of non-zero width corresponding to the resolution of the system, and sidelobes which trail off some distance from the mainlobe.
By substituting $g(\hat{t}) = p_r(\hat{t} - 2\rho)$ into Eq. (3.1), the PSF of the backprojection process for a single scatterer at (r_0,θ_0) is given by

$$f(r,\phi) = \int_0^{2\pi} p_r[2(\rho(\phi;r,\theta) - \rho(\phi;r_0,\theta_0))]d\phi \tag{3.14}$$

where $2\rho(\phi;r,\theta)$ is the round-trip distance between the target at (r_0,θ_0) and the array element at (R,ϕ) and

$$\rho(\phi;r,\theta)-\rho(\phi;r_0,\theta_0)= \sqrt{R^2+r^2-2Rr\cos(\theta-\phi)}-\sqrt{R^2+r_0^2-2Rr_0\cos(\theta_0-\phi)} \quad (3.15)$$

or

$$\rho(\phi;r,\theta)-\rho(\phi;r_0,\theta_0)=R\left[\sqrt{1+(r/R)^2-2rR^{-1}\cos(\theta-\phi)}-\sqrt{1+(r_0/R)^2-2r_0R^{-1}\cos(\theta_0-\phi)}\right] \quad (3.16)$$

This equation may be approximated by the Taylor expansion (i.e., $\sqrt{1+x}=1+\frac{x}{2}-\frac{x^2}{8}\ldots$) and assuming that the aperture circle is large enough so that $(r/R)^2 << 1$ and $(r_0/R)^2 << 1$, it can be written

$$\rho(\phi;r,\theta)-\rho(\phi;r_0,\theta_0)\approx X\cos(\phi-Y)+\gamma_1+\gamma_2\cos 2(\phi-\alpha) \quad (3.17)$$

where X is the distance between the point reflector at (r_0,θ_0) and the point under reconstruction at (r,θ)

$$X=\sqrt{r_0^2+r^2-2r_0r\cos(\theta-\theta_0)} \quad (3.18)$$

and
$$\tan Y=\frac{r_0\sin\theta_0-r\sin\theta}{r_0\cos\theta_0-r\cos\theta} \quad (3.19)$$

$$\gamma_1=\frac{r^2-r_0^2}{4R} \text{ and } \gamma_2=\tfrac{1}{4R}\sqrt{r_0^4+r^4-2r_0^2r^2\cos 2(\theta-\theta_0)} \quad (3.20)$$

$$\tan\alpha=\frac{r_0^2\sin 2\theta_0-r^2\sin 2\theta}{r_0^2\cos 2\theta_0-r^2\cos 2\theta} \quad (3.21)$$

It can be shown (KAK 1988, NORTON *et al.* 1979a) that both γ_1 and γ_2 are small, if the aperture radius, R, is large compared to both the radii r and r_0, and both the target and the image points are close to the center of the array. Thus, Eq. (3.17) can be simplified to

$$\rho(\phi;r,\theta)-\rho(\phi;r_0,\theta_0)\approx X\cos(\phi-Y) \quad (3.22)$$

Let now $P_r(\hat{v})$ denote the Fourier transform (spectrum) of the received pulse $p_r(\hat{t})$ in Eq. (3.13), hence

$$p_r(\hat{t})=\int_{-\infty}^{\infty}P_r(\hat{v})e^{i\hat{\omega}\hat{t}}\,d\hat{v} \quad (3.23)$$

where the frequency $\hat{v}$ and angular frequency $\hat{\omega}=2\pi\hat{v}=2\pi v/c$ is expressed in units of reciprocal length. Substituting (3.22) and (3.23) into (3.14) gives

$$f(r,\theta)\approx\int_0^{2\pi}d\phi\int_{-\infty}^{\infty}d\hat{v}P_r(\hat{v})e^{i\hat{\omega}2X\cos(\phi-Y)} \quad (3.24)$$

Finally, making use of the Bessel identity

$$J_0(r) = \frac{1}{2\pi}\int_0^{2\pi} d\phi e^{ir\cos(\phi - q)} \tag{3.25}$$

where J_0 is the Bessel function of the first kind and zero order (GOODMAN 1996), the point spread function (PSF) for the backprojection process can be written

$$f(r,\theta) \approx 2\pi \int_{-\infty}^{\infty} P_r(\hat{v}) J_0(2\hat{\omega}X) d\hat{v} \tag{3.26}$$

This equation will be used in the following analysis to derive the point spread function for an optimum pulse shape.

In order to determine the optimum shaped pulse for the backprojection process, $P_r(\hat{v})$ has to be such that $f(r,\theta)$ in Eq. (3.26) is as close to the Dirac delta function as possible, i.e.,

$$f_{(1)}(r,\theta) \approx 2\pi \int_{-\infty}^{\infty} P_r(\hat{v}) J_0(2\hat{\omega}X) d\hat{v} = \frac{\delta(X)}{\pi|X|} \tag{3.27}$$

where the delta function is expressed in polar coordinates. The optimum shaped pulse is then found by noting the identity (GOODMAN 1996)

$$\int_{-\infty}^{\infty} J_0(X\hat{v})|\hat{v}| d\hat{v} = \frac{2\delta(X)}{|X|} \tag{3.28}$$

and using the fact that $J_0(\bullet)$ is an even function. It can be seen that the expression of the optimum received pulse is

$$P_r(\hat{v}) = |\hat{v}| \tag{3.29}$$

This "optimum filter" is not practical since it emphasizes high frequencies. Generally, a more realistic filter is a low pass filtered version of the optimum filter, i.e.,

$$P_r(\hat{v}) = |\hat{v}|\, rect(\hat{v} / 2\hat{v}_c) \qquad rect(u) = 1 \quad for \quad |u| < \hat{v}_c \tag{3.30}$$

where *rect* is the rectangular function with cutoff frequency $\hat{v}_c$. Using this filter function in Eq. (3.26) and integrating, the PSF for the backprojection process becomes

$$f_{(1)}(r,\theta) = \frac{\hat{v}_c J_1(2\hat{\omega}_c X)}{X} \tag{3.31}$$

where J_1 is the Bessel function of the first kind and first order.

The distance, δ_{Rayl}, between the peak of the PSF and its first zero is often used to measure the width of the mainlobe. It is referred to as the Rayleigh resolution distance by GOODMAN (1996). From Eq. (3.31) this distance is

$$\delta_{Rayl} = 0.30\frac{2\pi}{\hat{\omega}_c} = 0.30\lambda_c \tag{3.32}$$

where λ_c is the wavelength of the wave corresponding to the angular cutoff frequency $\hat{\omega}_c$. The asymptotic envelope of Eq. (3.31) is $X^{-1.5}$.

In the previous analysis, the PSF for the monostatic mode was considered in which the same point transducer served as transmitter and receiver, and data was backprojected along circular paths. However, the monostatic mode can be used to analyze two complex "bistatic" modes: In the first mode, transmitter and receiver is separated with fixed separation and backprojection is performed along elliptic paths. In the second mode, transmitter and receiver is distinct with a varying separation.
The first complex mode, where transmitter and receiver are separated with a fixed angle 2β, is a more general case than the monostatic mode. In this mode the received A-scan echoes are evaluated at time $(\rho_1+\rho_2)/c$, where ρ_1 and ρ_2 represents the round-trip delay between the transmitter and receiver, respectively, to the point under reconstruction. The propagation time for the sound wave present, therefore, an elliptic path whose foci coincide with the transmitter and receiver. In this case, a reconstruction of a point reflector (PSF) is found analogous to the monostatic case. For a single scatterer at (r_0,θ_0) the PSF of the backprojection process is given by

$$f_{(2)}(r,\phi) = \int_0^{2\pi} p_r\begin{bmatrix}2(\rho_1(\phi+\beta;r,\theta)+\rho_2(\phi-\beta;r,\theta)\ldots\\ -\rho_1(\phi+\beta;r_0,\theta_0)-\rho_2(\phi-\beta;r_0,\theta_0))\end{bmatrix}d\phi \tag{3.33}$$

where

$$\begin{aligned}\rho_1(\phi+\beta;r,\theta) &= \sqrt{R^2+r^2-2Rr\cos(\theta-(\phi+\beta))}\\ \rho_2(\phi-\beta;r,\theta) &= \sqrt{R^2+r^2-2Rr\cos(\theta-(\phi-\beta))}\end{aligned} \tag{3.34}$$

Analogous to Eqs. (3.14-16), Eq. (3.34) may be approximated by the Taylor expansion (i.e., $\sqrt{1+x} = 1+\frac{x}{2}-\frac{x^2}{8}\ldots$) and assuming that the aperture circle is large enough so that $(r/R)^2 << 1$ and $(r_0/R)^2 << 1$. This gives

$$\begin{aligned}&\rho_1(\phi+\beta;r,\theta)+\rho_2(\phi-\beta;r,\theta)-\rho_1(\phi+\beta;r_0,\theta_0)-\rho_2(\phi-\beta;r_0,\theta_0)\\ &\qquad\approx 2X\cos\beta\cos(\phi-Y)\end{aligned} \tag{3.35}$$

where

$$X = \sqrt{r_0^2+r^2-2r_0r\cos(\theta-\theta_0)} \tag{3.18'}$$

$$\tan Y = \frac{r_0\sin\theta_0 - r\sin\theta}{r_0\cos\theta_0 - r\cos\theta} \tag{3.19'}$$

Thus, comparing Eqs. (3.35) and (3.22) it can be seen that the only difference is the factor $\cos\beta$. Parallel to the deviation of Eq. (3.26), the above expression for the PSF can be written

$$f_{(2)}(r,\theta) \approx 2\pi \int_{-\infty}^{\infty} P_r(\hat{v}) J_0(2\hat{\omega} X \cos\beta) d\hat{v} \tag{3.36}$$

substituting $P_r(\hat{v}) = |\hat{v}| rect(\hat{v} / 2\hat{v}_c)$ into Eq. (3.36) and integrating the PSF for the backprojection process becomes

$$f_{(2)}(r,\theta) = \frac{\hat{v}_c J_1(2\hat{\omega}_c X \cos\beta)}{X \cos\beta} \tag{3.37}$$

and the Rayleigh distance is found to

$$\delta_{Rayl} = 0.30 \frac{2\pi}{\hat{\omega}_c \cos\beta} = \frac{0.3\lambda_c}{\cos\beta} \tag{3.38}$$

where λ_c is the wavelength of the wave corresponding to the angular cutoff frequency $\hat{\omega}_c$. The asymptotic envelope of Eq. (3.37) is $(X \cos\beta)^{-1.5}$.

Eq. (3.37) shows that the PSF is identical to Eq. (3.31), except for the presence of a $\cos\beta$ factor. Thus, the PSF is broadened by a factor $(\cos\beta)^{-1}$, concluding that, if backprojection is performed along elliptical paths, the mainlobe width is broadened by a factor proportional to the cosine of half the angle subtending the transmitter and receiver.

The second complex mode corresponds to transmitting from one transducer and receiving with all remaining transducers in the circular array. This mode may be thought of as generating line integrals data over all possible elliptical paths intersecting the object. Thus, it may be regarded as a linear and coherent superposition of images from the above mode and the same linear reconstruction algorithm derived for "fixed angles" is applicable in this case. Thus, the PSF obtained for this mode is an average of Eq. (3.37) over a specified range of β, e.g.,

$$f(r,\theta) = \int_{-\pi}^{\pi} w(\beta) f(\beta; r, \theta) d\beta \tag{3.39}$$

where $w(\beta)$ is an averaging filter. Notice also, that this mode requires $N^2 \times A$-scans, whereas, the former modes only requires $N \times A$-scans.

Finally, the PSF of the backprojection process is computed for a variety of pulse shapes using Eq. (3.26). For example, if the received pulse has a narrowband spectrum about a center frequency, $\hat{v}_0$, it may be expressed as $P_r(\hat{v}) = \delta(\hat{v} - \hat{v}_0)$ and substituted into Eq. (3.26) to give the PSF:

$f_{(3)}(r,\theta) = 2\pi J_0(2\hat{\omega}_0 X)$, with an asymptotic envelope of $X^{-0.5}$.

Fig. 3.16 shows the PSF for a narrowband, an optimum and a wideband pulse. The narrowband pulse has a narrow mainlobe, but the sidelobes are high with an envelope of $X^{-0.5}$. The wideband pulse has a broad mainlobe, while the sidelobe envelope is improved to X^{-1}. The optimum pulse is narrower than the wideband pulse and exhibit the best side lobe response with an envelope of $X^{-1.5}$.

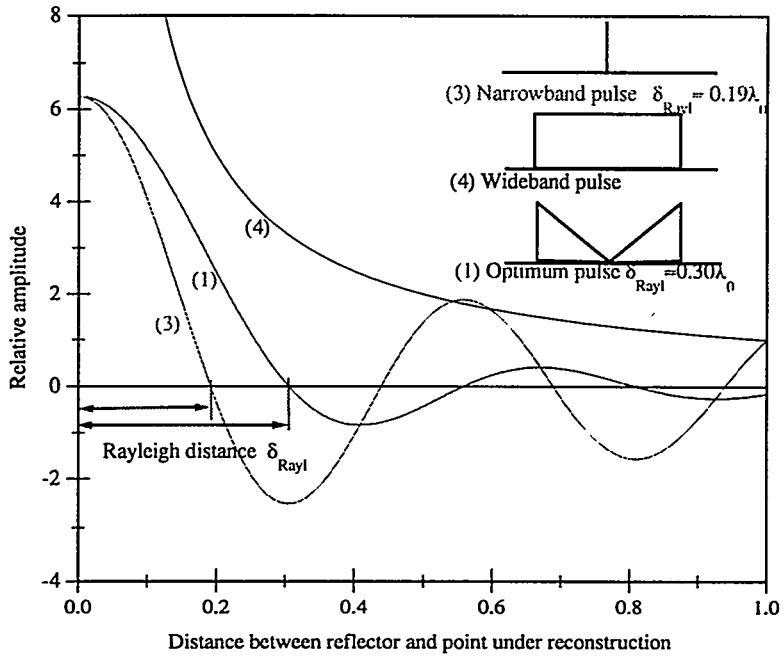

Figure 3.16. Point Spread Function (PSF) for the backprojection process applying a narrowband, an optimum and a wideband pulse. Monostatic imaging is assumed in a circular aperture array.

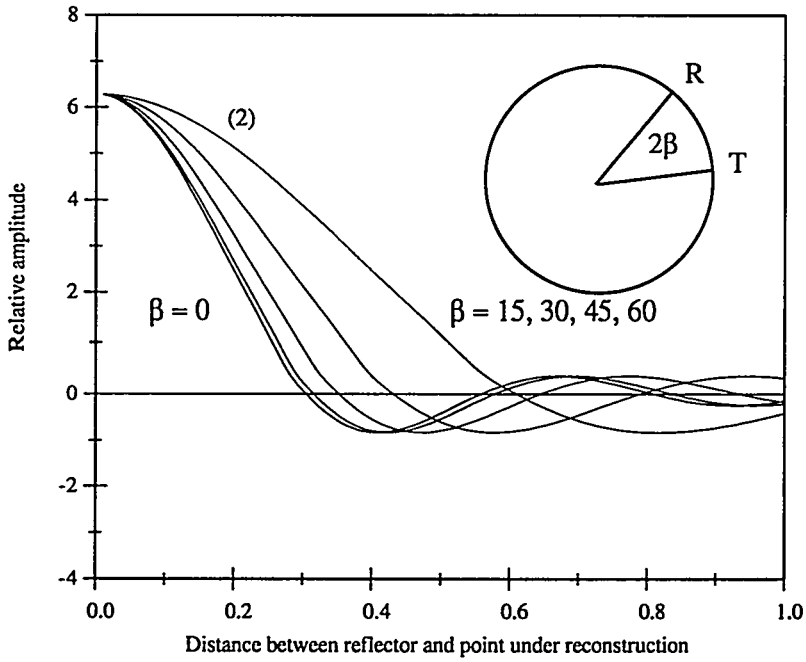

Figure 3.17. Point Spread Function (PSF) for an optimum pulse in a circular aperture array. Bistatic imaging is assumed and a fixed separation between transmitter (T) and receiver (R) is used (β = 0°, 15°, 30°, 45°, 60°).

Fig. 3.17 shows the PSF for the optimum pulse, where a fixed separation between transmitter and receiver is used (β = 0°, 15°, 30°, 45°, 60°). It demonstrates that the mainlobe is broadened for increasing angle separation, but also that the minimum Rayleigh distance occurs for β=0, i.e., for the monostatic case.

The corresponding PSF and Rayleigh distances are presented in Table 3.5 for the narrowband pulse, the wideband pulse and the optimum pulses.

Table 3.5. Fourier spectrum of received pulse, point spread function (PSF), envelope and Rayleigh distances for three different pulse shapes.

Pulse	Spectrum $P_r(\hat{\nu})$	PSF $f(r,\theta)$	PSF *envelope*	Rayleigh dist. δ_{Rayl}
(1) Optimum*	$\lvert\hat{\nu}\rvert rect(\hat{\nu}/2\hat{\nu}_c)$	$\frac{J_1(2\hat{\omega}_c X)}{X}$	$X^{-1.5}$	$0.30\lambda_c$
(2) Optimum**	$\lvert\hat{\nu}\rvert rect(\hat{\nu}/2\hat{\nu}_c)$	$\frac{J_1(2\hat{\omega}_c X\cos\beta)}{X\cos\beta}$	$(X\cos\beta)^{-1.5}$	$0.30\lambda_c/\cos\beta$
(3) Narrowband	$\delta(\hat{\nu}-\hat{\nu}_0)$	$2\pi J_0(2\hat{\omega}_0 X)$	$X^{-0.5}$	$0.19\lambda_0$
(4) Wideband	$P = const.$	$P/\lvert X\rvert$	X^{-1}	*undefined*

* for monostatic imaging. ** for "bistatic" imaging.

In conclusion, for a circular aperture that surrounds the specimen entirely, the minimum width of the PSF (indicating best resolution) is found for an optimum pulse in the monostatic mode. In this case, the resolution is bandwidth limited only and does not depended on the aperture, in contrast to conventional imaging systems, where resolution is, in general, aperture limited.
However, a limiting factor to the above theoretical analysis was the finite transducer size. When finite size transducers are applied, the directivity function of the transmitter and the receiver should be taken into account (see e.g. Fig. 3.15). For example, the characteristic directivity function for a circular piston transducer is $2J_1(x)/x$, where J_1 is the first-order Bessel function, KINSLER *et al.* (1982).
Furthermore, if a transmitter (with its directivity function) scans the specimen, the received signal must also be weighted by the same directivity function. The overall effect is the same as a weighting function applied to the entire aperture. Hence, the transducer directivity has the same effect as limiting the aperture length, leading to a poor lateral resolution. This effect is increased when the transmitter is moved away from the center, due to the effect of the directivity function. Hence, the aperture is weighted with a directivity function given by the product of the two directivity functions.

3.4 Volumetric imaging - Experimental technique (IV)

There have been numerous efforts to inspect specimens by ultrasonic reflectivity (or pulse-echo) measurements. In these inspections ultrasonic reflectivity is often used to observe changes in the acoustical impedance, and from this observation to localize defects in the specimen. However, the term *defect* is related to any discontinuity within the specimen and, consequently, more information is needed than only ultrasonic reflectivity to define the discontinuity as a defect. This information may be provided by three-dimensional ultrasonic reflection tomography and *a priori* knowledge about the specimen (e.g., the specimen fabrication process, its design, the intended purpose and the material). A more comprehensive review of defect characterization and related nondestructive evaluation (NDE) methods is provided elsewhere by RHEINLÄNDER *et al.* (1997).

In this section, discontinuities in cylindrical specimens were studied by ultrasonic reflection tomography. The aim was threefold. First, to localize discontinuities from circular C-scan images. Second, to reconstruct quantitative cross-sectional images from circular B-scan profiles (i.e., reflection tomograms). Finally, to obtain three-dimensional information (i.e., discontinuity location, dimension and type) by stacking these reflection tomograms in multiple planes, in the third dimension.

In order to ensure perpendicular beam incidence on the cylindrical specimen, the circular B-scan profiles were acquired by high frequency (narrow beam) transducers in a synthetic circular aperture array. From these profiles two-dimensional reflection tomograms were reconstructed using a filtered backprojection technique. Straight line propagation was assumed. Several artificial discontinuity types in a cylindrical Plexiglas specimen were compared with similar artificial discontinuities in a cylindrical *AlSi*-alloy. The *AlSi*-alloy was manufactured in the European Brite/Euram project TALMAC (Thixoforming of advanced light metals for automotive components). Furthermore, examples of real discontinuities (a porosity and a feed head) in the cylindrical *AlSi*-alloy are presented.

3.4.1 Circular C-scan imaging

Some of the problems often encountered during ultrasonic inspection of plane specimens are also found on cylindrical specimens. For example, problems associated with the directional characteristic of the ultrasonic transducer. Furthermore, the discontinuity influences the shape and propagation direction of a reflected pulse, causing wave mode transformation. In addition, the specimen influences the shape and amplitude of the reflected pulse by sound absorption, scattering and anisotropy. Therefore, for inspection of cylindrical specimens a perpendicular incidence of the ultrasonic beam is normally required. The imaging system proposed by NIELSEN *et al.* (1997), and applied in this work, is a synthetic array with transducer elements distributed uniformly along a circular aperture. The positioning of the transducer elements minimizes refraction effects, due to a perpendicular incidence of the ultrasonic beam on the specimen. Furthermore, the circular array can be moved up or down to scan different radial planes of the cylinder.

Some discontinuities may be identified by a conventional two-dimensional ultrasonic technique, from which the well-known C-scan image is the most popular. The C-scan technique is relatively easy to implement and the results from several NDE studies have been very encouraging. In the case of cylindri-

cal specimens, a circular C-scan image is convenient to show discontinuity information. The circular C-scan image shows the peak amplitude of a backscattered pulse received in the circular array. The axial scan direction on the image is shown as a function of transducer position in the circular array. The circular C-scan image serves also as an initial step for choosing circular B-scan profiles. The latter provides a mapping between distance to the discontinuity and transducer position in the circular array.
As mentioned above, several artificial discontinuities in a cylindrical Plexiglas specimen were compared with similar real and artificial discontinuities in a cylindrical *AlSi*-alloy. The examined diameter of both cylinders were 20 mm in diameter and 50 mm long. A circular C-scan image of the cylindrical *AlSi*-alloy was, for example, obtained using a transducer rotating in a circle of 360° (plus 90° to insure that all discontinuities were imaged) and using one of three time gates. The three time gates were set to measure the peak amplitude of a backscattered pulse from the cylinder. Gate 1 covered the interface echo, gate 2 covered the echo from a discontinuity and gate 3 covered the echo from the back of the cylinder. The gates are specified in Fig. 3.18, where only one transducer element is active in the circular array.

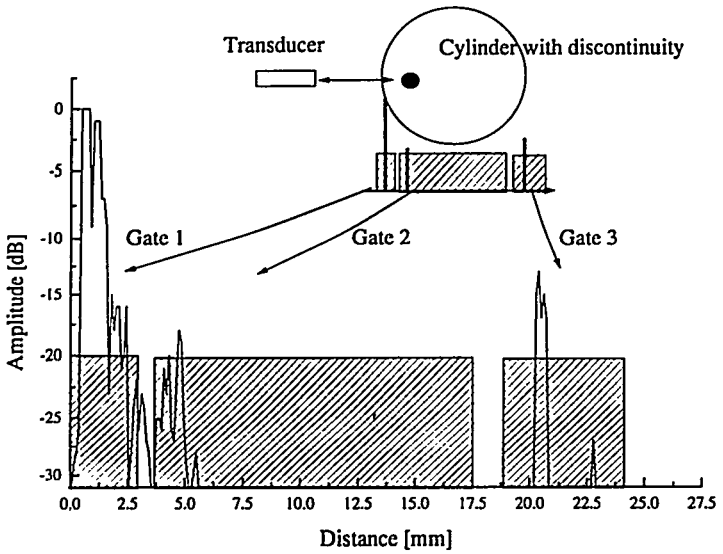

Figure 3.18. Three time gates set to measure backscattered pulse from cylinder: interface echo (gate 1), echo from discontinuity (gate 2) and back echo (gate 3).

As an example, Fig. 3.19 shows a circular C-scan image corresponding to the backscattered echo from the discontinuity (gate 2). The Figure specifies six discontinuity types in an increasing axial distance from the edge of the 50 mm long cylinder (one type is solid material). The corresponding cross sections are denoted (a), (b), (c), (d), (e) and (f), throughout this section. Notice, that only the *AlSi*-alloy has an inclusion and a feed head from the casting process.
Although the discontinuities may be seen clearly in the circular C-scan image, the image represents only a projection of discontinuities in a specific direction (i.e., a shadow of overlapping discontinuities). More information of the discontinuities according to location, dimension and type may be achieved by ultrasonic computed tomography (UCT) imaging.

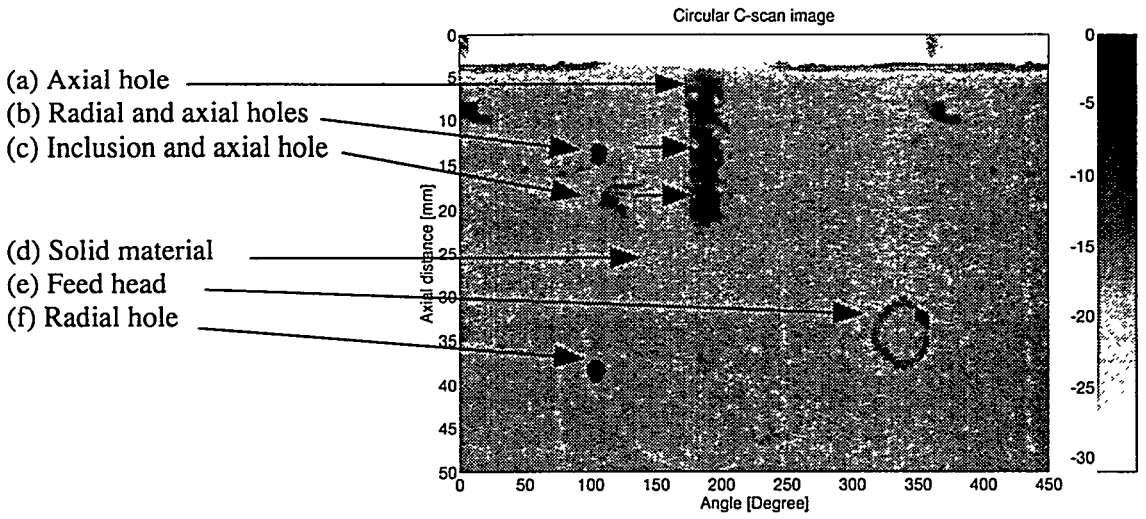

Figure 3.19. Circular C-scan image of AlSi-alloy cylinder showing six discontinuity types. Grey scale in [dB] of echo from discontinuity (gate 2).

3.4.2 Experimental procedure (IV)

There has been considerable interest in computed tomography with ultrasound, as mentioned in chapter 2, since the successful introduction of computed tomography with X-rays. This is mainly due to the fact that UCT may generate cross-sectional images (tomograms) of three different material properties of interest: (*i*) an attenuation tomogram representing the ultrasonic energy loss due to scatter and absorption in the material (see subsection 2.4.2); (*ii*) a velocity tomogram representing a measure of the elastic constants in the material (see subsection 2.4.4); and, (*iii*) a reflection tomogram representing a map of ultrasonic impedance mismatch from boundaries and discontinuities (see subsection 3.3.2). In particular, the reflection tomogram is of interest for most cylindrical materials (like: pipelines, rods and axles) because it only requires one active transducer element at a time.

In an early study, GREENLEAF *et al.* (1975) reported reconstructions of ultrasonic velocity from time-of-flight profiles. Since then there has been periodic activity in using ultrasound to determine the transmission properties: attenuation or refractive index.

A recently developed prototype for such imaging consists of a pair of transducers mounted on an assembly that moves linearly in steps of few micrometers and rotates about the center axis. See chapter 2 and NIELSEN *et al.* (1995*a*). The assembly is enclosed in a water tank. At each position one transducer transmits a short pulse and a second transducer, located on the opposite side of the material, receives it. The peak amplitude (or travel time) is determined by a time gate. Several of such profiles, each collected from a specific direction, are used for reconstructing an image by assuming straight line propagation. However, at low imaging frequencies, sound does not travel in a straight line and there may be noticeable diffraction that leads to imaging artifacts. Furthermore, when dealing with a cylindrical specimen, refraction effects and total reflection are very dominant in such an assembly.

More recently, the circular array was proposed to assess the reflectivity of cylindrical specimens (this chapter and NIELSEN *et al.* 1997). First, a circular C-scan image was obtained. The total scan time was about 25 min., which does not include a relatively time consuming alignment of the specimen. From the circular C-scan image, circular B-scan profiles were chosen in specific planes.

The transducer was a focused, high frequency transducer with a center frequency of 25 MHz. This frequency corresponds to a wavelength of 0.11 mm and 0.25 mm in the Plexiglas specimen and the *AlSi*-alloy, respectively. Additional experimental parameters are presented in Table 3.6.

Table 3.6. Experimental parameters (IV) for reflection tomograms.

Center frequency	25 MHz
Wavelength. Plexiglas (*AlSi*-alloy)	0.11 mm (0.25 mm)
Sound velocity. Plexiglas (*AlSi*-alloy)	2720 m/s (6320 m/s)
Aperture radius	15 mm
Time resolution $\Delta\tau$ (samples)	80 ns (256)
Aperture resolution $\Delta\phi$ (N samples)	1.8° (360°/200)
Image resolution (pixels)	26 μm x 26 μm (1000x1000)
Dynamic range of image	5 bit (0-31 dB)
Reconstruction time* (scan time**)	15 min. (25 min.)

* Pentium (166 MHz). ** for a circular C-scan image.

Under ideal conditions (e.g., point sources producing spherical waves and no multiple reflections) a rectified backscattered signal represents line integrals of the ultrasonic reflectivity over concentric arcs centered at the transducer position. To reconstruct the reflection tomogram the amplitude is backprojected over an arc with a radius similar to the circular array. Using the high frequency transducer, the ultrasonic reflectivity, $\mu(x,y)$, may be found using the filtered backprojection technique in chapter 2, i.e., the relationship

$$\mu(x,y) = \int_0^{2\pi} \int_{-\infty}^{\infty} |\omega| \langle P(\omega,\theta) \rangle \, e^{i\omega\rho} \, d\omega d\rho \tag{3.40}$$

where $\langle P(\omega,\theta) \rangle$ represents the Fourier transformation of the circular B-scan profiles measured with the transducer face at an angle θ to the horizontal and $\rho = x\cos\theta + y\sin\theta$.

Zero-padding and a low-pass cosine filter (see chapter 2), implemented using Fast Fourier Transformation, was used to enhance edges before backprojection. The reconstruction time was 15 min. for each 1000 x 1000 tomogram and 15 sec. for a 100 x 100 tomogram.

3.4.3 Results and discussion - volumetric imaging

Direct three-dimensional (or volumetric) imaging have been performed e.g. by SIRE *et al.* (1991). In their work the whole specimen is insonified by a cone beam and reconstructed directly. In the present work the three-dimensional information was obtained by constructing two-dimensional reflection tomograms and stacking these in multiple continuous planes in the third dimension, as indicated in Fig. 3.20. This approach needs less processing time and data storage than for direct reconstruction. Therefore, the stacking technique has been adopted for this NDE study, NIELSEN *et al.* (1998). Once the data are mapped into a volumetric matrix composed of cubic voxels it can be numerically dissected in any plane. Fig. 3.20 also shows the six discontinuity types, i.e., (a)-(f) in an increasing axial distance from the edge of the 50 mm long cylinder.

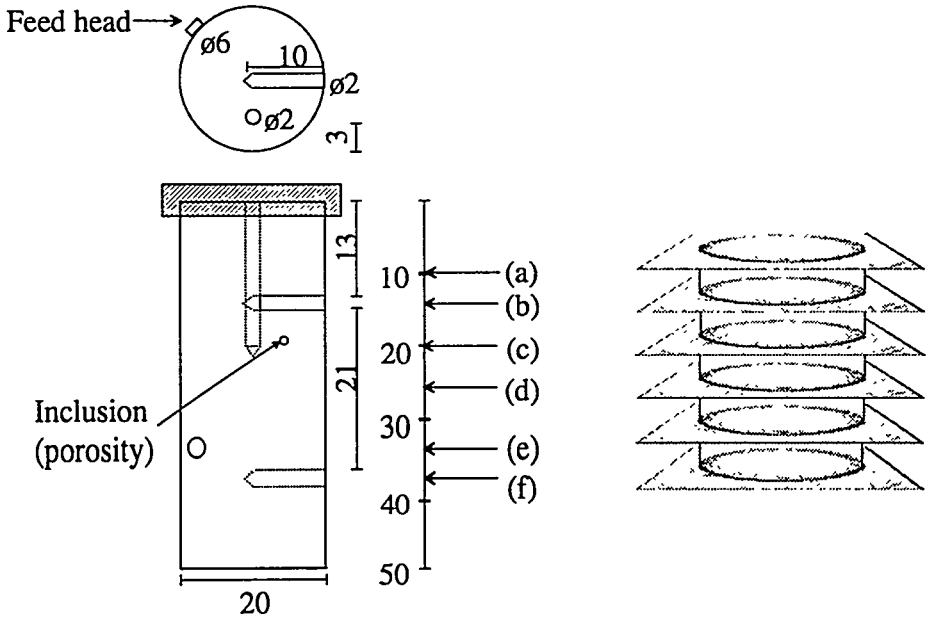

Figure 3.20. Schematic details of cylinder (left) and volumetric imaging of cylinder by stacking reflection tomograms (right). Dimensions in [mm].

Fig. 3.21. shows six ultrasonic reflection tomograms. Three of these are from the Plexiglas specimen (shown left) and three are from the *AlSi*-alloy (shown right). The tomograms are reconstructed from reflection data measured across the plane (a), (b) and (c), respectively. The dark regions indicate high reflectivity and represent specimen interfaces and discontinuities.

The reflection tomograms (a) show the location of the axial hole in both cylinders. The axial hole is located approximately 3.1 mm from the edge, as specified in Fig. 3.20. Multiple reflections from the measurement were ignored in the calculation of the Plexiglas tomogram (left). This is seen as a bright circle. The non circular appearance of the *AlSi*-tomogram (right) may be due to a non centered alignment of the specimen and the fact that the specimen was not quite cylindrical.

The reflection tomograms (b) clearly show the location of the axial and radial hole in both cylinders. While the radial hole is detected at the correct location in both cases, approximately 6.0 mm from the edge, it is barely visible in the *AlSi*-alloy where it should be 10 mm long. This tomogram indicates as expected, that radial holes may not be seen as effectively as axial holes.

The reflection tomograms (c) show the axial hole in the Plexiglas specimen, but also a real discontinuity in the *AlSi*-alloy. The internal discontinuity is located 6 mm from the edge, 50° from the axial hole and its dimension is about 1-2 mm. The discontinuity was also seen on a X-ray image. This may be an inclusion or a porosity (void).

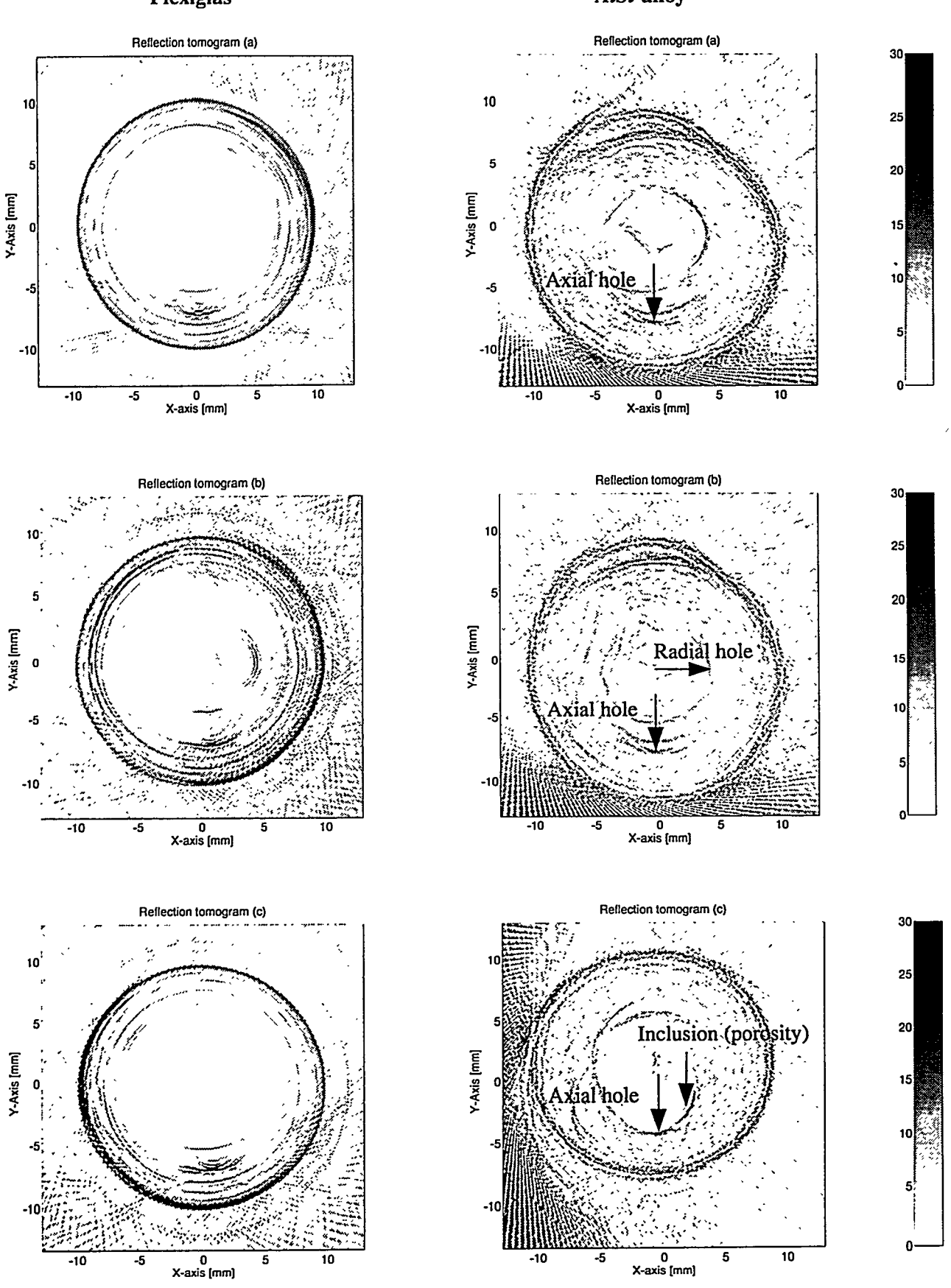

Figure 3.21 Reflection tomograms in Plexiglas and AlSi-alloy cylinders, respectively, reconstructed from data measured across plane (a), (b) and (c). High reflectivity is indicated by dark regions [-dB].

Fig. 3.22. shows the six remaining ultrasonic reflection tomograms. As above, three of these are from the Plexiglas specimen (shown left) and three are from the *AlSi*-alloy (shown right). These tomograms are reconstructed from reflection data measured across the plane (d), (e) and (f), respectively.
The reflection tomograms (d) and (e) show, as expected, solid material in the Plexiglas specimen. A feed head from the casting process is seen clearly in the *AlSi*-alloy. The diameter of the feed head is about 6 mm in accordance with Fig. 3.19.
The reflection tomograms (f) show a barely visible reflection from the radial hole. This tomogram indicates, compared with tomogram (b) that radial holes may not be seen as effectively as axial holes. The reason may be due to the limited lateral resolution of the transducer and due to the fact that no compensation was performed for spreading of the sound field after it was scattered by the discontinuity.
The six pairs of reflection tomograms are listed in Table 3.7, showing the artificial and real discontinuities in the Plexiglas and the *AlSi*-alloy cylinder, respectively.

Table 3.7. Discontinuities in Plexiglas specimen and AlSi-alloy.

Distance [mm]	Discontinuity type	Plexiglas	*AlSi*-alloy
8	(a) Axial hole	✓	✓
12	(b) Radial and axial holes	(✓)	(✓)
17	(c) Inclusion* and axial hole	✓	✓
27	(d) Solid material	✓	✓
33	(e) Solid material or feed head*	✓	✓
38	(f) Radial hole	(✓)	(✓)

* No inclusion and feed head in Plexiglas cylinder.

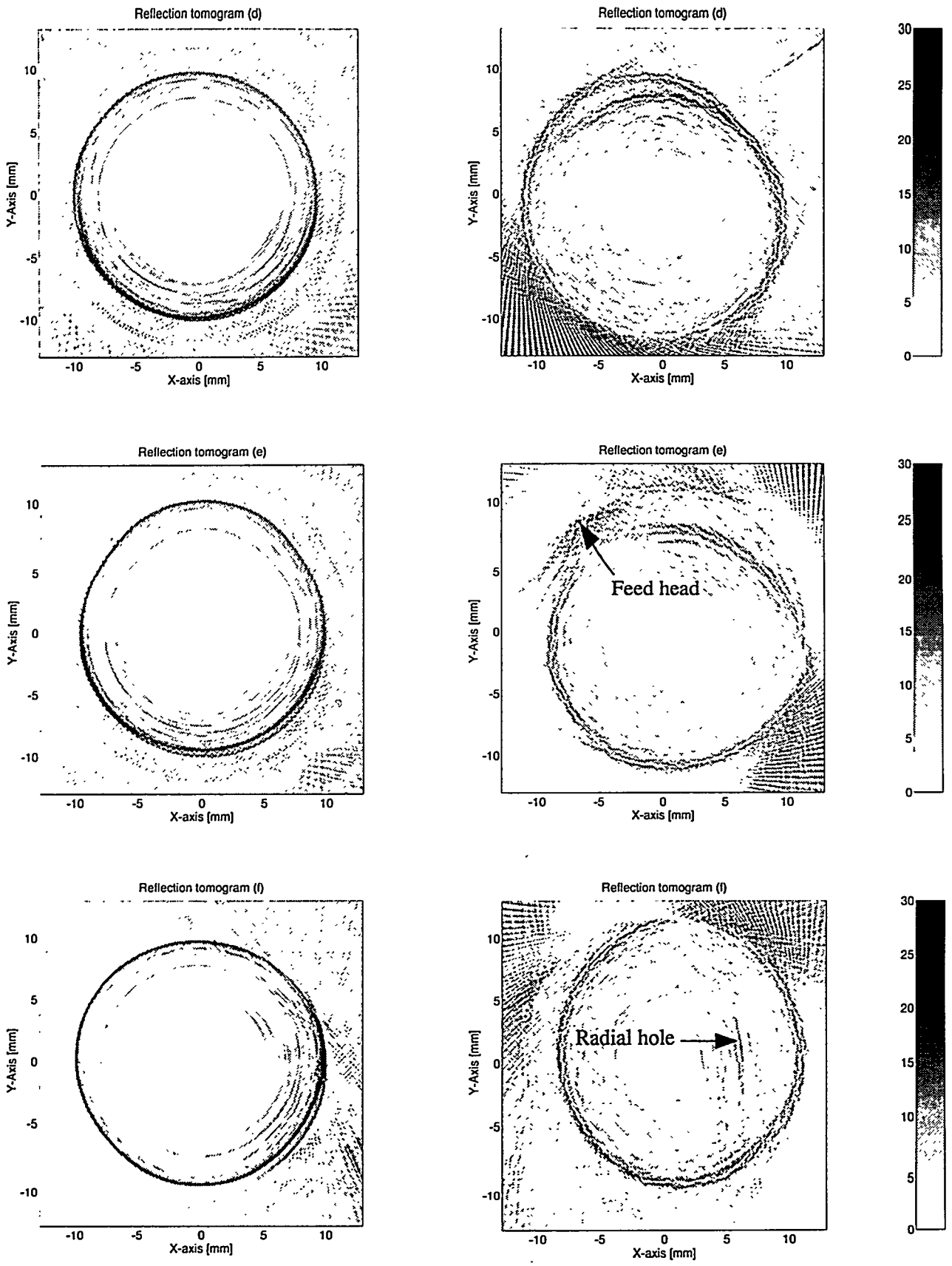

Figure 3.22 Reflection tomograms in Plexiglas and AlSi-alloy cylinders, respectively, reconstructed from data measured across plane (d), (e) and (f). High reflectivity is indicated by dark regions [-dB].

3.5 UCT limitations

All the above experimental techniques were based on the geometrical-optics ray arguments (SCHUELER *et al.* 1984), were straight-line propagation could be assumed and UCT-tomograms where obtained of scattering objects larger than the applied ultrasonic wavelength ($\lambda << a$). The corresponding *ka*-values for the water filled ellipse in the Plexiglas cylinder were, e.g., $ka \approx 87$ - 96, where k was the wavenumber (Table 3.4) and $a = 4$ - 10 mm the semi axes of the ellipse (i.e. minor and major axis).
For these high *ka*-values, the interpretation of the backscattered pulse could be limited by later arriving creeping waves (or leaky waves), that could interfere with the scattered wave (CAPINERI *et al.* 1988, 1992). As an example, consider the simple case: a backscattered pulse from the surface of a void in a solid (i.e., a rigid sphere with radius a) and a creeping wave, propagate around the circumference of the void, arriving at time $t = (2 + \pi)a/v_l$ later, where v_l is the speed-of-sound of the longitudinal wave (KINO 1987). In this case, the received pulse may consists of the superposition of three different signals: the reflected signals from the top of the void, the refracted signal from the bottom and finally a creeping wave traveling around the void. Hence, creeping waves may limit the applications of monostatic UCT.

The arguments of straight-line propagation are not true when the wavelength is larger than the size of scatters ($\lambda >> a$) and the result may be a significant diffraction of the sound wave (JONES 1993, SPONHEIM *et al.* 1991 and POURJAVID *et al.* 1991). Simple scatters, like spheres and cylinders, can be treated theoretically and is fundamental to the understanding of more complicated structures (MORSE *et al.* 1968 and KINO 1987). For example, the backscattered pressure in a distance r from a small rigid sphere (in water) is $p_r / p_t = 5k^2a^3 / (6r)$, where p_r and p_t is the received and transmitted pressure, respectively. Hence, the scattered pressure varies as the square of the frequency and is proportional to the volume of the scattering sphere. However, in the NDE field, the problem of diffraction is extremely difficult because of the complicated and less controllable nature of advanced composite materials. For example, as discussed in the next chapter, glass fibers with a, e.g., 5 μm radius in a polymeric matrix exhibit, collectively, attenuation in form of Rayleigh scattering (KINO 1987). The corresponding *ka*-value for the glass fiber is $ka \approx 0.02$ (using a wavelength of 2.7 mm in glass and a speed-of-sound in glass of 6000 m/s and a 2.25 MHz probe frequency). A different evaluation procedure for composite materials will be discussed in chapter 6.

When diffraction effects are included in the measurements, the wave equation has to be solved. This technique has, since its introduction in 1979, been called diffraction tomography (MUELLER *et al.* 1979, 1980) and has since then been the subject for numerous investigations, using mainly synthesized data (see, e.g., YOKOYAMA *et al.* 1993, KATAOKA *et al.* 1994, YAMADA 1994 and JANEE *et al.* 1996). Unlike the assumptions of straight-line propagation in UCT, diffraction tomography does not require any assumption on the way ultrasonic energy propagate from a transmitter to a receiver. Moreover, it can be shown (BUCHSTABER *et al.* 1990) that UCT is, essentially, the limiting case of diffraction tomography when the wavelength tends to zero. However, diffraction tomography requires a weak scattering object and has, therefore, mainly been found in medical applications (SEHGAL 1991 and GRASSIN *et al.* 1995). More research has to be done in this area for NDE applications.

3.6 Summary and conclusions

In this chapter, ultrasonic imaging techniques were discussed using a synthetic array with transducer elements distributed uniformly along a circular aperture. The techniques were based on ultrasonic projections and referred to as ultrasonic computed tomography (UCT).

Section 3.1: Introduced two kinds of ultrasonic tomography, acquired from the synthetic circular aperture array: bistatic and monostatic imaging (Fig. 3.1). Some general experimental requirements to the implementation of the two techniques were discussed. The circular aperture array was realized by object rotation and ultrasonic signals were acquired via two single mobile transducers, acting as transmitter and/or receiver, respectively (Fig. 3.2). Sound field parameters of two broadband, focused transducers were found (Tables 3.1-3.2 and Appendix 3.1).

Section 3.2: Discussed bistatic reconstruction. An experimental procedure (II) was reviewed using amplitude data. In this procedure, diverging ultrasonic beams were used to insonify the cylindrical specimen, and the resultant transmitted signals were recorded by only considering received signals measured over a sector (Table 3.3). Alternative strategies were suggested (Fig. 3.3). The fan-beam tomogram obtained in this experiment (Figs. 3.4-5) showed improvements in imaging the elliptic shape compared with experiment (I). However, the fan-beam tomogram exhibited severe artifacts due to alignment and a reference specimen was necessary in order to account for the sound field divergence. Different reconstruction artifacts associated with tomograms were discussed. It was found that non sufficient zero-padding could introduce a DC-shift in the amplitude (Fig. 3.6). The number of projections and the number of samples per projection should be of equal size (Fig. 3.7). For the fan-beam tomogram, the beam should be wide enough to cover the inspection area (Figs. 3.8-9).

Section 3.3: Discussed monostatic reconstruction and a related experimental procedure (III) (Table 3.4). Reconstruction of backscattered data were discussed using a backprojection technique (Figs. 3.10-12). Experimental data were obtained from cylindrical polymeric specimens (Plexiglas) containing defects with strong reflection boundaries (Figs. 3.13-14). Good qualitative agreement was obtained compared to real dimensions and improvements were found compared with experiment (I) and (II). Theoretical resolution criteria were discussed for various configurations of the circular aperture array. For the bistatic imaging procedure an expression for the lateral resolution was derived (Fig. 3.15). For the monostatic imaging procedure the point spread function was derived, assuming point sources (Table 3.5). The lateral resolution was found only to depend on bandwidth. In terms of the Rayleigh distance an optimum pulse was found to be superior to other pulse forms (Figs. 3.16-17).

Section 3.4: Verified the monostatic procedure by volumetric imaging. In this experiment (IV) artificial and real discontinuities in a cylindrical *AlSi*-alloy were compared with similar discontinuities in a Plexiglas specimen. Several discontinuity types in Plexiglas and *AlSi*-alloy cylindrical specimens were studied by three different ultrasonic imaging techniques. First, by circular array imaging: A synthetic circular aperture array was used to obtain circular C-scan images (Figs. 3.18-19). These images displayed the location of different discontinuity types, although only shadow images were obtained.

Second, by ultrasonic tomography imaging: Reflection tomograms were generated from circular B-scan profiles. A relatively fast reconstruction algorithm was applied, based on the straight beam approximation. This approximation was assumed due to broadband, high frequency pulse propagation (Table 3.6). The tomograms shown in Figs. 3.21-22 demonstrates that it is technologically feasible to obtain high resolution images. However, multiple reflections and time consuming alignment could limit the application. Radial holes were difficult to localize (Table 3.7). Finally, by volumetric imaging: Three-dimensional information was obtained by stacking reflection tomograms from multiple planes (Fig. 3.20). Using this stacking technique, cubic voxels were obtained and could be numerically dissected in any plane. Although there are several attractive features related to this technique, there are also several questions which need to be addressed before it can be used for industrial applications. For example, the applied sound field must be further characterized.

In conclusion, the results indicate that, for characterizing defects with strong boundaries, reflection ultrasonic tomography can be successfully used, while transmission tomography is not practical for such application. There is great potential for reflection UCT in Non-Destructive Evaluation (NDE) of isotropic, homogeneous materials, where each scan is processed separately and the final image is formed by superimposing the two images. These images give more information of the specimen than either of the individual images would do on their own. The experimental method described here may be applicable to many industrial cylindrical-shaped materials, such as axles, pipes, rods, cranks, cylinders etc. However, an extension to advanced materials, e.g. fiber composites would require more advanced reconstruction methods. Further validation and quantification of the latter technique is necessary to better understand the composition of advanced materials and to extract more information from divergent ultrasonic signals.

3.7 References to chapter 3

ANDRÉ, M.P.; JANÉE, H.S.; MARTIN, P.J.; OTTO, G.P. and JONES, J.P. (1996). Reduction of phase aberration in a diffraction tomography system for breast imaging. In Acoustical Imaging, Vol. 22, Ed. P. Tortoli and L. Masotti, Plenum Press, 151-157.

ANDRÉ, M.P.; JANÉE, H.S.; MARTIN, P.J.; OTTO, G.P.; OLSON, L.K.; BARRETT, T.K.; SPIVEY, B.A. and PALMER, D.A. (1997*a*). A new consideration of diffraction computed tomography for breast imaging: Studies in phantoms and patients. In Acoustical Imaging, Vol. 21, Ed. J.P. Jones, Plenum Press, 379-390.

ANDRÉ, M.P.; JANÉE, H.S.; MARTIN, P.J.; OTTO, G.P.; SPIVEY, B.A. and PALMER, D.A. (1997*b*). High-speed data acquisition in a diffraction tomography system employing large scale torodial arrays. Intl. J. Imaging Syst. and Technol., Vol. 8, 137-147.

BJØRNØ, L. and NIELSEN, S.A. (1994). A novel broadband, high-frequency ultrasonic transducer. 11th Int. FASE symposium, Vol. 1, Valencia, 81-84.

BLYTH, B.; CAVAYE, G.; CLEARY, M.; FLEMING, R.; KOCH, R.; MEARA, L.; MCCAFFREY, J. and WHITING, J. (1979). An ultrasonic computer-assisted tomographic scanner. Australasian Physical Sciences in Medicine, Vol. 2-3, No. 80, 141-153.

BUCHSTABER, V.M. and MASLOV, V.K. (1990). Mathematical models and algorithms of tomographic synthesis of wave fields and inhomogeneous media, Trans. of Mathematical Monographs, Vol. 81, 225-267.

CAPINERI, L.; CASTELLINI, G.; MASOTTI, L. and ROCCHI, S. (1988). Broadband tomography system. International School of Physical Acoustics, 3rd Course on Ultrasonic Signal Processing, Erice, Italy. Publisher: World Scientific, Singapore, 245-253.

CAPINERI, L.; TATTERSALL, H.G.; TEMPLE, J.A.G. and SILK, M.G. (1992). Time-of-flight diffraction tomography for NDT applications, Ultrasonics, Vol. 30, No. 5, 275-288.

CHIAO, R.Y. and THOMAS, L.J. (1994). Analytic Evaluation of Sampled Aperture Ultrasonic Imaging Techniques for NDE, IEEE Transactions on Ultrasonics Ferroelectrics and Frequency Control, Vol. 41, No. 4, 484-493.

DEFRANOULD, P. (1981). Acoustical Fan-beam measurements by transducer arrays for tomography reconstruction. IEEE Transactions on Sonics and Ultrasonics, Vol. SU-28, No. 6., 418-425.

DREIKE, P. and BOYD, P. (1976). Convolution reconstruction of fan beam projections. Computer Graphics and Image Processing, Vol. 5, 459-469.

ERMERT, H.; PALLAKOWSKI, M. and BERNUS, L. (1995). Acoustical imaging using an optimal combination of signal prefiltering and pulse compression. In Acoustical Imaging, Vol. 21, Ed. J.P. Jones, Plenum Press, 337-347.

GLOVER, G.H. and SHARP, J.C. (1977). Reconstruction of ultrasonic propagation speed distributions in soft tissue: Time-of-flight tomography. IEEE Transactions on Sonics and Ultrasonics, Vol. SU-24, No. 4, 229-234.

GOODMAN, J.W (1996). Introduction to Fourier Optics. The McGraw-Hill Companies. Inc., 2.ed.,USA.

GREENLEAF, J.F.; JOHNSON, S.A.; SAMAYOA, W.F. and DUCK, F.A. (1975). Algebraic reconstruction of spatial distributions of acoustic velocities in tissue from their time-of-flight profiles. In Acoustical Holography, Vol. 6, Ed. N. Booth, Plenum Press, 71-90.

GRASSIN, P: DECHENE, B. and TABBARA, W. (1995). Diffraction tomography some applications and extension to 3-D ultrasound imaging. In Acoustical Imaging, Vol. 21, Ed. J.P. Jones, Plenum Press, 337-347.

GUNDTOFT, H.E. and NIELSEN, T. (1982). Accurate three-dimensional characterization of ultrasonic sound fields (by computer controlled rotational scanning), Materials Evaluation, Vol. 40, No. 1, 78-83.

HAVLICE, J.F and TAENZER, J.C. (1979). Medical ultrasonic imaging: An overview of principles and instrumentation. Proc. of the IEEE, Vol. 67, No. 4, 620-640.

HERMENT, A.; GUGLIELMI, P.; DUMEE, P.; PERONNEAU, P. and DELOUCHE, P. (1987). Limitations of ultrasound imaging and image restoration. Ultrasonics, Vol. 25, 267-273.

HORN, B.K.P. (1979). Fan-beam reconstruction methods. Proc. of the IEEE, Vol. 67, No. 12, 1616-1623.

JANÉE, H.S.; JONES, J.P. and ANDRÉ, M.P. (1996). Analysis of scatter fields in diffraction tomography experiments. In Acoustical Imaging, Vol. 22, Ed. P. Tortoli and L. Masotti, Plenum Press, 21-26.

JONES, H.W. (1993). Recent activity in ultrasonic tomography, Ultrasonics, Vol. 31, No. 5, 353-360.

KAK, A. (1979). Computerized tomography with X-ray, emission, and ultrasound sources. Proc. of the IEEE, Vol. 67, No. 9, 1245-1272.

KAK, A.C. and SLANEY, M. (1988). Principles of computerized tomographic imaging, IEEE Press, USA.

KATAOKA, H.; YOKOYAMA, T.; MIZUTANI, K. and NAGAI, K. (1994). Image reconstruction of ultrasonic diffraction tomography from data acquired with transmitter and receiver arrays, Japanese Journal of Applied Physics, Part 1 [Regular Papers & Short Notes], Vol. 33, No. 5B, 3190-3192.

KEATING P.A; SAWATARI, T. and ZILINSKAS, G. (1979). Signal processing in acoustic imaging. Proc. of the IEEE, Vol. 67, No. 4, 469-510.

KINO, G.S. (1979). Acoustic imaging for nondestructive evaluation. Proc. of the IEEE Vol. 67, No. 4, 510-525.

KINO, G.S. (1987). Acoustic waves: Devices, imaging and analog signal processing, Prentice -Hall Inc., USA.

KINSLER, L.E. (1982). Fundamentals of acoustics, John Wiley, New York.

KRAUS, H.G. (1983). Generalized synthetic aperture, focused transducer, pulsecho, ultrasonic scan data processing for non-destructive inspection. Ultrasonics, Vol. 22, No. 1, 11-18.

KRAUTKRÄMER, J. AND KRAUTKRÄMER, H. (1990). Ultrasonic testing of materials, 4th edition, Springer-Verlag, Germany.

LANGENBERG, K.J.; BERGER, M.; KREUTTER, T.; MAYER, K. and SCHMITZ, V. (1986). Synthetic aperture focusing technique signal processing. NDT International, Vol. 19, No. 3, 177-189.

MACOVSKI, A. (1979). Ultrasonic imaging using arrays. Proc. of the IEEE, Vol. 67, No. 4, 484-495.

MORSE, P.M. and INGAR, K.U. (1968). Theoretical Acoustics. McGraw-Hill Book Company, USA.

MOSHFEGHI, M. and HANSTEAD, P.D. (1985*a*). Three-dimensional acoustic images of cylindrical objects. IEEE Ultrasonic Symposium, Vol. 2, Ed. B.R. McAvoy, 1012-1015.

MOSHFEGHI, M. and HANSTEAD, P.D. (1985*b*). Combined shear-compression ultrasound reflection tomography. In Acoustical Imaging, Vol. 14, Ed. A.J. Berkhout, J. Ridder and L.F. Van der Wal, Plenum Press, New York, 425-436.

MUELLER, R.K; KAVEH, M. and WADE, G. (1979). Reconstructive tomography and applications to ultrasonics. Proc. of the IEEE (67), No. 4, 567-587.

MUELLER, R.K; KAVEH, M. and IVERSON, R.D. (1980). A new approach to acoustic tomography using diffraction techniques. In Acoustical Imaging, Vol. 8. Ed. A. Metherell, Plenum Press, New York, 615-628.

NIELSEN, S.A.; BORUM, K.K. and GUNDTOFT, H.E. (1995*a*). Verifying an ultrasonic reconstruction algorithm for non-destructive tomography. Proc. of 1st World Conference on Ultrasonics, 447-450.

NIELSEN, S.A. and BJØRNØ, L. (1995*b*). A broadband, high-frequency ultrasonic bistatic transducer, Proc. of 18th Scandinavian Symp. in Physical Acoustics, Ed. by H. Hobæk and M. Vestreheim, 15-16.

NIELSEN, S.A. and BJØRNØ, L. (1997). Bistatic circular array imaging with gated ultrasonic signals. In Acoustical Imaging, Vol. 23, Ed. Lees and Ferrari, Plenum Press, 441-446.

NIELSEN, S.A.; RHEINLÄNDER, J.T. BORUM, K.K. and GUNDTOFT, H.E. (1998). Three-dimensional ultrasonic reflection tomography of cylindrical shaped specimens. Proc. of 7th European Conference on Non-Destructive Testing, 2458-2465.

NORTON, S.J. and LINZER, M. (1979*a*). Ultrasonic reflectivity tomography: Reconstruction with circular transducer arrays. In Ultrasonic Imaging, Vol. 1, No. 1, 154-184.

NORTON, S.J. and LINZER, M. (1979*b*). Ultrasonic reflectivity imaging in three dimensions: Reconstruction with spherical transducer arrays. Ultrasonic Imaging, Vol. 1, No. 2, 210-231.

NORTON, S.J. and LINZER, M. (1981). Ultrasonic reflectivity imaging in three dimensions: Exact inverse scattering solutions for plane, cylindrical and spherical apertures. IEEE Trans. on Biomed. Eng., Vol. BME-28, No. 2, 202-220.

PETERS, T.M. and LEWITT, R.M. (1977). Computed tomography with fan beam geometry. Journal of Computer Assisted Tomography, Vol. 1, 429-436.

POURJAVID, S. and TRETIAK, O. (1991). Ultrasound imaging through time-domain diffraction tomography. IEEE Transactions on Ultrasonics, Ferroelectrics and Frequency Control, Vol. 38, No. 1, 74-85.

QIN, Z.D.; YLITALO, J.: OKSMAN, J. and LÜ, W. (1989). Circular-array ultrasound holography imaging using the linear-array approach. IEEE Transactions on Ultrasonics, Ferroelectrics and Frequency Control, Vol. 36, No. 5, 485-493.

RHEINLÄNDER, J.T.; NIELSEN, S.A.; BORUM, K.K. and GUNDTOFT, H.E. (1997). NDE of polymeric composites: a comparison of techniques. 18th Risø Intern. Symp. on Materials Science, Vol. 1, 101-125.

ROEHRLEIN, G. and ERMERT, H. (1985). Limited angle reflection mode computerized tomography. In Acoustical Imaging, Vol. 14, Ed. A.J. Berkhout, J. Ridder and L.F. Van der Wal, Plenum Press, New York, 413-424.

SCHUELER, C.F.; LEE, H. and WAVE, G. (1984). Fundamentals of digital ultrasonic imaging. IEEE Transactions on Sonics and Ultrasonics, Vol. SU-31, No. 4, 195-217.

SEHGAL, C.M. and GREENLEAF, J.F. (1991). Ultrasonic computed tomography for imaging bones and adjoining soft tissues, Mat. Res. Soc. Symp. Proc., Vol. 217, 157-165.

SIRE, P.; GRANGEAT, P.; LEMASSON, P.; MÉLENNEC, P. and PIZO, P. (1991). NDT applications of the 3D Radon transform algorithm for cone beam reconstruction, Mat. Res. Soc. Symp. Proc., Vol. 217, Ed. J.L. Ackerman and W.A. Ellingson, 129-134.

SOUMEKH, M. (1994). Fourier array imaging, Prentice Hall, USA.

SPONHEIM, N. and JOHANSEN, I. (1991). Experimental results in ultrasonic tomography using a filtered backprojection algorithm. Ultrasonic Imaging,Vol.13, 56-70.

WANG, L. (1977). Cross-section reconstruction with a fan beam geometry. IEEE Transactions on Computers, Vol. 26, 264-268.

YAMADA, A. and KURAHASHI, K. (1993). Experimental image quality estimation of ultrasonic diffraction tomography. Japanese Journal of Applied Physics, Part 1 [Regular Papers & Short Notes], Vol. 32, No. 5B, 2507-2509.

YAMADA, A. (1994). Quality improvement of ultrasonic diffraction tomography based on knowledge of background velocity, Japanese Journal of Applied Physics, Part 1 [Regular Papers & Short Notes], Vol. 33, No. 5B, 3187-3189.

YOKOYAMA, T.; NAGAI, K. and MIZUTANI, K. (1993). Imaging properties of the diffraction tomography by compound-scanning transmitter- receiver pair transducers, Japanese Journal of Applied Physics, Part 1 [Regular Papers & Short Notes], Vol. 32, No. 5B, 2510-2512.

ZEQIRI, B. and HODNETT, M. (1998). A systematic investigation of the effect of collimators on the characteristics of ultrasonic NDT transducers. Insight, Vol. 40, No. 1, 28-33.

4 Elastic Constants of Fiber Reinforced Composites

This chapter discusses relations between the elastic stiffness constants of a fiber reinforced composite and the elastic engineering constants of its constituents (fiber and matrix). The aim is to identify the elastic stiffness constants for a unidirectional glass/PET (Poly Ethylene Teraphthalate) laminate. The results will be discussed further in chapter 5, where the circular aperture is applied to determine the elastic stiffness constants for this laminate by ultrasound.
Section 4.1 gives a short introduction to fiber reinforced composites and discusses terms like continuous fibers and unidirectional laminates.
Section 4.2 discusses fiber orientation, fiber concentration (in terms of volume fraction), composite homogeneity and elastic properties of the constituents. The glass/PET laminate is introduced by microscope pictures.
Section 4.3 reviews the number of elastic stiffness constants for four significant types of fiber reinforced composites: general anisotropic, orthotropic, transverse isotropic and isotropic. Relations between elastic stiffness constants and engineering constants (i.e., Young's moduli, shear moduli and Poisson's ratios) are discussed for an orthotropic composite.
Section 4.4 combines elastic engineering constants to the fiber volume fraction. Six micro-mechanical theories are reviewed, and expressions predicting the elastic engineering constants are given.
Section 4.5 compares the theoretical elastic stiffness constants for the unidirectional glass/PET laminate with compression and vibration tests (TOFTEGAARD 1997 and FREDERIKSEN 1997). Section 4.6 concludes this chapter.

4.1 Introduction to fiber reinforced composites

The success of advanced materials result often from the ability to combine the properties of two or more different materials. Fiber reinforced composites consist of a fiber reinforcement phase embedded into a matrix phase, which gives a flexible light weight composite with high stiffness and strength. The high stiffness and strength, per unit weight, means that heavy (e.g. metal) components can be replaced by light weight composites. This is a factor of great importance, especially in all forms of transportation, where reductions in weight result in greater efficiency and energy savings. As a result, industries such as aircraft, medicine and electronic are quite dependent on design, manufacture and non-destructive evaluation (NDE) of composites.

A common classification scheme for one class of fiber reinforced composites is shown in Fig. 4.1, where the composites are divided according to number of layers, fiber length and fiber orientation. A single-layered composite consists of layers having the same elastic properties. Each of these layers are generally referred to as a lamina or a ply. A multi-layered composite is constructed by stacking several of these lamina in a specific sequence of orientation. If the stack of lamina are bonded together, the structure is called a laminate.
The fiber length may be either continuous or discontinuous, meaning that the fiber length is either much longer or shorter than the fiber diameter.
Finally, the fiber orientation may be divided into unidirectional (UD) or multidirectional (MD) laminates. A UD laminate has all fibers aligned in one direction. It is therefore very strong in the fiber (longitudinal) direction, but generally weak in the perpendicular (transverse) direction. A MD laminate has

normally several fiber directions in one fiber laminate. An example of the latter is a cross-ply laminate.
Hence, UD lamina can be considered as the basic structure element of the fiber reinforced laminate. Therefore, the total elastic property of a laminate is governed by the weighted sum of elastic properties of each individual UD lamina (See Appendix 4.1).

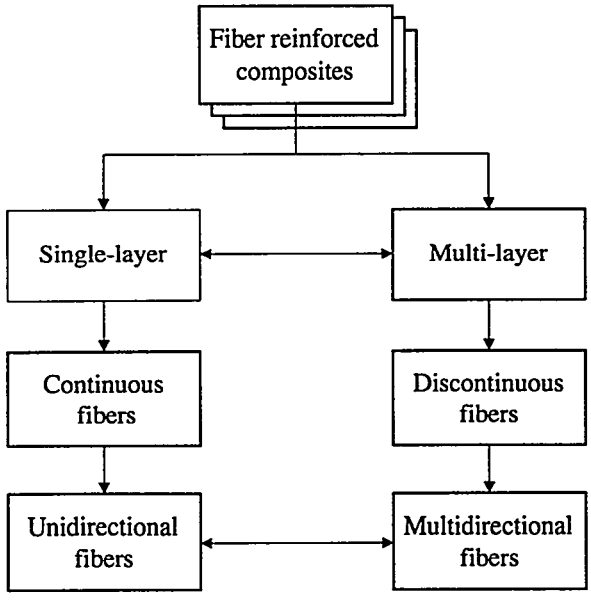

Figure 4.1. Classification of fiber reinforced composites.

In the present work, emphasis is placed on a single-layered, continuous and unidirectional fiber reinforced laminate.

4.2 Parameters influencing elastic properties

Elastic properties of fiber reinforced composites are dependent on a complicated interaction between the constituent materials (fiber reinforcement and matrix). Therefore, a total mapping of parameters that influence the elastic properties is very complex and may involve a variety of research fields (e.g., chemical, mechanical and electrical parameters).
However, for an ultrasonic determination of the elastic properties it is often sufficient to distinguish between: fiber orientation, fiber concentration (in terms of volume fraction), composite homogeneity and the elastic properties of the constituent. Of these parameters are fiber orientation and fiber concentration often considered to be the most important. They are therefore discussed first.

The presence of fibers, orientated in different directions, affects the anisotropy of the composite; meaning that the elastic properties vary in different directions (see section 4.3). Fiber orientation is, therefore, an important issue in controlling the anisotropy of a fiber reinforced composite. This anisotropy is, as mentioned, controlled by stacking unidirectional lamina in specific directions into laminates.

Fiber orientation may be estimated from the cross section of a circular fiber by an ultrasonic or optical NDE method. The shape of this cross section is, in general elliptical (recall that the specimens in chapter 2 and 3 had an elliptical shaped hole. This hole could be thought of as a *large scale* cross section of a fiber). The angle, α, between the ellipses major axis and the reference axis, y, defines the orientation of the fiber in the plane, as seen in Fig. 4.2. The orientation perpendicular to this plane is determined by the angle $\beta = \sin^{-1}(b/a)$, where a and b is the minor and major axis of the ellipse, respectively.

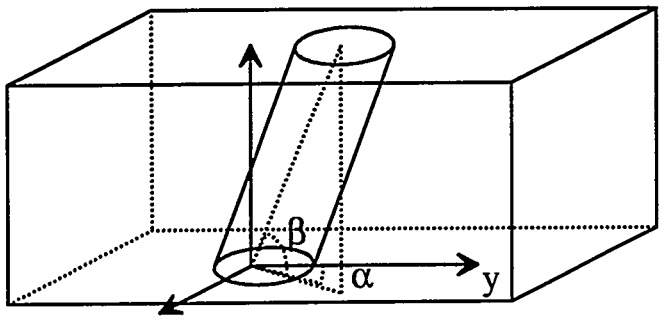

Figure 4.2. Fiber orientation in and out of the plane.

The overall elastic properties of a glass fiber composite are determined by the fiber concentration (see section 4.4). The fiber volume fraction is determined by first burning the matrix and then measuring the weight and volume of fibers, according to the ASTM D3171-76. It is interesting to estimate the maximum obtainable volume fraction of hexagonal and square packed fibers; when the fibers are identical and circular in cross section. The fiber volume fraction, V_f, of a hexagonal packing and a square packing is: $V_f = \pi \cdot r^2/(\sqrt{12}R^2)$ and $V_f = \pi \cdot r^2/(4R^2)$, respectively, where r is the radius of the fibers and R is the center to center spacing. Hence, the maximum obtainable fiber volume fraction is determined by the packing geometry, when fibers touch (i.e., $r = R$). This fiber volume is 91 and 79 volume percent, respectively, for the hexagonal packing and square packing. In practice, however, a limit is set to about 70 volume percent due to non-regular packing AGARWAL *et al.* (1981).

The UD glass/PET laminate, which is discussed in this chapter, is introduced by microscope (ESEM) pictures in Figs. 4.3 and 4.4. It is seen that the glass fibers have a circular cross section, which indicate a transverse cross section of the surface and the orientation angel β = 90°. The average fiber diameter is approximately 16 μm in diameter.
The fiber array appears to be quite random, although, some areas tend towards a hexagonal packing. The fiber volume fraction of this composite was measured to be 65.9 volume percent (see section 4.5). Fig. 4.4 shows three weft fibers used to stabilize the transverse direction.

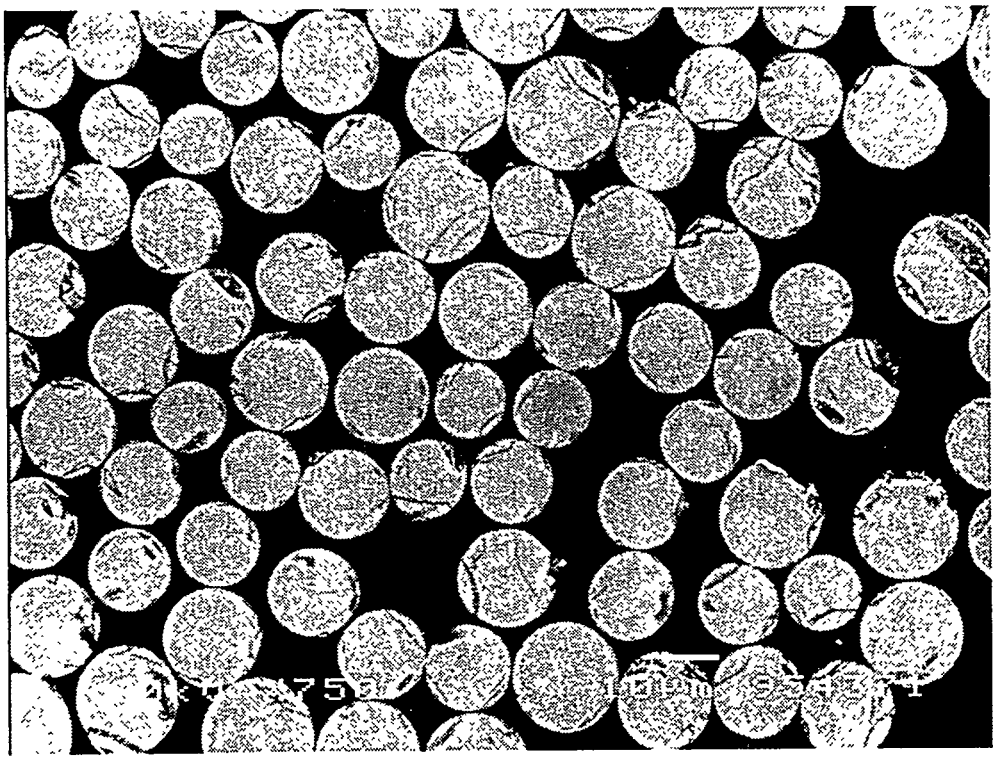

Figure 4.3. Microscope picture of a unidirectional glass/PET laminate cut in a transverse plane. The average glass fiber diameter is approximately 16 μm.

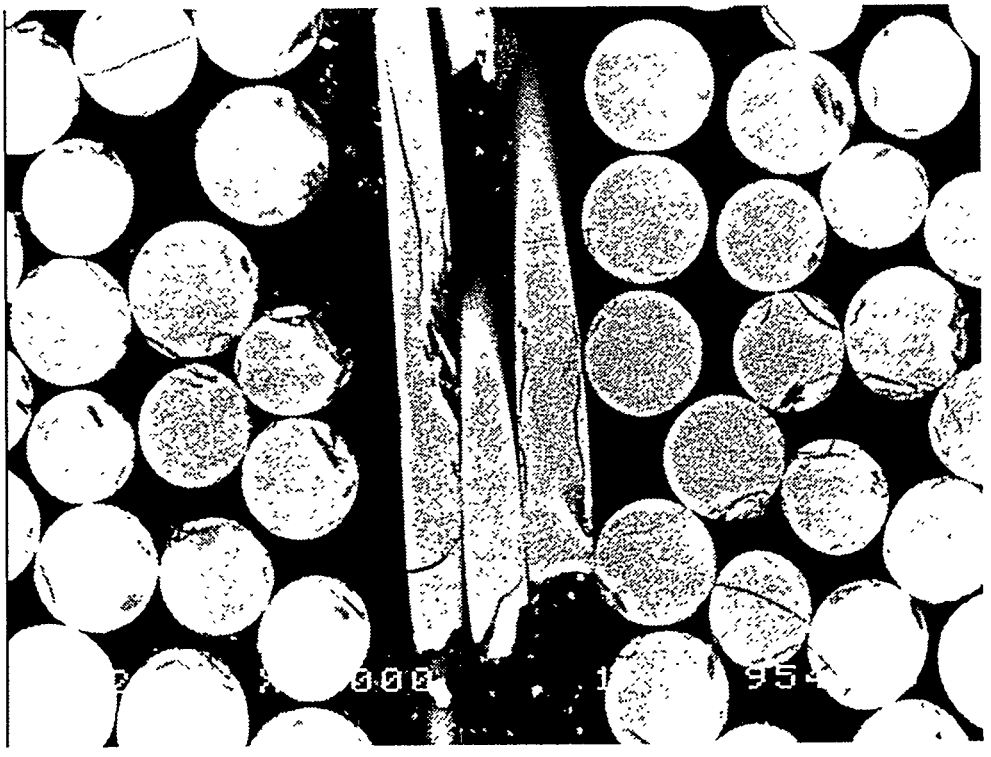

Figure 4.4. as Fig. 4.3, but showing three weft fibers.

Although fiber orientation and concentration is important for the overall elastic properties of the composite, composite homogeneity and the elastic properties of the constituent have yet to be discussed.
The homogeneity of the composite determines whether a specific volume differs in mechanical properties from the average properties of the composite. Inhomogeneties may be introduced to this volume, in the manufacturing process, by incomplete wetting of the fibers or by the presence of impurities in the matrix. The presence of inhomogeneties, for example matrix impurities (inclusions) or air bubbles (voids, porosity), reduce the stiffness and the interfacial shear strength of the composite. As a result, the interfacial bond between fibers and matrix is degraded. The interlaminar shear strength of composites decreases approximately 7% for each 1% of voids up to a total void content of about 4% according to HULL (1981).

Again from an ultrasonic NDE viewpoint, it is interesting to estimate the maximum fiber separation in a hexagonal array and, hence, estimate the size of an inhomogenity. The average separation of circular fibers, $\bar{s}$, in a hexagonal packed composite is

$$\bar{s} = \bar{d}_f\left[\sqrt{\left(\pi/V_f\sqrt{12}\right)}-1\right] \tag{4.1}$$

where $\bar{d}_f$ is the average fiber diameter and V_f is the fiber volume fraction HULL (1981).
The fiber separation, is shown in Fig. 4.5, as a function of fiber volume. The fiber diameters 8 and 16 micrometer are chosen as limits.

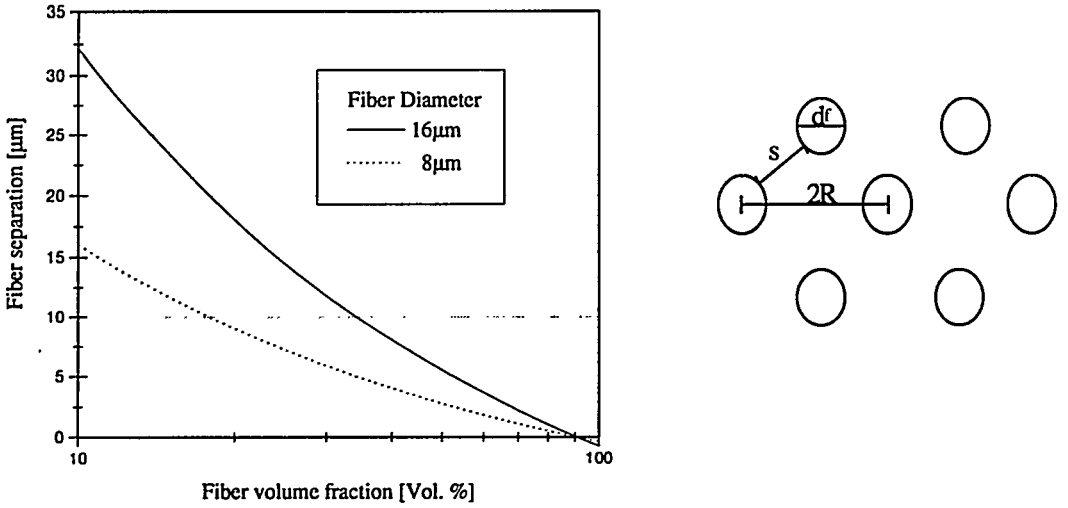

Figure 4.5. Fiber separation in a hexagonal array versus fiber volume fraction (Logarithmic scale).

It is seen, that the size (diameter) of an inhomogenity may be in the range of 1-17 micrometer in a 20-70 volume percent, hexagonal packed array (if the fiber diameter is between 8-16 micrometer).

4.2.1 Fiber and matrix properties

The design goal for fiber reinforced composites are, as mentioned in the introduction, to find a fiber material with high elastic modulus (and strength) and preferably low density; and then to arrange the fibers in a matrix to a suitable structure to give useful engineering properties to the finished product.

Many different materials may be used for fiber reinforcement of composites. However, the most typical materials are glass, carbon or organic fibers (Kevlar). Table 4.1 presents typical fiber properties arranged in order of decreasing density. E-glass fibers (E for electric), are the most common used glass fibers. Their properties are (in contrast to carbon and Kevlar fibers) isotropic, so that for example, the elastic modulus along a fiber is the same as transverse to the fiber. Carbon fibers are superior to E-glass fibers in terms of specific modulus (elastic modulus divided by density), and Kevlar fibers significantly better than E-glass. In addition, Kevlar fibers have a specific strength (tensile strength divided by density), about 50% greater than E-glass and Carbon (II) fibers. It may be observed from Table 4.1 that Carbon (I) fibers have a high modulus and Carbon (II) fibers have a high strength. Due to the fact that no bulk material has a specific stiffness modulus higher than 30 makes Carbon and Kevlar fibers important in composite design. For example, the specific modulus of steel is 27 Mm^2s^{-2}

Table 4.1. Average diameter and typical properties of fibers.

Fiber materials	E-glass	Carbon (I)	Carbon (II)	Kevlar
Average fiber diameter [μm]	11	8	8	12
Density [10^3 kg m^{-3}]	2.54	1.90	1.90	1.50
Elastic modulus [GNm^{-2}]	72.4	390	240	130
Tensile strength [GNm^{-2}]	3.5	2.1	2.5	2.8
Spec. modulus [Mm^2s^{-2}]	28.5	205.0	126.0	87.0
Spec. strength [Mm^2s^{-2}]	1.4	1.1	1.3	1.9

Ref.: AGARWAL *et al.* (1981) and HULL (1981).

A matrix is required to arrange the fibers into a useful structure. The matrix serves to bind the fibers together. This has three main functions: to protect the surface of individual fibers, to cement bundles of fibers into a composite and to transfer externally applied loads onto the strong fibers. The most common matrix materials, for fiber reinforced composites, are thermosetting and thermoplastic polymers. Thermosetting resins, as for example epoxy and polyester resins, are usually isotropic. Their most characteristic property is in response to heat, since unlike thermoplastics (e.g., polypropylene, polyaramid or polycarbonate), they do not melt on heating. However, they lose their stiffness properties at the heat distortion temperature and this defines an effective upper limit for their use in structural components. Thermoplastic polymers may have anisotropic properties depending on the conditions during solidification. Typical mechanical properties of thermosetting and thermoplastic polymers are presented in Table 4.2.

Table 4.2. Typical properties of thermosetting and thermoplastic polymers.

Matrix materials	Epoxy	Poly-ester	Poly-propylene	Poly-aramid	Poly-carbonate
Density [10^3 kg m^{-3}]	1.4	1.5	0.9	1.1	1.2
Elastic modulus[GNm^{-2}]	5	3	1	2	2
Tensile strength [GNm^{-2}]	0.09	0.06	0.03	0.07	0.05
Spec. modulus [Mm^{2}s^{-2}]	3.6	2.0	1.1	1.8	1.7
Spec. strength [Mm^{2}s^{-2}]	0.06	0.04	0.03	0.06	0.04

Ref.: AGARWAL *et al.* (1981) and HULL (1981).

A more comprehensive presentation of fiber and matrix properties can be found in works of AGARWAL *et al.* (1981) and HULL (1981).

4.3 Elastic stiffness constants

The elastic properties of fiber reinforced composites can be defined by the *generalized Hook's law* (LANDAU *et al.* 1985 and TIMOSHENKO *et al.* 1982) relating volume average stresses σ_{ij} and volume average of strains ε_{kl} by the stiffness tensor C_{ijkl}, in the form

$$\sigma_{ij} = C_{ijkl}\varepsilon_{kl} \quad \text{or} \quad \varepsilon_{ij} = S_{ijkl}\sigma_{kl} \tag{4.2}$$

where S_{ijkl} is the inverse compliance tensor and ($i, j, k, l = 1, 2, 3$).
The number of elastic stiffness constants (elements in stiffness tensor) is in general 81. However, due to symmetry of strain (i.e., $C_{ijkl} = C_{ijlk}$), symmetry of stress (i.e., $C_{ijkl} = C_{jikl}$) and the existence of a strain energy density function (i.e., $C_{ijkl} = C_{klij}$) (LANDAU *et al.* 1985) the number of elastic stiffness constants reduces to 21 for an anisotropic material.
Thus, it is convenient to write Hook's law in contracted notation as

$$\sigma_i = C_{ij}\varepsilon_j \qquad (i, j = 1,2,3,4,5,6) \tag{4.3}$$

or

$$\begin{bmatrix}\sigma_1\\ \sigma_2\\ \sigma_3\\ \sigma_4\\ \sigma_5\\ \sigma_6\end{bmatrix} = \begin{bmatrix}C_{11} & C_{12} & C_{13} & C_{14} & C_{15} & C_{16}\\ C_{12} & C_{22} & C_{23} & C_{24} & C_{25} & C_{26}\\ C_{13} & C_{23} & C_{33} & C_{34} & C_{35} & C_{36}\\ C_{14} & C_{24} & C_{23} & C_{44} & C_{45} & C_{46}\\ C_{15} & C_{25} & C_{35} & C_{45} & C_{55} & C_{56}\\ C_{16} & C_{26} & C_{36} & C_{46} & C_{56} & C_{66}\end{bmatrix}\begin{bmatrix}\varepsilon_1\\ \varepsilon_2\\ \varepsilon_3\\ \varepsilon_4\\ \varepsilon_5\\ \varepsilon_6\end{bmatrix} \tag{4.4}$$

where C_{ij} is the stiffness matrix. The engineering stresses and strains corresponds to the tensor notation in the following way:

$$\sigma_1 = \sigma_{11}, \sigma_2 = \sigma_{22}, \sigma_3 = \sigma_{33}, \qquad \sigma_4 = \sigma_{23} = \tau_{23}, \sigma_5 = \sigma_{13} = \tau_{13}, \sigma_6 = \sigma_{12} = \tau_{12}$$
$$\varepsilon_1 = \varepsilon_{11}, \varepsilon_2 = \varepsilon_{22}, \varepsilon_3 = \varepsilon_{33}, \qquad \varepsilon_4 = 2\varepsilon_{23} = \gamma_{23}, \varepsilon_5 = 2\varepsilon_{13} = \gamma_{13}, \varepsilon_6 = 2\varepsilon_{12} = \gamma_{12}$$

where the first suffix in the tensor notation refers to the direction normal to the plane, in which a stress (or strain) is acting; and the second suffix refers to the direction in which the stress is acting. Notice, that an engineering shear strain is twice the corresponding tensor shear strain.

4.3.1 Orthotropy and transverse isotropy

For fiber reinforced composites the significant cases to consider are orthotropy, transverse isotropy and isotropy. An orthotropic elastic laminate has three perpendicular (orthogonal) planes of material symmetry; and the properties at any point are different in the perpendicular directions, defined by a Cartesian coordinate system with three perpendicular axis (x_1, x_2, x_3). The direction parallel to the fibers (x_1) is called the longitudinal direction. The direction perpendicular to the fibers, in the plane of fibers (x_2) and out of plane (x_3), respectively, is called the transverse directions.

A transverse isotropic laminate is a particular case of an orthotropic laminate. It possess an axis of symmetry, in the sense that all elastic properties perpendicular to this axis are equivalent (isotrope). This symmetry axis is often the fiber direction, x_1, as indicated in Fig. 4.6. Finally, an isotropic laminate is, as mentioned, characterized by having the same properties in all directions.

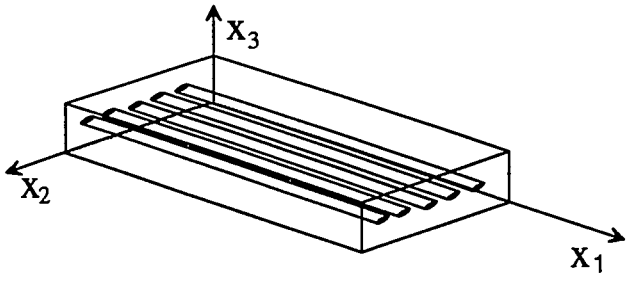

Figure 4.6. Transverse isotropic laminate.

The number of independent elastic stiffness constants reduces to 9, for an orthotropic laminate (for example a cross-ply laminate) and the stiffness matrix takes the form

$$\begin{bmatrix}\sigma_1\\ \sigma_2\\ \sigma_3\\ \sigma_4\\ \sigma_5\\ \sigma_6\end{bmatrix} = \begin{bmatrix} C_{11} & C_{12} & C_{13} & 0 & 0 & 0\\ C_{12} & C_{22} & C_{23} & 0 & 0 & 0\\ C_{13} & C_{23} & C_{33} & 0 & 0 & 0\\ 0 & 0 & 0 & C_{44} & 0 & 0\\ 0 & 0 & 0 & 0 & C_{55} & 0\\ 0 & 0 & 0 & 0 & 0 & C_{66}\end{bmatrix}\begin{bmatrix}\varepsilon_1\\ \varepsilon_2\\ \varepsilon_3\\ \varepsilon_4\\ \varepsilon_5\\ \varepsilon_6\end{bmatrix} \tag{4.5}$$

where C_{11}, C_{22}, C_{33}, C_{44}, C_{55}, C_{66}, C_{12}, C_{13} and C_{23} are the elastic stiffness constants.

In terms of engineering constants the stiffness constants are related by

$$C_{11} = \left(1-\nu_{23}^2 E_{33}/E_{22}\right)\frac{E_{11}}{V} \tag{4.6}$$

$$C_{12} = \left(\nu_{12}+\nu_{13}\nu_{23} E_{33}/E_{22}\right)\frac{E_{22}}{V} \tag{4.7}$$

$$C_{13} = \left(\nu_{13}+\nu_{12}\nu_{23}\right)\frac{E_{33}}{V} \tag{4.8}$$

$$C_{23} = \left(\nu_{23}+\nu_{12}\nu_{13} E_{22}/E_{11}\right)\frac{E_{33}}{V} \tag{4.9}$$

$$C_{22} = \left(1-\nu_{13}^2 E_{33}/E_{11}\right)\frac{E_{22}}{V} \tag{4.10}$$

$$C_{33} = \left(1-\nu_{12}^2 E_{22}/E_{11}\right)\frac{E_{33}}{V} \tag{4.11}$$

$$C_{44} = G_{23}, C_{55} = G_{13}, C_{66} = G_{12} \tag{4.12}$$

$$V = \left[1-\nu_{12}\left(\nu_{12} E_{22}/E_{11}+2\nu_{23}\nu_{13} E_{33}/E_{11}\right)-\nu_{13}^2 E_{33}/E_{11}-\nu_{23}^3 E_{33}/E_{22}\right] \tag{4.13}$$

where the 9 independent engineering constants are Young's moduli E_{11}, E_{22}, E_{33}, the shear moduli G_{12}, G_{13}, G_{23} and Poisson's ratios ν_{12}, ν_{13}, ν_{23}. The following relationships exist between the Young's moduli and the Poisson's ratios WHITNEY (1987): $E_{11}\nu_{21} = E_{22}\nu_{12}$, $E_{22}\nu_{32} = E_{33}\nu_{23}$, $E_{33}\nu_{13} = E_{11}\nu_{31}$.

A unidirectional laminate is assumed to be transverse isotropic, where the (x_1)-axis is aligned along the fiber direction and is perpendicular to the $(x_2$-$x_3)$-plane of isotropy. The number reduces to 5 independent engineering constants due to

$$E_{33} = E_{22} = 2G_{23}(1+\nu_{23}), G_{13} = G_{12}, \nu_{13} = \nu_{12} \tag{4.14}$$

The stiffness matrix takes the form

$$\begin{bmatrix}\sigma_1\\ \sigma_2\\ \sigma_3\\ \sigma_4\\ \sigma_5\\ \sigma_6\end{bmatrix} = \begin{bmatrix} C_{11} & C_{12} & C_{12} & 0 & 0 & 0\\ C_{12} & C_{22} & C_{23} & 0 & 0 & 0\\ C_{13} & C_{23} & C_{22} & 0 & 0 & 0\\ 0 & 0 & 0 & C_{44} & 0 & 0\\ 0 & 0 & 0 & 0 & C_{66} & 0\\ 0 & 0 & 0 & 0 & 0 & C_{66}\end{bmatrix}\begin{bmatrix}\varepsilon_1\\ \varepsilon_2\\ \varepsilon_3\\ \varepsilon_4\\ \varepsilon_5\\ \varepsilon_6\end{bmatrix} \tag{4.15}$$

where C_{11}, $C_{22} = C_{33}$, $C_{55} = C_{66}$, $C_{12} = C_{13}$, and C_{23} are the five independent elastic stiffness constants and $C_{44} = (C_{22} - C_{23})/2$.
Notice, if the (x_2)-axis instead is chosen as the axis of symmetry (fiber direction), the five independent elastic stiffness constants then are C_{22}, $C_{11} = C_{33}$, $C_{44} = C_{66}$, $C_{12} = C_{23}$ and C_{13}, (and $C_{55} = (C_{33} - C_{13})/2$). Notice, also that if the (x_3)-axis is the axis of symmetry the five independent elastic stiffness constants are C_{33}, $C_{11} = C_{22}$, $C_{44} = C_{55}$, $C_{13} = C_{23}$ and C_{12} (and $C_{66} = (C_{11} - C_{12})/2$).

If only a unidirectional stress (i.e., $\sigma_3 = \sigma_4 = \sigma_5 = 0$) is applied to the composite the reduced stiffness matrix takes the form

$$\begin{bmatrix} \sigma_1 \\ \sigma_2 \\ \tau_{12} \end{bmatrix} = \begin{bmatrix} Q_{11} & Q_{12} & 0 \\ Q_{12} & Q_{22} & 0 \\ 0 & 0 & \tfrac{1}{2}(Q_{11} - Q_{12}) \end{bmatrix} \begin{bmatrix} \varepsilon_1 \\ \varepsilon_2 \\ \gamma_{12} \end{bmatrix} \tag{4.16}$$

where *Q's* are used instead of *C's*. The elastic stiffness constants are expressed in engineering constants in the following way (see Appendix 4.2)

$$Q_{11} = \frac{E_{11}}{1 - \nu_{12}\nu_{21}}, \quad Q_{22} = \frac{E_{22}}{1 - \nu_{12}\nu_{21}}, \tag{4.17-4.18}$$

$$Q_{12} = \frac{\nu_{12}E_{22}}{1 - \nu_{12}\nu_{21}}, \quad Q_{66} = \tfrac{1}{2}(Q_{11} - Q_{12}) = G_{12} \tag{4.19-4.20}$$

which gives 4 elastic stiffness constants expressed in engineering constants.
The reduced elastic stiffness constants Q can be found in a new coordinate system *(x, y, z)*, at an angle θ relative to the principal material direction (see also Appendix 4.3). The transformed reduced stiffness matrix $\overline{Q}$ is found as a multiplication between the inverse transformation matrix, the stiffness matrix Q and the transformation matrix T. The inverse transformation matrix can be found if θ is changed to minus θ.

$$\begin{bmatrix} \sigma_x \\ \sigma_y \\ \tau_{xy} \end{bmatrix} = \begin{bmatrix} \overline{Q}_{11} & \overline{Q}_{12} & \overline{Q}_{16} \\ \overline{Q}_{12} & \overline{Q}_{22} & \overline{Q}_{16} \\ \overline{Q}_{16} & \overline{Q}_{16} & \overline{Q}_{66} \end{bmatrix} \begin{bmatrix} \varepsilon_x \\ \varepsilon_y \\ \gamma_{xy} \end{bmatrix} \tag{4.21}$$

where $[\overline{Q}] = [T]^{-1}[Q][T]$ and $[T] = \begin{bmatrix} \cos^2\theta & \sin^2\theta & 2\sin\theta\cos\theta \\ \sin^2\theta & \cos^2\theta & -2\sin\theta\cos\theta \\ -\sin\theta\cos\theta & \sin\theta\cos\theta & \cos^2\theta - \sin^2\theta \end{bmatrix}$

which gives

$$\begin{aligned}
\overline{Q}_{11} &= Q_{11}\cos^4(\theta) + 2(Q_{12} + 2Q_{66})\sin^2(\theta)\cos^2(\theta) + Q_{22}\sin^4(\theta) \\
\overline{Q}_{22} &= Q_{11}\sin^4(\theta) + 2(Q_{12} + 2Q_{66})\sin^2(\theta)\cos^2(\theta) + Q_{22}\cos^4(\theta) \\
\overline{Q}_{12} &= (Q_{11} + Q_{22} - 4Q_{66})\sin^2(\theta)\cos^2(\theta) + Q_{12}(\sin^4(\theta) + \cos^4(\theta)) \\
\overline{Q}_{66} &= (Q_{11} + Q_{22} - 2Q_{12} - 2Q_{66})\sin^2(\theta)\cos^2(\theta) + Q_{66}(\sin^4(\theta) + \cos^4(\theta)) \\
\overline{Q}_{16} &= (Q_{11} - Q_{22} - 2Q_{66})\sin(\theta)\cos^3(\theta) + (Q_{12} - Q_{22} + 2Q_{66})\sin^3(\theta)\cos(\theta) \\
\overline{Q}_{26} &= (Q_{11} - Q_{22} - 2Q_{66})\sin^3(\theta)\cos(\theta) + (Q_{12} - Q_{22} + 2Q_{66})\sin(\theta)\cos^3(\theta)
\end{aligned}$$

Finally, for complete isotropy the number of independent elastic stiffness constants is reduced to 2. That is, C_{11}, C_{12} (and $C_{66}=(C_{11}-C_{12})/2$).

4.4 Elastic engineering constants

A major problem in ultrasonic characterization of fiber reinforced composites consist in deriving relations between the elastic stiffness constants, Eqs. (4.6-4.13), and ultrasonic phase velocity. This problem will be discussed in chapter 5.

Another problem is to predict the elastic engineering constants from the properties of the constituents (matrix and fibers). This problem is discussed below for a transverse isotropic (unidirectional) composite.

The five engineering elastic constants are: (1) the longitudinal Young's modulus E_{11}, (2) the transverse Young's modulus E_{22} (=E_{33}), (3) the in-plane shear modulus G_{12} (=G_{13}), (4) the major in-plane ν_{12} (=ν_{13} or minor ν_{21}) Poisson's ratio and (5) the out-of-plane Poisson's ratio ν_{23}. The out-of-plane shear modulus G_{23} depends on E_{22} and ν_{23}, according to Eq. (4.14).

The section is divided into six sets of equations, representing micromechanical theories in terms of empirical expressions by AGARWAL *et al.* (1981), CHAMIS (1984), TSAI *et al.* (1980), HALPIN *et al.* (1976), WHITNEY *et al.* (1966), HASHIN *et al.* (1964), ZIMMER *et al.* (1970) and GRESZCZUK (1971).

4.4.1 Rule-of-mixtures

A simple relation between the longitudinal Young's modulus of the composite in the fiber direction, E_{11}, and the elastic moduli of fiber and matrix is the *rule-of-mixtures*

$$E_{11} = E_f V_f + E_m V_m \tag{4.22}$$

where V_f and V_m=$(1-V_f)$ are the fiber and matrix volume fractions, respectively. E_f and E_m is the Young's moduli of the fiber and the matrix, respectively. The *rule-of-mixtures* assumes a perfect (infinitesimal thin) bounding between fiber and matrix. It also assumes that the Poisson's ratio in fiber and matrix is equal AGARWAL *et al.* (1981). Similar mixture rules are

$$E_{22} = \frac{E_f E_m}{E_f V_m + E_m V_f} \tag{4.23}$$

$$G_{12} = \frac{G_f G_m}{G_f V_m + G_m V_f} \tag{4.24}$$

$$\nu_{12} = \nu_f V_f + \nu_m V_m \tag{4.25}$$

$$\nu_{21} = \frac{E_{22}}{E_{11}} \nu_{12} \tag{4.26}$$

where E_{22} and G_{12} is the transverse Young's modulus and in-plane shear modulus, respectively. ν_{12} and ν_{21} is the major and minor Poisson's ratio, respectively.

4.4.2 Chamis equations

The following equations for the transverse and in-plane shear moduli in the plane is obtained by MALLICK (1993) and CHAMIS (1984)

$$E_{22} = \frac{E_f E_m}{E_f - \sqrt{V_f}(E_f - E_m)} \tag{4.27}$$

$$G_{12} = \frac{G_f G_m}{G_f - \sqrt{V_f}(G_f - G_m)} \tag{4.28}$$

The longitudinal Young's modulus and major Poisson's ratio is given by the *rule-of-mixtures* Eqs. (4.22 and 4.25).

4.4.3 Tsai-Hahn equations

Similar equations are obtained by TSAI *et al.* (1980)

$$E_{22} = \frac{(V_f + \eta_{22} V_m) E_f E_m}{E_m V_f + \eta_{22} V_m E_f} \tag{4.29}$$

$$G_{12} = \frac{(V_f + \eta_{12} V_m) G_f G_m}{G_m V_f + \eta_{12} V_m G_f} \tag{4.30}$$

where $\eta_{22} = 0.516$ and $\eta_{12} = 0.316$.
Again, the longitudinal Young's modulus and major Poisson's ratio is given by the *rule-of-mixtures* Eqs. (4.22 and 4.25).

4.4.4 Halpin-Tsai equations

An approximation to the results of more exact micro-mechanics (Finite-element analysis) is obtained by HALPIN *et al.* (1976). Their equations take the general form

$$E_x = E_m \frac{1 + \zeta \eta V_f}{1 - \eta V_f} \qquad \eta = \frac{(E_f / E_m) - 1}{(E_f / E_m) + \zeta} \tag{4.31}$$

where ζ is a constant. For the present study of circular glass fibers, the Halpin-Tsai equations are set to

$$E_{11} = E_m \frac{1 + \zeta_{11} \eta_{11} V_f}{1 - \eta_{11} V_f} \qquad \eta_{11} = \frac{(E_f / E_m) - 1}{(E_f / E_m) + \zeta_{11}} \tag{4.31a}$$

$$E_{22} = E_m \frac{1 + \zeta_{22} \eta_{22} V_f}{1 - \eta_{22} V_f} \qquad \eta_{22} = \frac{(E_f / E_m) - 1}{(E_f / E_m) + \zeta_{22}} \tag{4.31b}$$

$$G_{12} = G_m \frac{1 + \zeta_{12} \eta_{12} V_f}{1 - \eta_{12} V_f} \qquad \eta_{12} = \frac{(G_f / G_m) - 1}{(G_f / G_m) + \zeta_{12}} \tag{4.31c}$$

$$G_{23} = G_m \frac{1+\zeta_{23}\eta_{23}V_f}{1-\eta_{23}V_f} \qquad \eta_{23} = \frac{(G_f/G_m)-1}{(G_f/G_m)+\zeta_{23}} \tag{4.31d}$$

$$\nu_{23} = \frac{1+\zeta_{23}\eta'_{23}V_f}{1-\eta'_{23}V_f} \qquad \eta'_{23} = \frac{(\nu_f/\nu_m)-1}{(\nu_f/\nu_m)+\zeta_{23}} \tag{4.31e}$$

where $\zeta_{11} = 2l_f/d_f + 40V_f^{10}$, $\zeta_{22} = 2+40V_f^{10}$, $\zeta_{12} = 1+40V_f^{10}$ and $\zeta_{23} = 1+40V_f^{10}$. The fiber length and diameter is set to l_f= 20 cm and d_f= 16 μm, respectively. The major Poisson's ratio is given by the *rule-of-mixtures* Eq. (4.25).

4.4.5 Whitney equations

WHITNEY *et al.* (1966) assumes a cylindrical fiber embedded in a cylindrical matrix. They developed approximate equations, applying Airy stress functions to the fiber and matrix with boundary conditions, requiring continuity of displacements across the fiber-matrix interface and continuity of the appropriate stresses. Their equations take the form

$$E_{11} = E_f V_f + E_m V_m + \frac{2(\nu_f-\nu_m)^2 E_m E_f V_m V_f}{E_m V_m L_f + [L_m V_f + (1+\nu_m)]E_f} \tag{4.32}$$

$$E_{22} = \frac{2K(1-\nu_{23})E_{11}}{E_{11}+4K\nu_{12}^2}, \quad K = \frac{(K_f+G_m)K_m-(K_f-K_m)G_m V_f}{(K_f+G_m)-(K_f-K_m)V_f} \tag{4.33}$$

$$G_{12} = \frac{[(G_f+G_m)+(G_f-G_m)V_f]G_m}{(G_f+G_m)-(G_f-G_m)V_f} \tag{4.34}$$

$$\nu_{12} = \nu_m - \frac{2(\nu_m-\nu_f)(1-\nu_m^2)E_f V_f}{E_m V_m L_f + [L_m V_f + (1+\nu_m)]E_f} \tag{4.35}$$

$$\nu_{23} = \nu_f V_f + \nu_m V_m \tag{4.36}$$

where $L_f = 1-\nu_f-2\nu_f^2$ and $L_m = 1-\nu_m-2\nu_m^2$. G_{23} is calculated according to Eq. (4.14).

4.4.6 Hashin-Rosen equations

In the Hashin-Rosen equations, HASHIN *et al.* (1964), for the elastic constants of fiber reinforced composites it is assumed that the composite is transverse isotropic. It is also assumed that the matrix and fiber are linearly elastic, isotropic and homogeneous. The fibers are also assumed to be identical and to form a hexagonal array in the transverse plane. The composite is modeled as a matrix cylinder surrounding a central fiber. The Young's moduli and shear moduli and Poisson ratio's are

$$E_{11} = V_f E_f + V_m E_m \tag{4.37}$$

$$E_{22} = \frac{4K_{23}G_{23}}{K_{23} + \psi G_{23}}\psi = 1 + \frac{4K_{23}\nu_{12}^{\,2}}{E_{11}} \tag{4.38}$$

$$G_{12} = G_m + \frac{V_f}{(G_f - G_m)^{-1} + V_m(2G_m)^{-1}} \tag{4.39}$$

$$G_{23} = G_m \frac{(1+\alpha_1 V_f^{\,3})(\alpha_2 + \beta_1 V_f) - 3V_f V_m^{\,2}\beta_1^2}{(1+\alpha_1 V_f^{\,3})(\alpha_2 - V_f) - 3V_f V_m^{\,2}\beta_1^2} \tag{4.40}$$

$$\nu_{12} = \frac{V_f E_f L_1 + V_m E_m L_2 \nu_m}{V_f E_f L_3 + V_m E_m L_2} \tag{4.41}$$

$$\nu_{23} = \frac{K_{23} - \psi G_{23}}{K_{23} + \psi G_{23}} \tag{4.42}$$

with the constants

$$L_1 = 2\nu_f(1-\nu_m^{\,2})V_f + V_m(1+\nu_m)\nu_m$$

$$L_2 = V_f(1-\nu_f - 2\nu_f^{\,2})$$

$$L_3 = 2V_f(1-\nu_m^{\,2}) + V_m(1+\nu_m)$$

$$\alpha_1 = \frac{\beta_1 - (G_f/G_m)\beta_2}{1+(G_f/G_m)\beta_2}, \qquad \alpha_2 = \frac{(G_f/G_m)+\beta_1}{(G_f/G_m)-1}$$

$$\beta_1 = \frac{1}{3-4\nu_m}, \qquad \beta_2 = \frac{1}{3-4\nu_f}$$

$$K_{23} = K_m + \frac{V_f}{(K_f - K_b)^{-1} + V_m(K_m + G_m)^{-1}}$$

4.5 Results and discussions

In the following section, the elastic properties for the glass/PET laminate are compared with the six sets of equations.
This laminate was made from UD weave of E-glass fibers with a weight fraction of 98.5 in the longitudinal direction and 1.5 in the transverse direction, respectively (the fibers in the transverse direction are seen in Fig. 4.3). It was assumed that the glass fibers were identical with a circular cross section and the fiber diameter was d_f = 16 μm, as seen in Fig. 4.2. The matrix was a thermoplastic polyester called PET (Poly Ethylene Teraphtalate) in form of a film. It was also assumed that the fibers and matrix were linear elastic, isotropic, and homogeneous, as discussed in subsection 4.2.1.
The volume fraction of fibers, matrix and porosity was measured, as mentioned in subsection 4.2, to be 0.659, 0.326 and 0.015, respectively. However, in the following discussion porosity was ignored.
Table 4.3 presents the assumed material properties for the laminate under discussion.

Table 4.3. Material properties for E-glass fiber and PET matrix.

	E-glass fiber	PET matrix
Volume fraction, V_f - V_m	0.66	0.34
Poisson ratio, ν_f - ν_m	0.22	0.38
Stiffness modulus, E_f - E_m [GPa]	72.0	4.5
Bulk modulus, K_f - K_m [GPa]	42.9	6.3
Shear modulus, G_f - G_m [GPa]	29.5	1.7

$$G_f = E_f / (2(1+V_f)); \quad K_f = E_f / (3(1-2V_f)); \quad d_f = 16\mu m$$

Finally, the laminate was considered as transverse isotropic, with five independent elastic constants, as discussed above.
The longitudinal Young's modulus is plotted in Fig. 4.7 as a function of fiber volume fraction, according to the *rule-of-mixtures* Eq. (4.22) and the equations (4.31a), (4.32), (4.37). The fiber and matrix stiffness moduli, from Table 4.3, are also plotted in the Figure and a vertical dotted line is used to indicate the 66 volume percent glass/PET laminate. The calculated stiffness moduli on this line (i.e., theoretical values for V_f= 0.66) is written in the Figure, in order of highest moduli.
The theoretical stiffness values were compared with experimental values from compression tests by TOFTEGAARD (1997) and vibration tests by FREDERIKSEN (1997).

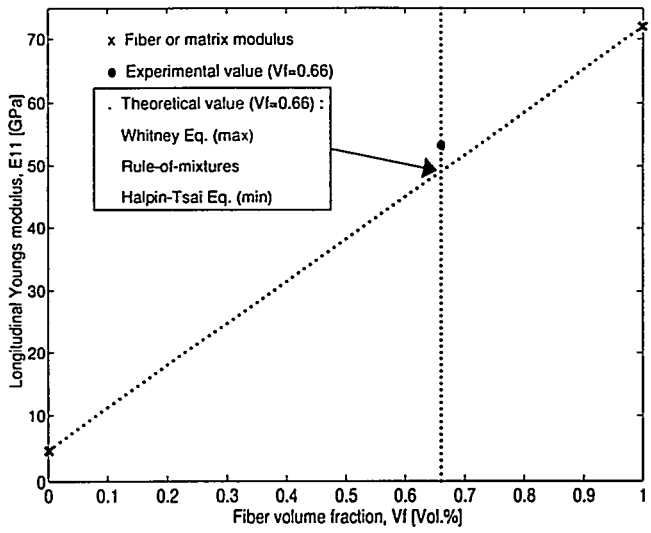

Figure 4.7. Longitudinal Young's modulus versus fiber volume fraction.

The calculated longitudinal Young's moduli were nearly the same for the three equations and found within 1 % of the *rule-of-mixtures*. The Whitney equation gave the maximum value, while the Halpin-Tsai equations gave the minimum value. However, the moduli were in general 9% lower than the experimental obtained modulus. Hence, the experimental longitudinal Young's modulus, E_{11}, deviated 9 % from the theoretical maximum value.

The transverse Young's modulus was calculated from the Eqs. (4.23, 4.27, 4.29, 4.31b, 4.33, 4.38), respectively, and plotted in Fig. 4.8. The vertical dotted line is again used to indicate the 66 volume percent glass/PET laminate.

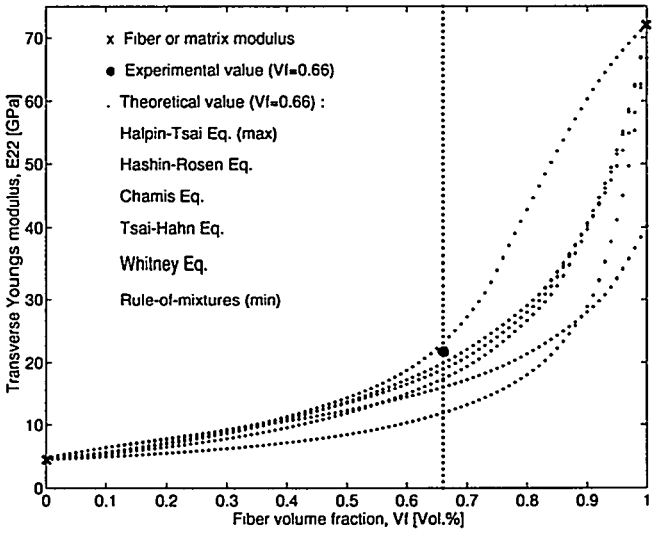

Figure 4.8. Transverse Young's modulus versus fiber volume fraction.

In this case, the Halpin-Tsai equation gave the maximum value, while the *rule-of-mixtures* gave the minimum value. The experimental transverse Young's modulus, E_{22}, deviated 6 % from the Halpin-Tsai equations.

The in-plane shear modulus, G_{12}, was calculated from the Eqs. (4.24, 4.28, 4.30, 4.31c, 4.34, 4.39), respectively, and plotted in Fig. 4.9.

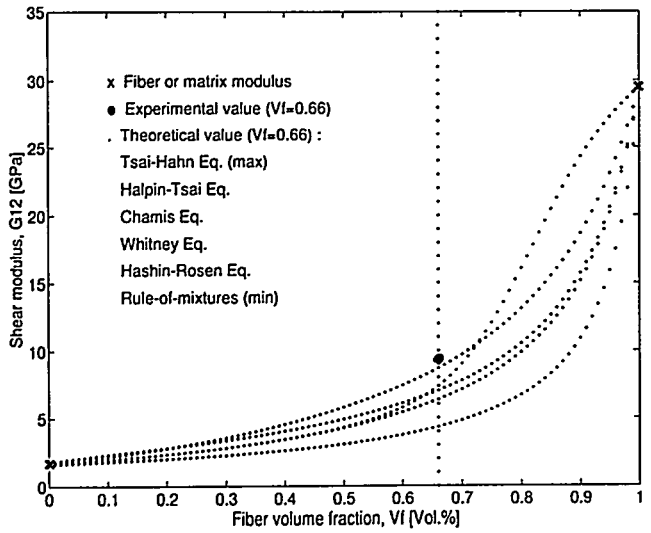

Figure 4.9. In-plane shear modulus versus fiber volume fraction.

Here, the Tsai-Hahn equation gave the maximum value, while the *rule-of-mixtures* gave the minimum value. The experimental in-plane shear modulus, G_{12}, deviated 8 % from the maximum value.

The out-of-plane shear modulus, G_{23}, was calculated from the Eqs. (4.14, 4.31d, 4.40), respectively, and plotted in Fig. 4.10.

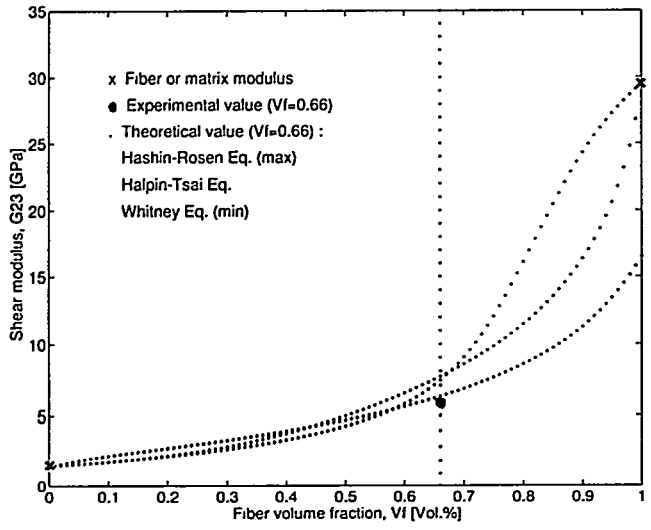

Figure 4.10. Out-of-plane shear modulus versus fiber volume fraction.

The Hashin-Rosen equation gave the maximum value, while the Whitney equations gave the minimum value. The out-of-plane shear modulus, G_{23}, deviated 7 % from the minimum value.

The major (in-plane) Poisson's ratio, ν_{12}, was determined by Eqs. (4.25, 4.35, 4.41), respectively, and plotted in Fig. 4.11.

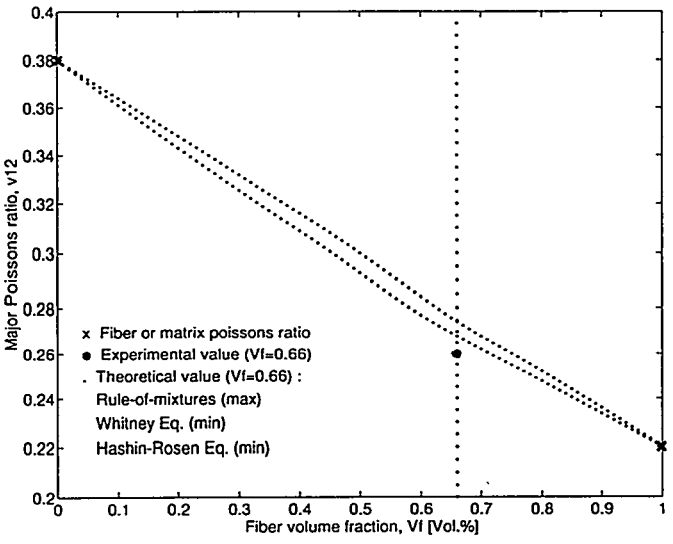

Figure 4.11. Major in-plane Poisson's ratio versus fiber volume fraction.

In this case, the *rule-of-mixtures* gave the maximum value, while the Whitney and Hashin-Rosen equations gave the minimum value. The major Poisson's ratio, ν_{12}, deviated 3 % from the minimum value.

The out-of-plane Poisson's ratio, ν_{23}, was determined by Eqs. (4.31e, 4.36, 4.42), respectively, and plotted in Fig. 4.12.

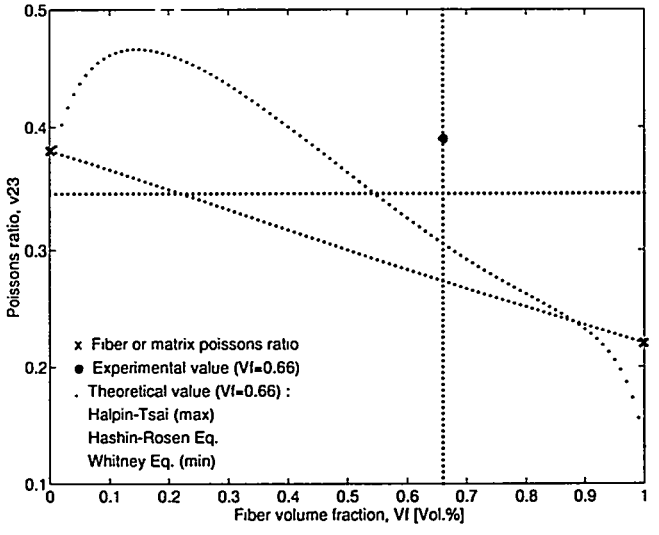

Figure 4.12. Out-of-plane Poisson's ratio versus fiber volume fraction.

The Halpin-Tsai equation gave the maximum value, while the Whitney equations gave the minimum value. The out-of-plane Poisson's ratio, ν_{23}, deviated 12 % from the maximum value.

The minor (in-plane) Poisson's ratio, ν_{21}, was determined by Eqs. (4.26) and plotted in Fig. 4.13. E_{11} and E_{22} was calculated like in Figs. 4.7-4.8. The difference in the minor Poisson's ratio, reflected the difference in the longitudinal and transverse Young's moduli.

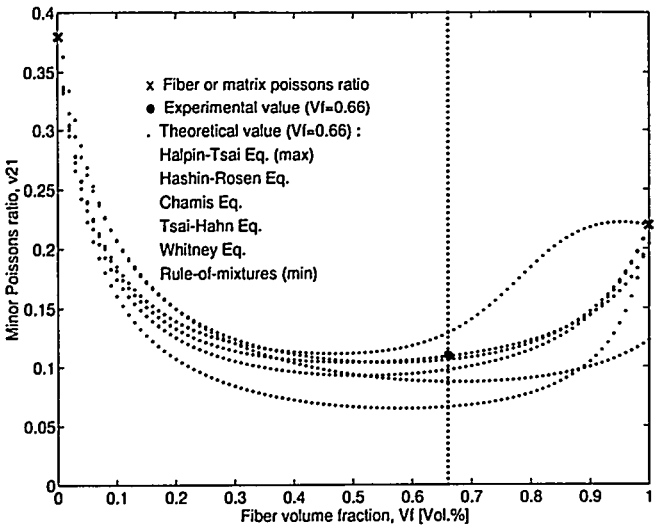

Figure 4.13. Minor Poisson's ratio versus fiber volume fraction.

The Halpin-Tsai equation gave the maximum value, while the *rule-of-mixtures* gave the minimum value. The minor Poisson's ratio, ν_{21}, deviated 1 % from the Hashin-Rosen equation.
Elastic engineering constants for the six sets of equations and the experimental obtained values are summarized in Table 4.4.

Table 4.4. Elastic engineering constants for a 66 Vol. % glass/PET laminate.*

	Experi-mental**	*Rule-of-mixtures*	Chamis	Tsai - Hahn	Halpin - Tsai	Whitney	Hashin - Rosen
E_{11} [GPa]	53.4	49.05	49.05	49.05	49.04	49.08	49.05
E_{22} [GPa]	21.8	11.80	18.88	17.35	23.02	15.94	19.89
E_{33} [GPa]	21.9	11.80	18.88	17.35	23.02	15.94	19.89
G_{12} [GPa]	9.4	4.33	7.01	8.69	7.36	6.34	6.34
G_{13} [GPa]	7.7	4.33	7.01	8.69	7.36	6.34	6.34
G_{23} [GPa]	5.8	-	-	-	7.36	6.26	7.62
ν_{12}	0.26	0.274	0.274	0.274	0.274	0.268	0.268
ν_{13}	0.28	0.274	0.274	0.274	0.274	0.268	0.268
ν_{23}	0.39	-	-	-	0.345	0.274	0.305
ν_{21}	0.11	0.066	0.105	0.097	0.129	0.087	0.109

* Transverse isotropic laminate with circular, linear elastic isotropic glass fibers.
** TOFTEGAARD (1997) and FREDERIKSEN (1997).

The presented Figures and Table show that the elastic engineering constants for the glass/PET laminate could be identified, with the smallest variation, by the equations of Whitney and Hashin-Rosen. Hence, using these equations, the elastic stiffness constants were calculated from Eqs. (4.6-4.13). The experimental stiffness constants were calculated from the experimental values in Table 4.4.
Figs. 4.14-4.18 show the elastic constants, C_{11}, C_{22}, C_{12}, C_{23} and C_{66} as function of fiber volume fraction.

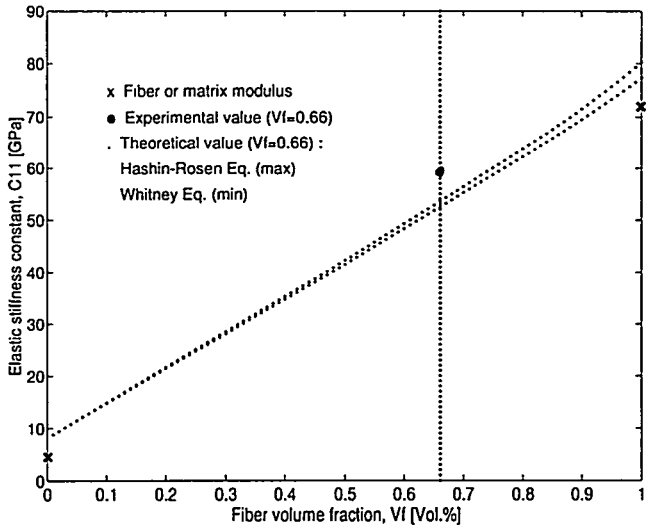

Figure 4.14. Elastic stiffness constant C_{11} versus fiber volume fraction.

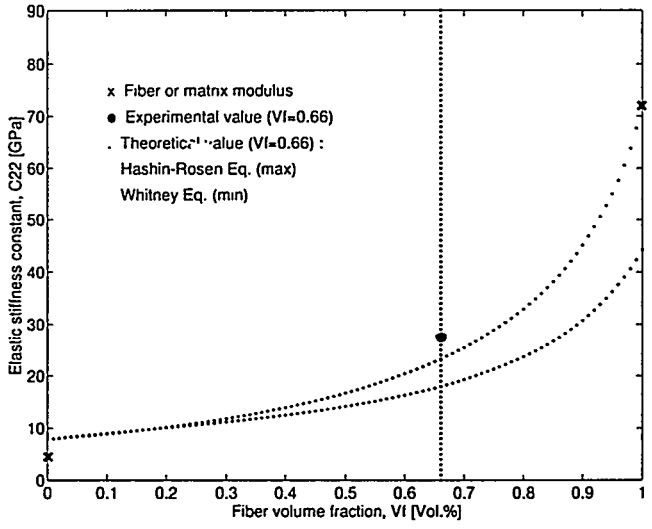

Figure 4.15. Elastic stiffness constant C_{22} versus fiber volume fraction.

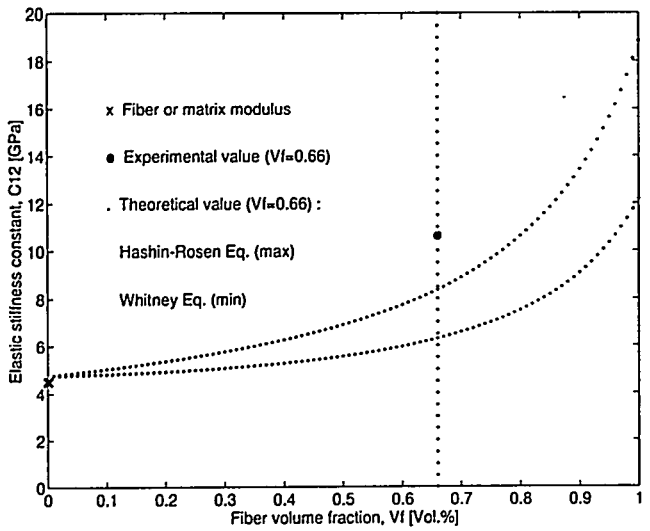

Figure 4.16. Elastic stiffness constant C_{12} versus fiber volume fraction.

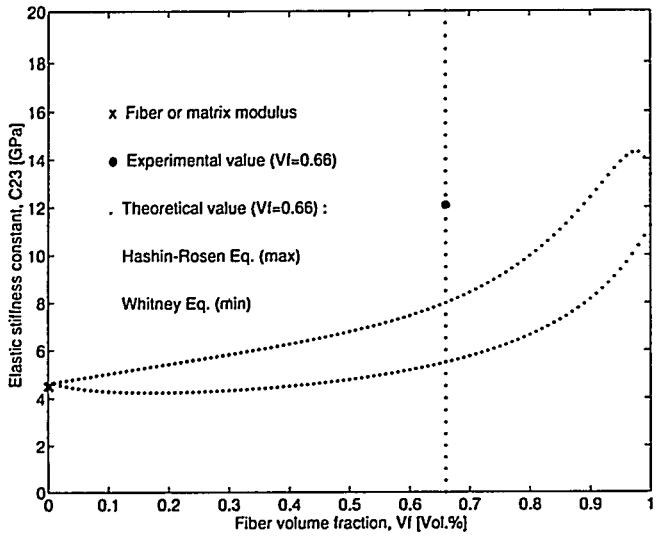

Figure 4.17. Elastic stiffness constant C_{23} versus fiber volume fraction.

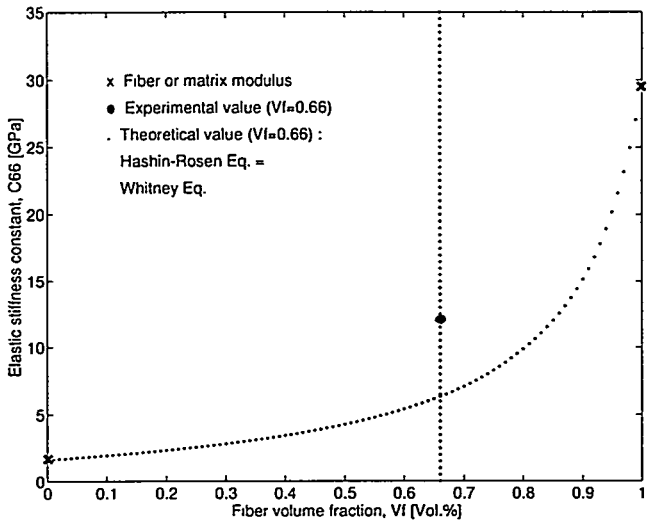

Figure 4.18. Elastic stiffness constant C_{66} versus fiber volume fraction.

The elastic stiffness constants are summarized in Table 4.5.

Table 4.5. Elastic stiffness constants for a 66 Vol. % glass/PET laminate.*

	Experimental**	Whitney	Hashin-Rosen
C_{11} [GPa]	59.3	52.45	53.54
$C_{33}=C_{22}$ [GPa]	27.6	18.00	23.24
$C_{55}=C_{66}$ [GPa]	9.4	6.34	6.34
C_{23} [GPa]	12.1	5.48	8.00
$C_{13}=C_{12}$ [GPa]	10.6	6.29	8.40

* Transverse isotropic laminate with circular, linear elastic, isotropic

** TOFTEGAARD (1997).

It is seen, that the best set of equations to predict the elastic stiffness constants for the glass/PET laminate is found by Hashin-Rosen. The deviation is less than 10 % for C_{11} and up to 34 % for C_{23}.
Notice, also that the reduced stiffness constants was [GPa]: $Q_{11} = 50.5$, $Q_{22} = 20.5$, $Q_{12} = 5.5$ and $Q_{66} = 22.5$, according to Eqs. (4.16-4.20) and the Hashin-Rosen engineering constants in Table 4.4. Thus, the reduced stiffness constants are sufficient smaller than the values in Table 4.5.

The next chapter presents an ultrasonic method to identify the elastic stiffness constants by the circular aperture.

4.6 Summary and conclusions

Section 4.1 gave a short introduction to fiber reinforced composites. A classification scheme was presented (Fig. 4.1) in which the composites were divided according to layers, fiber length and fiber orientation.

Section 4.2 discussed parameters that could influence the elastic properties of fiber reinforced composites. Such as: fiber orientation (Fig. 4.2), fiber volume fraction, composite homogeneity and elastic properties of the constituents. ESEM pictures were presented of a glass/PET laminate (Figs. 4.3-4.4) and the size of inhomogeneities in a hexagonal array was estimated (Fig. 4.5). Typical fiber and matrix properties were presented (Tables 4.1-4.2).

Section 4.3 reviewed the number of elastic stiffness constants for orthotropic and transverse isotropic fiber reinforced composites. Relations between elastic stiffness and engineering constants were discussed for an orthotropic and transverse isotropic (Fig. 4.6) laminate.

Section 4.4 combined elastic engineering constants to the fiber volume fraction. Six sets of equations predicting the engineering elastic constants were given.

Section 4.5 compared the equations for a unidirectional glass/PET laminate with experimental data (Table 4.3). Young's moduli, shear moduli and Poisson's ratio's were presented as a function of fiber volume fraction (Figs. 4.7-4.13). The experimental values were predicted (Table 4.4) by the: Whitney equation (the longitudinal Young's modulus was 9% below), Halpin-Tsai equation (the transverse Young's modulus was 6% above), Tsai-Hahn equation (the shear modulus was 8% below), Whitney equation (the shear modulus was 7% above), Hashin-Rosen equation (the Poisson's ratio was 3% above), Halpin-Tsai equation (the Poisson's ratio was 12% below) and Hashin-Rosen equation (the Poisson's ratio was 1% below). Hence, all elastic engineering constants (except ν_{23}) were within 10 % of the experimental obtained data.
The elastic stiffness constants versus fiber volume fraction were presented (Figs. 4.14-4.17) for the Hashin-Rosen and the Whitney equations. The elastic stiffness constants were compared (Table 4.5) with experimental values. The Hashin-Rosen equations were found to be closest to the experimental values.

In conclusion, this chapter has discussed relations between the elastic stiffness constants of a fiber reinforced composite and the elastic engineering constants of its constituents (fiber and matrix).
The elastic moduli for a glass/PET laminate were compared with six different sets of equations. It is not obvious which set of equation that apply best to the elastic stiffness constants of the laminate. No sets of equations were unique to identify all elastic constants.
It should be inquired further whether the present sets of equations include sufficient information for unique determination of the elastic properties for other types of unidirectional composites (e.g., carbon fibers with a thermoplastic matrix).

4.7 References to chapter 4

AGARWAL, B.D. and BROUTMAN, L. J. (1981). Analysis and performance of fibercomposites. J.Wiley and Son.

ASTM D 3171-76. Standard test method for fiber content of resin-matrix composites by matrix digestion.

CHAMIS, C.C. (1984). Simplified composite micromechanics equations hygral, thermal and mechanical properties. Sample Querterly, Vol. 14, 14-19.

FREDERIKSEN, P. S. (1997). Numerical studies for the identification of orthotropic elastic constants of thick plates. Eur. Jour. Mech. A/Solids, Vol. 16, No. 1, 117-140.

GRESZCZUK, L.B. (1971). Interfiber stresses in filamentary composites. Journal of American Institute of Aeronautics - AIAAJ, Vol. 9, 1274-1280.

HALPIN, J. C, and KARDOS, J. L. (1976). The Halpin-Tsai equations: A review. Polymer Eng. Sci, Vol. 16, 344-351.

HASHIN, Z. and ROSEN, B. W. (1964). The elastic moduli of fiber-reinforced materials. Journal of Applied Mechanics,Vol. 31, 223-232.

HULL, D. (1981). An introduction to composite materials. Cambridge University Press.

KEDWARD, K.T. (1996). Lecture notes to "Design of composite structures", USCB.

LANDAU, L. D. and LIFSHITZ, E. M. (1985). Theory of elasticity. Vol. 7 of Course of Theoretical Physics, Pergamon Press.

MALLICK, P. K. (1993). Fiber-reinforced composites: materials, manufacturing, and design. Marcel-Dekker.

TIMOSHENKO, S. P. and GOODIER, J. N. (1982). Theory of elasticity. 3 Ed. McGraw-Hill Book Company.

TOFTEGAARD, H. (1997). Elastic constants from simple compression tests. Proc. of Risø Int. Symp. on Mat. Science, ed. S.I. Andersen *et al.*, 497-502.

TSAI, S.W. and HAHN, H.T. (1980). Introduction to composite materials. Technomic Pub. Co., Lancaster, USA.

WHITNEY, J. M and RILEY, M. B. (1966). Elastic properties of fiber reinforced composite materials. Journal of American Institute of Aeronautics - AIAAJ, Vol. 4, 1537-1542.

WHITNEY, J. M. (1987). Structural analysis of laminated anisotropic plates. Tech. Publishing Company Inc. USA.

ZIMMER, J. E. and COST, J. R. (1970). Determination of the elastic constants of a unidirectional fiber composite using ultrasonic velocity measurements. Journal of the Acoustic Society of America, Vol. 47, No. 3, Part 2, 795-803.

5 Ultrasonic Determination of Elastic Constants

This chapter describes an ultrasonic method to determine the elastic stiffness constants of fiber reinforced composites. The aim is to identify the stiffness constants for the unidirectional glass/PET laminate and compare them with the micromechanical predictions discussed in chapter 4. The main component in the method is the circular aperture array introduced in chapter 3.
Section 5.1 gives an introduction to qualitative and quantitative ultrasonic evaluation of anisotropic materials.
Section 5.2 discusses the theory of wave propagation in anisotropic materials with emphasis on fiber reinforced composites. Energy flux propagation and attenuation of ultrasonic waves are considered and velocity surfaces are calculated for different planes of interest.
Section 5.3 discusses some experimental methods that previously have been used to determine elastic stiffness constants. The circular aperture array is then used to determine the elastic constants of the unidirectional glass/PET laminate.
Section 5.4 discusses the obtained results and compares them with an empirical model for transverse isotropic materials. The capabilities and limitations of the applied ultrasonic method are also discussed. Section 5.5 ends this chapter with a summary of results.

5.1 Quantitative ultrasonic evaluation

Ultrasound is often used as a nondestructive evaluation (NDE) tool to classify discontinuities (defects) in fiber reinforced composites. The defects may be classified *qualitatively* according to size, type and location using a suitable ultrasonic image technique (B-, or C-scanning). The mentioned technique can be based on transmitted or reflected pulses from the composite, corresponding to an image information of attenuation or reflectivity, respectively. All of these images may be processed by using the peak amplitude or the time-of-flight of the ultrasonic pulse. The applications of some ultrasonic imaging techniques for qualitatively NDE of fiber reinforced composites have been reviewed by, e.g., RHEINLÄNDER *et al.* (1997). However, ultrasound may also be used, *quantitatively*, as a tool to evaluate elastic stiffness constants of the composite. The ultrasonic time-of-flight and corresponding phase velocity is directly related to the elastic constants of the composite. The number of independent elastic constants is related to the degree of anisotropy, as discussed in chapter 4. An orthotropic fiber composite has nine independent elastic constants. Of these nine constants are only five independent for a transverse isotropic composite: C_{11}, $C_{22} = C_{33}$, $C_{44}=(C_{22}-C_{23})/2$, $C_{55} = C_{66}$, $C_{12} = C_{13}$, C_{23} (the subscript *1* refers to the fiber direction). An example of the latter is a unidirectional fiber reinforced laminate.
The aim of the present chapter is to investigate an experimental method that can be used to evaluate all elastic constants of thick composite specimens (i.e., 20-40 mm) with high attenuation. The determination of all elastic constants is important for two reasons: It serves as a NDE tool after manufacturing of the composite and generates data for the design of composite structures.

5.2 Wave propagation in anisotropic materials

It is well known that ultrasonic waves change their mode of propagation when they hit the surface of a medium at an oblique angle. Mode conversion results from a change in phase velocity and obeys Snell's refraction law. (See, e.g., KRAUTKRÄMER *et al.* 1990). However, Snell's law in its simple form is only valid for isotropic materials, where two pure modes of wave propagation are possible. One mode is a longitudinal wave mode (or a pressure wave mode), where the particle displacement is along the direction of propagation. The second mode is a transverse wave mode (or shear wave mode), where the particle displacement is perpendicular to the direction of propagation. The sound velocity of these two pure wave modes are determined by the density of the material, the modulus of elasticity and the Poisson ratio only, as shown in Appendix 5.1. This contrasts with anisotropic materials, like a unidirectional laminate, where different wave modes may occur. Although the direction of particle displacement for these wave modes is mutually perpendicular, they are in general neither parallel nor perpendicular to the normal direction of the wavefront, as seen in Fig. 5.1. These wave modes are termed quasi-modes (MUSGRAVE, 1954). Thus, in anisotropic materials any given wavefront is associated with three quasi-modes: a quasi-longitudinal wave mode and two quasi-transverse wave modes. Each of these wave modes is propagating with a characteristic phase velocity.

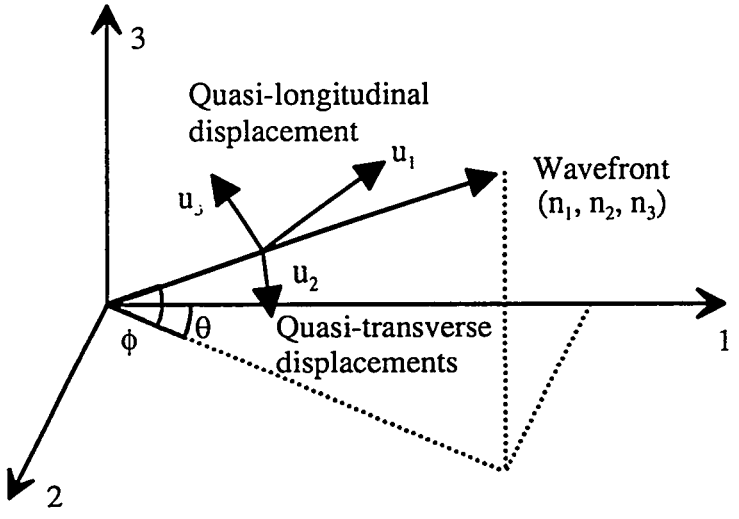

Figure 5.1. Coordinate system defining quasi-transverse and quasi-longitudinal wave modes.

5.2.1 Elastic constants of anisotropic materials

To obtain an expression for the phase velocity in terms of the elastic constants one has to solve the Christoffel equation for either of the three quasi-modes. The Christoffel equation may be obtained by substituting the *generalized Hook's law* (see chapter 4)

$$\sigma_{ij} = C_{ijkl}\varepsilon_{kl} \qquad (i, j, k, l = 1, 2, 3) \qquad (5.1)$$

where $$\varepsilon_{kl} = \frac{1}{2}\left(\frac{\partial u_k}{\partial x_l} + \frac{\partial u_l}{\partial x_k} + \frac{\partial u_l}{\partial x_k}\frac{\partial u_k}{\partial x_l}\right) \approx \frac{1}{2}\left(\frac{\partial u_k}{\partial x_l} + \frac{\partial u_l}{\partial x_k}\right) \qquad (5.2)$$

into the equation of motion (neglecting strains of higher order due to small displacements), to give

$$\rho\frac{\partial^2 u_i}{\partial t^2} = C_{ijkl}\frac{\partial^2 u_i}{\partial x_j \partial x_k} \qquad (i, j, k, l = 1, 2, 3) \qquad (5.3)$$

where ρ is the density of the material, u_i the displacement vector and C_{ijkl} the stiffness tensor.
Now, consider a plane harmonic (monochromatic) elastic wave

$$u_i = (u_1, u_2, u_3)\exp\left\{-i\tfrac{2\pi}{\lambda}(n_1x_1 + n_2x_2 + n_3x_3 - v_pt)\right\} \qquad (5.4)$$

where (u_1, u_2, u_3) represent the amplitudes of the particle displacements in the direction of the coordinate axes. λ is the wavelength, n_j are the direction cosines of the wave vector measured from the principal material axis (1, 2, 3) and v_p is the phase velocity along n_j (x_i and t are the independent position and time variables, respectively).
Substituting equation (5.4) into the equation of motion (5.3) gives

$$\begin{aligned}
(\Gamma_{11} - \rho v_p^{\,2})u_1 + \Gamma_{12}u_2 + \Gamma_{13}u_3 &= 0 \\
\Gamma_{12}u_1 + (\Gamma_{22} - \rho v_p^{\,2})u_2 + \Gamma_{23}u_3 &= 0 \\
\Gamma_{13}u_1 + \Gamma_{23}u_2 + (\Gamma_{33} - \rho v_p^{\,2})u_3 &= 0
\end{aligned} \qquad (5.5)$$

where $\Gamma_{ik} = C_{ijkl}n_jn_l$ is the Christoffel's stiffness matrix (see Appendix 5.2). The equations (5.5) have non-zero solutions only if the determinant of the coefficients (u_1, u_2, u_3) is zero, that is

$$\begin{vmatrix}
\Gamma_{11} - \rho v_p^{\,2} & \Gamma_{12} & \Gamma_{13} \\
\Gamma_{12} & \Gamma_{22} - \rho v_p^{\,2} & \Gamma_{23} \\
\Gamma_{13} & \Gamma_{23} & \Gamma_{33} - \rho v_p^{\,2}
\end{vmatrix} = 0 \qquad (5.6)$$

The solution to equation (5.6) is

$$\begin{aligned}&\left(\Gamma_{11}-\rho v_p^2\right)\left(\Gamma_{22}-\rho v_p^2\right)\left(\Gamma_{33}-\rho v_p^2\right)+2\Gamma_{12}\Gamma_{23}\Gamma_{13}\\&-\Gamma_{13}{}^2\left(\Gamma_{22}-\rho v_p^2\right)-\Gamma_{23}{}^2\left(\Gamma_{11}-\rho v_p^2\right)-\Gamma_{12}^2\left(\Gamma_{33}-\rho v_p^2\right)=0\end{aligned} \tag{5.7}$$

where the Christoffel stiffnesses are given for an orthotropic material by

$$\begin{aligned}\Gamma_{11}&=C_{11}n_1^2+C_{66}n_2^2+C_{55}n_3^2\\\Gamma_{23}&=(C_{23}+C_{44})n_2n_3\\\Gamma_{22}&=C_{66}n_1^2+C_{22}n_2^2+C_{44}n_3^2\\\Gamma_{13}&=(C_{13}+C_{55})n_1n_3\\\Gamma_{33}&=C_{55}n_1^2+C_{44}n_2^2+C_{33}n_3^2\\\Gamma_{12}&=(C_{12}+C_{66})n_1n_2\end{aligned} \tag{5.8}$$

Here is $n_1=\cos\theta\cos\phi$, $n_2=\sin\theta\cos\phi$ and $n_3=\sin\phi$, as defined in Fig. 5.1.

Equation (5.5) is an eigenvalue problem with three different eigenvalues determined by the characteristic equation (5.7), and corresponding eigenvectors, u_i, for each phase velocity.

The Chistoffel's stiffness matrix is symmetric ($\Gamma_{ik}=\Gamma_{ki}$) and positive definite ($\Gamma_{ik}u_iu_k\geq 0$), which means that all eigenvalues of Eq. (5.5) are real and positive and their corresponding eigenvectors are orthogonal. Therefore, for a given direction of propagation defined by the wave vector (i.e., n_j), there will be three waves with mutually perpendicular displacement vectors with different phase velocities. Hence, these waves will as mentioned, not be longitudinal or transverse, but have quasi-longitudinal or quasi-transverse forms in which the displacement vector is neither in the direction of, nor perpendicular to, the direction of propagation, as shown in Fig. 5.1.

However, for certain special directions of propagation, which are usually directions of symmetry, one wave is pure longitudinal and the other two are pure transverse.

Now consider two examples applying these special directions. The relevant equations are derived from Eq. (5.5) to (5.8) by setting n_1=0, n_2=0 or n_3=0, respectively.

Consider first, a plane wave traveling in the 1-axis direction in the (1-3)-plane. In this direction ($\theta=0$, $\phi=0$) and by setting ($n_1=1$, $n_2=n_3=0$) equation (5.6) becomes

$$\begin{vmatrix}C_{11}-\rho v_p{}^2 & 0 & 0\\0 & C_{66}-\rho v_p{}^2 & 0\\0 & 0 & C_{55}-\rho v_p{}^2\end{vmatrix}=0 \tag{5.9}$$

or

$$\left(C_{11}-\rho v_p^2\right)\left(C_{66}-\rho v_p^2\right)\left(C_{55}-\rho v_p^2\right)=0 \tag{5.10}$$

The three roots of this equation are in general different, giving rise to three different phase velocities. By substituting each of these velocities into equation (5.5), it is seen that one is a pure longitudinal wave: $v_{p,l} = \sqrt{C_{11}/\rho}$ and two are pure transverse waves: $v_{p,t} = \sqrt{C_{66}/\rho}$ and $v_{p,t} = \sqrt{C_{55}/\rho}$ with displacement vectors in the plane and normal to the plane, respectively.
Consider next, a plane wave traveling along an axis 45° to the 1-axis and 3-axis. That is ($n_1 = n_3 = 1/\sqrt{2}$, $n_2 = 0$). In this case equation (5.6) gives

$$\begin{vmatrix} \frac{1}{2}(C_{11}+C_{55}) - \rho v_p^2 & 0 & \frac{1}{2}(C_{13}+C_{55}) \\ 0 & \frac{1}{2}(C_{66}+C_{44}) - \rho v_p^2 & 0 \\ \frac{1}{2}(C_{13}+C_{55}) & 0 & \frac{1}{2}(C_{55}+C_{33}) - \rho v_p^2 \end{vmatrix} = 0 \quad (5.11)$$

where one solution to the determinant (5.11) represents a pure transverse wave with phase velocity

$$v_{p,t} = \sqrt{(C_{66}+C_{44})/2\rho} \quad (5.12)$$

and the two remaining solutions are determined by quasi-longitudinal and quasi-transverse waves, respectively

$$\left(\tfrac{1}{2}(C_{11}+C_{55}) - \rho v_p^2\right)\left(\tfrac{1}{2}(C_{55}+C_{33}) - \rho v_p^2\right) - \left(\tfrac{1}{2}(C_{13}+C_{55})\right)^2 = 0 \quad (5.13)$$

Connections between the propagation plane, the wave direction and the phase velocity for the (2-3)-plane, the (1-3)-plane and the (1-2)-plane in orthotropic materials are given in Table 5.1. The subscript (t) and (l) refers to pure transverse and pure longitudinal waves, respectively.

Table 5.1. Propagation plane, wave direction and phase velocity in orthotropic materials for specific directions of propagation (e.g., directions of symmetry).

Propagation plane	Wave direction	Displacement vector and phase velocity		
		u_1	u_2	u_3
(2-3)	2	$v_{p,t} = \sqrt{C_{66}/\rho}$	$v_{p,l} = \sqrt{C_{22}/\rho}$	$v_{p,t} = \sqrt{C_{44}/\rho}$
(n_1=0)	3	$v_{p,t} = \sqrt{C_{55}/\rho}$	$v_{p,t} = \sqrt{C_{44}/\rho}$	$v_{p,l} = \sqrt{C_{33}/\rho}$
(1-3)	1	$v_{p,l} = \sqrt{C_{11}/\rho}$	$v_{p,t} = \sqrt{C_{66}/\rho}$	$v_{p,t} = \sqrt{C_{55}/\rho}$
(n_2=0)	3	$v_{p,t} = \sqrt{C_{55}/\rho}$	$v_{p,t} = \sqrt{C_{44}/\rho}$	$v_{p,l} = \sqrt{C_{33}/\rho}$
(1-2)	1	$v_{p,l} = \sqrt{C_{11}/\rho}$	$v_{p,t} = \sqrt{C_{66}/\rho}$	$v_{p,t} = \sqrt{C_{55}/\rho}$
(n_3=0)	2	$v_{p,t} = \sqrt{C_{66}/\rho}$	$v_{p,l} = \sqrt{C_{22}/\rho}$	$v_{p,t} = \sqrt{C_{44}/\rho}$
(2-3),(n_1=0)	45°	$v_{p,t} = \sqrt{(C_{66}+C_{55})/2\rho}$	(*)	
(1-3),(n_2=0)	45°	(5.13)	$v_{p,t} = \sqrt{(C_{66}+C_{44})/2\rho}$	(5.13)
(1-2),(n_3=0)	45°	(**)		$v_{p,t} = \sqrt{(C_{55}+C_{44})/2\rho}$

(*) $\left(\tfrac{1}{2}(C_{22}+C_{44}) - \rho v_p^2\right)\left(\tfrac{1}{2}(C_{44}+C_{33}) - \rho v_p^2\right) - \left(\tfrac{1}{2}(C_{23}+C_{44})\right)^2 = 0$

(**) $\left(\tfrac{1}{2}(C_{11}+C_{66}) - \rho v_p^2\right)\left(\tfrac{1}{2}(C_{66}+C_{22}) - \rho v_p^2\right) - \left(\tfrac{1}{2}(C_{12}+C_{66})\right)^2 = 0$

In order to describe transverse isotropic materials, only five independent elastic constants are used, e.g., C_{11}, $C_{22} = C_{33}$, $C_{55} = C_{66}$, $C_{44}=(C_{22}-C_{23})/2$, $C_{12} = C_{13}$, C_{23}. Hence, more simplified equations are obtained in Table 5.1 for these materials.

5.2.2 Energy flux propagation

In the derivation so far, the wave propagation in anisotropic materials is expressed in terms of a phase velocity vector (or the wave vector) for each wave mode. The phase velocity is defined as the speed with which a point of constant phase moves through a specimen (see, e.g., WANG 1996, BOLTZ *et al.* 1993 and CHIEN *et al.* 1993).
Another aspect of anisotropic materials is energy flux propagation. The energy flux vector (or the ray vector or group velocity vector) associated with each wave mode is, by definition, the rate at which energy is propagated across a specimen, per unit area (if the energy vector is normal to the direction of wave propagation). The corresponding velocity of the energy flux vector is the group velocity, v_g. The group velocity vector can be found as (AULD, 1990)

$$v_g = -\frac{\nabla_n \Omega}{\partial \Omega / \partial v_p} \tag{5.14}$$

where Ω is the expression in Eq. (5.7) and the gradient of Ω is taken with respect to n_j.
In isotropic, homogeneous materials, the phase and group velocity vector coincide. This might be the reason why the group velocity vector has been given very little attention in the literature. However, in (lossless) anisotropic materials the phase and group velocity vector are generally different both in magnitude and in direction. Thus, the group velocity vector deviates from the phase velocity vector by an angle ψ, as seen in Fig. 5.2. The Figure indicates also that a phase velocity vector always is lying in a plane of incidence, whereas the group velocity vector may deviate from this plane. In such cases the angle of deviation between the phase and group velocity has both in-plane, α, and out-of-plane, β, components, with respect to the phase velocity vector. The group velocity deviation angle is then measured with respect to the phase velocity vector and is related as (PEARSON 1985 and 1986)

$$v_g = v_p \cos\psi \tag{5.15}$$

where

$$\cos\psi = \cos\alpha \cos\beta \tag{5.16}$$

For a unidirectional composite material, with fibers lying in principal planes, both the group velocity vector and the phase velocity vector is lying in the same plane (i.e., $\beta = 0$) (STIJNMAN, 1995). Furthermore, in directions of high symmetry, such as the principal directions, the phase and group velocity vector coincide.
The deviation of the energy flux propagation from the wave propagation in anisotropic materials has many practical consequences that are never seen in isotropic materials; (1) to measure the ultrasonic velocity one measures the ultrasonic time-of-flight and determines the length of the ultrasonic path. The velocity determined in this way is the group velocity. Thus, the time-of-flight measured in a composite material corresponds to the group velocity, while the equations for calculations use the phase velocity (ROKHLIN *et al.*, 1989).

(2) if the angle of incidence is changed in a plane, the refracted beam may shift to a new plane. A consequence is that the receiver must be placed outside this plane of incidence in an optimum receiving position. This is difficult to do in a precise manner and, therefore, an error may be introduced into time-of-flight measurements. In worst case, if two transducers are not set up at the correct angles, the receiver will not detect a signal from the transmitter at all (although a very weak signal may often be detected, in practice, due to beam spread).
These consequences have to be taken into consideration when experimental studies are to be performed to characterize anisotropic materials. Thus, experimental studies may lead to misinterpretations of the results unless one is ready to take them into account.

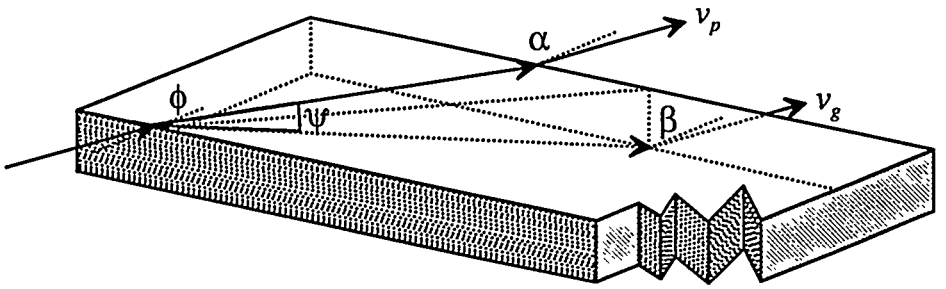

Figure 5.2. The angle of deviation, ψ, between phase and group velocity has, in general, both in-plane, α, and out-of-plane, β, components for an ultrasonic wave incident from fluid onto an anisotropic material.

The possible movement of the receiver is one of the advantages of a circular aperture array and the setup in chapter 3 was, therefore, used in the present experimental method. To measure the time-of-flight one scans with the circular array to find the position at which the ultrasonic signal is maximum. When the group velocity deviates from the incident scanning plane one scans, in addition, in a plane parallel to the incident plane. Thus, the refraction angle for the group velocity can be measured. To find the length of the acoustic path for the phase velocity one needs the phase velocity refraction angle. While the refraction angle of the phase velocity is directly related to the angle of incidence through Snell's law, they cannot be calculated immediately since the phase velocity in the material is unknown.
ROKHLIN *et al.* (1992) has shown, among others, that the phase path, l_p, can be found as

$$l_p = \frac{L\cos\psi}{\cos(\phi+\psi)} \tag{5.17}$$

where L is the thickness of the specimen, ψ is the deviation angle and ϕ the refraction angle of the phase velocity.

5.2.3 Calculation of velocity surfaces

In section 5.2.1 the Christoffel equation (5.5) was solved as an eigenvalue problem. The corresponding characteristic equation (5.7) had three eigenvalues which can be graphed as three unique velocity surfaces, i.e., three wave velocities as a function of propagation direction. Thus, three phase (or normal velocity) surfaces exist corresponding to the three roots of Eq. (5.7) in every plane of interest.

For example, in the (1-3)-plane (i.e., $\theta = 0$, $n_1 = \cos\phi$, $n_2 = 0$, $n_3 = \sin\phi$ in Eq. (5.8)) two phase velocity surfaces are found as

$$v_p = \left\{ \begin{array}{l} \frac{1}{2\rho}\left|C_{11}\cos^2\phi + C_{33}\sin^2\phi + C_{55}\right| \\ \pm\frac{1}{2\rho}\left\{ \begin{array}{l} \left(\left|C_{11}\cos^2\phi + C_{33}\sin^2\phi + C_{55}\right|\right)^2 - 4\left[C_{55}\left(C_{11}\cos^4\phi + C_{33}\sin^4\phi\right)\right. \\ \left. +\left(C_{11}C_{33} - 2C_{13}C_{55} - C_{13}^2\right)\sin^2\phi\cos^2\phi \;\right] \end{array} \right\}^{1/2} \end{array} \right\}^{1/2} \quad (5.18)$$

where (+) determines the quasi-longitudinal wave surface and (-) determines the quasi-transverse wave surface. The third root has the phase velocity

$$v_{p,t} = \left\{\left(C_{66}\cos^2\phi + C_{44}\sin^2\phi\right)/\rho\right\}^{1/2} \quad (5.19)$$

corresponding to a pure transverse wave surface.
The phase velocity surfaces for the (1-3)-plane and (2-3)-plane are calculated for a transverse isotropic composite with the elastic constants [GPa]:

$$C_{11} = 61.1, \quad C_{22} = C_{33} = 30.3, \quad C_{55} = C_{66} = 8.7,$$
$$C_{12} = C_{13} = 11.4, \quad C_{23} = 10.2, \quad C_{44} = 10.0$$

Fig. 5.3 shows a polar representation of the three different phase velocity surfaces in the (1-3)-plane. In the Figure, the axes 1 and 3 are directions of symmetry for the material, and the scale values are the phase velocity in meter per second. Thus, to determine the phase velocity for any given direction in the plane between the 1-axis and 3-axis direction, a radial line is drawn from the origin and parallel to the desired direction. The length of this line, between the origin and the points of intersection with the curves drawn in Fig. 5.3, determines the three phase velocities in that direction. A negative value of phase velocity implies that the waves are propagating in the negative direction. Intersections of these phase velocity surfaces with the isotropic (2-3)-plane yield three concentric circles with pure longitudinal or pure transverse waves, as shown in Fig. 5.4. Notice that, the two transverse velocities do not coincide as they would do in isotropic materials.
Two other velocity surfaces are graphed; the slowness (or inverse velocity) surfaces and the group velocity surfaces (or ray surface). The slowness surfaces, in Fig. 5.5 and Fig. 5.6, show the inverse of the phase velocity in the (1-3)-plane and the (2-3)-plane, respectively. A connection between the slowness surface and the group velocity vector is, as indicated in Fig. 5.5, that the group velocity vector is normal to the slowness surface (AULD, 1990).
Equation (5.14) is used to calculate the group velocity surfaces in the (1-3)-plane, shoving plots of the energy flux velocity versus the energy flow direction, for the quasi-longitudinal and the quasi-transverse wave, respectively. Fig. 5.7. shows the group velocity surface for a quasi-longitudinal wave in the (1-3)-plane. The phase velocity surface, Fig. 5.3, is superimposed in order to emphasize the difference.

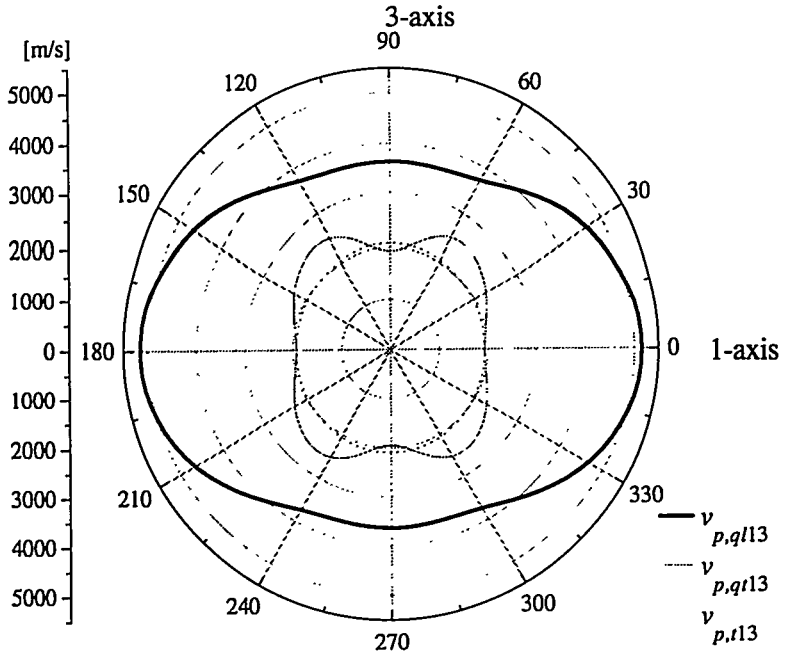

Figure 5.3. Phase velocity surface of the quasi-longitudinal ($v_{p,ql13}$), quasi-transverse ($v_{p,qt13}$) and transverse wave ($v_{p,t13}$) in the (1-3)-plane of a unidirectional (transverse-isotropic) composite [m/s].

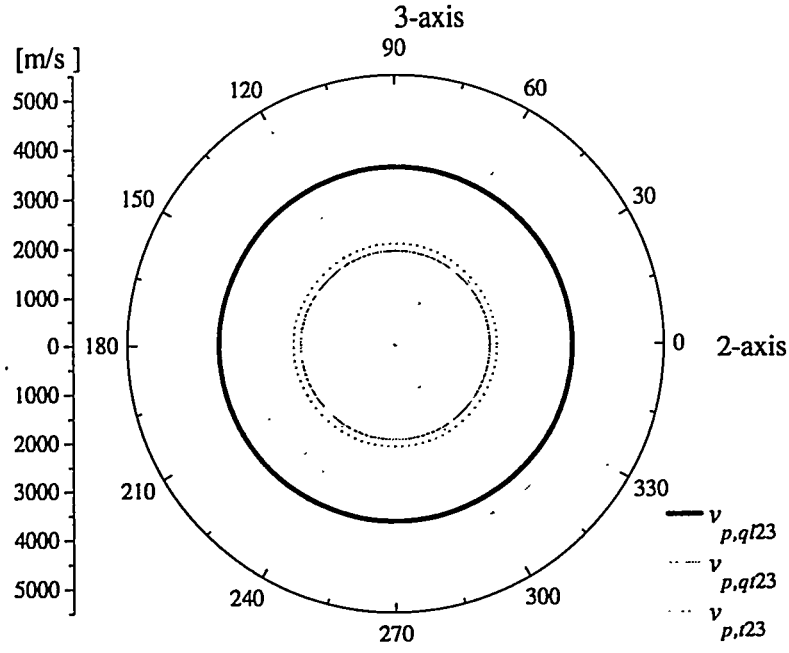

Figure 5.4. Phase velocity surface of the quasi-longitudinal ($v_{p,ql23}$), quasi-transverse ($v_{p,qt23}$) and transverse wave ($v_{p,t23}$) in the (2-3)-plane of a unidirectional (transverse-isotropic) composite [m/s].

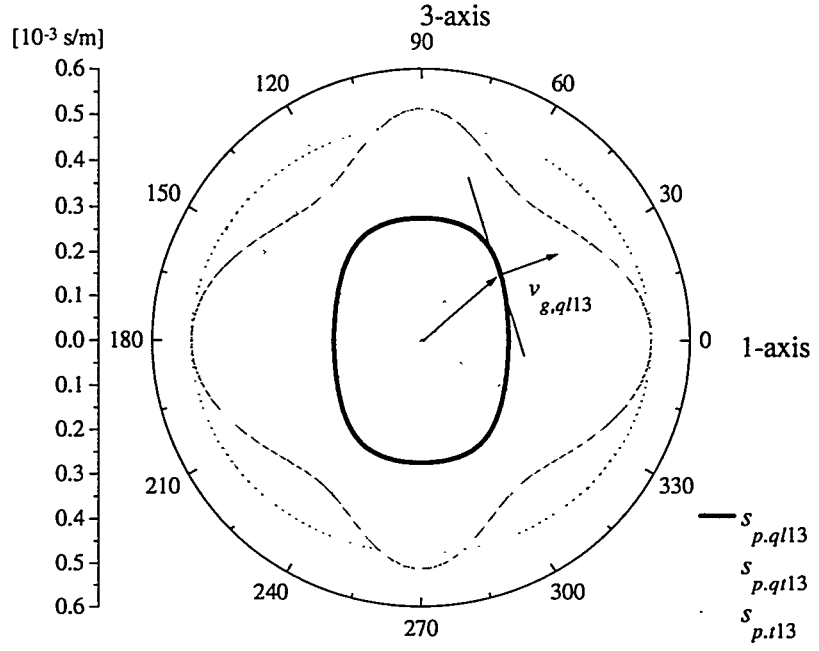

Figure 5.5. Slowness surface of the quasi-longitudinal ($s_{p,ql13}$), quasi-transverse ($s_{p,qt13}$) and transverse wave ($s_{p,t13}$) in the (1-3)-plane of a unidirectional (transverse-isotropic) composite. The group velocity vector is normal to the slowness surface [10^{-3} s/m].

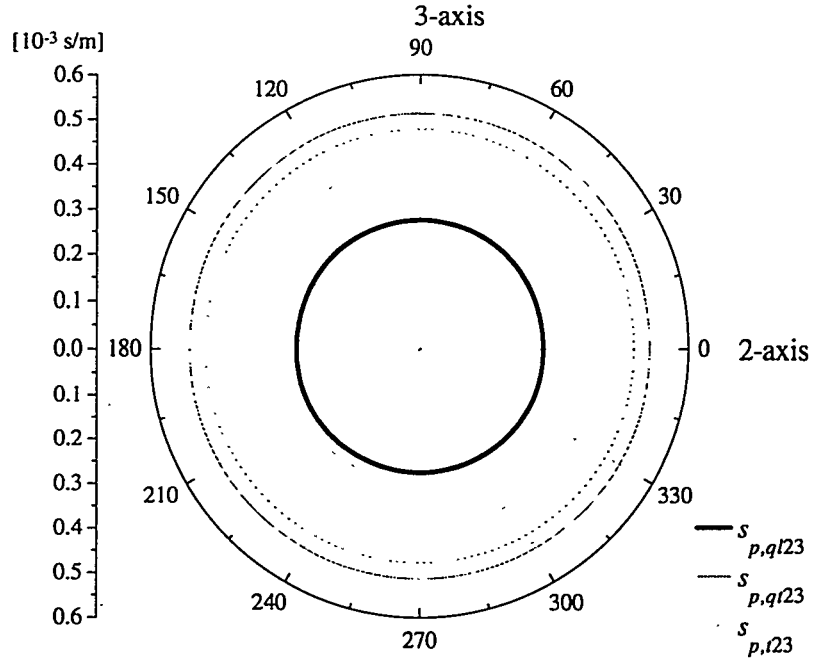

Figure 5.6. Slowness surface of the quasi-longitudinal ($s_{p,ql23}$), quasi-transverse ($s_{p,qt23}$) and transverse wave ($s_{p,t23}$) in the (2-3)-plane of a unidirectional (transverse-isotropic) composite [10^{-3} s/m].

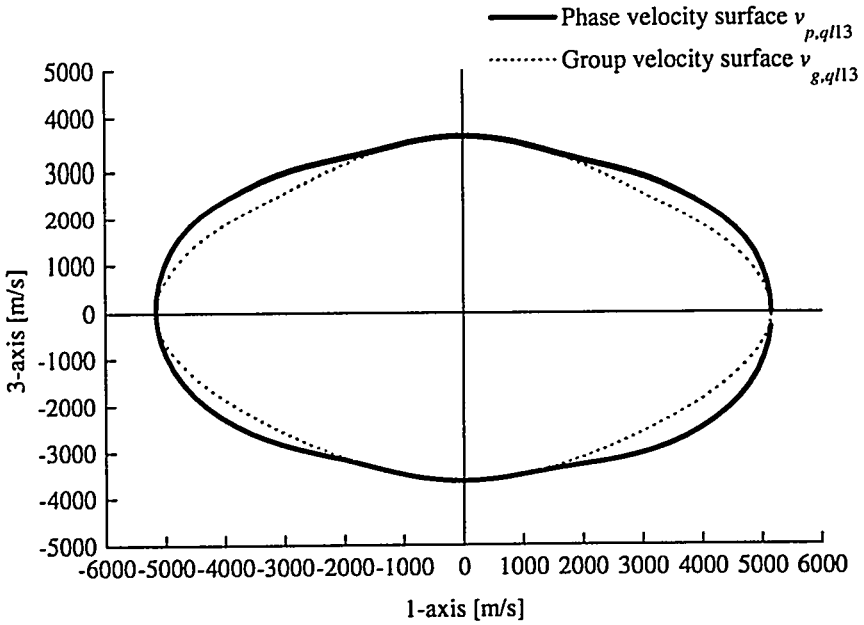

Figure 5.7. Phase velocity surface ($v_{p,qI13}$), and group velocity surface ($v_{g,qI13}$) of quasi-longitudinal wave in the (1-3)-plane [m/s].

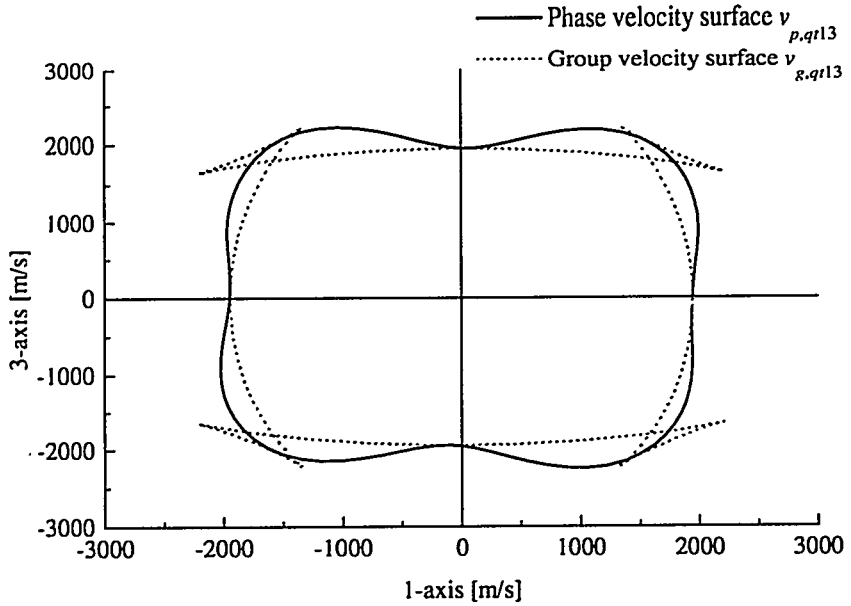

Figure 5.8. Phase velocity surface ($v_{p,qt13}$), and group velocity surface ($v_{g,qt13}$) of quasi-transverse wave in the (1-3)-plane [m/s].

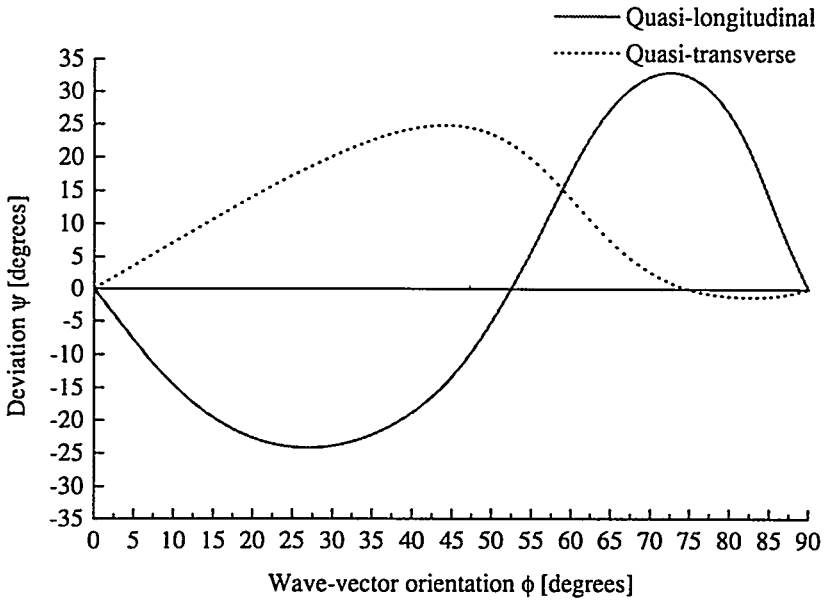

Figure 5.9. Deviation angle, ψ, versus wave-vector orientation, ϕ, for a quasi-longitudinal and quasi-transverse wave in the (1-3)-plane of a unidirectional (transverse-isotropic) composite [degrees].

Fig. 5.8 shows the group velocity surface for the quasi-transverse wave in the (1-3)-plane and the corresponding phase velocity is added. The cusps (AULD, 1990) observed on the group-velocity surface in Fig. 5.8 results from the three group velocity vectors that correspond to energy along a specific direction (two of these have the same energy velocity).
Fig. 5.9 shows the deviation angle, as a function of wave-vector orientation. It is seen that the deviation angle may be as large as 33.4° (for ϕ=72°) for this material. However, for some anisotropic materials it may be up to 40°. See KRIZ *et al.* (1979, 1981, 1985), LEDBETTER *et al.* (1982), PAPADAKIS *et al.* (1991) and MUSGRAVE (1970). This means in practice must the receiver be placed at the optimum position to receive the ultrasonic wave energy.

5.2.4 Complex elastic constants

In section 5.2.1, it was seen how the phase velocity can be used to calculate the elastic constants of an orthotropic composite. Section 5.2.2 showed how the energy flux propagation influences the calculation by a deviation angle. In this subsection ultrasonic wave propagation in viscoelastic (lossy) composites is considered. Such composites exhibit significant anisotropic attenuation (HOSTEN, 1987) to the applied ultrasonic wave, although, interpretation of attenuation results is beyond the scope of this thesis. To simplify the present theory it is assumed that ultrasonic wave attenuation is caused only by the damping properties of the polymeric matrix (BALASUBRAMANIAM *et al.*, 1995; ROUX, 1990). Thus attenuation mechanisms like: absorption in water (KINSLER *et al.*, 1982), multiple scattering from fibers (UEDA *et al.*, 1990), interface reflection and transmission (HOSTEN, 1991) are not considered.

For a viscoelastic homogeneous material, the elastic constants in Hook's law Eq. (5.1) may be expressed as complex functions of frequency

$$C_{ij}^{*} = C_{ij}' + iC_{ij}'' \tag{5.20}$$

where the imaginary component, C''_{ij}, provides a model for wave attenuation, and the frequency dependency implies that the different harmonic components of the pulse travel with different velocities and are attenuated by different amounts. Thus, a pulse traveling in a viscoelastic material is attenuated and distorted, and a detailed analysis of the transmitted pulse would be required to determine the velocities and attenuation's of individual components (HOSTEN *et al.*, 1987, 1992).

To obtain an expression for the complex elastic constants, as a function of the attenuation coefficient, one may first express the phase velocity for each of the three wave modes as

$$v_p^{*} = v_p' + iv_p'' \tag{5.21}$$

where v_p' and v_p'' is the real and imaginary components, respectively. Second, in order to simplify the expression one can introduce the slowness components as

$$s_p^{*} = s_p' + is_p'' = 1/v_p^{*} \tag{5.22}$$

and combine the corresponding plane wave, Eq. (5.4), rewritten as

$$u_i = (u_1, u_2, u_3)\exp\left\{-i\omega\left[s_p^{*} n_j x_j - t\right]\right\}$$

to

$$u_i = (u_1, u_2, u_3)\exp(\omega s_p'' x_j)\exp\left\{-i\omega\left[(s_p' n_j x_j - t)\right]\right\} \tag{5.23}$$

in which ω is the angular frequency.

The attenuation coefficient, α, and the phase velocity are found from Eq. (5.23) to be: $\alpha = -\omega s_p''$ and $v_p = 1/s_p'$, respectively. Finally, using Eq. (5.22) the complex elastic constants can be expressed as

$$C_{ij}^{*} = \rho(v_p^{*})^2 = \frac{\rho\omega^2 v_p^2(\omega^2 - \alpha^2 v_p^2)}{(\omega^2 + v_p^2\alpha^2)^2} + i\frac{2\rho\omega^3\alpha v_p^3}{(\omega^2 + v_p^2\alpha^2)^2} \tag{5.24}$$

Thus, if the pulse amplitude and phase velocity are measured for various angles of incidence, C_{ij}^{*}, may be fitted to the elastic constants in Eq. (5.7) for each plane of interest, as will be seen in the experimental procedure (see subsection 5.4.3).

Notice; if the attenuation coefficient is small (i.e. $\alpha \to 0$), $C_{ij}^{*} = C_{ij}' = \rho v_p^2$.

5.3 Experimental evaluation of elastic constants

This section reviews ultrasonic methods to determine the elastic constants in composite materials. A description of an experimental setup and a scanning procedure using a circular aperture array is given.

During the past 20 years, only a few researchers have contributed to the experimental determination of elastic constants in composite materials using ultrasound. Most of these researchers have based their experimental work on MUSGRAVE (1954), who was among the first to establish a theory for elastic waves in anisotropic materials. The experimental methods fall into one of two groups: contact or immersion methods. Each group can be subdivided into reflection and transmission methods.

5.3.1 Contact or immersion methods

Contact methods involve experimental methods where two transducers are attached, by direct contact in air, to opposite sides of a composite specimen using a coupling medium. The coupling medium (usually oil or gel) is needed to assure transmission of ultrasound between transducer and the composite specimen.

ZIMMER *et al.* (1970) were among the first to apply this method to determine the elastic constants of transverse isotropic composites. In their work, the elastic constants were determined in (8 mm thick) glass-epoxy samples, cut in different directions relative to the fiber direction. Quartz transducers, polarized for transverse and longitudinal waves, were used to generate pulses with a center frequency of 5 MHz. The constants C_{11}, C_{22}, C_{44} and C_{66} were determined by calculating phase velocities of the pulses in preferred directions. Determination of C_{12} was achieved from samples with faces at an intermediate angle relative to the preferred direction. They found that attenuation and dispersion were limiting factors in this method. KRIZ *et al.* (1979) and SMITH (1972) have used similar methods.

Although, the contact method gave reasonable results, it suffers from the need to attach transducers to the specimen. Furthermore, different transducers, polarized for transverse or longitudinal waves, have to be used from each side of the specimen. In addition, the method is destructive; i.e. the specimen is cut in various angels relative to the fiber direction.

To overcome some of these problems immersion methods may be used. The immersion method involves immersing the composite specimen in a liquid (usually water), where the liquid functions as a coupling medium (HARTMANN, 1974; ROSE *et al.* 1973 and SELFRIDGE 1985).

MARKHAM (1970) suggested a method where a specimen, with known thickness, was mounted on a turntable inside a water tank and two transducers were placed on either side of the specimen. By rotating the turntable, the angle of incidence could be set to any desired value. At normal incidence, the wave entering the specimen was assumed to travel as a longitudinal wave. Then by measuring the difference in arrival time with and without the specimen, the velocity at normal incidence was calculated. By rotating the turntable and thus increasing the angle of incidence, the pulse on entering the composite was split by mode conversion into two components, one being quasi-longitudinal and the other quasi-transverse. After leaving the composite, the pulses were each arriving at the receiver and were identified by a separation in time on an oscilloscope. Finally, by measuring the difference in time for the waves to travel from the transmitter to the receiver, with and without the composite sample and also measuring the angle of incidence, the phase velocity could be calculated.

However, because of liquid viscosity and the mismatch between composite and liquid properties, the incident wave is essentially longitudinal and, if specimen faces are parallel and normal to the preferred direction, it is not possible to excite transverse waves in the specimen.
Markham achieved this by passing the incident wave at an oblique angle through a prism bonded to the specimen. This method again suffered from experimental problems associated with the bond. Thus, there is a need for research in experimental immersion methods.

5.3.2 Reflection or transmission methods

The contact and immersion method was explained in combination with transmission methods. That is, two transducers were placed on either side of the specimen under investigation; one for transmission and the other for receiving of ultrasonic pulses (DEAN *et al.* 1973; ROKHLIN *et al.* 1992; STIJNMAN 1995). Contact and immersion methods may also be combined with reflection methods, where one transducer both functions as transmitter and receiver. The advantage of reflection methods is, in general, that they only require access to one side of the specimen.
HANDLY *et al.* (1990) have used a reflection method in combination with contact transducers, polarized for longitudinal and transverse waves. Four elastic constants were determined by insonifying ultrasonic waves perpendicular and parallel to the fiber direction of a unidirectional composite. These measurements corresponded to pure mode measurements. In order to determine the last elastic constant three different specimens were fabricated with a specific fiber direction. BALASUBRAMANIAM *et al.* (1995) used a similar method: two 5 MHz transducers were mounted on a 30 degree aluminum wedge, to form a single angle beam transducer. Oil was used as a coupling between wedge and specimen. Recently, ROKHLIN *et al.* (1989*b*), MAL *et al.* (1993) and ANTICH *et al.* (1997) used a reflection method in combination with the immersion method, to determine the elastic constants in thin (1-5 mm) specimens. They found that specimens have to be thin, due to attenuation, in order to receive the signal which has traveled a double distance.
In this chapter, a transmission-immersion method was used in order to examine thick specimens with high attenuation. Consequently, using this method, the signal-to-noise ratio was higher compared with the reflection method due to the fact that the signal need not pass the specimen twice.

5.3.3 Setup for the circular aperture array

The elastic constants of a unidirectional laminate were determined from ultrasonic phase velocities measured using a circular aperture array of transducer elements (this arrangement was also used to image isotropic polymers by NIELSEN *et al.* (1997). Two mobile ultrasonic transducers, one acting as a transmitter and the other as a receiver, were used in preference to a circular array of fixed transducer elements. Both the transmitter (T) and receiver (R) could rotate around the specimen at a well-defined distance, as seen in Fig. 5.10a. The rotation fixture was positioned in a temperature controlled water tank. By using two transducers only, it was possible to vary:
(1) the transducer configuration (center frequency, focal point etc.). This is important because attenuation in the composite is frequency dependent and the focusing parameters determines the effective area of the composite to be examined. In this experiment two available Panametric transducers were used with center-frequency 2.5 MHz (transmitter) and 5 MHz (receiver), respectively. Both transducers had a 10 mm aperture diameter. (2) The distance between

transducer and specimen could be changed within the water tank dimensions. This is important when relative large specimens are examined. In conclusion, the setup may be used to examine relative large and thick specimens, which have high attenuation. For example, specimens with high porosity.

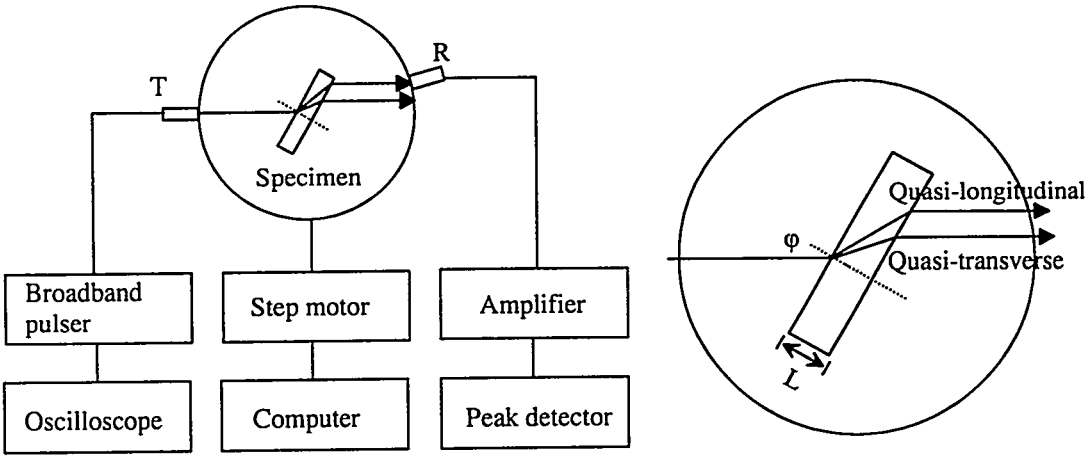

Figure 5.10. (a) Circular aperture array of transducers; transmitter T, and receiver R. (b) Detailed draft defining specimen thickness and angle of incidence.

5.3.4 Specimen and experimental procedure

A 32 mm thick glass/PET laminate was used as test specimen (see chapter 4). This laminate was made from unidirectional (UD) weave E-glass with 98.5 % weight fraction of the fibers in the 1(0°)-direction. The matrix was poly ethylene tetraphtalate (PET), in the form of film. The laminate was consolidated in an autoclave and cut into two planes relative to the fiber alignment (1 direction): A (1-3)-plane and a (2-3)-plane. The fiber volume fraction and density was measured to 66 Vol. % and 2298 kg/m^3, respectively.
The experimental procedure was the following: First, the specimen was positioned perpendicular to the transmitter and receiver. A broadband pulse was emitted from the transmitter and recorded by the receiver. The received pulse was amplified and a peak detector determined the maximal negative peak within a defined gate, as shown in Fig. 5.11 (the negative peak was found to be more stable than the positive peak). The receiver was then rotated by a step motor with 1° step resolution, and the time-of-flight was recorded as a function of the refracted angle. This procedure was followed in order to imitate a circular aperture array of receivers. The time-of-flight corresponding to the first peak in a time gate was finally stored. Second, the specimen was rotated using a second step motor in order to change the incident angle and the first procedure repeated.

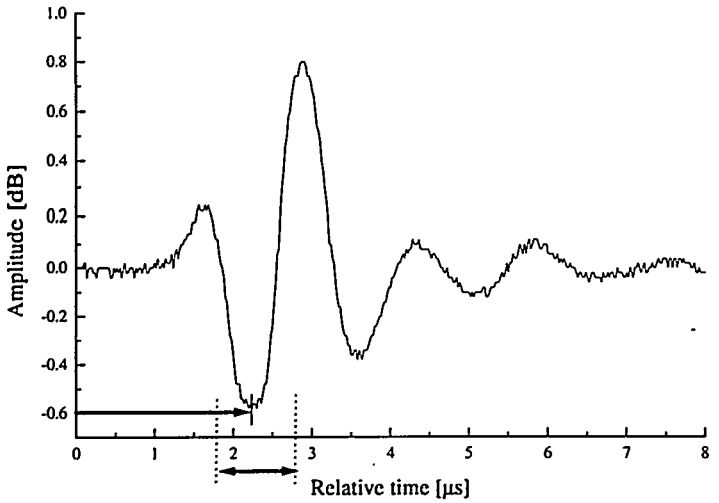

Figure 5.11. A typical received signal as a function of time. The time delay to the maximum negative peak value within a gate was measured.

Thirdly, from these time-of-flight measurements quasi-longitudinal and quasi-transverse phase velocities, v_p, were calculated for different angles of incidence, φ, using (ROKHLIN *et al.* 1992)

$$v_p = \left\{ \frac{1}{v_o^2} - \frac{2\Delta t \cos\varphi}{L\, v_o} + \left(\frac{\Delta t}{L}\right)^2 \right\}^{-0.5} \tag{5.25}$$

where v_o was the speed-of-sound in water, Δt was the total time-of-flight minus the time-of-flight in water (i.e. without a specimen present) and L was the thickness of the specimen, as indicated in Fig. 5.10b.
Finally, the phase velocities were fitted to the nonlinear function (5.7) in the sense of least squares to give the elastic constants: C_{11}, C_{33}, C_{13}, C_{55} in the (1-3)-plane; C_{11}, C_{22}, C_{12}, C_{44} in the (1-2)-plane and C_{22}, C_{33}, C_{23}, C_{66} in the (2-3)-plane. For example, in the (1-3)-plane, the phase velocities, Eq. (5.23), were fitted to the elastic constants

$$C' = \rho v_p^2 \tag{5.26}$$

or

$$C' = \tfrac{1}{2}\left|C_{11}\cos^2\phi + C_{33}\sin^2\phi + C_{55}\right| \pm \tfrac{1}{2}\left\{ \begin{array}{l} \left(\left|C_{11}\cos^2\phi + C_{33}\sin^2\phi + C_{55}\right|\right)^2 - 4\left[C_{55}\left(C_{11}\cos^4\phi + C_{33}\sin^4\phi\right)\right. \\ \left. + \left(C_{11}C_{33} - 2C_{13}C_{55} - C_{13}^2\right)\sin^2\phi\cos^2\phi \right] \end{array} \right\}^{\frac{1}{2}} \tag{5.27}$$

Here determines (+) and (-) the elastic constants C' governed by quasi-longitudinal and quasi-transverse waves, respectively. Recall from Table 5.1, that only along a preferred axis, the waves will be truly longitudinal or transverse. Thus, a longitudinal wave along the 1-axis is determined by the elastic constant C_{11} and along the 3-axis by the elastic constant C_{33} etc. Notice also that only the quasi-longitudinal and quasi-transverse waves polarized in the plane of

incidence are generated at the water-composite interface and give the information to identify these constants.

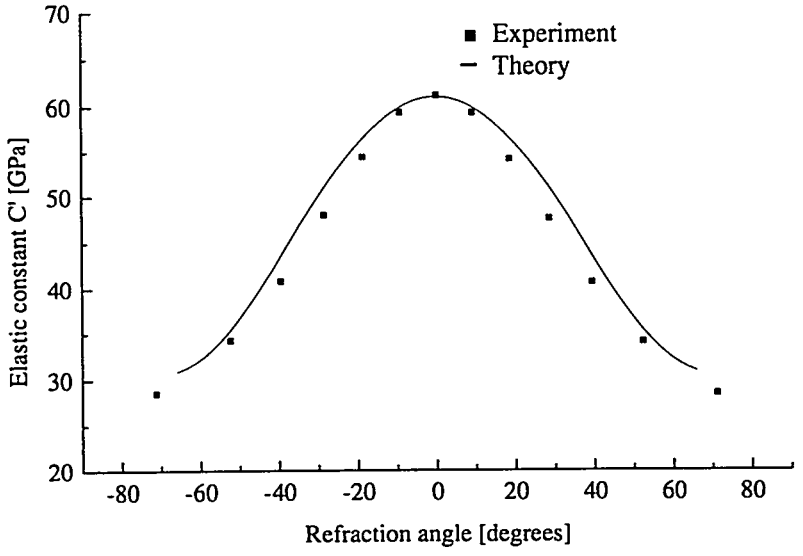

Figure 5.12. Quasi-longitudinal velocity in the (1-3)-plane of the composite as a function of refraction angle.

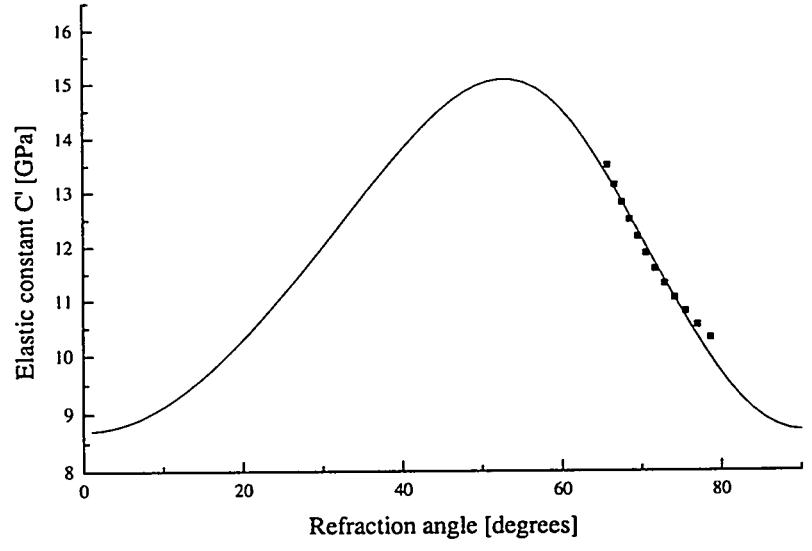

Figure 5.13. Quasi-transverse velocity in the (1-3)-plane of the composite as a function of refraction angle.

The elastic constants C' in the (1-3)-plane, as a function of refraction angle, determined by this procedure is shown in Fig. 5.12. The dotted points indicate experimentally obtained elastic constants while the solid line shows fitted values according to equation (5.27). The elastic constant, determined by the quasi-longitudinal phase velocity, was maximum at 0 degrees corresponding to a high stiffness in the fiber direction. It decreases with increasing angles. A result of the quasi-transverse velocity and corresponding elastic constant C' in the (1-3)-plane is presented in Fig. 5.13. The four elastic constants were fitted to the experimentally obtained values in Fig. 5.12 and Fig. 5.13. The fitting shows that

the elastic constants can be determined in this plane. The elastic constants were also determined in the (2-3)-plane.

5.4 Results and discussion

In the previous section four of the five independent elastic constants in a unidirectional composite were determined (i.e. C_{11}, C_{33}, C_{13}, C_{55}). This was done by fitting equation (5.27), in the sense of least-squares, to quasi-longitudinal and quasi-transverse velocities obtained experimentally in the (1-3)-plane. The remaining elastic constant, C_{23}, was determined using a similar procedure in the (2-3)-plane. The five (nine) elastic constants are shown in Table 5.2, where some may be equal. This is justified by the assumption that the unidirectional laminate was transverse isotropic in symmetry, so that: $C_{33}=C_{22}$, $C_{55}=C_{66}$, $C_{13}=C_{12}$ and $C_{44}=(C_{22}-C_{23})/2$. Thus, rather than using three planes of symmetry, which in general must be evaluated to determine nine elastic constants in an orthotropic composite, only two planes of symmetry were necessary to evaluate the unidirectional composite used in this work.

5.4.1 Accuracy of elastic constants

For the homogeneous composite specimen, several factors influenced the determination of elastic constants e.g. the unidirectional assumption and the quality of the specimen (specimen quality is discussed in section 5.4.4.). However, the accuracy in phase velocity was the most important. The accuracy in phase velocity may depend on: receiver position, pulse distortion due to dispersion and attenuation, and temperature.

The accuracy of the phase velocity was influenced by being measured as the time-of-flight of the group velocity vector. Thus, in order to make an accurate time-of-flight measurement it was important to place the receiving ultrasonic transducer in a position where the energy emerges from the specimen, not in an anticipated position based on Snell's refraction law. Snell's refraction law may in some cases lead to lower elastic constants due to a shorter propagation path. The time-of-flight measurement was, in some cases, also deteriorated by pulse distortion. Thus, the received pulse shape was distorted, and the resultant shift in crossover position gave rise to an apparent reduction of wave velocity. The pulse distortion was seen as a shift to lower frequencies for especially wave incidence normal to the fiber direction and may be explained by an enhanced dispersion or attenuation of the ultrasonic pulse, compared to wave incidence along the fiber direction.

ACHENBACK (1968) has given exact solutions to the dispersion curves for different cases of longitudinal and transverse waves propagated either normal to or in the fiber direction. For each case, the dispersion is shown to increase as the wave length decreases, to approach the fiber radius. However, for the fiber-to-wavelength ratio 10^{-12}, which is roughly the value used in the present study, dispersion effects upon the velocity were shown to be considerable less than the experimental error in phase velocity determination.

The quasi-transverse measurements were more difficult to perform than the quasi-longitudinal measurements, particularly at wide angles of incidence. In fact, in some cases, no reliable transversal measurement was possible due to attenuation. Attenuation of the ultrasonic pulse is discussed in section 5.4.3.

Table 5.2. Experimental and theoretical determined elastic constants.

Elastic constants	This experiment [GPa]	Estimated experimental accuracy [%]	Theory* [GPa]
C_{11}	61.1	6	53.5
$C_{33}=C_{22}$	30.3	6	23.2
$C_{55}=C_{66}$	8.7	10	6.3
C_{23}	10.2	20	8.0
$C_{13}=C_{12}$	11.4	20	8.4
$C_{44}=(C_{22}-C_{23})/2$	10.0	25	7.6

* HASHIN *et al.* (1964) with: Volume fraction, $V_f = 0.66$.
The subscript 1 refers to the fiber (f) alignment in the matrix (m):
Poisson ratio: $\nu_f = 0.22$; $\nu_m = 0.38$;
Stiffness: $E_f = 72.0$ GPa; $E_m = 4.5$ GPa;
Bulk modulus: $K_f = 42.9$ GPa; $K_m = 6.3$ GPa;
Shear modulus: $G_f = 29.5$ GPa; $G_m = 1.7$ GPa.

An increase in specimen temperature may also influence the phase velocity and decrease some of the elastic constants in fiber-reinforced composite materials (BAUDOUIN *et al.* 1996). The temperature was controlled within 1°C, but was not found to be important as long as the water volume was sufficiently large.
The unidirectional composites were described as unidirectional (transverse isotropic), with an isotropy plane. However, the arrangement of plies and fibers induces a small anisotropy in this plane. Thus, depending on the measurement accuracy and the precision sought in terms of the elastic constants, unidirectional composites should be considered as orthotropic materials.
A result of the different factors discussed above is that the elastic constants are determined with different accuracy for the various factors. The accuracy was determined from the estimated errors in the phase velocity and density measurements. C_{11} and C_{33} were the most accurate, as seen in Table 5.2. C_{44} was less accurate due to the small difference between relatively large C_{22} and C_{23}. In conclusion, the determination of the elastic constants was widely affected by the pulse shape. Alternative measurement procedures could be applied instead of thresholding, e.g. autocorrelation (HULL *et al.* 1985).

5.4.2 Comparison with Hashin's theory

Table 5.2 compares the five independent elastic constants of the composite with a classical laminate theory for transverse isotropic materials (HASHIN *et al.* 1964). The constituent material parameters, shown in the Table, were used in the micromechanical calculations in chapter 4. It was assumed that fiber and matrix were linèarly elastic, isotropic, and homogeneous. Although, isotropy may be a reasonable assumption for glass fibers, this may not be the case for other fiber types e.g. carbon fibers. The results from the ultrasonic experiment shows in general higher elastic constants than those predicted by the theory. No simple explanation can explain this deviation between theory and experiment. Theory and experiment deviate, however, at most 38% (C_{55}) from theory.
Ultrasonic measurements are performed at very low strain levels: An estimation of the strain, ε, imposed in the ultrasonic experiment showed that it was in the range 10^{-6}-10^{-8} and with a raise time in the pulse of approximately 10^{-6} s. This gives strain rates $d\varepsilon/dt$ ranging from 10^{-2} - 1.
The elastic constants determined by ultrasound may differ from the static ones due to the dynamic nature of the measurement (SZILARD 1982) and the fact that most matrix materials are viscoelastic (PRASSIANAKIS 1996). However, the es-

timated strain rates are lower than the rates that normally are expected to influence the stiffness properties appreciably (HARDING 1989). Besides, the stiffnesses determined by ultrasound are in good agreement with the static properties reported by TOFTEGAARD (1997) on the same material (see chapter 4). The difference between experimental and estimated values may thus be due to variation in the properties of the individual constituencies, as used for the micromechanical calculations. But also the geometry and configuration may be different from the ideal one anticipated in the theory. Finally, differences may be caused by viscoelastic effects.

5.4.3 Anisotropic attenuation

A complication to the determination of elastic constants is, as mentioned, pulse distortion which depends on the frequency band of the pulse. If the frequency band of a pulse is sufficiently narrow, it may be that the pulse does not vary significantly within the frequency range of interest. In this case the pulse propagates without change of shape. Thus, it can be assumed that the individual frequency components travel with the same velocity and have the same attenuation. On the other hand, if the frequency band of the pulse is broad, the pulse is short and easy to detect in the time domain. Furthermore, superposition of internal reflections inside the specimen may be avoided using the short pulse (HOSTEN, 1993). Therefore, a broadband low frequency pulse was used in all experiments, leading to possible dispersion and pulse distortion.

In order to investigate the influence of ultrasonic wave attenuation upon the elastic constants two experiments were performed. Firstly, the pulse amplitude of the transverse wave, propagating in the (1-3)-plane, was measured as a function of receiver position. This plane was used to estimate C_{55}^{*} in Eq. (5.24). Secondly, the pulse amplitude of the longitudinal wave, propagating in the (2-3)-plane, was measured. The direction normal to the fibers was used to estimate C_{33}^{*}.

In this study, the pulse amplitudes of longitudinal and transverse waves were measured in water before and after transmission through the specimen. Furthermore, the measurements of the pulse amplitudes and time-of-flights were obtained at the same time and separated into two files. This gave a fast data acquisition procedure.

Fig. 5.14 shows a contour plot of the pulse amplitude of transverse waves, propagating in the (1-3)-plane, as a function of incidence angle and receiver position (the labels in the figure corresponds to relative pulse amplitude in deci-Bell (dB)). The arrow shown in the figure gave the direction of the maximum pulse amplitude and implies the importance in moving the receiver position in the circular array. This direction may correspond to the direction of the group velocity vector, as discussed in section 5.2.2. However, the pulse amplitude along the receiver position axis depends on the transducer sound field, whereas the pulse amplitude along the axis of incidence angle depends on the thickness variation of the specimen.

From the pulse amplitude measurements along the arrow in Fig. 5.14, the pulse attenuation was calculated as a function of refracted angle. The attenuation coefficient was calculated as a function of refracted angle using the expression (5.17) for the phase path (it was assumed that the attenuation along the phase and group velocity direction was the same). Figure 5.15 shows the calculated attenuation coefficients along the arrow (in Fig. 5.14) versus refraction angle.

The dotted points indicate experimentally obtained attenuation coefficient while the solid line shows fitted values according to:

$\alpha = 18 - 0.28\phi + 0.04\phi^2$ Np/m. It was noticed that ultrasonic waves with a large wave path in the sample were damped considerably and that the center frequency of the waves in some cases were reduced to 0.75 MHz.

Fig. 5.16 shows a contour plot of the pulse amplitude of a longitudinal wave propagating in the (2-3)-plane, as a function of incidence angle and receiver position.

Fig. 5.17 shows the corresponding attenuation coefficient along the arrow in Fig. 5.16 versus refraction angle. The experimental values are fitted to: $\alpha = 16.1 + 045\phi$ Np/m.

Comparing Figs. 5.15 and 5.17, it is seen that the attenuation coefficient, in general, was greater for the transverse wave in directions of the fibers than for the longitudinal wave normal to the fiber direction.

The elastic constants C_{33}^* and C_{55}^* were estimated from equation (5.24) to give: $C_{33}^* = (30.3 + i\,0.74)$ GPa and $C_{55}^* = (9.6 + i\,0.13)$ GPa, respectively. A frequency of 0.75 MHz was used in these calculations due to the reduction in center frequency of the pulse. Thus, the elastic constant C_{33}^* was most affected by wave attenuation and, therefore, can be used to give an estimate of the maximal damping. These values are in accordance with BAUDOUIN *et al.* (1996) for unidirectional fiber reinforced composites.

An alternative method to determine (isotropic) attenuation coefficients is to measure the pulse amplitudes interacting with samples having different thickness (BATRA *et al.* 1985, STIJNMANN 1995 and SADRI *et al.* 1996). This method will, however, reduce the reproducibility of the experimental method.

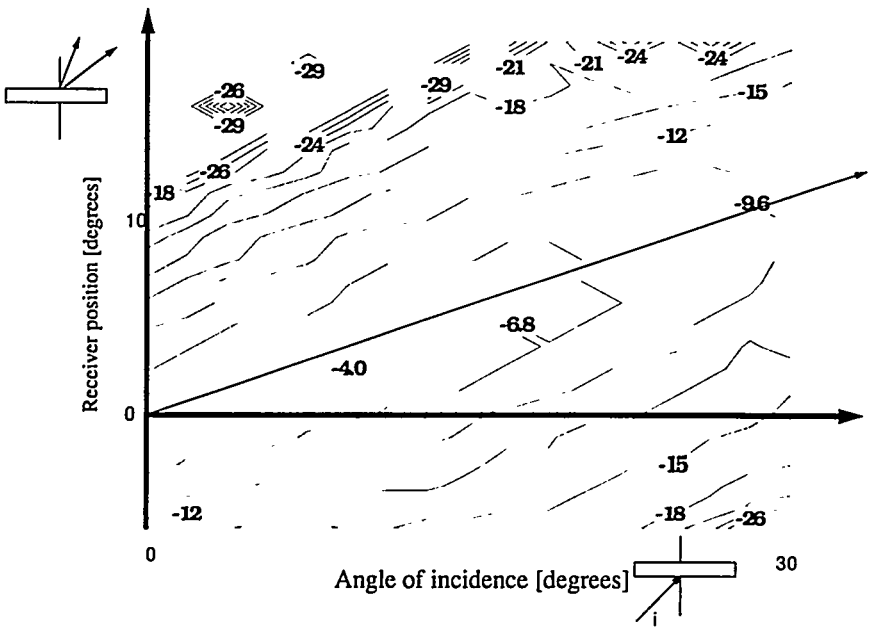

Figure 5.14. Pulse amplitude of transverse waves in the (1-3)-plane as a function of receiver position and angle of incidence (relative) [dB].

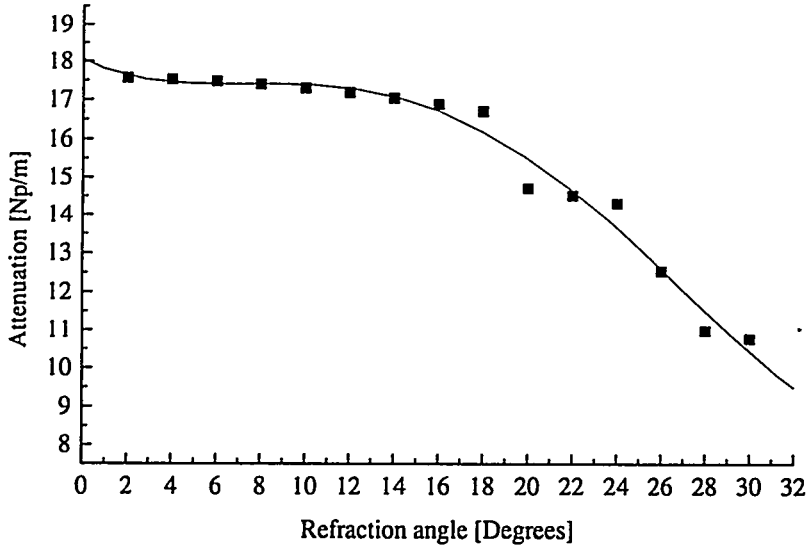

Figure 5.15. Attenuation coefficient of transverse wave in (1-3)-plane versus function refraction angle [Np/m at 0.75 MHz].

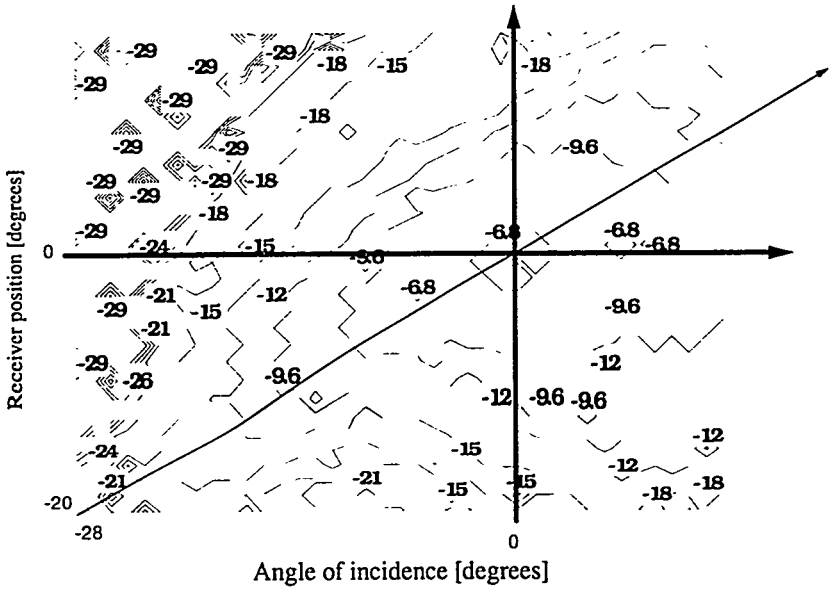

Figure 5.16. Pulse amplitude of longitudinal wave in the (2-3)-plane as a function of receiver position and angle of incidence [dB].

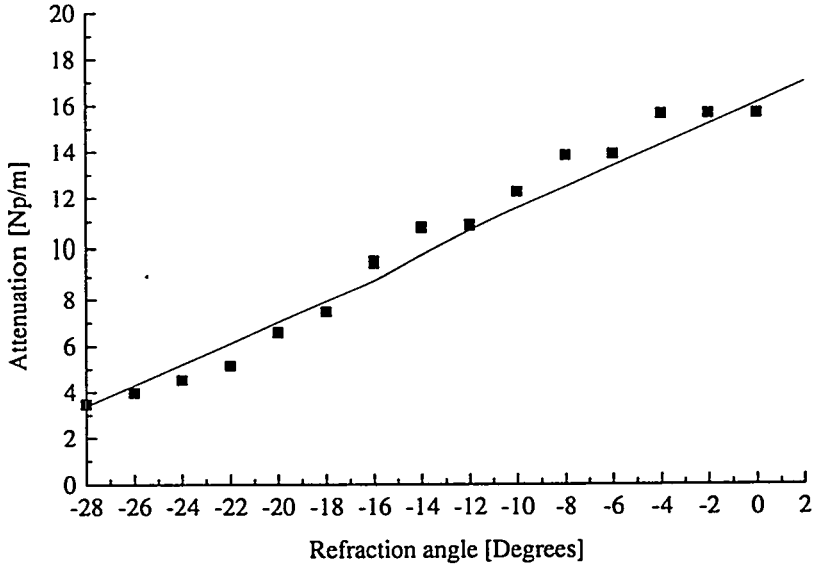

Figure 5.17. Attenuation coefficient of longitudinal wave in the (2-3)-plane versus refraction angle [Np/m at 0.75 MHz].

5.4.4 Specimen quality

Composites are, of course, not homogeneous materials, and to treat the propagation of waves in composites by theories established for such materials are not rigorously correct. In order to assume that the specimen is homogeneous, the typical pulse wavelength should be larger than the dimensions of the specimen inhomogeneties and at the same time smaller than the specimen thickness (32 mm). Since the wavelengths used were typically 0.8 mm to 3.0 mm for a 2.5 MHz pulse, the first condition was satisfied for the glass fiber diameters (20 μm) in the composite. The second condition was necessary in order to treat the laminate as an infinite plate without borders.
In general, the velocity of the wave that travels through inhomogeneous areas can be interpreted only to give volume average elastic constants. Thus, local variations in fiber alignment and presence of defects in the matrix, such as porosity and voids, will influence the velocity measurements that vary with the position in the specimen (GRUBER *et al.* 1986, STUBBS *et al.* 1995). Here, a C-scanning was used to verify that the standard deviation in time-of-flight was sufficiently small.

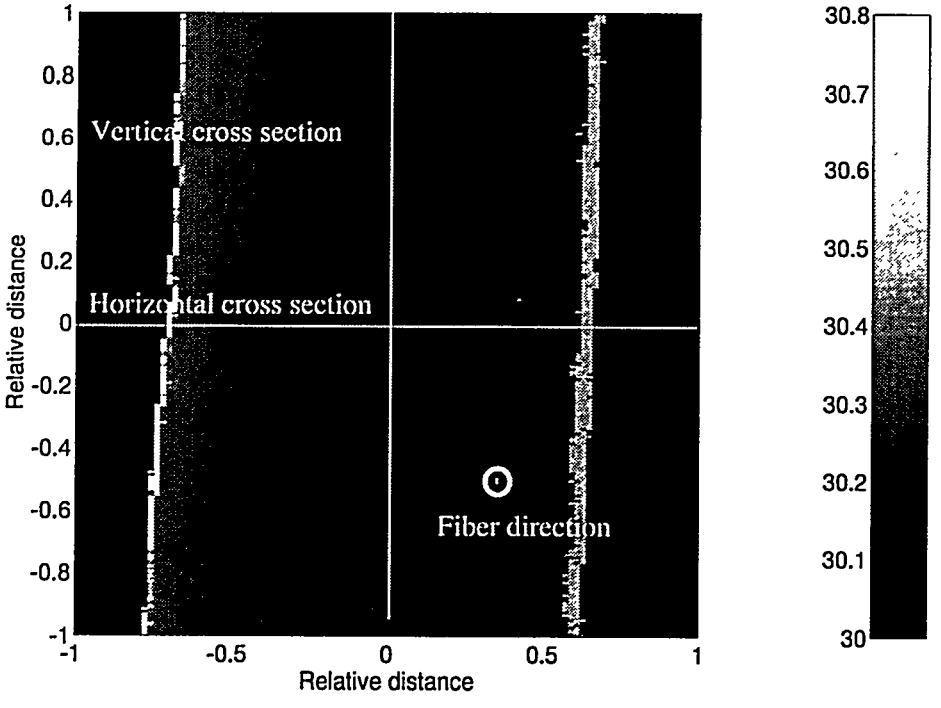

Figure 5.18. C-scan image in fiber direction of unidirectional PET-composite with 66 Vol.% glass fibers. Time-of-flight is in [μs] and the axes in relative units.

An indication of specimen homogeneity was obtained from a series of sound velocity measurements (C-scans) along the same fiber direction, but at different positions within the specimen. However, some considerations were necessary before interpretation of the image in a quantitative manner. In particular, edge effects and accuracy in the measurements may have influenced the interpretation.
Thus, in order to show edge effects and estimate the speed-of-sound accuracy in a C-scan image, two experiments were performed on an assumed homogeneous composite. One scan was in the direction of the fibers and the second scan was

normal to the fibers. In these C-scan experiments two ultrasonic transducers were positioned on each side of the specimen in order to transmit ultrasound through the sample. One of the transducers was used as a transmitter to emit high frequency (7.5 MHz) ultrasound with a narrow (focused) beam.
Fig. 5.18 shows an example of a C-scan image of the unidirectional (fiber direction 0°) PET-composite with 66 Vol.% glass fibers. The time-of-flight was measured in the fiber direction of a 20 mm thick sample and the time variation (plus the time-of-flight in water) is seen on a gray-scale code.

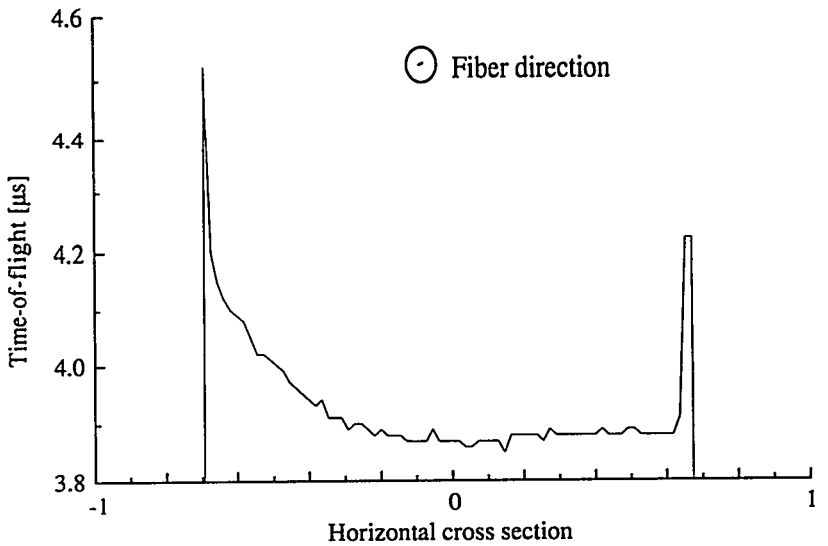

Figure 5.19. The horizontal cross section of time-of-flight in Fig. 5.18 minus time-of-flight in water.

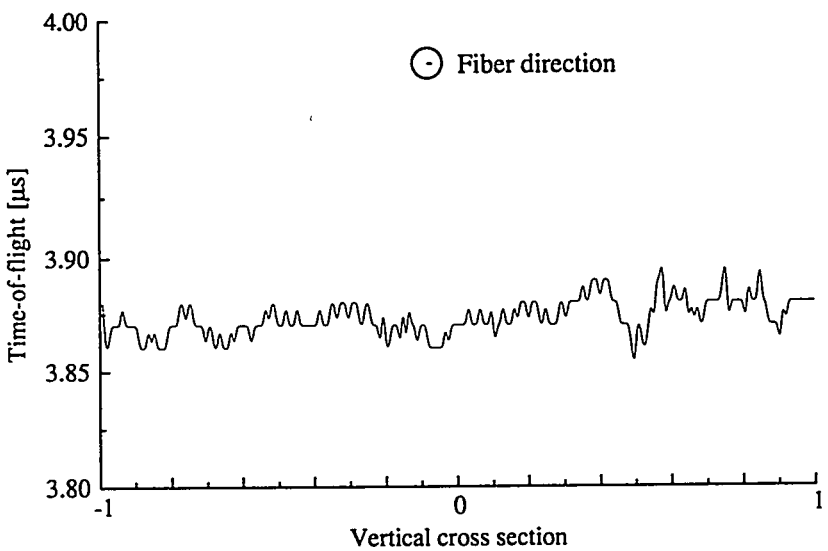

Figure 5.20. The vertical cross section of time-of-flight in Fig. 5.18 minus time-of-flight in water.

Fig. 5.19 and Fig. 5.20 shows the corresponding horizontal and vertical cross sectional cut through zero in Fig. 5.18 (minus the time-of-flight in water). The variation in time-of-flight data in the horizontal cross sectional cut was due to edge diffraction of the ultrasonic beam along the border. This is the edge effect. Thus, at a distance, approximately corresponding to the transducer aperture, from the edge of the composite, a higher time-of-flight may be introduced corresponding to a lower velocity in the material. The variation in the vertical cross sectional cut can then be interpreted as the accuracy of the ultrasonic measurement along this fiber direction. Using this, the speed-of-sound in the composite sample was calculated to 5160 ± 40 m/s, where the uncertainty was estimated using the standard deviation of the time-of-flight data.

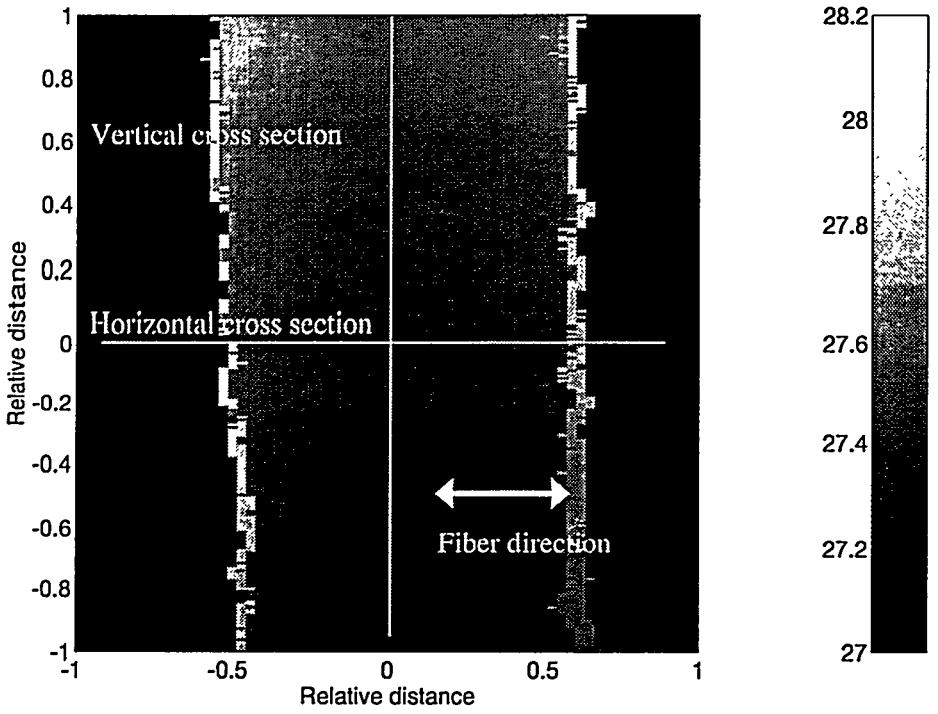

Figure 5.21. C-scan image perpendicular to fiber direction of unidirectional PET-composite with 66 Vol. % glass fibers. Time-of-flight is in [μs] *and the axes in relative units.*

Fig. 5.21 shows a similar C-scan image of the same composite, but measured perpendicular to the fiber direction of a 32 mm thick sample. The speed-of sound in this direction was calculated to 3620 ± 60 m/s, again using the standard deviation of the vertical cross section data. The speed-of-sound is in accordance with the expected lower stiffness normal to the fiber direction. It is seen by comparing the standard deviation in the vertical cross sections (Fig. 5.20 and Fig. 5.23), that the accuracy in time-of-flight may be of the same order. The increasing time-of-flight in the vertical cross section is due to a deviation in thickness of the sample.

In conclusion, the two measurements show that edge effects have to be avoided in an estimation of speed-of-sound accuracy and interpretation of specimen homogeneity.

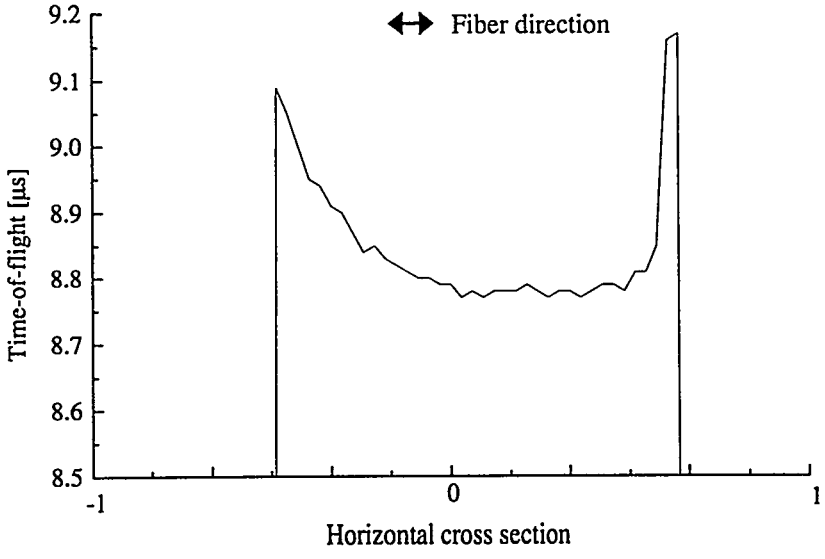

Figure 5.22. The horizontal cross section of time-of-flight in Fig. 5.21 minus time-of-flight in water.

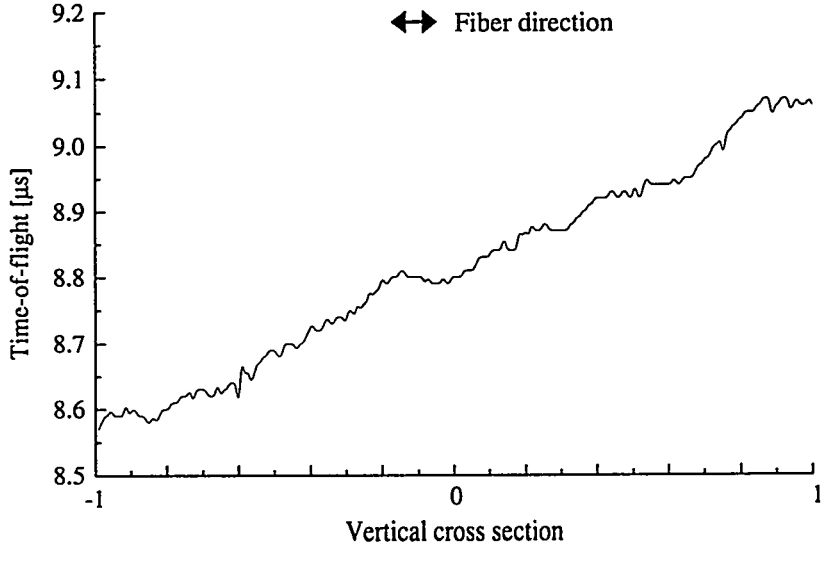

Figure 5.23. The vertical cross section of time-of-flight in Fig. 5.21 minus time-of-flight in water.

To a smaller degree, fiber misorientation and variation in fiber volume fraction will cause a variation in phase velocity, but the presence of defects in the matrix, and possibly the quality of the fiber-matrix interface, will also contribute.
The dependence of the elastic constants upon fiber fraction and, also, upon void content has been reported by MARTIN (1977). In this paper isotropic and anisotropic fibers were considered in relation to the typical fiber glass and carbon-fiber composites.
Results show that increasing the fiber content increases the ultrasonic longitudinal and transverse velocities. This can be attributed to the fact that the stiffness' of the fibers are larger than those of the matrix, so that an increase in the fiber content results in larger stiffness' of the composites and hence larger velocities.

Considering the presence of voids in the matrix, increasing the void content decreases the longitudinal and transverse velocities (if the assumption is made that voids are only present in the matrix). This is due to a decrease in the elastic constants of the composite with an increasing void content than in the case of no fibers. Thus, for a high fiber content a given void content will occupy less volume of the matrix altering its moduli. The porosity content was found to be small (about 1.5 Vol. %).

5.4.5 Specimen dimensions and applications of the method

In choosing specimens for the experiment it is necessary to consider specimen dimensions. A maximum specimen size is restricted by the circular aperture array in the immersion tank and should not exceed 50 cm, however, smaller specimens are usually chosen due to wave attenuation. The attenuation is caused mainly by wave absorption in the matrix, wave scattering from fibers and density variations. Thus, the specimen must be restricted in the direction of propagation so that a signal can be transmitted. A minimum specimen size is justified by the ability to separate the ultrasonic pulses from the reference pulses in water (i.e., without specimen).

In addition to the determination of the elastic constants of composite materials, the ultrasonic technique described in this chapter will be very useful in assessing some special properties of the material such as symmetry, fiber misorientation, fiber volume fractions, etc. For the determination of the axis of symmetry, measurements of wave velocities in three orthogonal planes allow the calculation of the elastic constants, and from examination of the obtained values the class of symmetry may be deduced. To estimate the fiber misorientation it is necessary to bear in mind that a deviation from unidirectional fiber alignment in a composite will result in a reduction of modulus along the preferred direction together with an increase in the transverse direction. The fiber fractions present may be estimated from the knowledge of the dependence of wave velocity upon fiber fraction.

5.5 Summary and conclusions

Section 5.1 gave a short introduction to quantitative ultrasonic evaluation of anisotropic materials.

Section 5.2 discussed the theory of wave propagation in anisotropic materials with emphasis on fiber reinforced composites. It was shown how the Christoffel equation could be applied to determine nine elastic constants of orthotropic composites. Three ultrasonic waves were possible: two quasi-waves and one pure wave (Fig. 5.1). However, for special directions these waves were pure (Table 5.1).
Energy flux propagation (Fig. 5.2) and attenuation of ultrasonic waves were considered and velocity surfaces were calculated, in two planes, for the three wave types (Figs. 5.3-5.8). The deviation of energy flux propagation from the wave propagation was considered and the deviation angle was found to be as large as 33° (Fig. 5.9).

Section 5.3 discussed contact and immersion methods in combination with reflection and transmission methods, to determine the elastic stiffness constants. It was demonstrated how the circular aperture array of transducers (Fig. 5.10) could be used to determine, non-destructively, five independent elastic constants of the unidirectional glass/PET laminate. This was done by fitting elastic constants in the (1-3)-plane to quasi-longitudinal and quasi-transverse velocities measured at different angles of incidence (Figs. 5.12 and 5.13). The remaining elastic constant was determined in the (2-3)-plane. Thus, rather than using three planes of symmetry, which in general must be evaluated to determine nine elastic constants in an orthotropic composite, only two planes of symmetry was necessary to evaluate the unidirectional laminate.

Section 5.4 discussed the results from the ultrasonic experiment and compared them with micromechanical theory (Hashin-Rosen's theory discussed in chapter 4). The experimental results were in general higher than predicted by theory (Table 5.2).
Complex elastic constants were considered for viscoelastic materials. The pulse amplitude was used to determine the imaginary part of C_{33}^* and C_{55}^* (Figs. 5.14-5.17).
The accuracy of the method depends mostly of the pulse shape (see Fig. 5.11).
Specimen homogeneity was examined from C-scan images (Figs. 5.18-5.23).

In conclusion, an ultrasonic method to determine the elastic stiffness constants of fiber reinforced composites using a circular aperture array was presented. The aim was to identify these constants for the unidirectional glass/PET laminate introduced in chapter 4.
The results indicate that the use of ultrasound may substantially improve material characterization of thick anisotropic specimens. An extension of the proposed method may provide a nondestructive procedure that can determine the fiber volume fraction, porosity content and anisotropic attenuation coefficients for unidirectional, as well as for multi-layered composite laminates.

5.6 References to chapter 5

ACHENBACH, J.D and HERRMANN, G. (1968). Dispersion of free harmonic waves in fiber reinforced composites, AIAA Journal, Vol. 6, No. 4, 1832-1836.

ANTICH, P.; MEHTA, S.; SMITH, B. and VAGUINE, V. (1997). Bone elastometric imaging using ultrasound critical-angle reflectometry. Acoustical Imaging, Vol. 23, Edited by Lees and Ferrari, Plenum press, New York, 145-150.

AULD, B.A. (1990). Acoustic fields and waves in solids, Vol. 1 and 2, John Wiley and Sons, New York, USA.

BALASUBRAMANIAM, K. *et al.* (1995). Ultrasonic and vibration methods for the characterization of pultruded composites. Composites Engineering, Vol. 5, No. 12, 1433-1451.

BATRA, N.K.; CHASKELIS, H.H and DELSANTO, P.P. (1985). Ultrasonic characterization of highly attenuative fiber-reinforced composites. IEEE Ult. Symp., Vol. 2, Ed. B.R. McAvoy, 975-978.

BAUDOUIN, S. and HOSTEN, B. (1996). Immersion ultrasonic method to measure elasticconstants and anisotropic attenuation in polymer-matrix and fiber-reinforced composite material. Ultrasonics, Vol. 34, 379-382.

BOLTZ, E.S. and GREEN, R.E. (1993). Ultrasonics in thick anisotropic materials. Review of progress in quantitative nondestructive evaluation, Vol. 12, Edited by D.O. Thompson and D.E. Chimenti, Plenum Press, New York, USA, 1241-1248.

CHIEN, H.; SHEEN, S. and RAPTIS, A. C. (1993) An acousto-ultrasonic NDE technique for monitoring material anisotropy. Review of Progress in Quantitative Nondestructive Evaluation, Vol. 12, Edited by D.O. Thompson and D.E. Chi-menti, Plenum Press, New York, USA, 1225-1232.

DEAN, G.D. and LOKETT, F.J. (1973). Determination of the mechanical properties of fiber composites by ultrasonic techniques. Proc. of analysis of the test methods for high modulus fibers and composites, ASTM STP 521, USA, 326-346.

GRUBER, J.J.; SMITH, J.M. and BROCKELMAN, R.H. (1986). Ultrasonic velocity C-scans for ceramic and composite material characterization. Materials Evaluation, Vol. 46, 90-94.

HANDLEY, S. M.; MILLER, J.G.; BARNES, A.E. and MADARAS E.I. (1990). Visualization of the engineering moduli of composites using measured ultrasonic velocities, Proc. of IEEE Ultrasonics Symposium, USA, 1061-1064.

HARTMANN, B. and JARZYNSKI, J. (1974). Immersion apparatus for ultrasonic measurements in polymers. J. Acoust. Soc. Am., Vol. 56, No. 5, 1569-1477.

HARDING, J.; Li, Y.L.; SAKA K. and TAYLOR, M.E.C. (1989). Properties of materials at high rates of strain. In Proc. 4th. Oxford Int. Conf. on Mech., 403-410.

HASHIN, Z. and ROSEN, B.W. (1964). The elastic moduli of fiber-reinforced materials, J. Applied Mechanics, Vol. 31, 223-232.

HOSTEN, B. and DESCHAMPS, M. (1987). Inhomogeneous wave generation and propa-gation in lossy anisotropic solids. Application to characterization of visco elastic composite materials. J. Acoust. Soc. Am., Vol. 82, No. 5, 1763-1770.

HOSTEN, B. (1991). Reflection and transmission of acoustic plane waves on an immersed orthotropic and viscoelastic solid layer. J. Acoust. Soc. Am., Vol. 89, No. 6, 2745-2752.

HOSTEN, B. (1992). Stiffness matrix invariants to validate the characterization of composite materials with ultrasound methods. Ultrasonics, Vol. 30, No. 6, 365-371.

HOSTEN, B. and CASTAINGS, M. (1993). Transfer matrix of multilayered absorbing and anisotropic media. Measurements and simulations of ultrasonic wave propagation through composite materials, J. Acoust. Soc. Am., Vol. 94, No. 3, 1488-1495.

HULL, D.R.; KAUTZ, H.E. and VARY, E. (1985). Measurement of ultrasonic velocity using phase-slope and cross-correlation methods. Materials Evaluation, Vol. 43, 1455 -1460.

KINSLER, L.E; FREY, A.R.; COPPENS, A.B. and SANDERS, J.V. (1982). Fundamentals of acoustics, John Wiley and Sons Inc. (3ed.), New York, USA.

KRAUTKRÄMER, J. and KRAUTKRÄMER H. (1990). Ultrasonic testing of materials, Springer-Verlag. Germany.

KRIZ, R.D. and STINCHCOMB, W.W. (1979). Elastic moduli of transversely isotropic graphite fibers and their composites. Experimental mechanics, Vol. 19, 41-49.

KRIZ, R.D. (1981). Absorbed moisture and stress-wave propagation in graphite/epoxy, Composite technology review, Vol. 3, 154-155.

KRIZ, R.D. and LEDBETTER, H.M. (1985). Elastic representation surfaces of unidirec-tional graphite/epoxy composites. Recent advantages in composites in the United States and Japan, ASTM STP 864, J.R. Vinson and M. Taya, Eds., American Society for Testing and Materials, Philadelphia, 661-675.

LEDBETTER, H.M. and KRIZ R.D. (1982). Elastic wave surfaces in solids, Phys. Stat. Sol. Vol. 114 (b), 475-480.

MAL, A.K.; LIH, S. and BAR-COHEN, Y. (1993). Ultrasonic determination of the elastic properties of unidirectional composites, Review of progress in quantitative nondestructive evaluation, Vol. 12, Edited by D.O. Thompson and D.E. Chimenti, Plenum Press, USA, 1233-1240.

MARKHAM, M.F. (1970). Measurement of elastic constants of fiber composites by ultrasonics. Composites, Vol. 1, USA, 145-149.

MARTIN, B.G. (1977). Ultrasonic wave propagation in fiber-reinforced solids containing voids. J. Applied Physics, Vol. 48, No. 8, 3368-3373.

MUSGRAVE, M.J.P. (1954). On the propagation of elastic waves in aeolotropic media. I. General principles. Proc. Roy. Soc. , A226, 339-355.

MUSGRAVE, M.J.P. (1954). On the propagation of elastic waves in aeolotropic media. II. Media of hexagonal symmetry. Proc. Roy. Soc., A226 , London, 356-366.

MUSGRAVE, M.J.P. (1970), Deviation of ray from wave normal for elastic waves in principal planes of crystal symmetry. J. Mech. Phys. Solids, Vol. 18, 207-211.

NIELSEN, S.A. and BJØRNØ, L. (1997). Bistatic circular array imaging with gated ultrasonic signals, Acoustical Imaging, Vol. 23, Edited by Lees and Ferrari, Plenum Press, New York, 441-446.

PAPADAKIS, E.P; PATTON T.; TSAI Y.; THOMSON, D.O. and THOMSON R.B. (1991). The elastic moduli of a thick composite as measured by ultrasonic bulk wave pulse velocity. J. Acoust. Soc. Am., Vol. 89, No. 6, 2753-2757.

PEARSON, L.H.; MURRI, W.J. and GARDINER, D.S. (1985). Ultrasonic detection of in-plane properties of composite laminates. IEEE Ult. Symp., Vol. 2, Ed. B.R. McAvoy, 983-989.

PEARSON, L.H. (1986). Measurement of ultrasonic wavespeeds in off-axis directions of composite materials. Review of Progress in Quantitative Nondestructive Evaluation, Vol. 63, Edited by D.O. Thompson and D.E. Chimenti, Plenum Press, New York, USA, 1093-1101.

PRASSIANAKIS, I.N. (1996). The NDT-Evaluation of material's modulus of elasticity E, using ultrasound, Proc. of Non Destructive Testing, Vol. 1, Edited by Van Hemelrijck and Anastassopoulos, Rotterdam, 267-271.

RHEINLÄNDER, J; NIELSEN, S.A; BORUM, K.K. and GUNDTOFT H.E. (1997). Non-destructive evaluation of polymeric composites - a comparison of techniques, Proc. of Polymeric Composites - Expanding the Limits, Risø, 101-125.

ROKHLIN, S.I., and WANG, W. (1989*a*). Ultrasonic evaluation of in-plane and out-of-plane plane elastic properties of composite materials. Review of progress in quantitative nondestructive evaluation, edited by D.O. Thompson and D.E. Chimenti Plenum Press, New York, Vol. 8B, 489-1497.

ROKHLIN, S.I. and WANG W. (1989*b*). Critical angle measurement of elastic constants in composite material. J. Acoust. Soc. Am., Vol. 86, No. 6, 1876-1882.

ROKHLIN, S.I. and WANG W. (1992). Double through-transmission bulk wave method for ultrasonic phase velocity measurement and determination of elastic constants of composites materials. J. Acoust. Soc. Am.,Vol. 91, No. 6, 3303-3312.

ROSE, J. L.; CARSON, J. M. and LEIDEL D. J. (1973). Ultrasonic procedures for inspec-tion composite tubes. Proc. of analysis of the test methods for high modulus fibers and composites, ASTM STP 521, American Socity for Testing and Materials, 311-325.

ROUX, J. (1990). Elastic wave propagation in anisotropic materials. Proc. of IEEE Ultrasonics Symposium. USA, 1065-1073.

SADRI, A.; HASSANI, F.P. and SALEK, K. (1996). Determination of concrete dynamic elastic constants using a minature seismic reflection system. Materials Evaluation, Vol. 55, No. 7, 817-820.

SELFRIDGE, A.R. (1985). Approximate material properties in isotropic materials. Proc. of IEEE transactions on sonics and ultrasonics, Vol. SU-32, No. 3, 381-394.

SMITH, R.E. (1972). Ultrasonic elastic constants of carbon fibers and their composites. J. Appl. Phys., Vol. 43, No. 6, 2555-2561.

STIJNMAN, P.W.A. (1995). Determination of the elastic constants of some composites by using ultrasonic velocity measurements. Composites, Vol.26, No.8, 597-604.

STUBBS, D.A. and ZAWANDA, L.P. (1995). Determination of porosity in glass ceramic matrix composites using an ultrasonic multi-gate C-scan technique. Materials Evaluation, Vol. 55, No. 7, 827-831.

SZILARD, J. (1982). Wave propagation techniques in determining the dynamic elastic properties of wires and fibers. In Ultrasonic Testing, John Wiley and Sons Ltd.,USA, 555-597.

TOFTEGAARD, H. (1997). Elastic constants from simple compression tests. Proc. of Polymeric Composites - Expanding the Limits, Risø, 497-502.

UEDA, M. and TAKIGUCHI, T. (1990). Measurement of transverse Young's modulus of carbon fibers by angular characteristics of ultrasonic scattering. Ultrasonics Symposium, 1081-1085.

ZIMMER, J.E. and COST, J.R. (1970). Determination of the elastic constants of a uni-directional fiber composite using ultrasonic velocity measurements. J. Acoust. Soc. Am., Vol. 47, No. 3, 795- 803.

WANG, L. (1996). Inverse scheme for determination of elastic constants of anisotropic media. Proc. of Non Destructive Testing, Vol. 1, Edited by Van Hemelrijck and Anastassopoulos, Rotterdam, 251-257.

6 Conclusions

6.1 Major conclusions in thesis

An ultrasonic imaging technique was discussed in chapter 2 for generating two-dimensional cross-sections in cylindrical shaped materials. The technique was based on ultrasonic projections and was referred to as ultrasonic computed tomography (UCT).
In the first experiment (I), UCT tomograms were obtained from ultrasonic parallel projections. The filtered backprojection algorithm was implemented with the choice of four different filters, zero padding and nearest neighbor interpolation. Two different measurement strategies of time-of-flight projections were considered. High frequency (i.e. directive) transducers were applied for data acquisition and the ultrasonic pulses were set to arrive when they first crossed a gate level. Experimentally obtained attenuation and velocity tomograms were presented of a water filled ellipse, positioned in a Plexiglas cylinder, and compared with a theoretical model for parallel projections.

- The attenuation tomograms of the small ellipse exhibited good quantitative agreement with the known composition of the testing material. Digital filters could be used to smooth the attenuation tomogram in the presence of noisy parallel projections. However, little quantitative agreement was obtained for velocity tomograms of two ellipses. The reason could be large changes in the refractive index between water and Plexiglas caused by the difference in characteristic impedance between water and the Plexiglas cylinder. This could cause ultrasonic wave propagation to deviate from the straight-ray model. Consequently, some or all of the transmitted energy would be refracted out of the receiving aperture, depending on the angle of incidence. Hence, a major limitation in experiment (I) was refraction of the ultrasonic beam and consequently deviation from the straight-ray model.

Three ultrasonic imaging techniques were discussed in chapter 3 using a synthetic array with transducer elements distributed uniformly along a circular aperture. The circular aperture array was realized by object rotation and ultrasonic signals were acquired via two single mobile transducers, acting as transmitter and/or receiver, respectively. Sound field parameters of two broadband, focused transducers were found experimentally. First, an experimental procedure (II) was reviewed in relation to bistatic amplitude data. In this procedure, diverging ultrasonic beams were used to insonify the cylindrical specimen, and the resultant transmitted signals were recorded by only considering received signals measured over a sector.

- The fan-beam tomogram obtained in this experiment showed improvements in imaging the elliptic shape compared with experiment (I). However, the fan-beam tomogram exhibited severe artifacts due to: the beam width of the transducer, its limited sensitivity and experimental difficulty in aligning the specimen on the rotational axis. In addition, a reference specimen was necessary in order to account for the sound field divergence. Different reconstruction artifacts associated with tomograms were discussed. It was found that non-sufficient zero-padding could introduce a DC-shift in the ampli-

tude. The number of projections should be higher than or equal to, the number of samples per projection (receivers). For the fan-beam tomogram, the beam should be wide enough to cover the inspection area.

Second, an experimental monostatic procedure (III) was suggested using the circular aperture array and for reconstruction of backscattered data (i.e. reflectivity) a backprojection technique was discussed.

- Experimental reflection data were obtained from the cylindrical Plexiglas specimens containing the elliptical defect with strong reflection boundary. Good qualitative agreement was obtained compared to real dimensions and improvements were found compared with experiment (I) and (II).

Theoretical resolution criteria were discussed for various configurations of the circular aperture array. For the bistatic imaging procedure an expression for the lateral resolution was derived. For the monostatic imaging procedure the point spread function was derived, assuming point sources.

- The resolution was found only to depend on bandwidth. In terms of the Rayleigh distance an optimum pulse was found to be superior to other pulse forms (narrow and broadband pulses) and modes (bistatic and complex modes).

Finally, the monostatic procedure was used in volumetric imaging. In this experiment (IV) artificial and real discontinuities in a cylindrical *AlSi*-alloy were compared with similar discontinuities in a Plexiglas specimen. Several discontinuity types in Plexiglas and *AlSi*-alloy cylindrical specimens were studied by three different ultrasonic imaging techniques: (1) circular array imaging was used to obtain circular C-scan images. (2) Reflection tomograms were generated from circular B-scan profiles. The relatively fast reconstruction algorithm was applied, based on the straight beam approximation. This approximation was assumed due to broadband, high frequency pulse propagation. (3) Three-dimensional information was obtained by stacking reflection tomograms from multiple planes. Using this stacking technique, the next step would be obtaining cubic voxels that could be numerically dissected in any plane.

- The reflection tomograms demonstrates that it is technologically feasible to obtain high resolution UCT-images. However, multiple reflections and time consuming alignment could limit the application. Radial holes were difficult to localize. The results indicate that, for characterizing defects with strong boundaries, reflection ultrasonic (monostatic) tomography can be successfully used, while transmission (bistatic) tomography is not practical for such application.

Elastic stiffness constants in anisotropic fiber reinforced composites were discussed in chapter 4. Parameters that could influence the elastic properties of fiber reinforced composites were discussed. Such as: fiber orientation, fiber volume fraction, composite homogeneity and elastic properties of the constituents. ESEM pictures were presented of a glass/PET laminate and the size of inhomogenities in a hexagonal array was estimated. Typical fiber and matrix properties were presented. Relations between elastic stiffness and engineering constants were discussed for an orthotropic and transverse isotropic laminate. In order to find useful micromechanical equations for the elastic stiffness constants for the glass/PET laminate, six sets of equations were given, predicting the elastic engineering constants. The elastic engineering constants were given and compared with mechanical obtained moduli for a unidirectional glass/PET laminate. The Young's moduli, shear moduli and Poisson's ratio's were presented as a function of fiber volume fraction. All calculated elastic engineering constants were within 12 % of the constants obtained by conventional mechanical techniques.

- The elastic stiffness constants were presented versus fiber volume fraction for a unidirectional glass/PET laminate. It was not obvious which set of equation that applied best to the elastic stiffness constants of the laminate. No set of equations was unique to identify all elastic constants. However, the Hashin-Rosen equations were found to be closest to the mechanically obtained values. It should be inquired further whether the present sets of equations include sufficient information for unique determination of the elastic properties for other types of unidirectional composites (e.g., carbon fibers with a thermoplastic matrix).

A short introduction to quantitative ultrasonic evaluation of anisotropic materials was given in chapter 5. The theory of wave propagation in anisotropic materials with emphasis on fiber reinforced composites was presented. It was shown how the Christoffel equation could be applied to determine nine elastic constants of orthotropic composites. Three ultrasonic waves are possibly: two quasi-waves and one pure wave. However, for special directions all three waves are pure. Energy flux propagation and attenuation of ultrasonic waves were considered and velocity surfaces were calculated, in two planes, for the three wave types. The deviation of energy flux propagation from the wave propagation was considered and the deviation angle between a quasi-longitudinal and a quasi-transverse wave was found to be as large as 33° in the (1-3)-plane of a unidirectional composite.
Contact and immersion methods were discussed in combination with reflection and transmission methods, to determine the elastic stiffness constants. It was demonstrated how the circular aperture array could be used to determine, non-destructively, five independent elastic constants of the unidirectional glass/PET laminate. This was done by fitting elastic constants in the (1-3)-plane to quasi-longitudinal and quasi-transverse velocities measured at different angles of incidence. The remaining elastic constant was determined in the (2-3)-plane. Thus, rather than using three planes of symmetry, which in general must be evaluated to determine nine elastic constants in an orthotropic composite, only two planes of symmetry was necessary to evaluate the unidirectional laminate. The results from the ultrasonic experiment were compared with micromechanical theory (Hashin-Rosen equation). The experimental results were in general higher than predicted by theory.

Complex elastic constants were considered for viscoelastic materials and specimen homogeneity was examined from C-scan images.

- The circular aperture array was used to determine the elastic stiffness constants of a fiber reinforced composite. Five elastic stiffness constants were identified for a unidirectional glass/PET laminate. The accuracy of the method depended mostly of the pulse shape.

6.2 Recommendation for future work

There is great potential for volumetric imaging, based on monostatic UCT, in Non-Destructive Evaluation (NDE) of isotropic, homogeneous materials. If each scan is processed separately, the final reflection tomogram is formed by superimposing (stacking) the images. These images give more information of the specimen than either of the individual images would do on their own. The experimental method described here may be applicable to many industrial cylindrically-shaped materials, such as axles, pipes, rods, cranks, cylinders etc. Although there are several attractive features related to this technique, there are also several questions which need to be addressed before it can be used for industrial applications. For example, the applied sound field must be further characterized. An extension to advanced materials, e.g. fiber composites would require more advanced reconstruction methods.

The determination of elastic constants indicate that the use of ultrasound may substantially improve material characterization of anisotropic specimens. An extension of the proposed method may provide a nondestructive procedure that can determine the fiber volume fraction, porosity content and anisotropic attenuation coefficients for unidirectional, as well as for multi-layered composite laminates.

Further validation and quantification of the proposed methods are necessary to better understand the composition of advanced materials and to extract more information from ultrasonic signals.

Appendices

Appendix 2.1 - Details of Plexiglas specimens

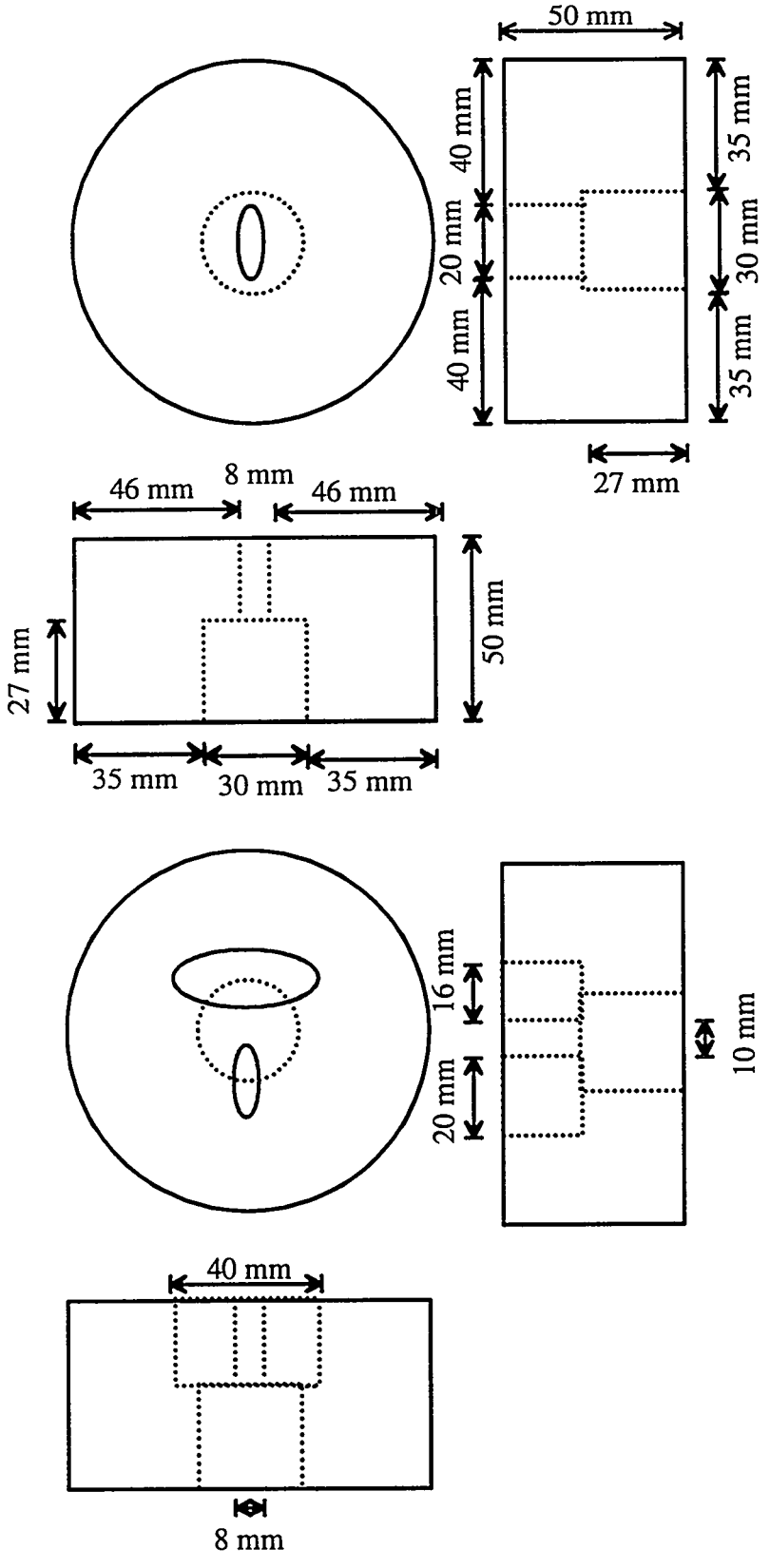

Appendix 3.1 - Sound field of immersion transducer

Sound fields from a focused ultrasonic immersion transducer were examined in three dimensions. A rotational scanning system was used where the transducer rotated around its own axis GUNDTOFT *et al.* (1982). In this system a ball reflector (2 mm in diameter) was moved relative to the transducer in two directions (x-y) by step motors and the maximum backscattered echo was recorded. Finally, a movement along the acoustical axis (z direction of the sound field) was performed. This procedure gave three different plots:

- A cross-sectional plot (x-y plot): representing isosonic lines in a cross-section at a certain distance from the transducer.
- A longitudinal plot (z-plot): showing a number of cross-sectional plots along the acoustical z-axis.
- A directional plot (y-plot): showing the relative sound field data in a specified cross section.

Results from two different transducers are shown below, in a distance 29.5 mm from the transducer:

Test No. 7030.

Fig. A3.1-1. The cross-sectional plot shows that the sound beam is circular and that the -6 dB beam diameter is about 2.7 mm.

Fig. A3.1-2. The longitudinal plot shows that the length of the -6 dB focal zone is about 36 mm (from 17 to 53 mm) in a plane 69°-249° relative to the markers in Fig. A3.1-1.

Fig. A3.1-3. The directional plot shows the sound field (beam diameter) in a radial direction.

Test No. 7034.

Fig. A3.1-4. The cross-sectional plot shows that the sound beam is cylindrical. It has two sound planes relative to the markers: a minor 80°-260° plane and major 170°-350° plane.

Fig. A3.1-5. The longitudinal plot shows that the length of the -6 dB focal zone is about 36 mm (from 29 to 65 mm) in the minor plane 80°-260°. The with of the -6 dB beam diameter is about 0.48 mm

Fig. A3.1-6. The longitudinal plot shows that the length of the -6 dB focal zone is about 48 mm (from 17 to 65 mm) in a plane 170°-350°. The with of the -6 dB beam diameter is about 3.37 mm.

Fig. A3.1-7. The directional plot shows the sound field (beam diameter) in the 170°-350° plane and in a radial direction.

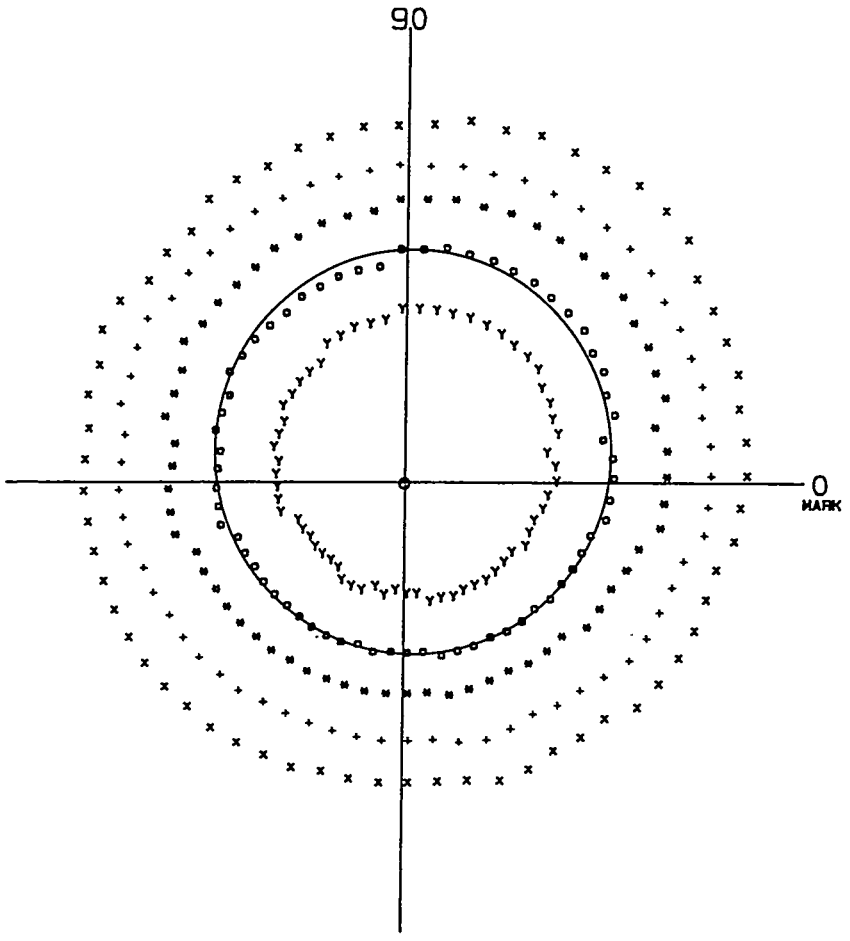

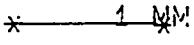

O	=	0 dB
Y	=	-3 dB
o	=	-6 dB
*	=	-9 dB
+	=	-12 dB
X	=	-15 dB

Figure A3.1-1. Cross-sectional plot (x-y plot). Distance from transducer: 29.6 mm.

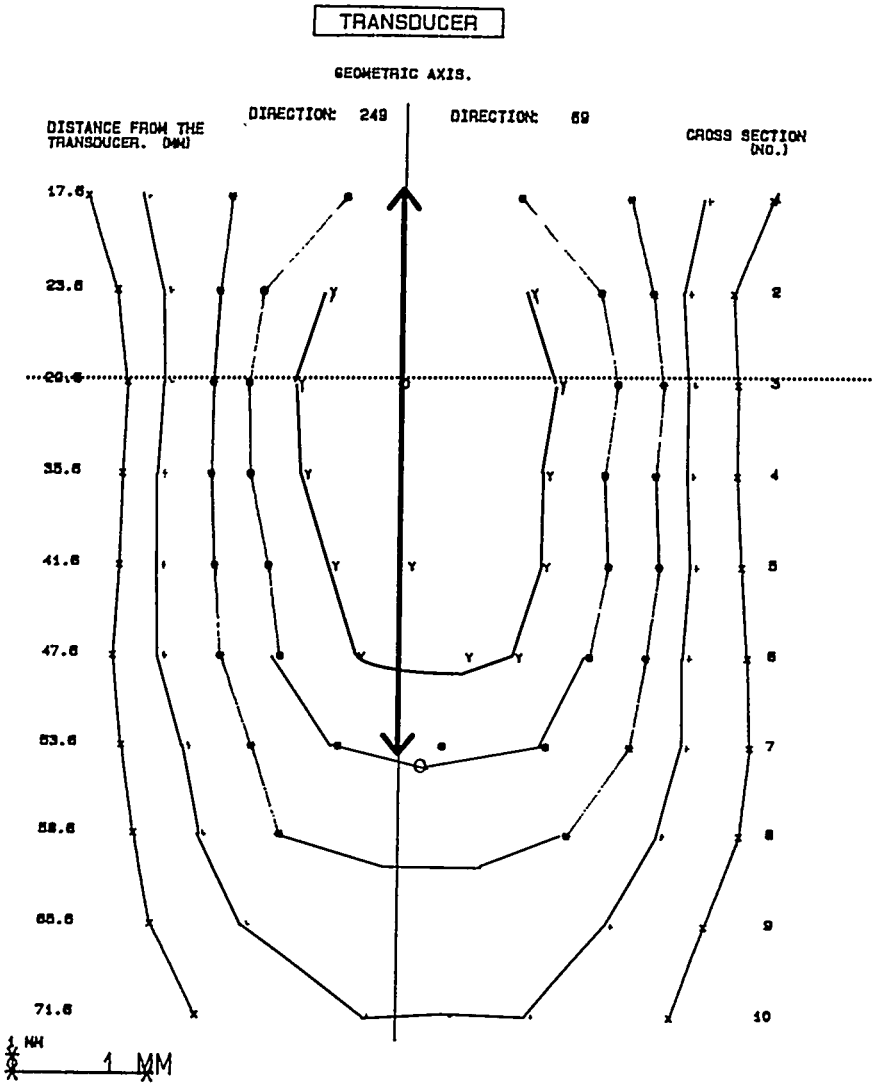

O	=	0 dB
Y	=	-3 dB
o	=	-6 dB
*	=	-9 dB
+	=	-12 dB
X	=	-15 dB

Figure A3.1-2. Longitudinal plot (z plot) in a plane 69°-249° relative to the markers in Fig. 3.1-1.

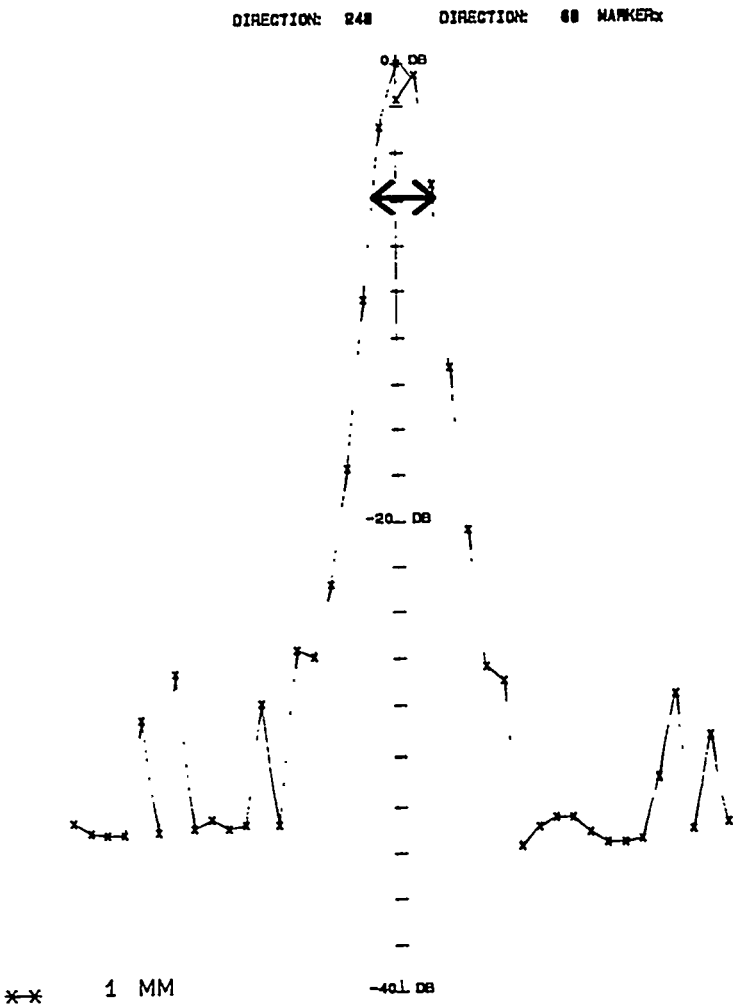

Figure A3.1-3. Directional plot (y-plot).
Distance from transducer: 29.6 mm.

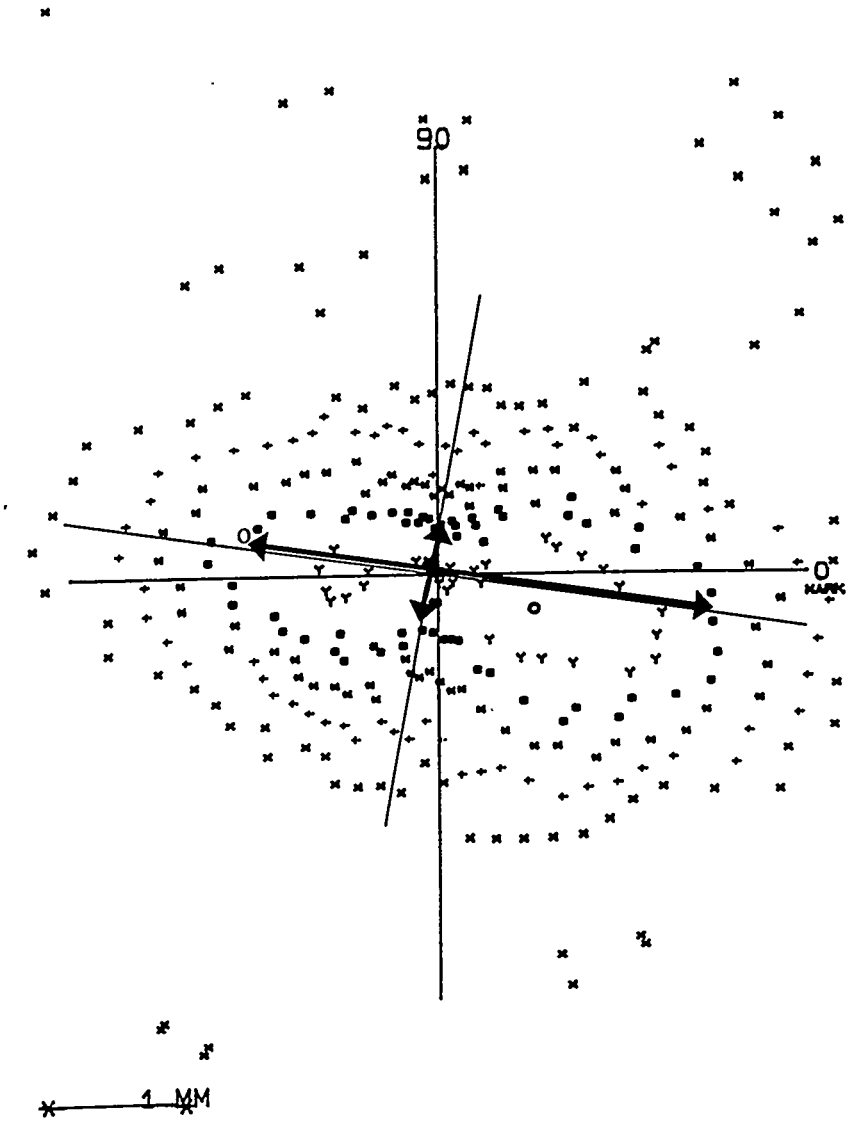

O	=	0 dB
Y	=	-3 dB
o	=	-6 dB
*	=	-9 dB
+	=	-12 dB
X	=	-15 dB

Figure A3.1-4. Cross-sectional plot (x-y plot).
Distance from transducer: 29.6 mm.

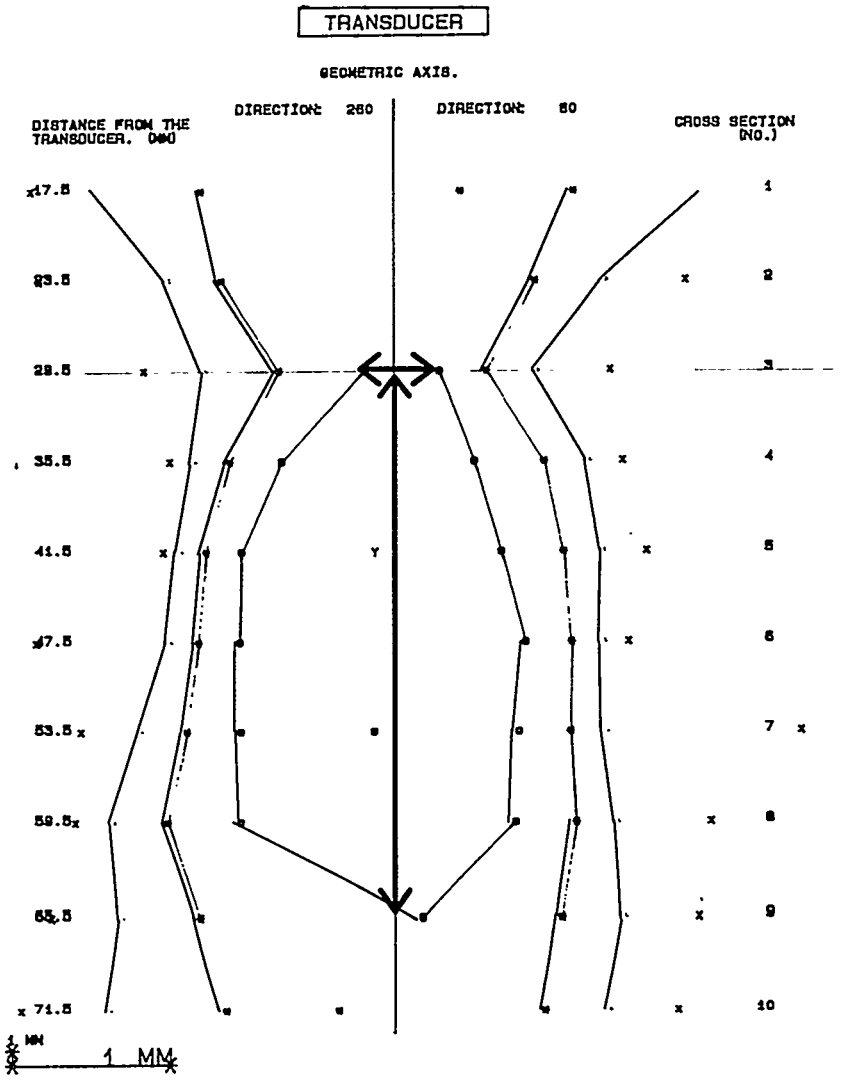

O	=	0 dB
Y	=	-3 dB
o	=	-6 dB
*	=	-9 dB
+	=	-12 dB
X	=	-15 dB

Figure A3.1-5. Longitudinal plot (z plot) in the minor plane (80°-260° relative to the markers in Fig. 3.1-4).

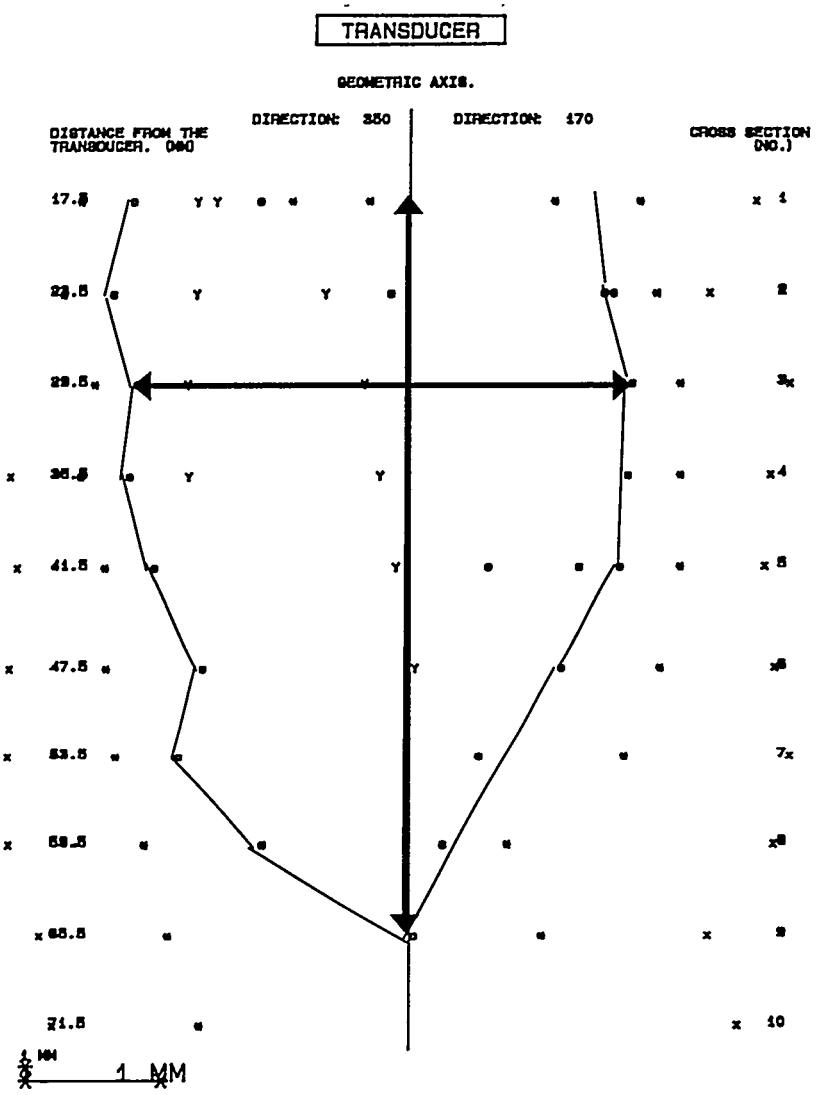

O	=	0 dB
Y	=	-3 dB
o	=	-6 dB
*	=	-9 dB
+	=	-12 dB
X	=	-15 dB

Figure A3.1-6. Longitudinal plot (z plot) in the major plane (80°-260° relative to the markers in Fig. 3.1-4).

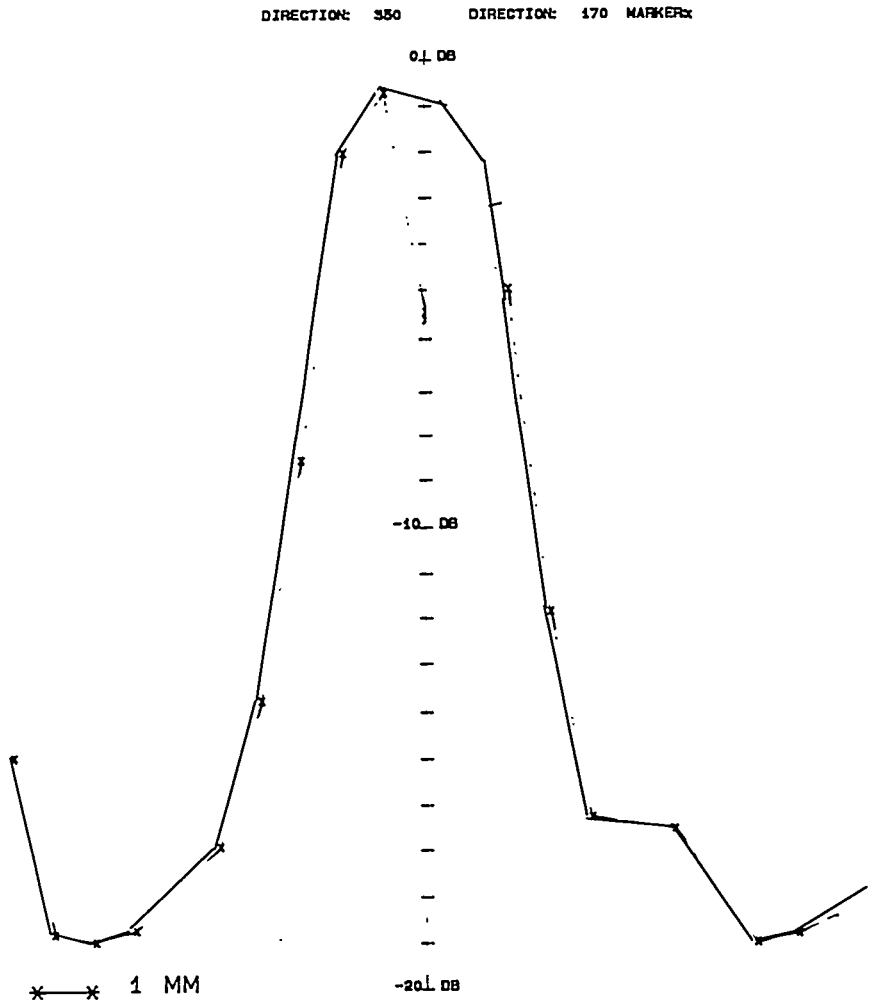

Figure A3.1-7. Directional plot (y plot). Distance from transducer: 29.6 mm.

Appendix 4.1 - Laminate theory

Recall, that a laminate is formed from two or more lamina bonded together to act as an integral structure. Consider a laminate consisting of n orthotropic lamina with thickness z. The laminate is described by three matrices $[A]$, $[B]$ and $[D]$, where A_{ij} is the extensional stiffness matrix coefficients, B_{ij} is the coupling stiffness matrix coefficients and D_{ij} is the bending stiffness matrix coefficients, respectively, given by

$$A_{ij} = \sum_{k=1}^{m} Q_{ij}^{k}(z_k - z_{k-1})$$

$$B_{ij} = \sum_{k=1}^{m} Q_{ij}^{k}(z_k^2 - z_{k-1}^2)$$

$$D_{ij} = \sum_{k=1}^{m} Q_{ij}^{k}(z_k^3 - z_{k-1}^3)$$

Some of these coefficients is zero depending on the stacking sequence KEDWARD (1996).
$A_{16} = A_{26} = 0$ if the laminate is balanced (i.e., for every lamina with certain properties there exist another lamina with the same properties and thickness, but orientated at an equal negative angle. This means that there is no coupling between midplane normal stresses and shear strains (shearing)).
$B_{ij} = 0$ for symmetric laminates. That is, for each lamina above a midplane there exist an identical lamina placed an equal distance below the midplane. This means that there is no coupling between bending and stretching.
$D_{16} = D_{26} = 0$ for cross-ply laminates where all the laminae are orientated 0° or 90°. But also for angle-ply laminates (then $B_{ij} \neq 0$) D_{16} and D_{26} become small, particular if the number of lamina is large. This means that there is no coupling between bending and twisting.

Appendix 4.2 - Reduced stiffness matrix

If only a longitudinal stress is applied to the lamina, the following equations are valid

$$\sigma_1 = Q_{11}\varepsilon_1 + Q_{12}\varepsilon_2 \quad \sigma_2 = Q_{12}\varepsilon_1 + Q_{22}\varepsilon_2$$

Assume first $\sigma_2 = \tau_2 = 0$, which leads to

$$\varepsilon_1 = \frac{Q_{22}\sigma_1}{D} \quad \varepsilon_2 = -\frac{Q_{12}\sigma_1}{D}$$

$$E_{11} = \frac{\sigma_1}{\varepsilon_1} = \frac{D}{Q_{22}} \quad \nu_{12} = -\frac{\varepsilon_2}{\varepsilon_1} = \frac{Q_{12}}{Q_{22}}$$

where D is a determinant (the longitudinal modulus E_{11} is defined as stress divided by strain. The major Poisson ratio ν_{12} is defined as the transverse strain caused by a longitudinal strain).
Assume next $\sigma_1 = \tau_1 = 0$

$$\varepsilon_1 = \frac{Q_{12}\sigma_2}{D} \quad \varepsilon_2 = -\frac{Q_{22}\sigma_2}{D}$$

$$E_{22} = \frac{\sigma_2}{\varepsilon_2} = \frac{D}{Q_{11}} \quad \nu_{21} = -\frac{\varepsilon_1}{\varepsilon_2} = \frac{Q_{12}}{Q_{11}} \quad G_{12} = \frac{\tau_{12}}{\gamma_{12}} = Q_{66}$$

the transverse elastic modulus E_{22}, minor Poisson ration ν_{21} and shear ratio G_{12}, is derived. This gives the 4 elastic constants expressed in engineering constants

$$Q_{11} = \frac{E_{11}}{1 - \nu_{12}\nu_{21}} \qquad Q_{22} = \frac{E_{22}}{1 - \nu_{12}\nu_{21}}$$

$$Q_{12} = \frac{\nu_{12}E_{22}}{1 - \nu_{12}\nu_{21}} \qquad Q_{66} = \tfrac{1}{2}(Q_{11} - Q_{12}) = G_{12}$$

Appendix 4.3 - Transformation of engineering constants

A transformation of the engineering constants gives an expression for modulus as a function of fiber orientation. If only stress in the x_1 direction is considered, then is the strains in the longitudinal and transverse directions given by $\varepsilon_x = \varepsilon_1 \cos^2\theta + \varepsilon_2 \sin^2\theta - \gamma_{12} \sin\theta \cos\theta$. From the inverse transformation law one gets

$$\varepsilon_1 = \frac{\sigma_1}{E_1} - \nu_{21}\frac{\sigma_2}{E_2} = \sigma_x\left(\frac{\cos^2\theta}{E_1} - \nu_{21}\frac{\sin^2\theta}{E_2}\right)$$

$$\varepsilon_2 = \frac{\sigma_2}{E_2} - \nu_{12}\frac{\sigma_1}{E_1} = \sigma_x\left(\frac{\sin^2\theta}{E_2} - \nu_{12}\frac{\cos^2\theta}{E_1}\right)$$

$$\gamma_{12} = \frac{\tau_{12}}{G_{12}} = -\sigma_x\left(\frac{\cos\ \theta \sin\theta}{G_{12}}\right)$$

The symbols are explained in then Nomenclature.

The first expression for the rotated elastic modulus E_x is

$$\frac{1}{E_x} = \frac{1}{E_1}\cos^4(\theta) + \left(\frac{1}{G_{12}} - \frac{2\nu_{12}}{E_1}\right)\sin^2(\theta)\cos^2(\theta) + \frac{1}{E_2}\sin^4(\theta)$$

where θ is the angle of fiber orientation with the stress axis.

The longitudinal modulus and the transversal modulus are calculated after the *rule-of- mixtures* or Halpin-Tsai equations, as seen in Fig. A43a.

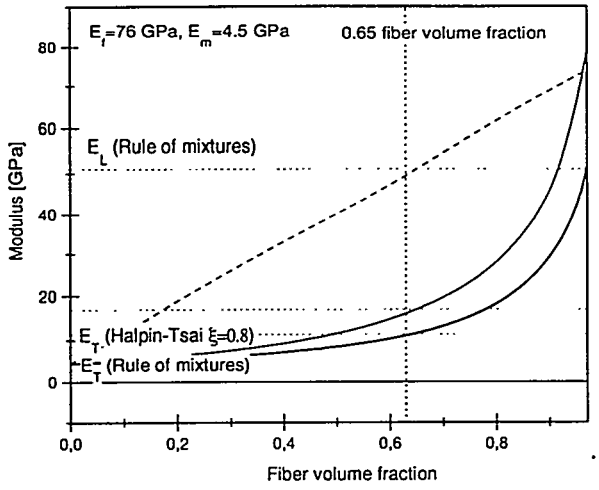

Figure A43a. Transverse modulus for a glass/PET laminate according to the rule-of-mixtures and the Halpin-Tsai equations.

Modulus as a function of orientation is shown in a polar coordinate system in Fig. A43 for a unidirectional glass/polyester lamina. At zero and 90 degrees one get the longitudinal and transverse modulus, respectably.

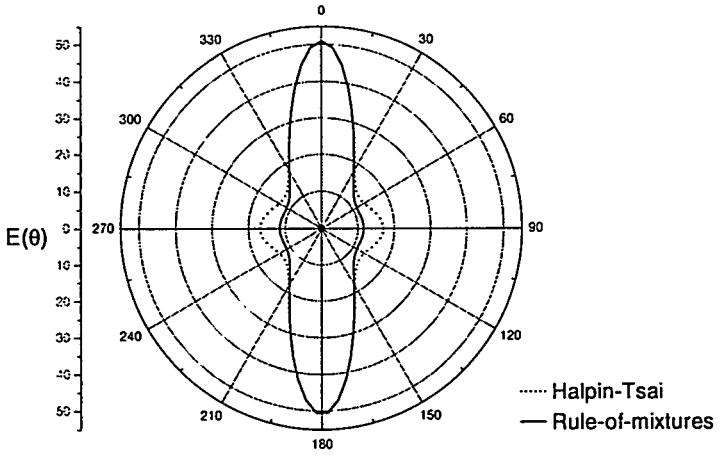

Figure A43b. Stiffness modulus for a glass/PET laminate.

Appendix 5.1 - Elastic waves in isotropic materials

The equations of motion for an isotropic, homogeneous, elastic medium is given by LANDAU *et al.* (1986)

$$\rho\ddot{\underline{u}} = \frac{E}{2(1+\nu)}\Delta\underline{u} + \frac{E}{2(1+\nu)(1-2\nu)}\nabla\, div\, \underline{u}$$

where the Gradient, the Divergence, the Curl and the Laplacian are defined as

$$\nabla u = \frac{\partial u}{\partial x}\bar{i} + \frac{\partial u}{\partial y}\bar{j} + \frac{\partial u}{\partial z}\bar{k} \qquad div\,\bar{u} = \frac{\partial u_1}{\partial x} + \frac{\partial u_2}{\partial y} + \frac{\partial u_3}{\partial z}$$

$$curl\,\bar{u} = \left(\frac{\partial u_3}{\partial y} - \frac{\partial u_2}{\partial z}\right)\bar{i} + \left(\frac{\partial u_1}{\partial z} - \frac{\partial u_3}{\partial x}\right)\bar{j} + \left(\frac{\partial u_2}{\partial x} - \frac{\partial u_1}{\partial y}\right)\bar{k}$$

$$\Delta\bar{u} = \nabla^2\bar{u} = \frac{\partial^2\bar{u}}{\partial x^2} + \frac{\partial^2\bar{u}}{\partial y^2} + \frac{\partial^2\bar{u}}{\partial z^2}$$

Consider a plane wave in an infinite isotropic medium

$$\frac{\partial^2 u_x}{\partial x^2} - \frac{1}{v_{p,l}^2}\frac{\partial^2 u_x}{\partial t^2} = 0 \qquad \frac{\partial^2 u_y}{\partial x^2} - \frac{1}{v_{p,t}^2}\frac{\partial^2 u_y}{\partial t^2} = 0$$

where the displacement u is a function of only one coordinate, x, and of the time t.
Here, the velocity of the longitudinal wave and the transversal wave is, respectively:

$$v_{p,l} = \sqrt{\frac{E(1-\nu)}{\rho(1+\nu)(1-2\nu)}} \qquad v_{p,t} = \sqrt{\frac{E}{2\rho(1+\nu)}}$$

where ρ is the density of the material, E is the modulus of elasticity (Young's modulus) and ν is the Poisson ratio.
The two phase velocities are linked together by the following relation

$$v_{p,t} = v_{p,l}\sqrt{\frac{1-2\nu}{2(1-\nu)}}$$

For all solid isotropic materials Poisson's ratio lies between 0 and 0.5, so that the numerical value of the expression

$$\sqrt{\frac{1-2\nu}{2(1-\nu)}}$$

always lies between 0 and 0.7.

Ref.: LANDAU, L.D. and LIFSHITZ, E.M. (1986).
Theory of elasticity. Course of theoretical physics, Vol. 7.

Appendix 5.2 - Christoffel stiffness for some anisotropic materials

1. Anisotropic materials in general

The Christoffel stiffness matrix for anisotropic materials includes 21 elastic constants (C_{ij}) (MUSGRAVE, 1954):

$$\Gamma_{11} = C_{11}n_1^2 + C_{66}n_2^2 + C_{55}n_3^2 + 2C_{56}n_2n_3 + 2C_{15}n_1n_3 + 2C_{16}n_1n_2$$
$$\Gamma_{22} = C_{66}n_1^2 + C_{22}n_2^2 + C_{44}n_3^2 + 2C_{24}n_2n_3 + 2C_{46}n_1n_3 + 2C_{26}n_1n_2$$
$$\Gamma_{33} = C_{55}n_1^2 + C_{44}n_2^2 + C_{33}n_3^2 + 2C_{34}n_2n_3 + 2C_{34}n_1n_3 + 2C_{35}n_1n_2$$
$$\Gamma_{23} = C_{56}n_1^2 + C_{24}n_2^2 + C_{34}n_3^2 + (C_{23} + C_{44})n_2n_3 + (C_{36} + C_{45})n_1n_3 + (C_{25} + C_{46})n_1n_2$$
$$\Gamma_{13} = C_{15}n_1^2 + C_{46}n_2^2 + C_{35}n_3^2 + (C_{36} + C_{45})n_2n_3 + (C_{13} + C_{55})n_1n_3 + (C_{14} + C_{56})n_1n_2$$
$$\Gamma_{12} = C_{16}n_1^2 + C_{26}n_2^2 + C_{45}n_3^2 + (C_{25} + C_{46})n_2n_3 + (C_{14} + C_{56})n_1n_3 + (C_{12} + C_{66})n_1n_2$$

2. Orthotropic materials

For orthotropic materials, as for example a cross-ply laminates, the stiffness matrix has nine independent elastic constants (C_{11}, C_{22}, C_{33}, C_{44}, C_{55}, C_{66}, C_{12}, C_{13}, C_{23}). This is the same number of elastic constants required to describe an orthorombic crystal.

3. Transverse isotropic materials

For a unidirectional composite with transverse isotropy, e.g. a unidirectional fiber composite, the preferred direction is the fiber direction (1-axis in the preferred direction) and five independent elastic constants (C_{11}, $C_{22} = C_{33}$, $C_{55} = C_{66}$, $C_{44}=(C_{22}-C_{23})/2$, $C_{12} = C_{13}$, C_{23}) are used. These are the same elastic constants required to describe fully the elastic properties of a single crystal with hexagonal symmetry.

$$\Gamma_{11} = C_{11}n_1^2 + C_{66}n_2^2 + C_{55}n_3^2$$
$$\Gamma_{22} = C_{66}n_1^2 + C_{22}n_2^2 + C_{44}n_3^2$$
$$\Gamma_{33} = C_{55}n_1^2 + C_{44}n_2^2 + C_{33}n_3^2$$
$$\Gamma_{23} = (C_{23} + C_{44})n_2n_3$$
$$\Gamma_{13} = (C_{13} + C_{55})n_1n_3$$
$$\Gamma_{12} = (C_{12} + C_{66})n_1n_2$$

Ref.: MUSGRAVE, M.J.P. (1954). On the propagation of elastic waves in aeolotropic media. I. General principles. Proc. Roy. Soc. , A226 (1954), 339-355.

List of Figures

Chapter 1-2 Page

Chapter 3 Page

Chapter 4 Page

Chapter 5 Page

List of Tables

Chapter 2-3 Page

Chapter 3-4 Page

Nomenclature

According to: *Letter Symbols and Abbreviations for Quantities used in Acoustics* (ANSI/ASME Y10.11 - 1984).

Symbol	Unit	Meaning of quantity
a, b	m	Radius, constant
c, c_0	m/s	Speed of sound (water)
f	m^{-1}	Point spread function,
Δf	Hz	Frequency, bandwidth
g	-	Backscattered signal
h	-	Impulse response
k	m^{-1}	Wavenumber
n	-	Direction of propagation
p_r, p_t	Pa	Received/transmitted pulse
$<p>$	-	Projection
t	s	Time
v	m/s	Longitudinal velocity
v_p	m/s	Phase velocity
x,y	m	Image coordinates
x_1, x_2, x_3	-	Axis defining a Cartesian coordinate syst
r, d, s	m	Fiber radius, diameter, separation
s_p	s/m	Slowness velocity
w, l, d	m	Width, length, depth
A/B	-	Relative distance
C_{ijkl}	Pa	Stiffness tensor
$C_{11}, C_{12}..C_{66}$	Pa	Elastic stiffness constants
D	m	Aperture
E_m, E_f	Pa	Elastic modulus of matrix and fiber
E_{11}, E_{22}, E_{33}	Pa	Young's moduli
F, F_{ref}	m	Focal point (reference)
G_m, G_f	Pa	Shear modulus of matrix and fiber
G_{12}, G_{13}, G_{23}	Pa	Shear moduli
H, S	-	Transfer function
J_n	-	Bessel function of order n
K_m, K_f	Pa	Bulk modulus of matrix and fiber
K	Pa	Hashin-Rosen value
L	-	Whitney constant
M	-	Number of projections
N	-	Number of transducer elements
P	1/m	Spectrum
Q	Pa	Reduced stiffness matrix
R	m	Aperture radius
SR	m	Scan radius
V_m, V_f	Vol. %	Volume percent of matrix and fiber
X,Y	m or °	Distance or angle

Symbol	**Unit**	Quantity
α	**°**	Half angle beam
β	**rad**	Angle
γ	**-**	Constant
δ	**m**	Rayleigh resolution, beam diameter
δ	**-**	Kronecker Delta
ε_{kl}	**-**	Strain tensor
η, ζ	**-**	Halpin-Tsai constants
$\theta, \Delta\theta$	**°/rec.**	Angular point pos., sector resolution
λ	**m**	Wavelength
u	**m**	Displacement vector
ν	**Hz**	Frequency
ν_m, ν_f	**-**	Poisson's ratio of matrix and fiber
ν_{12}, ν_{21}	**-**	Major and minor Poisson's ratio
ν_{13}, ν_{23}	**-**	Poisson's ratio out-of-plane
ρ	**m** **kg/m^3**	Trans.-point distance, Density of composite
σ_{ij}	**Pa**	Stress tensor
$\tau, \Delta\tau$	**s**	Pulse delay, time resolution
$\phi, \Delta\phi$	**°/proj.**	Angular trans. pos., aperture resolution
ω	**rad/s**	Angular frequency
Γ	**Pa**	Cristofell's stiffness

Abbreviations

AFM	Materials Research Department.
AlSi	Aluminium Silicon alloy.
ART	Algebraic Reconstruction Technique.
DC	Direct Current.
DIM	Dimension file.
DTU	Technical University of Denmark.
ESEM	Environmental Scanning Electron Microscope.
FFT	Fast Fourier Transformation.
GH	Generalized Hamming filter.
HFUS	High Frequency Ultrasonic System.
IBT	*Ingenieur Büro für Technische Informatik.*
IEEE	Institute of Electrical and Electronic Engineers.
LPC	Low-Pass Cosine filter.
MD	Multi-Directional.
NDE	Non-Destructive Evaluation.
PET	Poly (Ethylene Teraphthalate).
Plexiglas	PMMA, Poly (Methyl MethAcrylat), Perspex, Acrylic, Lucite.
PSF	Point Spread Function
RISØ	Risø National Laboratory, Denmark.
RL	Ram-Lak filter.
SL	Shepp-Logan filter.
TOF	Time Of Flight.
UCT	Ultrasonic Computed Tomography.
UD	Uni-Directional.
USCB	University of California at Santa Barbara.

Photo gallery

Photo 1. Fixture for synthetic circular aperture array experiment.

Photo 2. Typical setup for ultrasonic computed tomography.

Photo 3. Detail of cylindrical Plexiglas specimen with elliptical hole.

Photo 4. Detail of water tank and step motors.

Photo 5. Selection of ultrasonic transducers.

Photo 6. Selection of test specimens.

Photo 7. Ball reflector in water tank.

Photo 8. Setup for sound field examination.

Photo 9. Detail of experiment with elastic constants at McDonnell Douglas Aerospace, Long Beach, USA.

Photo 10. Setup for ultrasonic determination of elastic constants at McDonnell Douglas Aerospace, Long Beach, USA.

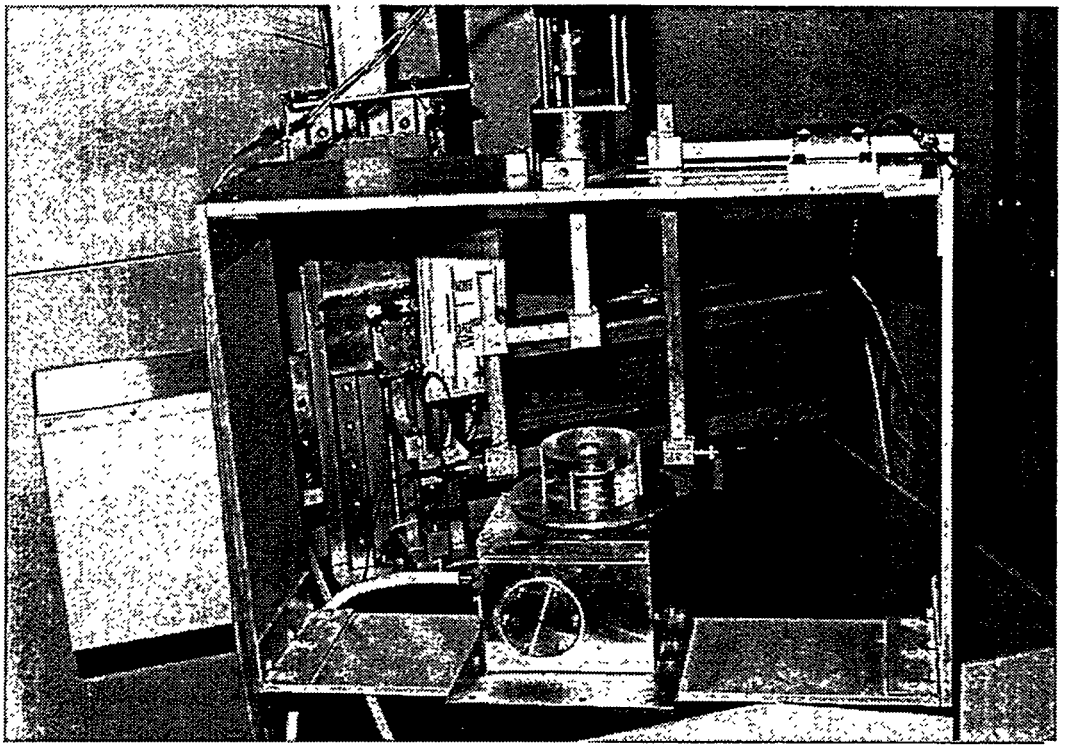

Photo 1.

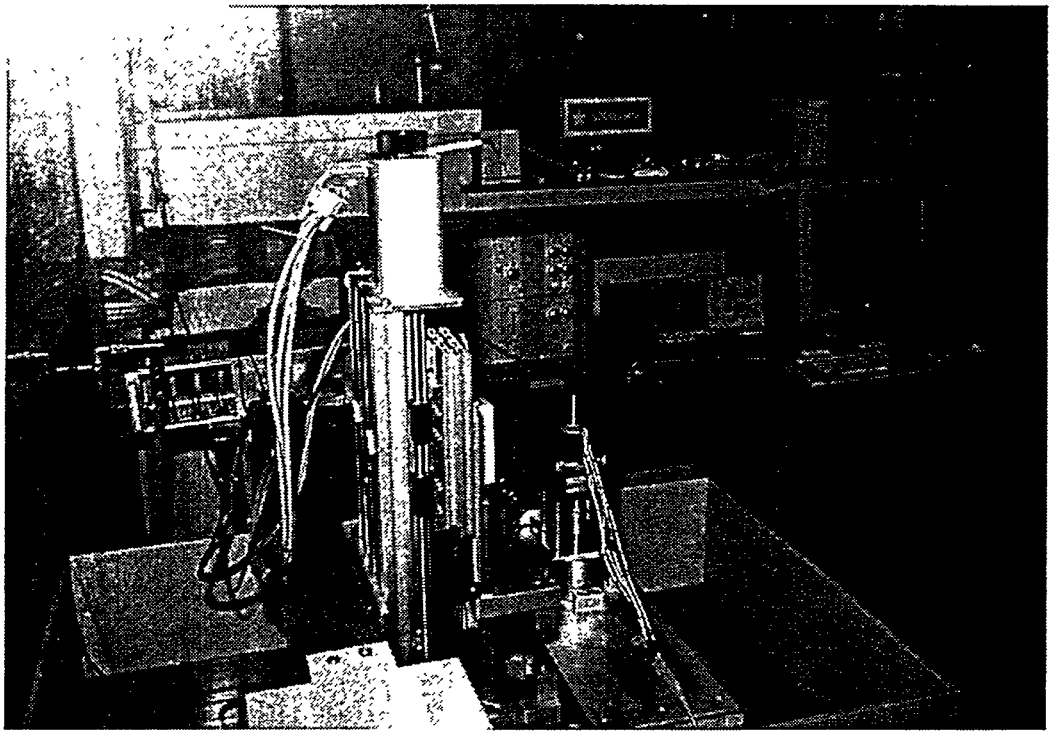

Photo 2.

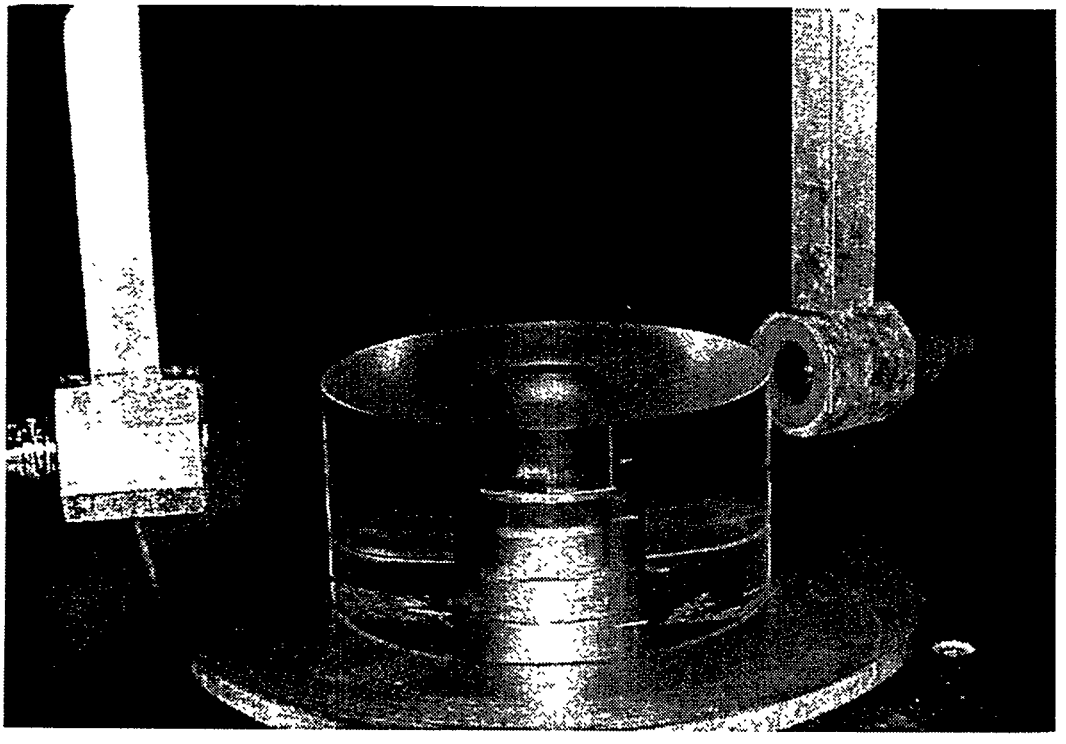

Photo 3.

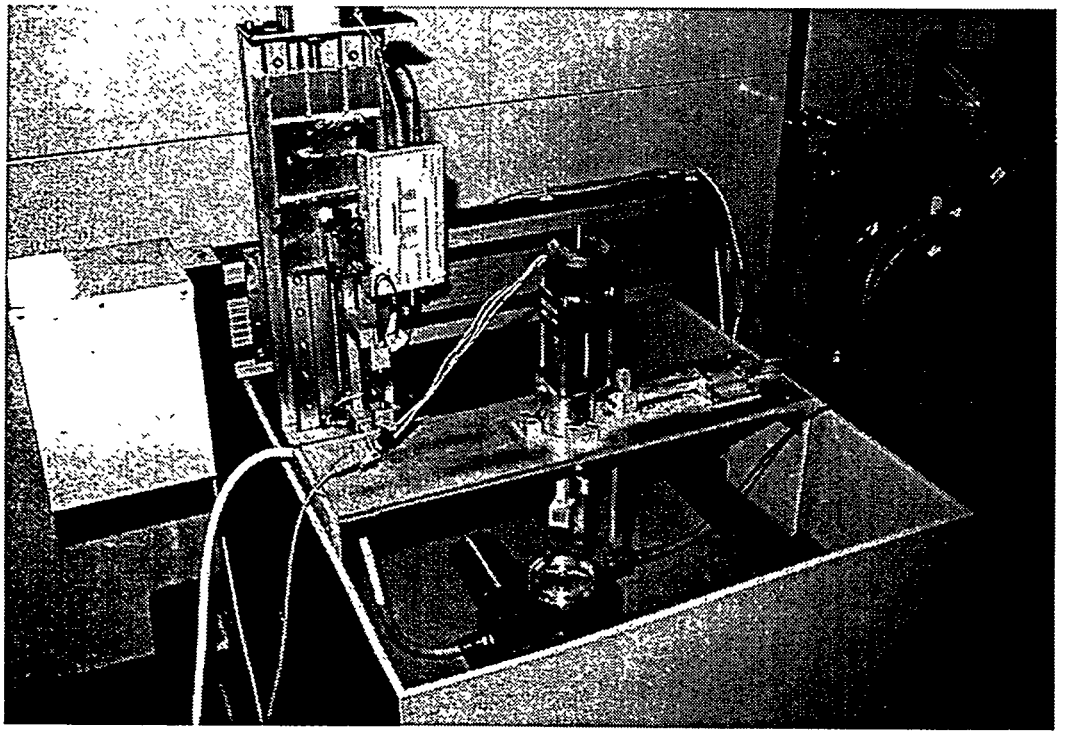

Photo 4.

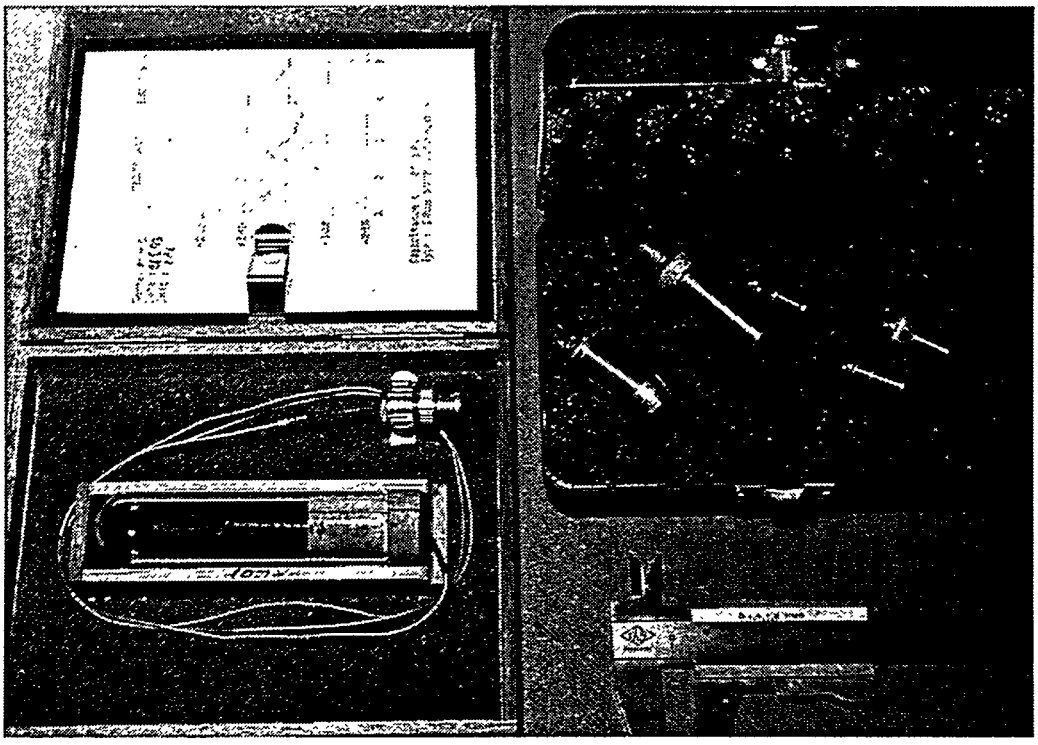

Photo 5.

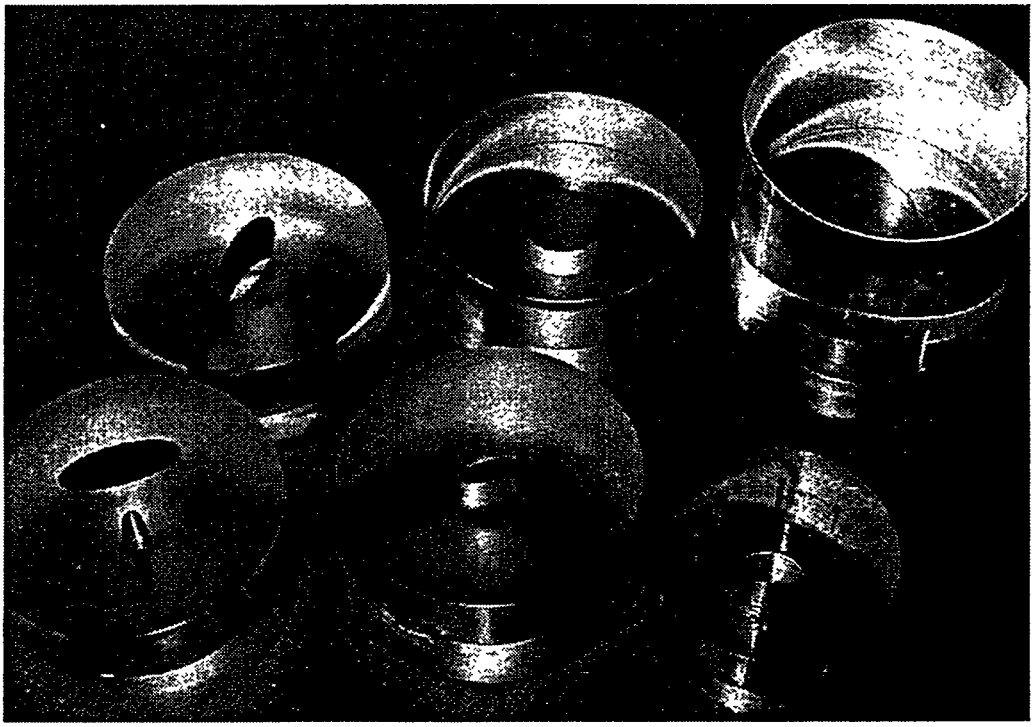

Photo 6.

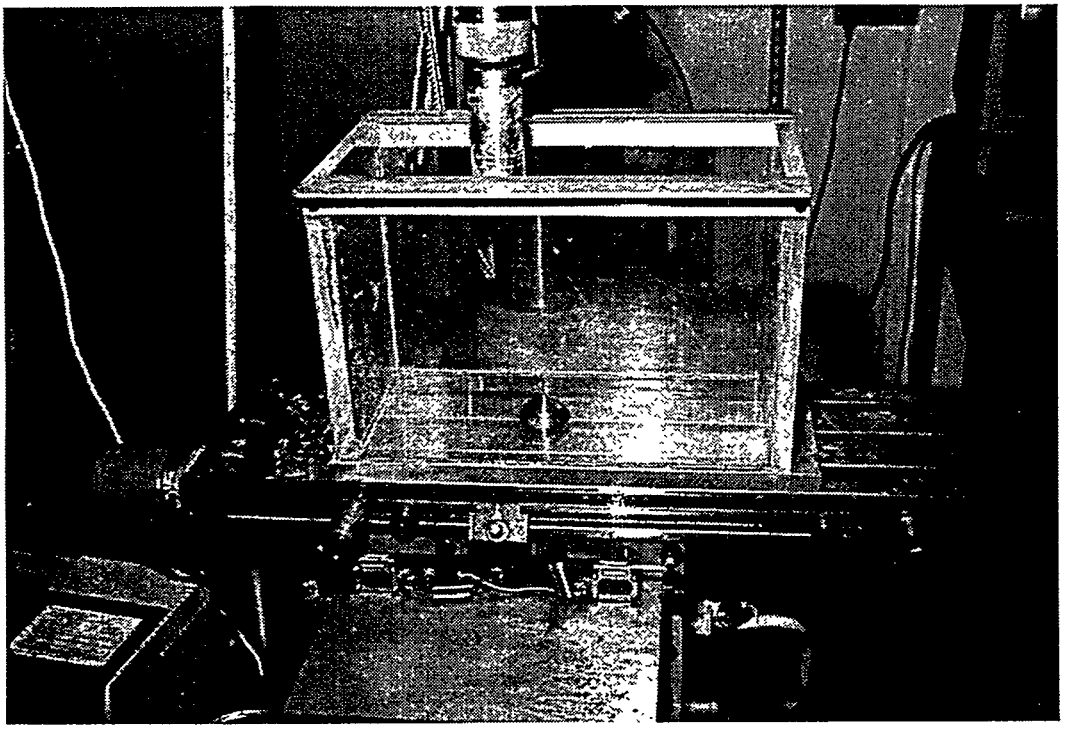

Photo 7.

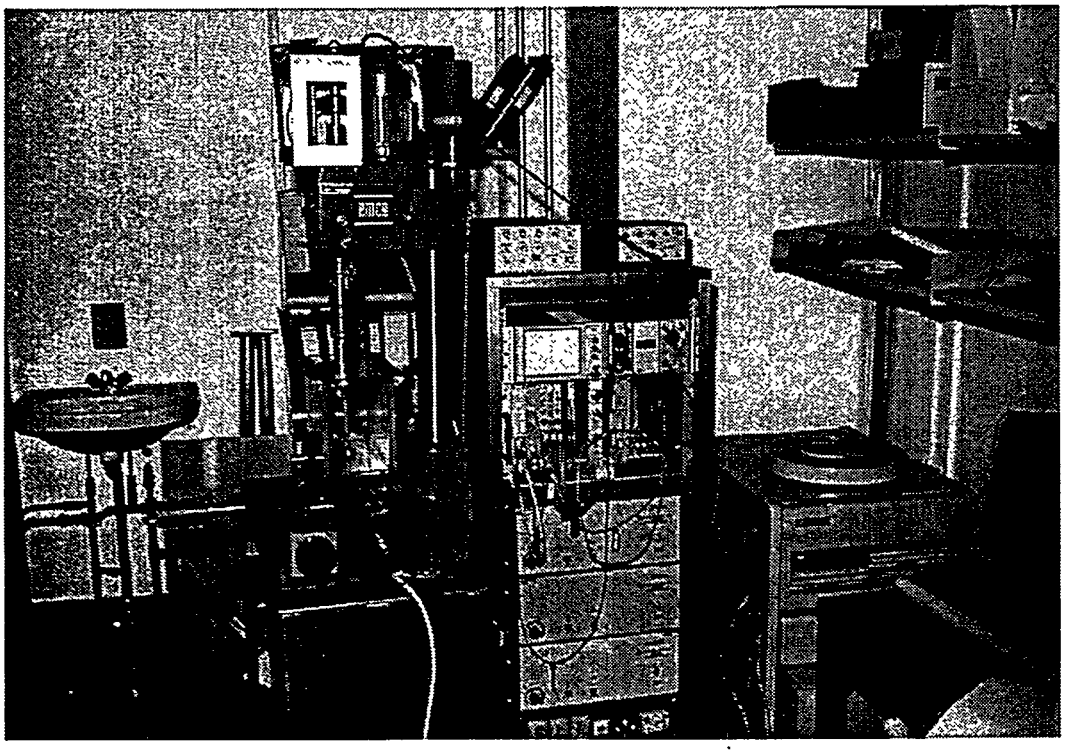

Photo 8.

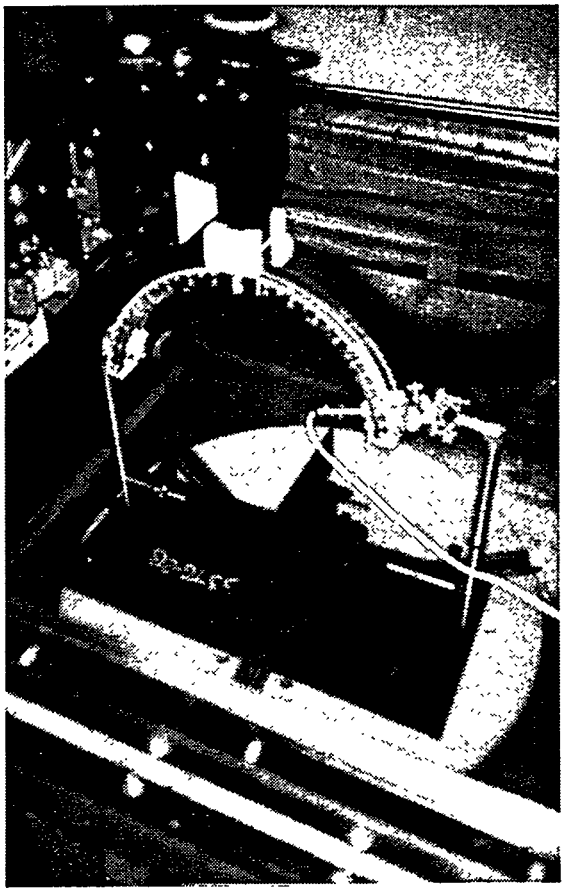

Photo 9.

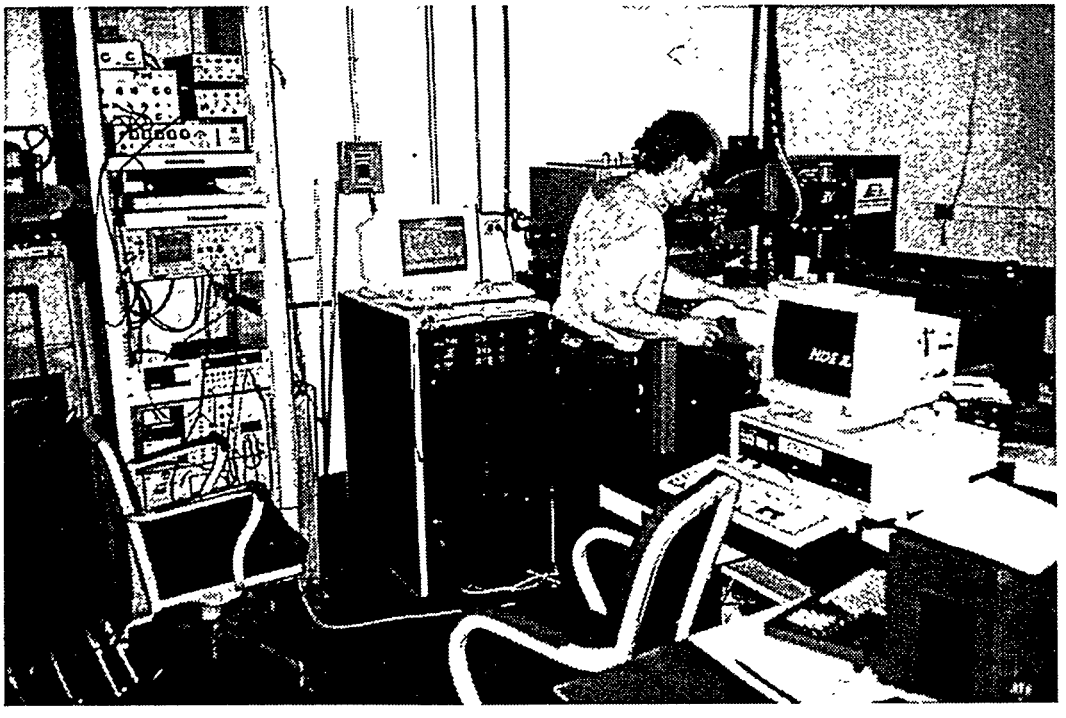

Photo 10.

Bibliographic Data Sheet **Risø-R-1057(EN)**

Title and author

A Circular Aperture Array for Ultrasonic Tomography and Quantitative NDE

Steen Arnfred Nielsen

(This thesis is part of the requirements to obtain the Ph.D. degree from the Technical University of Denmark)

ISBN	ISSN
87-550-2400-9	0106-2840

Department	Date
Materials Research Department	August 1998

Pages	Tables	Illustrations	References
167	15	103	203

Abstract (max. 2000 characters)

The main topics of this thesis are ultrasonic tomography and ultrasonic determination of elastic stiffness constants. Both issues are based on a synthetic array with transducer elements distributed uniformly along a circular aperture, i.e., a circular aperture array. The issues are treated both theoretically and experimentally by broadband pulse techniques.

Ultrasonic tomography, UCT, from a circular aperture is a relatively new imaging technique in Non-destructive Evaluation (NDE) to acquire cross sectional images in bulk materials. A filtered back-projection algorithm is used to reconstruct images in four different experiments and results of attenuation, velocity and reflection tomograms in Plexiglas or *AlSi*-alloy cylinders are presented. Two kinds of ultrasonic tomography are introduced: bistatic and monostatic imaging. Both techniques are verified experimentally by Plexiglas cylinders. Different reconstruction artifacts are discussed and theoretical resolution constraints are discussed for various configurations of the circular aperture array. The monostatic technique is used in volumetric imaging. In the experimental verification artificial and real discontinuities in a cylindrical *AlSi*-alloy are compared with similar discontinuities in a Plexiglas specimen. Finally, some limitations to UCT are discussed.

The circular aperture array is used to determine five independent elastic stiffness constants of a unidirectional glass/PET (Poly Ethylene Teraphthalate) laminate. Energy flux propagation and attenuation of ultrasonic waves are considered and velocity surfaces are calculated for different planes of interest. Relations between elastic stiffness constants and engineering constants (i.e., Young's moduli, shear moduli and Poisson's ratios) are discussed for an orthotropic composite. Six micromechanical theories are reviewed, and expressions predicting the elastic engineering constants are evaluated. The micromechanical predicted elastic stiffness constants for the unidirectional glass/PET laminate are compared with ultrasonic and mechanical test results. Finally, the capabilities and limitations of the applied ultrasonic method are discussed.

Descriptors INIS/EDB

Available on request from Information Service Department, Risø National Laboratory, (Afdelingen for Informationsservice, Forskningscenter Risø), P.O.Box 49, DK-4000 Roskilde, Denmark.
Telephone +45 46 77 46 77, ext. 4004/4005, Telefax +45 46 77 40 13